In search of the electron's electric dipole moment in thorium monoxide: an improved upper limit, systematic error models, and apparatus upgrades

A Dissertation
Presented to the Faculty of the Graduate School
of
Yale University
in Candidacy for the Degree of
Doctor of Philosophy

by
Brendon R. O'Leary

Dissertation Director: David DeMille

December 2016

Contents

List of Figures

List of Tables

Acknowledgements

I owe a great debt of gratitude to all those who made possible the work described in this thesis. This work was done under the supervision of, in collaboration with, and with the support of many people two whom I must say "thank you" including:

My advisor David DeMille who would always make time to talk through even the most trivial problems, and who providided useful insights when we were stuck.

John Doyle and Jerry Gabrielse who taught me more than I ever wanted to know about engineering and design and provided great advice.

Emil who taught me to wrangle lasers and helped me navigate the lab when I was starting out.

All of my colleagues in the ACME Collaboration who preceded me and with whom I worked, who made my time spent in the group a good experience.

The DeMille, Doyle, and Gabrielse groups with whom I could always chat about crazy ideas or from whom I could always borrow parts.

Daphne Klemme and Jan Ragusa who helped me with paperwork and administrative issues associated with working at both Yale and Harvard.

Dave Johnson, Stan Cotreau, Jim MacArthur, and Steve Sansone who taught me to make things and made it possible to continue to make things.

Anala who has always been there for me.

Abstract

In search of the electron's electric dipole moment in thorium monoxide: an improved upper limit, systematic error models, and apparatus upgrades

Brendon R. O'Leary

2016

Searches for violations of discrete symmetries can be sensitive probes of physics beyond the Standard Model. Many models, such as supersymmetric theories, introduce new particles at higher masses that include new CP-violating phases which are thought to be of order unity. Such phases could generate measurable permanant electric dipole moments (EDMs) of particles. The ACME collaboration has measured the electron's EDM to be consistent with zero with an order of magnitude improvement in precision compared to the previous best precision (J. Baron et al., ACME collaboration, *Science* **343** (2014), 269–272) with a spin precession measurement performed in the H state of a beam of thorium monoxide (ThO). This limit constrains time-reversal violating physics for particles with masses well into the TeV scale. In this thesis I discuss the details of this measurement with an emphasis on the data analysis, search for systematic errors, and systematic error models that contributed to this result. I also discuss implemented and planned upgrades to the experimental apparatus intended to both improve the statistical sensitivity and reduce its susceptibility to systematic errors. At this time, the upgraded apparatus has been demonstrated to have a statistical sensitivity to the electron EDM that is more than a factor of $10\times$ more precise than our previous measurement.

Chapter 1

Introduction

> Every mystery ever solved had been a puzzle from the dawn of the human species right up until someone solved it.
>
> Eliezer Yudkowsky, Harry Potter and the Methods of Rationality

1.1 Symmetry in Physics

We as humans tend to have a bias toward a world with more symmetry rather than less [60]. Perhaps this is unsurprising since Occam's razor would prefer a hypothesis with symmetry over one with asymmetry assuming both hypotheses were consistent with the available data. Consider as an example the evolution of our knowledge of the structure of the Solar System. Around 350 BC Plato postulated that the earth was a point of symmetry in the cosmos and all celestial bodies rotated around the earth with circular orbits and fixed angular velocity [29]. However, in order to remain consistent with furthur astronomical measurements this geocentric model was reduced in symmetry by introducing epicycles in the circular orbits and shifting the earth away from the point of symmetry.

More surprising is the fact that the laws of physics do, in fact, tend to exhibit a considerable amount of symmetry [60]. After contributions to a heliocentric model by Copernicus and Kepler, Newton postulated his spherically symmetric law of gravity which perhaps outdid even the Platonian model in terms of simplicity, but had far more explaining power with respect to astronomical observations [29].

Nevertheless, the symmetries postulated in the laws of physics must be supported by experiment, and measured deviations in these symmetries can provide clues regarding im-

provements that can be made to our current understanding of physics. For example, observed violations of parity (P) symmetry [176] and charge-parity (CP) symmetry [32] have provided motivation for and aided in understanding the weak and strong forces [94, 106] respectively. Additionally, precision measurements of charge-parity-time (CPT) invariance and Lorentz invariance [10, 16, 40, 45, 63, 80, 81, 97, 114] provide experimental support for the assumptions that underlie modern quantum field theories [151].

This thesis concerns my contributions as a member of the ACME Collaboration, with much credit due to those with whom I worked, to measurements of the permanent electric dipole moment (EDM) of the electron in a beam of thorium monoxide (ThO) molecules. These measurements are the most recent and most sensitive [6] in a series of EDM measurements that are a part of a tradition that began more than 50 years ago with Purcell and Ramsey's proposal to test the validity of time reversal symmetry (T) in the laws of physics of elementary particles [139]. Since then many measurements have been performed with ever increasing precision and with ever increasing diversity of systems. For more on the history of these measurements, I direct the reader to references [92] and [35].

In this thesis, I do not attempt to provide a full detailed account of the ACME experiment, and hence will frequenctly direct the reader to additional details to our published works [6, 93, 129, 135] and other theses [69, 77, 86, 158, 164]. Instead, I will provide details of the first ACME measurement, referred to as ACME I throughout, with an emphasis on the data analysis, search for systematic errors, and systematic error models that contributed to that result. I also discuss implemented and planned upgrades to the experimental apparatus intended to both improve the statistical sensitivity and reduce its susceptibility to systematic errors in a future measurement, referred to as ACME II.

1.2 The Standard Model and Beyond

The Standard Model (SM), which provides our current best understanding of particle physics, has an impeccable track record when it comes to providing predictions that are consistent with experiments. Some of the most impressive include agreement between the SM and the measurement of the electron's magnetic moment [72], and the discovery of the Higgs Boson [30, 56]. However the SM is known to be incomplete in that it does not currently provide answers to the following large open questions in physics:

1. **Dark Matter:** What is dark matter? [20]

2. **Baryon Asymmetry:** Why do we observe so much more matter than antimatter despite the laws of physics treating both nearly equivalently? [44]

3. **Hierarchy Problem:** Why is gravity so weak and why is the Higgs mass close to the electroweak scale rather than the Plank scale? [178]

Theories beyond the Standard Model (BSM) attempt to solve these problems by introducing new particles or interactions and in doing so result in measurable differences between the SM and BSM models.

For example, Supersymmetric models introduce a symmetry between known fermions and unknown bosons and between known bosons and unknown fermions. These as-of-yet undiscovered particles, termed "super-partners", must be at or above the electroweak energy scale, or else they would likely have been detected in earlier accelerator experiments, assuming that they do not interact too weakly with the known particles. The contributions to the Higgs mass due to each particle/super-partner pair would nearly cancel which could provide a solution to the hierarchy problem [110, 178]. Furthurmore, if one of these as-of-yet undiscovered particles is stable, this particle could constitute a Weakly Interacting Massive Particle (WIMP) which is a class of candidates for explaining Dark Matter [89]. Additionally, this array of postulated new particles would introduce a large number of possible CP violating phases in their interactions with other particles (in analogy to the phases in the CKM matrix [18]). Given that similar phases in the Standard Model have been observed to be of order unity, there is no reason to expect these phases to be small or exactly zero. Hence, these phases could provide sufficient CP violation to satisfy conditions that Sakharov determined [144] would be necessary to generate the observed matter/antimatter asymmetry during the evolution of the early universe[1] [84].

BSM models such as Supersymmetry (SUSY) are currently being tested with a number of complementary methods including high-energy accelerator experiments [1, 2, 13], dark matter experiments [3, 7, 8], and electric dipole moment measurements [6, 82, 108]. An

1. Sakharov's conditions for *bariogenesis* [144], the generation of a baryon number excess $B > 0$ assuming that we start with a baryon symmetric universe $B = 0$, include 1.) B-number violating interactions, 2.) C and CP violating interactions, 3.) Thermodynamic Non-equilibrium in the early universe. All of these conditions are satisfied by the Standard Model, but it is generally agreed that it does not include sufficient CP-interactions to generate the size of baryon asymmetry that we currently observe [65, 83]

examination by Feng [59] of the SUSY parameter space that has been excluded, under a set of assumptions that are considered reasonable by some theorists, indicates that each of these experimental methods are indeed complementary and that each method is probing SUSY mass scales at or higher than the TeV scale. Based on experimental progress in improvements in sensitivities of each of these types of experiments, it is possible that in the not too distant future we will either discover Supersymmetry, exclude all of the viable parameter space in the eyes of most theorists, or theorists will significantly shift their definitions of what constitutes viable parameter space (hopefully for a well founded reason). In any case, progress will have been made in our understanding of physics.

The current best limit on the electron EDM was produced by the ACME I experiment in 2014 [6]:[2]

$$d_e \leq 9.3 \times 10^{-29}\ e \cdot \text{cm (at a 90\% confidence level)}. \tag{1.1}$$

Many extensions to the SM predict electron EDM values many orders of magnitude higher than the SM prediction of $< 10^{-38}\ e \cdot \text{cm}$ [92,137,138], meaning measurement of a non-zero electron EDM at current experimental sensitivity would be a clear signature of new physics. Some examples of electron EDM predictions are shown in figure 1.2 and are depicted as leading order Feynman diagrams that contribute to the modification of the interaction between the electron and the electromagnetic field in the presence of the electron EDM interaction.

The Minimal Supersymmetric model (MSSM) generates an electron EDM at 1-loop order in perturbation theory due to a coupling between the electron and it's superpartner, the selectron, which is predicted to be in the range of $10^{-25} - 10^{-27}\, e \cdot \text{cm}$, assuming that the supersymmetric particles have masses around $.1 - 1$ TeV and the CP-violating phase for the interaction is in the range of $\sin\phi_{\text{CP}} \sim .1 - 1$ [54]. This model has been fairly well constrained by the ACME I and previous EDM measurements. The Split Supersymmetric model (SSUSY) has leading order contributions to the electron EDM at 2-loop order [15, 54,66] which predicts an electron EDM in the range of $10^{-27} - 10^{-29} e \cdot \text{cm}$ with comparable assumptions. A large swath of the parameter space in this model was constrained by ACME I.

2. Note that the limit we report here uses an updated value for $\mathcal{E}_{\text{eff}} = 78.4$ GV/cm which is obtained by averaging the results from references [61, 154].

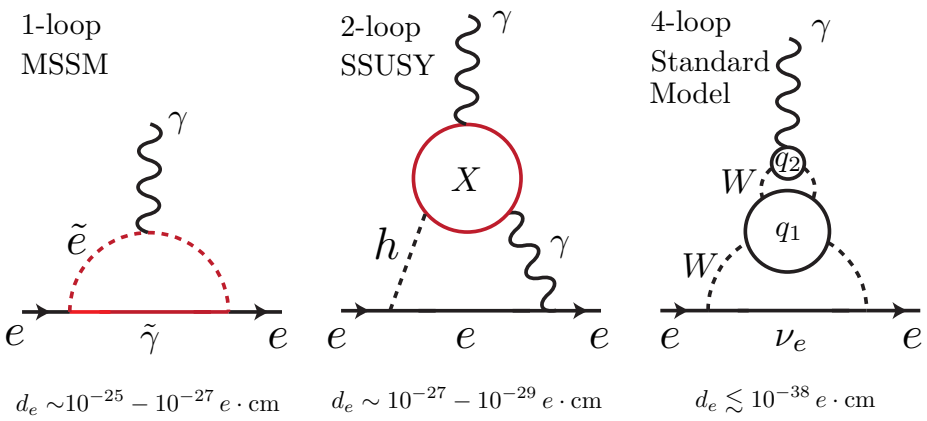

Figure 1.1: Comparison of Supersymmetric and Standard Model electron EDM predictions. These predictions are depicted as leading order Feynman diagrams, where the electron EDM appears as a modification in the interaction between the electron, e, and the electromagnetic field, γ. Left: In the Minimal Supersymmetric Model (MSSM), the electron couples to the selectron, $\tilde{e}$, and generates an electron EDM at 1-loop order in the range of $10^{-25} - 10^{-27}\, e \cdot$ cm [54] which has been experimentally excluded. Center: In Split Supersymmetry (SSUSY) the leading contribution to the electron EDM is a Barr-Zee diagram [15,66] at 2-loop order which is in the range of $10^{-27} - 10^{-29}\, e \cdot$ cm which we partially excluded with ACME I. Right: The Standard Model generates an electron EDM at 4-loop order (or higher) with a magnitude smaller than $10^{-38}\, e \cdot$cm [24]– since the Standard Model background is predicted to be beyond current experimental sensitivity, any observed signal must come from physics beyond the Standard Model.

From a more generic perspective, given a CP-violating phase ϕ_{CP}, and a sensitivity δd_e to the electron EDM, we can estimate the mass scale Λ of new physics being probed, according to the following formula for an n-loop process [54]:

$$\Lambda^2 = e\frac{m_e}{\delta d_e}\left(\frac{\alpha}{4\pi}\right)^n \sin\phi_{CP} \tag{1.2}$$

where e is the electron charge, m_e the electron mass, α is the fine structure constant, and ϕ_{CP} is a CP-violating phase. Assuming that $\sin(\phi_{CP}) \sim 1$ [137], we find that the ACME I result interrogates energy scales for one-loop processes up to around 10 TeV. Similar analysis shows that our result was sensitive to two-loop effects up to around the 1 TeV mass scale. While any such estimates are inherently model-dependent, with reasonable assumptions the ACME I experiment is probing high energy physics at energy scales usually associated with the largest particle accelerators with a very precise low energy experiment.

1.3 Sensitivity of atoms and molecules to the electron EDM

The electron's EDM, $\vec{d_e}$, is a vector quantity that is aligned along (or against) the axis of the electron's spin, $\vec{S}$ [92]. By convention, we relate define the electron EDM vector as $\vec{d_e} = 2d_e\vec{S}$, such that a measurement of any Cartesian component of $\vec{d_e}$ yields a value of $\pm d_e$. (Here and throughout, we set $\hbar = 1$.) For an electron moving non-relativistically, the electron's EDM interacts with an electric field $\vec{\mathcal{E}}$ via the dipole Hamiltonian

$$\mathcal{H}_{\mathrm{EDM}} = -\vec{d_e} \cdot \vec{\mathcal{E}} \propto \vec{S} \cdot \vec{\mathcal{E}}. \tag{1.3}$$

Under time reversal, T, $\vec{S}$ reverses direction, but $\vec{\mathcal{E}}$ is unchanged. Similarly, under space inversion, P, $\vec{S}$ is unchanged, but $\vec{\mathcal{E}}$ reverses direction. Hence $\mathcal{H}_{\mathrm{EDM}}$ is odd under P and T, which implies that if a nonzero electron EDM is found, the theory of nature is T, and P violating, and assuming CPT invariance, CP-violating as well. Hence a measured non-zero EDM could contribute to an understanding of the observed Baryon asymmetry of the universe as per the discussion in the previous section.

To measure the electron EDM, we can look for an energy shift due to the interaction in equation 1.3. Since 1964, every improvement in experimental sensitivity to d_e has been obtained by measuring this shift for electrons bound in neutral atoms or molecules [4, 33, 82, 101, 118, 136, 141, 147, 159, 168]. This might seem surprising at first glance, since Schiff's theorem states that there can be no net electric field acting on a non-relativistic point particle bound in a neutral system [149]. However, in 1958 Salpeter showed that, when relativistic effects are taken into account, a neutral species can experience an energy shift due to an electron EDM when an external electric field $\mathcal{E}_{\mathrm{ext}}$ is applied [145]. In 1965 Sandars showed, that the size of the resulting energy shifts can be much larger than $d_e\mathcal{E}_{\mathrm{ext}}$ [146], resulting in an enhancement in sensitivity when using bound electrons over free ones.

More detailed explanations of the evasion of Schiff's theorem can be found elsewhere, e.g. [34, 36, 92], but we summarize the basic principle here. The relativistic interaction between the electron EDM and an electric field $\vec{\mathcal{E}}$ and magnetic field $\vec{\mathcal{B}}$ is given by the Dirac Hamiltonian,

$$\mathcal{H}_{\mathrm{EDM}} = -d_e(\gamma^0\vec{\Sigma} \cdot \vec{\mathcal{E}} + i\vec{\gamma} \cdot \vec{\mathcal{B}}), \tag{1.4}$$

acting on 4-component spinors where $\gamma^\mu = (\gamma^0, \vec{\gamma})$ are the Dirac gamma matrices, and

$\vec{\Sigma} = \gamma^0\gamma^5\vec{\gamma}$ is the relativistic spin operator. Neglecting the relativistic interaction between the electron EDM and the magnetic field, expanding the Dirac wavefunction in terms of plane waves with well defined velocity $\vec{\beta} = \vec{v}/c$, and projecting on the electron subspace of the 4-component Dirac spinor, this interaction takes the form of a relativistically length contracted electron EDM interacting with an applied electric field,

$$\mathcal{H}_{\text{EDM}} = -2d_e\left(\vec{S} - \frac{\gamma}{1+\gamma}\vec{\beta}\cdot\vec{S}\vec{\beta}\right)\cdot\vec{\mathcal{E}}, \tag{1.5}$$

where γ is the Lorentz factor. The first term in this expression is the non-relativistic EDM interaction that vanishes by Schiff's theorem. The second, relativistic term results in non-zero energy shifts to the bound states in atoms and molecules which are typically parameterized in analogy to equation 1.3,

$$\langle\mathcal{H}_{\text{EDM}}\rangle \equiv -\langle\vec{d}_e\rangle\cdot\vec{\mathcal{E}}_{\text{eff}}. \tag{1.6}$$

where $\vec{\mathcal{E}}_{\text{eff}}$ is the sensitivity of a given state to the existence of the electron's EDM in a given species. Detailed calculations show that this "effective electric field" within an atom or molecule can be significantly larger in magnitude than the applied external field. The size of $\mathcal{E}_{\text{eff}}$ is maximal for systems where a valence electron has significant wavefunction amplitude near a highly-charged nucleus. In such species with a nucleus of atomic number Z, $\mathcal{E}_{\text{eff}}$ scales approximately as [92]

$$\mathcal{E}_{\text{eff}} \propto P_{\mathcal{E}}Z^3R(Z), \tag{1.7}$$

where $P_{\mathcal{E}} \in [0,1)$ is the degree of electric polarization of the state and R is a relativistic factor that is roughly constant for $Z \ll \alpha^{-1}$, but grows quickly as Z approaches α^{-1} [34, 42, 78, 92]. For fully polarized systems with $Z \approx 90$ (as with our molecule of choice, ThO), the effective electric field can reach values as large as $\mathcal{E}_{\text{eff}} \approx 100$ GV/cm. In practice, the maximum polarization attainable with atoms, even in the highest laboratory static electric fields (~ 100 kV/cm), is $P_{\mathcal{E}} \sim 10^{-3}$. Nevertheless, this can lead to values of $\mathcal{E}_{\text{eff}}$ nearly 1,000 times larger than the applied laboratory field (e.g. $\mathcal{E}_{\text{eff}}\sim 70$ MV/cm in Tl atoms [141]). Using this kind of enhancement, the limit on d_e was reduced by six orders of magnitude by the first atom-based electron EDM measurement [147]. Further improvement

is afforded by working with polar molecules, which can be completely polarized, $P_{\mathcal{E}} \sim 1$ due to having much more closely spaced levels of opposite parity, which are associated with their rotational motion [34, 42, 78]. In ThO, the effective electric field has been calculated to be about $\mathcal{E}_{\text{eff}} \approx 78.4$ GV/cm [61, 154].

To measure the electron's EDM, the electron spin[3] is prepared in a superposition of states parallel and antiparallel to $\vec{\mathcal{E}}_{\text{eff}}$. After an interaction time τ, the energy shift in equation 1.3 produces a relative phase accumulation $2\phi_{\text{EDM}} = -2d_e\mathcal{E}_{\text{eff}}\tau$ between these states. Colloquially, we frequently speak of the experiment in analogy to a classically precessing top. We can think of the prepared spin state, the top, as having been aligned orthogonal to $\vec{\mathcal{E}}_{\text{eff}}$, which plays the role of the gravitational force, which then results in a spin precession about $\vec{\mathcal{E}}_{\text{eff}}$ by an angle ϕ_{EDM}.

For a shot-noise-limited measurement, the uncertainty in the electron EDM, δd_e, is given by

$$\delta d_e = \left(2\tau\mathcal{E}_{\text{eff}}\sqrt{N}\right)^{-1}, \tag{1.8}$$

where N is the number of measurements. The large values of $\mathcal{E}_{\text{eff}}$ accessible in many molecules have motivated several recent electron EDM searches [49, 82, 105].

1.4 Thorium monoxide for an electron EDM search

Thorium monoxide (^{232}Th^{16}O) has a number of properties that make it well-suited to an electron EDM measurement, both by enhancing statistical sensitivity and by suppressing systematic errors relative to previous measurements [82, 141]. We performed our measurements in the H electronic state of ThO, which has two valence electrons in a $(\sigma\delta)^3\Delta_1$ molecular state. Such states were first proposed for use in an electron EDM measurement in reference [113]. The σ orbital valence electron wavefunction has a large amplitude near the heavy Th nucleus, facilitating the relativistic speeds required for a large electron EDM sensitivity, $\mathcal{E}_{\text{eff}}$, as described in section 1.3. The H state of ThO has one of the largest calculated values of $\mathcal{E}_{\text{eff}} \approx 78$ GV/cm [61, 154]. We note that the value of $\mathcal{E}_{\text{eff}}$ in our experiment with ThO is more than 5 times larger than that attained in experiments using YbF, which set the previous best electron EDM limit [5, 116, 148] before the ACME I result, and

3. the spin of the valence electron with large wavefunction overlap with the heavy nucleus

over 1,000 times larger than that in experiments using Tl atoms [141].

All $^3\Delta_1$ states have very small magnetic moments [76] since the $\delta_{3/2}$ orbital valence electron serves to nearly cancel the magnetic moment of the $\sigma_{1/2}$ orbital. The actual magnetic moment of H deviates from zero primarily because of mixing with other states on the 1% level [135]. We express ThO molecule states using the basis $|Y, J, M, \Omega\rangle$, where Y is the electronic state, J is the total angular momentum, M is the projection of J onto the laboratory $\hat{z}$-axis, and Ω is the projection of the electronic angular momentum onto the internuclear axis, $\hat{n}$, which points from the lighter nucleus (O) to the heavier nucleus (Th). We used the $|H, J = 1, M, |\Omega| = 1\rangle$ rotational manifold for our measurement, for which the magnetic moment is $\mu_{H,J=1} = g_{H,J=1}\mu_\mathrm{B}$, where $g_{H,J=1} = -0.00440(5)$ is the associated g-factor [135, 167] and μ_B is the Bohr magneton. This small g-factor, generic to all molecules with this structure, ensures that the H state is particularly insensitive to spurious magnetic fields that could cause systematic errors.

States with nonzero Ω, $|\Omega| > 0$, have closely spaced pairs of opposite-parity levels with identical values of J and M, called "Ω-doublets" (also referred to as Λ doublets), which are split by energy $\Delta_{A,J}$ (where A is the electronic state and J is the total angular momentum) due to the Coriolis effect in the rotating molecule [27,75,102]. The application of an electric field $\vec{\mathcal{E}}$ mixes the $M \neq 0$ opposite-parity levels via the Stark interaction, $-\vec{D} \cdot \vec{\mathcal{E}}$, where D is the electric dipole operator, and from here on $\vec{\mathcal{E}}$ is the applied (laboratory) field. In the limit $|\langle\vec{D}\rangle \cdot \vec{\mathcal{E}}| \gg \Delta_{A,J}$, the molecule is fully polarized, the internuclear axis is nearly aligned or anti-aligned with the applied electric field, and the alignment orientation is described by quantum number $\tilde{\mathcal{N}} \equiv \hat{\mathcal{E}} \cdot \hat{n} = \pm 1$. This structure is shown for the H state of ThO in figure 1.2.

The use of molecules with Ω-doublet structure for an electron EDM measurement, first explored in in the context of experiments using PbO for such a measurement [41, 42], is of great importance to our experiment. The $|H, J = 1\rangle$ manifold has an Ω-doublet splitting $\Delta_{H,J=1} \approx 2\pi \times 360$ kHz[4] [86] and an electric dipole moment $D_{H,J=1} \equiv |\langle H, J = 1, M = \pm 1, \Omega|\vec{D} \cdot \hat{z}|H, J = 1, M = \pm 1, \Omega\rangle| \approx 2\pi \times 1$ MHz/(V/cm) [77]; this permits full (>99%) polarization of the state in small applied electric fields, $\mathcal{E} > 10$ V/cm, allowing us to take full advantage of the large $\mathcal{E}_\mathrm{eff}$ in ThO. The Ω-doublet structure is also useful in rejecting

4. Throughout the paper, we give numerical values of energies (with $\hbar = 1$) in terms of angular frequencies by using the notation $2\pi \times f$, where f is a linear frequency in units of Hz.

systematic errors since it allows for spectroscopic reversal of $\vec{\mathcal{E}}_{\text{eff}} \propto -\hat{n}$ by addressing different $\tilde{\mathcal{N}}$ states without reversing the applied electric field, thereby reversing the sign of the electron EDM energy shift [90]. This is discussed in greater detail in section 3.3.

The H state in ThO is metastable with a lifetime ≈ 1.8 ms [165], limiting our measurement time to $\tau \approx 1$ ms. We note that this is comparable to previous beam-based eelectron EDM measurements where the atomic/molecular states used had significantly longer lifetimes [82, 140, 165], but shorter than the precession times now being observed in trap-based EDM experiments [23, 108].

As with many other species, ThO proved nicely compatible with a new approach to creating molecular beams, the hydrodynamically enhanced cryogenic buffer gas beam [87, 111, 132]. This method provides a cold, high-flux and low-divergence beam [88] yielding a large number of molecules in the few lowest-lying quantum states. The molecule beam's forward velocity (≈ 180 m/s) was also lower than a typical supersonic beam, which helped minimize the apparatus length for a given coherence time.

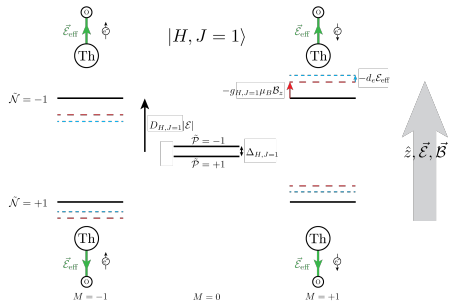

Figure 1.2: Energy level diagram of the states in the $|H, J = 1\rangle$ state manifold in ThO in the presence of a fully polarizing electric field, $\vec{\mathcal{E}}$. In the absence of applied fields, opposite-parity states $|H, J = 1, M, \tilde{\mathcal{P}}\rangle \equiv |H, J = 1, M\rangle(|\Omega = -1\rangle - \tilde{\mathcal{P}}|\Omega = +1\rangle)/\sqrt{2}$, where $\tilde{\mathcal{P}} = \pm 1$ is the state parity, are separated by energy $\Delta_{H,J=1} \approx 2\pi \times 360$ kHz. For each $M = \pm 1$, the two $\tilde{\mathcal{P}} = \pm 1$ states are nearly fully mixed by an electric field $\mathcal{E} > 10\,\text{V/cm}$. These fully polarized states are approximately given by $|H, J = 1, M, \tilde{\mathcal{N}}\rangle \approx |H, J = 1, M, \Omega = M\tilde{\mathcal{N}}\tilde{\mathcal{E}}\rangle$ where $\tilde{\mathcal{N}} = \pm 1$ denotes the alignment orientation of the molecule with respect to the applied electric field. The Stark, Zeeman, and electron EDM energy shifts are depicted for the states $|H, J = 1, M = \pm 1, \tilde{\mathcal{N}} = \pm 1\rangle$ with the black, red, and light blue arrows respectively. The orientation of $\vec{\mathcal{E}}_{\text{eff}}$ (green arrows), the spin of the valence electron in the σ orbital (black arrow next to molecule), the external electric field $\vec{\mathcal{E}}$, and the external magnetic field $\vec{\mathcal{B}}$ are shown relative to the laboratory $\hat{z}$ direction which is oriented upwards on the page.

Chapter 2

Measurement Scheme and Data Analysis

> "Did I do anything wrong today," he said, "or has the world always been like this and I've been too wrapped up in myself to notice?"
>
> Douglas Adams, The Hitchhiker's Guide to the Galaxy

2.1 The spin precession measurement

We performed a spin precession measurement, resembling previous beam-based electron EDM experiments [33, 82, 141], on ^{232}Th^{16}O molecules in a pulsed molecular beam generated by a cryogenic buffer gas beam source. Figure 2.1 shows a simplified schematic of the ACME I apparatus and figure 2.3 illustrates the measurement scheme for the ACME I spin precession measurement. The molecules fly at velocity $v \approx 180$ m/s into a magnetically shielded region with nominally uniform and parallel electric $\vec{\mathcal{E}}$ and magnetic $\vec{\mathcal{B}}$ fields. Molecule population is transferred from $|X^1\Sigma^+, J = 1, M = \pm 1\rangle$ in the electronic ground state to the metastable $|H, J = 1, M = \pm 1, \Omega = \pm\tilde{\mathcal{N}}\tilde{\mathcal{E}}\rangle \equiv |\pm, \tilde{\mathcal{N}}\rangle$ state manifold (in the $|\pm, \tilde{\mathcal{N}}\rangle$ nomenclature we use $\pm$ to refer to $M = \pm 1$) by optical pumping through the short-lived $|A^3\Pi_{0^+}, J = 0, M = 0\rangle$ state with a 943 nm laser, which partially decays to $|H\rangle$. This results in an even distribution of population in an incoherent mixture of the four $|\pm, \tilde{\mathcal{N}}\rangle$ states in H. Figure 2.2 shows the electronic states of ThO and transition wavelengths relevant to the electron EDM measurement in ACME I and II.

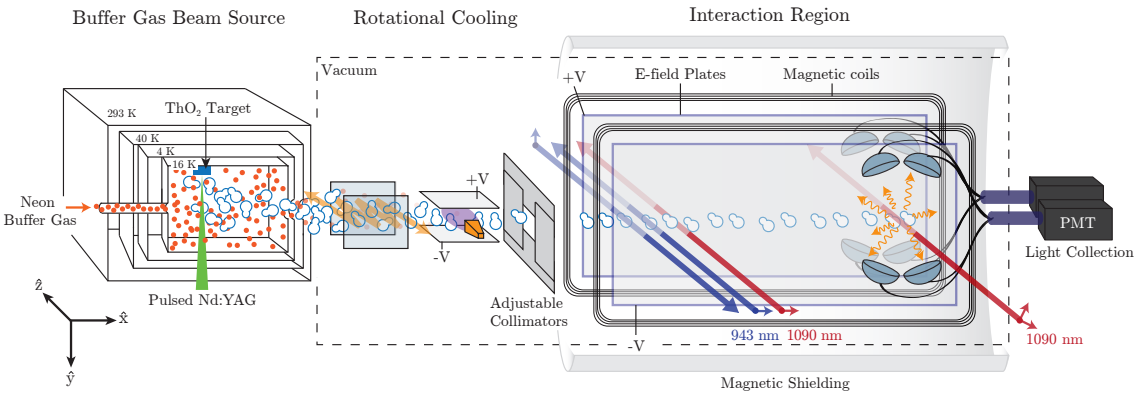

Figure 2.1: A schematic of the ACME I apparatus. A beam of ThO molecules was produced by a cryogenic buffer-gas-cooled source. After exiting the source, the molecules were rotationally cooled via optical pumping and microwave mixing and then collimated before entering a magnetically shielded spin-precession region where nominally uniform magnetic and electric fields were applied. Using optical pumping, the molecules were transferred into the H state and then prepared into a coherent spin state. The spin precesses for a distance of $\approx 22\,\mathrm{cm}$ and is then read out via laser-induced fluorescence. The fluorescence photons were collected by lenses and passed out of the chamber for detection by photo-multiplier tubes (PMTs).

Our experiment coordinate system, depicted in both figures 2.1 and 2.3, is defined as follows: The $\hat{z}$ direction is fixed in the lab and is either aligned or anti-aligned with respect to the applied electric field $\vec{\mathcal{E}}$, with the relative orientation specified by $\tilde{\mathcal{E}} = \hat{\mathcal{E}} \cdot \hat{z} = \pm 1$. $\hat{x}$ is specified approximately by the velocity of the molecule beam $\hat{x} \approx \hat{v}$, but is constrained to be perpendicular to $\hat{z}$. $+\hat{y}$ is approximately aligned with acceleration due to earths gravity, but is also specified to be perpendicular to $\hat{z}$ and $\hat{x}$. These three Cartesian coordinate directions constitute a right handed orthogonal coordinate system. Just as we defined $\tilde{\mathcal{E}}$ to specify the orientation of the applied electric field relative to $\hat{z}$, we also define the direction of the applied magnetic field by $\tilde{\mathcal{B}} \equiv \mathrm{sgn}(\hat{z} \cdot \vec{\mathcal{B}}) = \pm 1$. Since the directions of the fields are encoded by $\tilde{\mathcal{E}}$ and $\tilde{\mathcal{B}}$, we define the magnitudes of the fields along the $\hat{z}$ direction simply as $\mathcal{B}_z \equiv |\mathcal{B}_z|$ and $\mathcal{E} \equiv |\vec{\mathcal{E}}|$.

A superposition of the $M = \pm 1$ sub-levels in $|H, J = 1\rangle$ is prepared by optically pumping on the $X \to C$ transition at 1090 nm between states $|\pm, \tilde{\mathcal{N}}\rangle$ and $|C^1\Pi_1, J = 1, M = 0\rangle(|\Omega = +1\rangle - \tilde{\mathcal{P}}|\Omega = -1\rangle)/\sqrt{2} \equiv |C, \tilde{\mathcal{P}}\rangle$, where $\tilde{\mathcal{P}} = \pm 1$ is the excited state parity, with laser light linearly polarized in the xy plane. The state preparation laser frequency is tuned to spectroscopically select the molecule alignment $\tilde{\mathcal{N}}$, while the nearly degenerate $M = \pm 1$ states remain unresolved. The excited state C, which decays at a rate $\gamma_C \approx 2\pi \times 0.3$

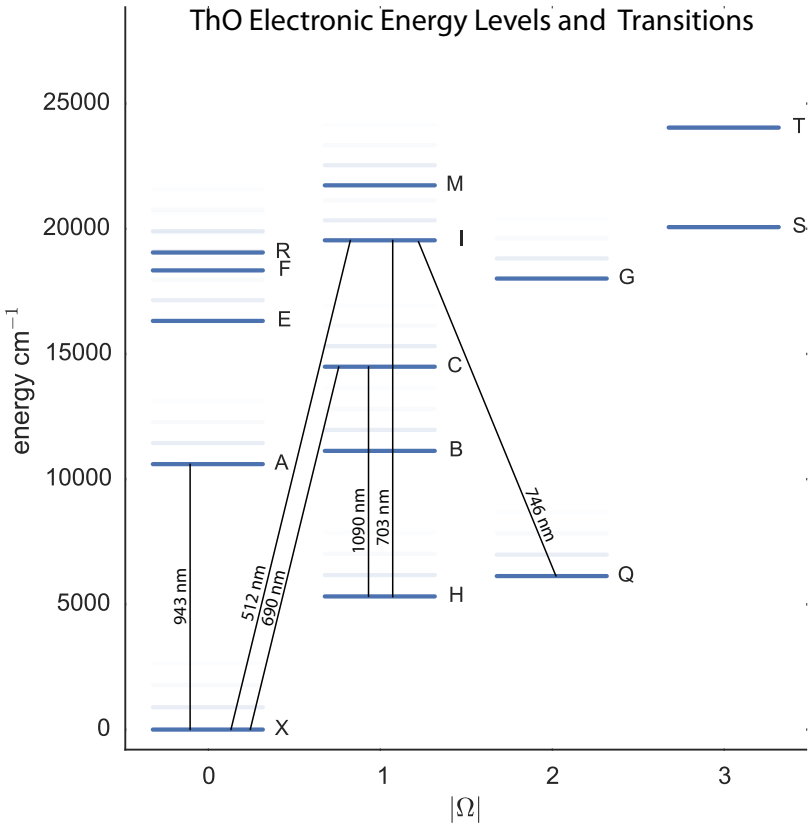

Figure 2.2: Levels and transitions in ThO used in our measurement of the electron EDM, based on [51, 133, 165]. Solid blue lines denote electronic states and the transparent blue lines denote vibrationally excited states corresponding to those excited states. Black lines indicate transitions that are relevant to either ACME I or ACME II, labeled by the transition wavelength in nm.

MHz, decays primarily (≈ 70 % [77]) to the ground state, and has negligible decay back to $|H\rangle$, so that one superposition of the two $|\pm,\tilde{\mathcal{N}}\rangle$ states is optically pumped out of H and the remaining orthogonal superposition, which is "dark" to the preparation laser beam, is the prepared state. The linear polarization of the state preparation laser beam, $\hat{\epsilon}_{\text{prep}}$, sets the relative coupling of each of the two $|\pm,\tilde{\mathcal{N}}\rangle$ states to $|C,\tilde{\mathcal{P}}\rangle$ and determines the spin alignment angle of the remaining state in the laboratory frame. The bright superposition $|B(\hat{\epsilon}_{\text{prep}})\rangle$ is pumped away, and the orthogonal dark superposition $|D(\hat{\epsilon}_{\text{prep}})\rangle$ remains.

For the moment, we consider the specific case $\tilde{\mathcal{P}} = +1$ and $\hat{\epsilon}_{\text{prep}} = \hat{x}$, (the general case will be discussed in section 2.2). In this case, the prepared state

$$|\psi(t=0),\tilde{\mathcal{N}}\rangle = \frac{1}{\sqrt{2}}(|+,\tilde{\mathcal{N}}\rangle - |-,\tilde{\mathcal{N}}\rangle) \tag{2.1}$$

has the electron spin aligned along the $\hat{y}$ axis. As the molecules traverse the spin precession region of length $L = 22$ cm (which takes a time $\tau \approx 1$ ms), the electric and magnetic fields exert torques on the electric and magnetic dipole moments, causing the spin to precess in the xy plane by angle ϕ; this corresponds to the state

$$|\psi(t=\tau), \tilde{\mathcal{N}}\rangle = \frac{1}{\sqrt{2}}(e^{-i\phi}|+, \tilde{\mathcal{N}}\rangle - e^{+i\phi}|-, \tilde{\mathcal{N}}\rangle), \tag{2.2}$$

where ϕ is given approximately by the sum of the Zeeman and electron EDM contributions to the spin precession angles,

$$\phi = -(\tilde{\mathcal{B}} g_{H,J=1} \mu_{\mathrm{B}} \mathcal{B}_z + \tilde{\mathcal{N}} \tilde{\mathcal{E}} d_e \mathcal{E}_{\mathrm{eff}})\tau. \tag{2.3}$$

The sign of the electron EDM term, $\tilde{\mathcal{N}}\tilde{\mathcal{E}}$, arises from the relative orientation between $\vec{\mathcal{E}}_{\mathrm{eff}}$ and the electron spin as illustrated in figure 1.2.

At the end of the spin precession region, we measure ϕ by optically pumping on the same $H \rightarrow C$ transition with the linearly polarized state readout laser beam. The polarization alternates rapidly between two orthogonal linear polarizations $\hat{X}$ and $\hat{Y}$, such that each molecule is subject to excitation by both polarizations as it flies through the detection region, and we record the modulated fluorescence signals F_X and F_Y from the decay of C to the ground state at 690 nm. This procedure amounts to a projective measurement of the spin onto $\hat{X}$ and $\hat{Y}$, which are defined such that $\hat{X}$ is at an angle θ with respect to $\hat{x}$ in the xy plane. To determine ϕ we compute the asymmetry,

$$\mathcal{A} \equiv \frac{F_X - F_Y}{F_X + F_Y} \propto \cos[2(\phi - \theta)]. \tag{2.4}$$

We set $\mathcal{B}_z$ and θ such that $\phi - \theta \approx (\pi/4)(2n+1)$ for integer n, so that the asymmetry is linearly proportional to small changes in ϕ and maximally sensitive to the electron EDM. A simplified schematic of the experimental procedure just described is shown in figure 2.3.

By repeating the measurement of ϕ after having reversed any one of the signs $\tilde{\mathcal{N}}$, $\tilde{\mathcal{E}}$ or $\tilde{\mathcal{B}}$, we may isolate the electron EDM phase from the Zeeman phase. In practice, we repeat the phase measurement under all 2^3 $(\tilde{\mathcal{N}}, \tilde{\mathcal{E}}, \tilde{\mathcal{B}})$ possible experiment states to reduce the sensitivity of the electron EDM measurement to other spurious phases, and we extract the phase $\phi^{\mathcal{N}\mathcal{E}} = -d_e \mathcal{E}_{\mathrm{eff}} \tau = \phi_{\mathrm{EDM}}$. Here, we have introduced the notation ϕ^u, discussed in

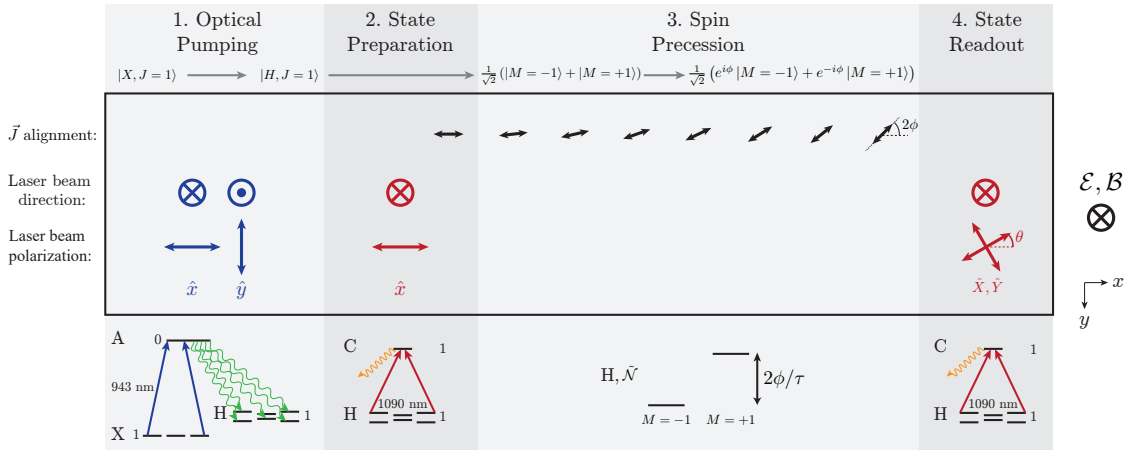

Figure 2.3: Simplified ACME I measurement scheme. **1.** Molecules in the $|X, J=1\rangle$ state are optically pumped via the A state into $|H, J=1\rangle$ by a retro-reflected (and offset in x) laser beam (blue arrows into/out of page), polarized along $\hat{x}$ and $\hat{y}$ (blue arrows). **2.** Molecules from one of the $\tilde{\mathcal{N}}$ states are then prepared in a superposition of M sub-levels ($M=-1,0,+1$ from left to right) by a linearly polarized laser beam (red) addressing the $H \to C$ transition. This aligns the molecule's angular momentum, $\vec{J}$, which in turn aligns the spin of the electron EDM-sensitive σ electron, which is on average aligned with $\vec{J}$. **3.** The angular momentum (and hence electron spin) then precesses due to the electric and magnetic fields present (into the page) by an angle ϕ. This precession is dominated by the magnetic interaction but also includes a term linear in d_e (see equation 2.3). **4.** The spin state is projected onto orthogonal superpositions of the M sublevels by laser beams polarized along $\hat{X}, \hat{Y}$ (red arrows). The resulting fluorescence is determined by the population in each superposition state and hence the precession angle ϕ. Here, the numbers next to the energy levels denote quantum number J.

detail in the next section, which we use throughout this document to refer to the component of ϕ that is odd under the set of switches listed in the superscript u, and implicitly even under those which are not listed (see section 2.2 and equation 2.16 for a rigorous definition). A component which is even under all switches is considered to be "non-reversing" and is given an "nr" superscript.

2.2 Experimental switching scheme to extract the electron EDM

To fully describe the method by which we extracted d_e from the data in section 2.3, and to describe the systematic error models in section 3, we must introduce some additional formalism to describe the spin precession measurement to generalize the simple case described in the previous section.

We work in the regime in which the Stark shift in $|H, J = 1, M, \tilde{\mathcal{N}}\rangle$ is approximately linear, $E_{\text{Stark}} \approx -\tilde{\mathcal{N}} D_{H,J=1}|\mathcal{E}|$, which holds when the Stark interaction energy is large compared to the Ω-doublet energy splitting $\Delta_{H,J=1}$ but small compared to the rotational splitting, described by the H-state rotational constant $B_{R,H} \approx 2\pi \times 9.8$ GHz, i.e. $\Delta_{H,J=1} \ll D_{H,J=1}\mathcal{E} \ll B_{R,H}$. In this regime, the molecular alignment is approximately related to Ω by $\tilde{\mathcal{N}} = \text{sign}(\tilde{\mathcal{E}} M \Omega)$; this relation is assumed throughout this document. This is a good approximation, but it is notable that due to the Stark interaction at first order in perturbation theory, each $|M, \tilde{\mathcal{N}}\rangle$ state is a superposition of all four $|H, J, M, \Omega\rangle$ states with $J = 1, 2$ and $\Omega = \pm 1$. This effect is discussed further in sections 4.2.3 and 5.6.1.

Let us consider the initial preparation of the spin-aligned state again. Starting from an incoherent mixture of the four $|\pm, \tilde{\mathcal{N}}\rangle$ states, we perform optical pumping on the electric dipole transition between $|\pm, \tilde{\mathcal{N}}\rangle$ and $|C, \tilde{\mathcal{P}}\rangle$, for a specific $\tilde{\mathcal{N}}$, with laser light of polarization $\hat{\epsilon}_{\text{prep}}$ that is nominally linear in the xy plane. This step depletes the bright superposition state (see e.g. [21])

$$|B(\hat{\epsilon}_{\text{prep}}), \tilde{\mathcal{N}}, \tilde{\mathcal{P}}\rangle = (\hat{\epsilon}^*_{+1} \cdot \hat{\epsilon}^*_{\text{prep}})|+, \tilde{\mathcal{N}}\rangle - \tilde{\mathcal{P}}(\hat{\epsilon}^*_{-1} \cdot \hat{\epsilon}^*_{\text{prep}})|-, \tilde{\mathcal{N}}\rangle, \tag{2.5}$$

where $\hat{\epsilon}_{\pm 1} = \mp(\hat{x} \pm i\hat{y})/\sqrt{2}$ are unit vectors for circular polarization. The corresponding dark state (with which the laser does not interact) is the orthogonal superposition

$$|D(\hat{\epsilon}_{\text{prep}}), \tilde{\mathcal{N}}, \tilde{\mathcal{P}}\rangle = (\hat{\epsilon}^*_{+1} \cdot \hat{\epsilon}_{\text{prep}})|+, \tilde{\mathcal{N}}\rangle + \tilde{\mathcal{P}}(\hat{\epsilon}^*_{-1} \cdot \hat{\epsilon}_{\text{prep}})|-, \tilde{\mathcal{N}}\rangle. \tag{2.6}$$

This dark state serves as the initial state, $|\psi(0), \tilde{\mathcal{N}}\rangle = |D(\hat{\epsilon}_{\text{prep}}), \tilde{\mathcal{N}}, \tilde{\mathcal{P}}_{\text{prep}} = +1\rangle$, for the spin-precession experiment, where we fixed the state preparation laser frequency to address the excited state with parity $\tilde{\mathcal{P}}_{\text{prep}} = +1$. The state preparation laser polarization can be parameterized as

$$\hat{\epsilon}_{\text{prep}} = -e^{-i\theta_{\text{prep}}} \cos\Theta_{\text{prep}} \hat{\epsilon}_{+1} + e^{+i\theta_{\text{prep}}} \sin\Theta_{\text{prep}} \hat{\epsilon}_{-1}, \tag{2.7}$$

where $\Theta_{\text{prep}} \approx \pi/4$ defines the ellipticity Stokes parameter $(S_3/I)_{\text{prep}} = \cos 2\Theta_{\text{prep}} \approx 0$, and θ_{prep} defines the linear polarization angle with respect to $\hat{x}$ in the xy plane. From here on, we refer to the ellipticity Stokes parameter as $S \equiv S_3/I$, for convenience of notation. There is a one-to-one correspondence between the dark state superposition and the projection of

the laser polarization $\hat{\epsilon}_{\text{prep}}$ onto the xy plane. If the laser polarization does not lie entirely in the xy plane, equations 2.5 and 2.6 are still appropriate, but require normalization. Note that if the laser is linearly polarized, switching the excited state parity $\tilde{\mathcal{P}}$ has the same effect on the dark state as rotating the laser polarization angle by $\pi/2$.

Following the initial state preparation, the molecules traverse the spin-precession region with their forward velocity nominally along $\hat{x}$. In this region there are nominally uniform and parallel electric ($\vec{\mathcal{E}}$) and magnetic ($\vec{\mathcal{B}}$) fields, which produce energy shifts given by

$$E(M,\tilde{\mathcal{N}}) = -|MD_{H,J=1}\mathcal{E}|\tilde{\mathcal{N}} - Mg_{H,J=1}\mu_{\text{B}}\mathcal{B}_z\tilde{\mathcal{B}} - M\eta_{H,J=1}\mu_{\text{B}}|\mathcal{E}|\mathcal{B}_z\tilde{\mathcal{N}}\tilde{\mathcal{B}} - Md_e\mathcal{E}_{\text{eff}}\tilde{\mathcal{N}}\tilde{\mathcal{E}}, \quad (2.8)$$

where $D_{H,J=1}$ is the electric dipole moment of $|H, J = 1\rangle$. Here $\eta_{H,J=1} = 0.79(1)$ nm/V accounts for the $\mathcal{E}$-dependent magnetic moment difference between the two sets of $\tilde{\mathcal{N}}$ levels in $|H, J = 1\rangle$ [135], as described in section 4.4. The energy shift terms that depend on the sign of M contribute to the spin precession angle ϕ, which is given by:

$$\phi = \frac{1}{2}\int_0^L (E(M=+1,\tilde{\mathcal{N}}) - E(M=-1,\tilde{\mathcal{N}}))\frac{\mathrm{d}x}{v}. \quad (2.9)$$

This phase is dominated by the Zeeman interaction phase. The Stark shift, proportional to $|M|$, does not contribute. The state then evolves to:

$$|\psi(\tau),\tilde{\mathcal{N}}\rangle = \left(e^{-i\phi}|+,\tilde{\mathcal{N}}\rangle\langle+,\tilde{\mathcal{N}}| + e^{+i\phi}|-,\tilde{\mathcal{N}}\rangle\langle-,\tilde{\mathcal{N}}|\right)|\psi(0),\tilde{\mathcal{N}}\rangle, \quad (2.10)$$

(recall $|\psi(0),\tilde{\mathcal{N}}\rangle = |D(\hat{\epsilon}_{\text{prep}}),\tilde{\mathcal{N}},\tilde{\mathcal{P}}_{\text{prep}} = +1\rangle$ per equation 2.6) and molecules enter a detection region where the state is read out by optically pumping again between the $|H, J = 1, M, \tilde{\mathcal{N}}\rangle \to |C, J = 1, M = 0, \tilde{\mathcal{P}}\rangle$. This optical pumping is performed alternately by two laser beams with nominally orthogonal linear polarizations $\hat{\epsilon}_X$ and $\hat{\epsilon}_Y$.[1] These beams excite the projection of $|\psi(\tau),\tilde{\mathcal{N}}\rangle$ onto the bright states

$$|B(\hat{\epsilon}_X),\tilde{\mathcal{N}},\tilde{\mathcal{P}}\rangle \quad \text{and} \quad |B(\hat{\epsilon}_Y),\tilde{\mathcal{N}},\tilde{\mathcal{P}}\rangle, \quad (2.11)$$

(with the same $\tilde{\mathcal{N}}$ that was addressed in the state preparation optical pumping step, but with an independent choice of $\tilde{\mathcal{P}}$) with probability $P_{X,Y}$ respectively. In the ideal case in

1. For convenience, the notation $\hat{\epsilon}_X$, $\hat{\epsilon}_Y$ is used interchangeably with the previously used notation $\hat{X}$, $\hat{Y}$.

which all laser polarizations are exactly linear, this probability is given by

$$P_{X,Y} = \left|\langle B(\hat{\epsilon}_{X,Y}, \tilde{\mathcal{N}}, \tilde{\mathcal{P}})|\psi(\tau), \tilde{\mathcal{N}}\rangle\right|^2 = \left[1 - \tilde{\mathcal{P}}\cos(2(\theta_{\text{prep}} - \theta_{X,Y} + \phi))\right]/2, \tag{2.12}$$

where $\theta_{X,Y}$ are the linear polarization angles of the state readout beams, with respect to $\hat{x}$. The result is a signal that varies sinusoidally with the precession angle ϕ and with the laser polarizations θ_{prep}, and $\theta_{X,Y}$. To measure these probabilities, we observe the associated modulated fluorescence signals, $F_{X,Y} = fN_0P_{X,Y}$, where N_0 is the number of molecules in the addressed $\tilde{\mathcal{N}}$ level at the state readout region, and f is the fraction of total fluorescence photons that are detected.

To distinguish between molecule number fluctuations and phase variations, we normalize with respect to the former by rapidly switching the state readout laser between the two orthogonal polarizations, $\hat{\epsilon}_{X,Y}$, every 5 μs. This is significantly quicker than fluctuations in the molecule number and is sufficiently quick that every molecule is interrogated by both polarizations (see section 2.3 or [93] for more details). We then form an asymmetry $\mathcal{A}$, which is immune to molecule number fluctuations, given by

$$\mathcal{A} = \frac{F_X - F_Y}{F_X + F_Y} = \tilde{\mathcal{P}}\cos[2(\phi - \theta)], \tag{2.13}$$

where we have assumed that the readout polarizations are exactly orthogonal, given by $\theta_X = \theta_{\text{read}}$ and $\theta_Y = \theta_{\text{read}} + \pi/2$, and where we have defined $\theta \equiv \theta_{\text{read}} - \theta_{\text{prep}}$.[2] In this equation and from now on unless otherwise noted, $\tilde{\mathcal{P}}$ refers to the excited state parity that is addressed by the state readout laser, not to be confused[3] with the excited state parity addressed by the state preparation laser, which is kept fixed with $\tilde{\mathcal{P}}_{\text{prep}} = +1$.

The value of $\mathcal{B}_z$ and the state preparation and readout laser beam polarizations are chosen so that $|\phi - \theta| \approx \pi/4$. This corresponds to the linear part of the asymmetry fringe in equation 2.13, where $\mathcal{A}$ is most sensitive to, and linearly proportional to, small changes in ϕ. A variety of effects including imperfect optical pumping, decay from C back to H, elliptical laser polarization and forward velocity dispersion, reduce the measurement sensitivity by a

2. Note that this reduces to equation 2.4 for $\theta_{\text{prep}} = 0$ (i.e. $\hat{\epsilon}_{\text{prep}} = \hat{x}$) and $\tilde{\mathcal{P}} = +1$.

3. The symbol $\tilde{\mathcal{P}}$ plays three roles in this document in actuality and we try to make it clear what we mean at each instance. 1.) it specifies the parity of a given state, 2.) it specifies one of the two opposite parity states in the excited state $|C, J = 1, M = 0, \tilde{\mathcal{P}}\rangle$, 3.) it specifies which of the two $|C, J = 1, M = 0, \tilde{\mathcal{P}}\rangle$ states is being addressed by the state read-out laser.

"contrast" factor

$$\mathcal{C} \equiv -\frac{1}{2}\frac{\partial \mathcal{A}}{\partial \theta} \approx \frac{1}{2}\frac{\partial \mathcal{A}}{\partial \phi}, \tag{2.14}$$

with $|\mathcal{C}| \leq 1$. We measure this parameter by dithering $\theta = \theta^{\mathrm{nr}} + \Delta\theta\tilde{\theta}$ (where θ^{nr} is the average or non-reversing polarization angle) between states of $\tilde{\theta} = \pm 1$, with amplitude $\Delta\theta = 0.05$ rad by changing the polarization angle of the state read-out lasers. We found that typically $|\mathcal{C}| \approx 0.94$. We then extract the measured phase, $\Phi = \mathcal{A}/(2\mathcal{C}) + q\pi/4$, by normalizing the asymmetry measurements according to the measured contrast — see section 2.3 for more details on the data analysis methods used to evaluate this quantity. In the ideal case, the measured phase matches closely with the precession phase, $\Phi \approx \phi$. However, a variety effects that are discussed in section 4 lead to slight deviations between these two quantities, which can contribute to systematic errors in the measurement. Unless explicitly specified, $\mathcal{C}$ is assumed to be an unsigned quantity from here on. In particular, when averaging over multiple states of the experiment, $|\mathcal{C}|$ is used.

To isolate the electron EDM term from other components of the energy shift in equation 2.8, the experiment is repeated under different conditions that are characterized by parameters whose sign is switched regularly during the experiment. The spin precession measurement is repeated for all 2^4 experiment states defined by the four primary binary switch parameters: $\tilde{\mathcal{N}}$, the molecular orientation relative to the applied electric field (changed every 0.5 s); $\tilde{\mathcal{E}}$, the direction of the applied electric field in the laboratory (2 s); $\tilde{\theta}$, the sign of the readout polarization dither (10 s); and $\tilde{\mathcal{B}}$, the direction of the applied magnetic field in the laboratory (40 s). For each $(\tilde{\mathcal{N}}, \tilde{\mathcal{E}}, \tilde{\mathcal{B}})$ state, the asymmetry $\mathcal{A}(\tilde{\mathcal{N}}, \tilde{\mathcal{E}}, \tilde{\mathcal{B}})$, contrast $\mathcal{C}(\tilde{\mathcal{N}}, \tilde{\mathcal{E}}, \tilde{\mathcal{B}})$, and measured phase $\Phi(\tilde{\mathcal{N}}, \tilde{\mathcal{E}}, \tilde{\mathcal{B}})$ are determined as described earlier. The data taken under all $2^4 = 16$ experimental states derived from these four binary switches constitutes a block of data.

We can write the phase $\Phi(\tilde{\mathcal{N}}, \tilde{\mathcal{E}}, \tilde{\mathcal{B}})$ in terms of components with particular parity with respect to the experimental switches:

$$\begin{aligned}\Phi(\tilde{\mathcal{N}}, \tilde{\mathcal{E}}, \tilde{\mathcal{B}}) =& \Phi^{\mathrm{nr}} + \Phi^{\mathcal{N}}\tilde{\mathcal{N}} + \Phi^{\mathcal{E}}\tilde{\mathcal{E}} + \Phi^{\mathcal{B}}\tilde{\mathcal{B}} \\ &+ \Phi^{\mathcal{N}\mathcal{E}}\tilde{\mathcal{N}}\tilde{\mathcal{E}} + \Phi^{\mathcal{N}\mathcal{B}}\tilde{\mathcal{N}}\tilde{\mathcal{B}} + \Phi^{\mathcal{E}\mathcal{B}}\tilde{\mathcal{E}}\tilde{\mathcal{B}} + \Phi^{\mathcal{N}\mathcal{E}\mathcal{B}}\tilde{\mathcal{N}}\tilde{\mathcal{E}}\tilde{\mathcal{B}}.\end{aligned} \tag{2.15}$$

We refer to these components as switch-parity channels, or correlations between the phase and certain experiment switches. A channel is said to be odd with respect to some sub-

set of switches (labeled as superscripts) if it changes sign when any of those switches is performed. It is implicitly even under all other switches. We use this general notation throughout this document to refer to correlations of various measured quantities and experimental parameters with experiment switches. To generalize, if we have k binary experiment switches $(\tilde{\mathcal{S}}_1, \tilde{\mathcal{S}}_2, \ldots, \tilde{\mathcal{S}}_k)$ such that $\tilde{\mathcal{S}}_i = \pm 1$, and we perform a measurement of the parameter $X(\tilde{\mathcal{S}}_1, \tilde{\mathcal{S}}_2, \ldots, \tilde{\mathcal{S}}_k)$ for a complete set of the 2^k switch states, then the component of X that is odd under the product of switches $\left[\tilde{\mathcal{S}}_a \tilde{\mathcal{S}}_b \ldots\right]$ is given by

$$X^{\mathcal{S}_a \mathcal{S}_b \cdots} \equiv \frac{1}{2^k} \sum_{\tilde{\mathcal{S}}_1 \ldots \tilde{\mathcal{S}}_k = \pm 1} \left[\tilde{\mathcal{S}}_a \tilde{\mathcal{S}}_b \ldots\right] X\left(\tilde{\mathcal{S}}_1, \tilde{\mathcal{S}}_2, \ldots, \tilde{\mathcal{S}}_k\right). \tag{2.16}$$

The switch parity behavior of a given component is expressed in the superscript which lists the experimental switches with respect to which the component is odd. We order the switch labels in the superscripts such that the fastest switches are listed first and the slowest switches are listed last. Some components give particularly important physical quantities. Most notably, the electron EDM precession phase is extracted from the $\tilde{\mathcal{N}}\tilde{\mathcal{E}}$-correlated component of the measured phase: that is, in the ideal case $\Phi^{\mathcal{N}\mathcal{E}} = -d_e \mathcal{E}_{\text{eff}} \tau$. Additionally, the Zeeman precession phase is nominally given by $\Phi^{\mathcal{B}} = -\mu_{\text{B}} g_{H,J=1} \mathcal{B}_z \tau$. Recall we label "non-reversing" components with an "nr" superscript. In a few cases, we drop the superscript parity because it is redundant. For example, we drop the superscript on the dominant components of the applied electric and magnetic fields, $\mathcal{E} \equiv \mathcal{E}^{\mathcal{E}}$ and $\mathcal{B}_z \equiv \mathcal{B}_z^{\mathcal{B}}$.

Many other experiment parameters are also varied between blocks of data to suppress and monitor known systematic errors (figure 2.4). These "superblock" switches include: excited-state parity addressed by the state readout laser beams, $\tilde{\mathcal{P}}$ (chosen randomly after every block, with equal probability of $\tilde{\mathcal{P}} = \pm 1$); simultaneous change of the power supply polarity and interchange of leads connecting the electric field plates to their voltage supply, $\tilde{\mathcal{L}}$ (every 4 blocks); a rotation of the state readout polarization basis by $\theta_{\text{read}} \to \theta_{\text{read}} + \pi/2$ to interchange the roles of the $\hat{X}$ and $\hat{Y}$ polarized state read-out beams, $\tilde{\mathcal{R}}$ (every 8 blocks); and a global polarization rotation of both state preparation and readout lasers by $\theta_{\text{read}} \to \theta_{\text{read}} + \pi/2$ and $\theta_{\text{prep}} \to \theta_{\text{prep}} + \pi/2$, $\tilde{\mathcal{G}}$ (every 16 blocks).

Additionally, the magnitude of the magnetic field, $\mathcal{B}_z$, was switched on the timescale of 64–128 blocks ($\sim$ 1 hour), and the magnitude of the applied electric field, $\mathcal{E}$, and the laser propagation direction, $\hat{k} \cdot \hat{z}$, were changed on timescales of $\sim$ 1 day and $\sim$ 1 week,

respectively.

On these longer timescales, we also alternated between taking electron EDM data under *Normal* conditions, for which all experiment parameters were set to their nominally ideal values, and taking data with *Intentional Parameter Variations* (IPVs), during which some experimental parameter was set to deviate from ideal so that we could monitor the size of the known systematic errors described in section 3. We took IPV data in which we varied (a) the non-reversing electric field $\mathcal{E}^{\mathrm{nr}}$ and (b) the $\tilde{\mathcal{N}}\tilde{\mathcal{E}}$-correlated Rabi frequency, $\Omega_{\mathrm{r}}^{\mathcal{N}\mathcal{E}}$, to measure the sensitivity of the electron EDM measurement to these parameters and we varied (c) the state preparation laser detuning Δ_{prep} to monitor the size of the residual $\mathcal{E}^{\mathrm{nr}}$ so that we would be able to identify changes in this quantity over time. These systematic errors are discussed in more detail in sections 3 and 4.

The details of the data analysis required to extract the electron EDM-correlated phase $\Phi^{\mathcal{N}\mathcal{E}}$ are described in section 2.3. A lower bound on the statistical uncertainty $\delta\Phi^{\mathcal{N}\mathcal{E}}$ of the electron EDM-correlated phase is given by photo-electron shot noise to be $\delta\Phi^{\mathcal{N}\mathcal{E}} = 1/(2|\mathcal{C}|\sqrt{N})$ for N detected photo-electrons [92, 164]. In the case where shot noise is the sole contribution, we can express the statistical uncertainty δd_e in our measurement of the electron EDM as

$$\delta d_e = \delta\Phi^{\mathcal{N}\mathcal{E}} \frac{1}{\mathcal{E}_{\mathrm{eff}}\tau} = \frac{1}{2|\mathcal{C}|\tau\mathcal{E}_{\mathrm{eff}}\sqrt{\dot{N}T}}, \tag{2.17}$$

where $\dot{N} \approx f\dot{N}_0$ is the measurement rate (equivalent to the photo-electron detection rate) and T is the integration time (recall f is the fraction of fluorescence photons detected and N_0 is the number of molecules in the addressed $\tilde{\mathcal{N}}$ level).

2.3 Data Analysis

In this section I describe the data analysis routine used to extract the electron EDM value, and other quantities, from our dataset of nearly 10^6 PMT fluorescence traces. The entire analysis was implemented with a "blind" offset on the electron EDM channel such that the channel's mean value was not known by us until after all the data had been acquired and the systematic error in the measurement had been determined. No analysis changes were made after the blind was revealed. Several data cuts were applied to ensure that the resulting electron EDM measurements would be nearly normally distributed and to filter data that was not taken under normal operating conditions.

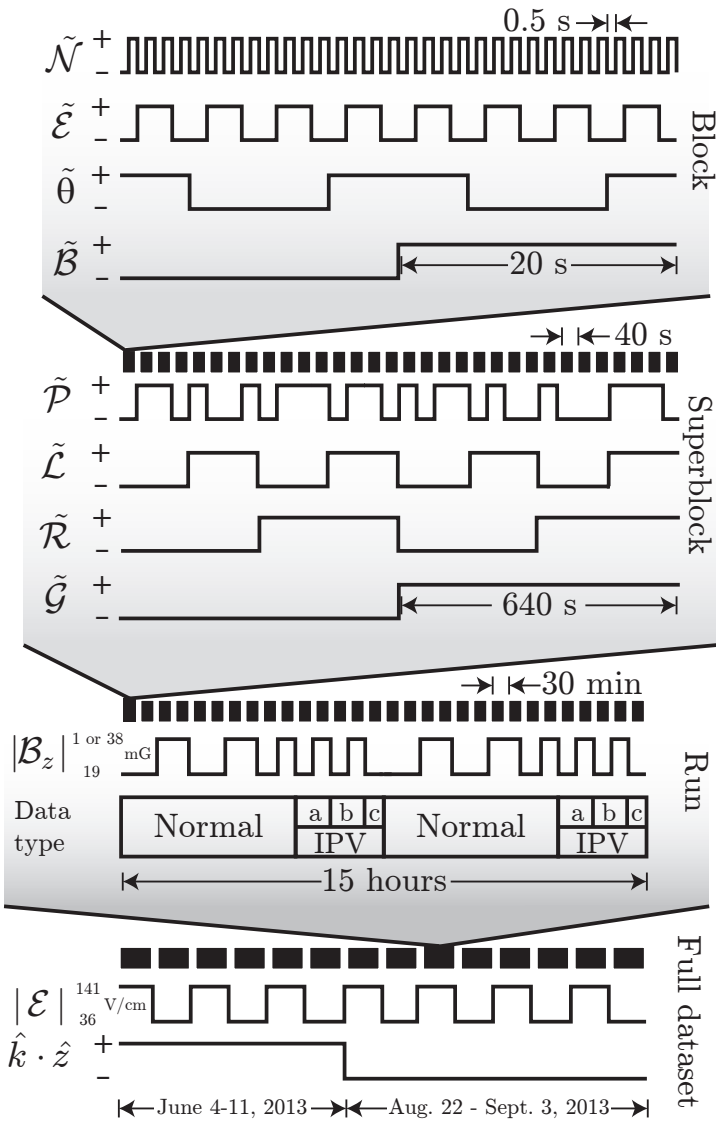

Figure 2.4: A schematic of the switches performed during ACME I and the associated timescales. See the main text for a description of each of the switch parameters and a description of the distinction between the *Normal* and IPV (*Intentional Parameter Variation*) data types. The 15-hour run time and $|\mathcal{E}|$ switching timescale are approximate.

2.3.1 Signal Asymmetry

As described in section 2.1, the accumulated phase Φ was read out by resonantly addressing the $H \rightarrow C$ transition with linearly polarized light and monitoring the resulting fluorescence. The state readout laser was switched between orthogonal polarizations, $\hat{X}$ and $\hat{Y}$, at 100 kHz (with 1.2 μs of dead time between polarizations) in order to normalize against molecular flux variations. By switching at a rate fast enough such that each molecule experienced both polarizations, we achieved nearly photon-shot-noise-limited phase measurements of some of the correlated phase channels such as $\Phi^{\mathcal{NE}}$ [93]. With a sufficiently wide laser beam, all molecules were completely optically pumped by both laser polarizations during their $\sim$20 μs fly-through time. We induced approximately one fluorescence photon from each molecule by projecting the molecule state onto the two orthogonal spin states excited by laser beams with orthogonal polarizations.

The rapid switching of the laser polarization resulted in a modulated PMT signal, $S(t)$, as shown in figure 2.5. For the following discussion we consider the polarization state to switch at a time $t = 0$. Immediately after, there is a rapid increase in fluorescence as the molecules in the laser beam are quickly excited; while $\Omega_r t \ll 1$, where $\Omega_r \sim 2\pi \times 1$ MHz is the Rabi frequency on the H to C transition, the fluorescence increases as $S(t) \propto (\Omega_{\mathrm{r}} t)^2$. At later times, when $\Omega_r t > 1$, population is about evenly mixed between the H and C states (since $\Omega_r > \gamma_C$); hence, $S(t)$ decays exponentially with a time constant of roughly $1/(2\gamma_C) \approx 1$ μs. Molecules that were not present at $t = 0$ continue to enter the laser beam, causing $S(t)$ to approach a steady state. The laser is then turned off and the signal decays exponentially with time constant $1/\gamma_C \approx 0.5$ μs. The next laser pulse, with orthogonal polarization, is turned on 1.2 μs $\approx 2.5/\gamma_C$ after the end of the previous one to prevent significant overlap of contributions to $S(t)$ induced by different polarizations. A low-pass filter in the PMT voltage amplifier with a cut-off frequency of $2\pi \times 2$ MHz removed any time dynamics from $S(t)$ that are much faster than γ_C, and prevented aliasing of high frequency components in the signal given our fixed digitization rate of the signal at 5 MSa/s.

To determine the laser-induced fluorescence $F(t)$ produced by each polarization state, we subtracted a time-dependent background signal, $B(t')$, taken from data with no molecule fluorescence present, i.e. $F(t) = S(t) - B(t')$. Examples of the extracted $F(t)$ and $B(t')$ time series are shown in figure 2.5A and B, respectively. $B(t')$ was modulated in time

due to scattered light from the state readout laser beam and has a DC electronic offset intrinsic to the PMTs. The first millisecond of data, which contains no fluorescence, was used to determine $B(t')$. We assumed that $B(t')$ was periodic with the switching of the laser polarization but did not depend on the polarization; we inferred its value by averaging together the recorded PMT signal across all polarization bins for ≈ 1 ms of data taken before the arrival of the molecule pulse. Since molecule beam velocity variations caused jitter in the temporal position of the molecule pulse within the trace, 9 ms of data were collected per pulse, despite the fact that only the $\approx$2 ms of strong signal with $F(t) \gg B(t')$ and ≈ 1 ms of background contained useful information for the spin precession measurement.

Integrating $F(t)$ over times associated with pairs of orthogonally polarized laser pulses resulted in signals F_X, F_Y. The integration was performed over a specified time window that we denote as a "polarization bin". The bottom of figure 2.3.4 shows the blinded measurements of the electron EDM, taken during the course of our searches for systematic errors, for different choices of polarization bin and illustrates that the extracted electron EDM is not significantly affected by this choice. Figure 3.5 shows that most of the extracted quantities did not vary linearly within the polarization bin (Pol. Cycle Time Dependence column).

After polarization binning, the data displayed a fluorescence signal modulated by the envelope of the molecule pulse, as in figure 2.5C. Figure 2.5D shows the asymmetry, $\mathcal{A}$, computed from these data. The asymmetry is computed for each 10 μs polarization cycle, so that for the i^{th} cycle we have

$$\mathcal{A}_i = \frac{F_{X,i} - F_{Y,i}}{F_{X,i} + F_{Y,i}}. \tag{2.18}$$

The molecule phase, and hence asymmetry (see equation 2.4), had a linear dependence on the time after ablation because the molecules precessed in a magnetic field over a fixed distance; the slower molecules, which arrive later, precessed more than the faster molecules, which arrived earlier. We applied a fluorescence signal threshold cut of around $F = (F_X + F_Y)/2 \geq 3 \times 10^5$ s^{-1}, indicated by dashed lines in figure 2.5C,D. Section 2.3.3 describes the threshold choice in detail.

To determine the statistical uncertainty in $\mathcal{A}$, I grouped $n \approx 18$ adjacent asymmetry points together. For each group, j, centered around a time after ablation t_j, we calculated

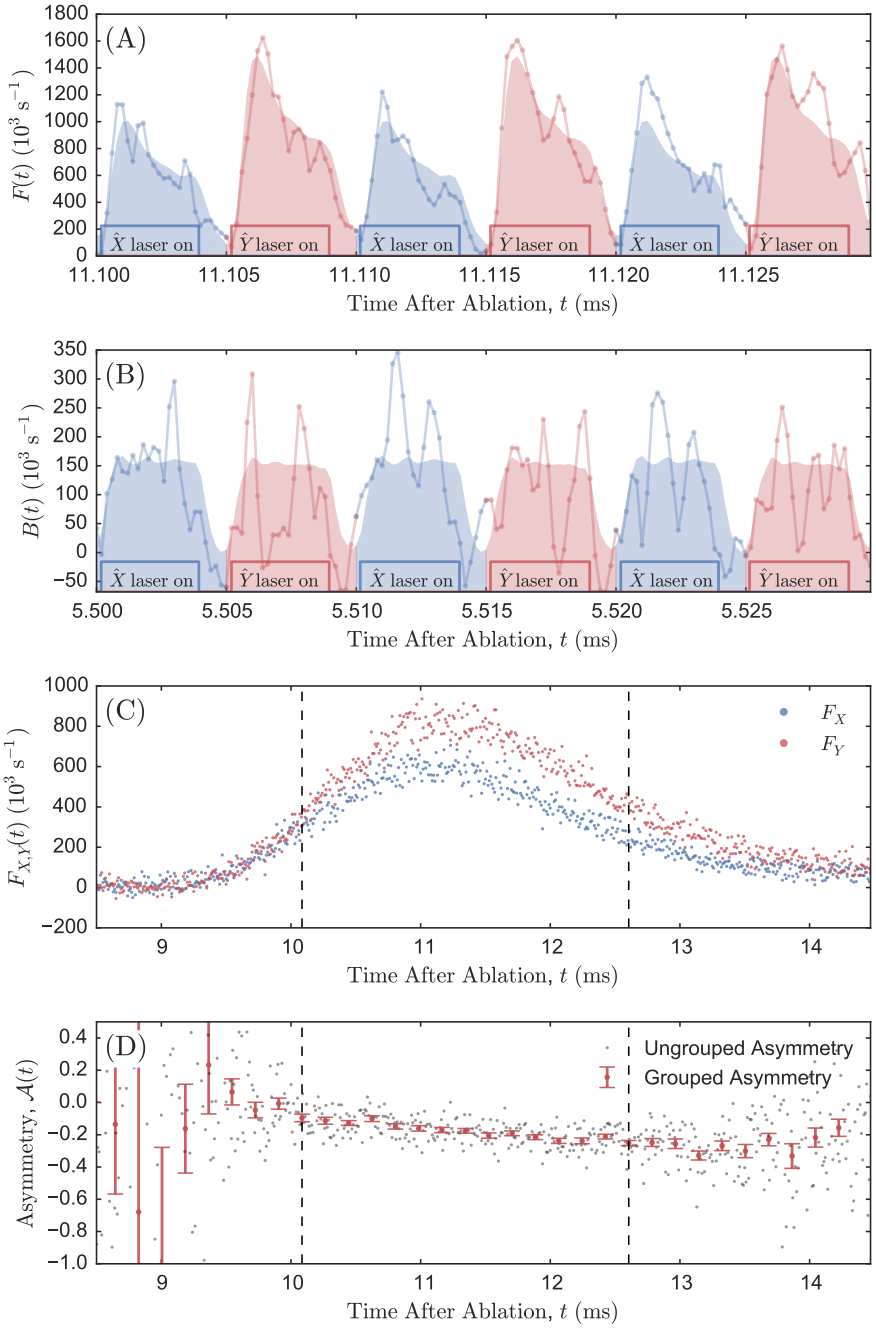

Figure 2.5: (A) Molecule fluorescence signal $F(t)$ in photo-electrons/s induced by $\hat{X}$ (blue) and $\hat{Y}$ (red) readout laser polarizations. Lines show the raw data for a single trace consisting of an average of 25 molecule pulses. Shaded regions show the waveform averaged over 16 traces. (B) Background signal $B(t')$ in photo-electrons/s obtained before the arrival of molecules in the state readout region. (C) Integrated fluorescence signals F_X and F_Y throughout the molecule pulse. Dashed lines denote the region with $F = (F_X + F_Y)/2 > 3 \times 10^5$ s^{-1}, used as a typical cut for inclusion in electron EDM data. Points are spaced by 5 μs. (D) Computed asymmetry throughout the molecule pulse. In this example, 18 of the ungrouped asymmetry points are grouped together to compute the mean and uncertainty shown as the grouped asymmetry.

the mean, $\bar{\mathcal{A}}_j$, and the uncertainty in the mean, $\delta\bar{\mathcal{A}}_j$, depicted as red points and error bars in figure 2.5D. For smaller n, the variance in the sample variance in the mean grows, in which case, error propagation that utilizes a weighted mean of data ultimately leads to an underestimate of the final statistical uncertainty [91]. For larger n, the mean significantly varies within the group due to velocity dispersion, and the variance in the mean grows in a manner not determined by random statistical fluctuations. For the range n = 15-30 we observed no significant change in any quantities which were deduced from the measured asymmetry.

As described earlier in this section, the background, $B(t')$, which we subtracted from the PMT signal, $S(t)$, was observed to be correlated with the fast switching of the readout laser beam polarization. This can arise, for example, if the two polarizations have different laser beam intensities or pointings. We chose to use a polarization independent $B(t')$ by averaging over the two polarization states, despite observing significantly different background signals for the two polarization states; we did this so that the uncertainty in the background asymmetry, which was not well characterized, would not contribute to the uncertainty in the signal asymmetry [124]. This choice produced an asymmetry offset as per equation 2.18 and hence a significant shift to Φ^{nr} associated with the polarization-dependent background. However, we did not consider Φ^{nr} to be a crucial physical or diagnostic quantity. We found that this methodology produced accurate estimates of the uncertainties of quantities computed from the measured asymmetry, as verified by χ^2 analysis of measurements of $\Phi^{\mathcal{NE}}$. We also found that none of the phase channels of interest changed significantly dependent on whether a polarization-dependent $B(t')$ was used.

2.3.2 Computing Contrast and Phase

To compute the measured phase Φ we must also measure the fringe contrast $\mathcal{C}$ and relative laser polarization angle $\theta = \theta_{\mathrm{read}} - \theta_{\mathrm{prep}}$, as described in section 2.1. The $\hat{X}$ and $\hat{Y}$ laser polarizations were set by a $\lambda/2$ waveplate and were determined absolutely by auxiliary polarimetry measurements [77]. The contrast, defined as either $2\mathcal{C} = -\partial\mathcal{A}/\partial\theta$ or $2\mathcal{C} = \partial\mathcal{A}/\partial\phi$[4], can be determined by dithering either the accumulated phase ϕ (by varying $\mathcal{B}_z$) or the relative laser polarization angle θ. We chose the latter as it could be changed quickly

4. Recall that in practice we consider $\mathcal{C}$ as an unsigned quantity for the purposes of data analysis.

(< 1 s) by rotating a half-wave plate with a stepper-motor-driven rotation stage in the state read-out laser beam path. We ran the experiment at the steepest part of the asymmetry fringe and measured the contrast, $\mathcal{C}_j$, for each asymmetry group, $\bar{\mathcal{A}}_j$, by switching θ between two angles, $\theta = \theta^{\rm nr} + \Delta\theta\tilde{\theta}$, for $\tilde{\theta} = \pm 1$ and $\Delta\theta = 0.05$ rad:

$$\mathcal{C}_j = -\frac{\bar{\mathcal{A}}_j(\tilde{\theta} = +1) - \bar{\mathcal{A}}_j(\tilde{\theta} = -1)}{4\Delta\theta}. \tag{2.19}$$

The fringe contrast was fairly constant over the duration of the molecule pulse (figure 2.6A), but did exhibit statistically significant variation that was not well understood. Since the contrast did vary over this timescale, we might have liked to normalize the measurement of each asymmetry group by the corresponding contrast group. Unfortunately, when only $n = 18$ points were averaged together the fractional uncertainty in the contrast, $\delta\mathcal{C}/\mathcal{C}$ is sufficiently large to significantly increase in the uncertainty in the measured phase relative to the measured asymmetry. As an alternative, I fit $\mathcal{C}_j$ to a 2nd-order polynomial as a function of time during the ablation pulse. This lead to a good fit to the data and negligible increase in the uncertainty of the phase measurement relative to the asymmetry.

We typically found $|\mathcal{C}| \approx 95\%$. We believe that this was limited by a number of effects including: imperfect state preparation/readout, decay from the C state back to the H state and dispersion in the spin precession. We also observed that this value was constant over a $\pm 2\pi \times 1$ MHz detuning range of the state preparation laser (figure 2.6B), indicating complete optical pumping over this frequency range. Recall that, as defined, $\mathcal{C}$ can be positive or negative, depending on the sign of the asymmetry fringe slope. Given that we worked near zero asymmetry where the fringe slope was steepest, and that $\theta^{\rm nr}$ was always chosen to be 0 or $\pi/4$, we computed the total accumulated phase as

$$\Phi_j = \frac{\bar{\mathcal{A}}_j(\tilde{\theta} = +1) + \bar{\mathcal{A}}_j(\tilde{\theta} = -1)}{4\mathcal{C}} + q\frac{\pi}{4}. \tag{2.20}$$

Here, $q = 0, \pm 1$ or ± 2, corresponds to applied magnetic fields of $\pm\frac{1}{20}\mathcal{B}_{\pi/4}$, $\pm\mathcal{B}_{\pi/4}$, and $\pm 2\mathcal{B}_{\pi/4}$ mG, respectively, where $\mathcal{B}_{\pi/4} = \frac{\pi/4}{\mu_B g_{H,J=1}\tau} \approx 20\,\text{mG}$. We chose to apply a small magnetic field, $\mathcal{B} = 1$ mG when operating at $q = 0$ rather than turning off the magnetic field completely so that we would not need to change the experimental switch sequence or data analysis routine for data taken under this condition.

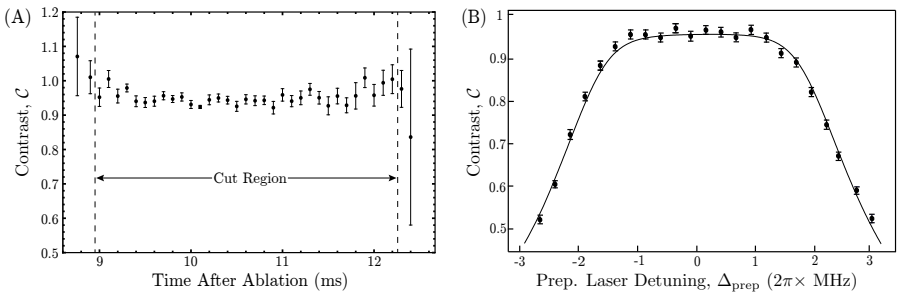

Figure 2.6: (A) Contrast vs time after ablation, averaged over 64 traces. The signal threshold window is indicated by dashed lines (cf. figure 2.5). (B) Contrast vs preparation laser detuning. Error bars were computed as the standard error associated with 64 averaged traces. The solid line is a fit of the form $\mathcal{C} = a\tanh(b\gamma_C^2/(4\Delta_{\text{prep}}^2 + \gamma_C^2))$, motivated by solution of a classical rate equation.

Accounting for Correlated Contrast

It was possible for the magnitude of the contrast $|\mathcal{C}|$ to vary between different experimental states. For example, if the state preparation laser detuning or fluorescence signal background were correlated with any of the block switches $\tilde{\mathcal{N}}$, $\tilde{\mathcal{E}}$, or $\tilde{\mathcal{B}}$, then contrast would also be correlated with those switches. As described in section 3, we observed both $\tilde{\mathcal{N}}$- and $\tilde{\mathcal{N}}\tilde{\mathcal{E}}$-correlated contrast. The latter was particularly troubling since it could lead to a systematic offset in the measured electron EDM if not properly accounted for: since $\mathcal{A} = \mathcal{C}\cos[2(\phi - \theta)]$, a nonzero $\mathcal{A}^{\mathcal{N}\mathcal{E}}$ could occur due to either $\mathcal{C}^{\mathcal{N}\mathcal{E}}$ or $\phi^{\mathcal{N}\mathcal{E}}$. We accounted for contrast correlations by calculating $\mathcal{C}$ separately for each combination of $\tilde{\mathcal{N}}$, $\tilde{\mathcal{E}}$, and $\tilde{\mathcal{B}}$ experimental states ("state-averaged" contrast[5]):

$$\mathcal{C}_j(\tilde{\mathcal{N}}, \tilde{\mathcal{E}}, \tilde{\mathcal{B}}) = \frac{\bar{\mathcal{A}}_j(\tilde{\theta} = +1, \tilde{\mathcal{N}}, \tilde{\mathcal{E}}, \tilde{\mathcal{B}}) - \bar{\mathcal{A}}_j(-\tilde{\theta} = -1, \tilde{\mathcal{N}}, \tilde{\mathcal{E}}, \tilde{\mathcal{B}})}{4\Delta\theta}. \tag{2.21}$$

As previously discussed, I applied a quadratic fit to all $\mathcal{C}_j(\tilde{\mathcal{N}}, \tilde{\mathcal{E}}, \tilde{\mathcal{B}})$ within a molecule pulse to compute $\bar{\mathcal{C}}_j(\tilde{\mathcal{N}}, \tilde{\mathcal{E}}, \tilde{\mathcal{B}})$. The precession phase was calculated from each state-specific asymmetry and contrast measurement (cf. equation 2.19):

$$\Phi_j(\tilde{\mathcal{N}}, \tilde{\mathcal{E}}, \tilde{\mathcal{B}}) = \frac{\bar{\mathcal{A}}_j(\tilde{\mathcal{N}}, \tilde{\mathcal{E}}, \tilde{\mathcal{B}})}{2\bar{\mathcal{C}}_j(\tilde{\mathcal{N}}, \tilde{\mathcal{E}}, \tilde{\mathcal{B}})} + q\frac{\pi}{4}, \tag{2.22}$$

5. Since there were $2^3 = 8$ different $\tilde{\mathcal{N}}$, $\tilde{\mathcal{E}}$, and $\tilde{\mathcal{B}}$ states in each 64-trace block, $64/8 = 8$ traces were averaged together to determine the contrast for each experimental state.

where

$$\bar{\mathcal{A}}_j(\tilde{\mathcal{N}},\tilde{\mathcal{E}},\tilde{\mathcal{B}}) = \frac{\bar{\mathcal{A}}_j(\tilde{\theta}=+1,\tilde{\mathcal{N}},\tilde{\mathcal{E}},\tilde{\mathcal{B}}) + \bar{\mathcal{A}}_j(\tilde{\theta}=-1,\tilde{\mathcal{N}},\tilde{\mathcal{E}},\tilde{\mathcal{B}})}{2} \tag{2.23}$$

is the average asymmetry over the two $\tilde{\theta}$ states in a data block that share identical values of $\tilde{\mathcal{N}}$, $\tilde{\mathcal{E}}$ and $\tilde{\mathcal{B}}$. By construction, phases computed from state-averaged contrast are immune to contrast correlations. We also computed phases by ignoring contrast correlations (i.e. treating contrast as independent of $\tilde{\mathcal{N}}$, $\tilde{\mathcal{E}}$, $\tilde{\mathcal{B}}$) and the result did not change significantly.

Computing Phase and Frequency Correlations

After extracting the measured phase $\Phi_j(\tilde{\mathcal{N}},\tilde{\mathcal{E}},\tilde{\mathcal{B}})$, we performed the basis change described in equation 2.16, from this experiment switch *state* basis to the experiment switch *parity* basis, denoted by Φ_j^p, where p is a placeholder for a given experiment switch parity.

We observed that the molecule beam forward velocity, and hence the spin precession time τ_j, fluctuated by up to 10% over a 10 minute time period. Since $\mathcal{B}_z$ and $g_{H,J=1}$ are known from auxiliary measurements to a precision of around 1%, we were able to extract τ_j from each block from the Zeeman precession phase measurement, $\Phi_j^{\mathcal{B}} = -\mu_{\mathrm{B}} g_{H,J=1} \mathcal{B}_z \tau_j$ (see section 2.2). Velocity dispersion caused τ_j to vary across the molecule pulse with a nominally linear dependence on time after ablation, t, however we observed significant deviations from linearity. Thus, I fit τ_j to a 3rd order polynomial in t in order to evaluate $\bar{\tau}_j$. Then, we evaluated the measured spin precession frequencies defined as

$$\omega_j^p = \Phi_j^p / \bar{\tau}_j, \tag{2.24}$$

for all phase channels p (see equation 2.15 for definition). We extracted the electron EDM from $\omega_j^{\mathcal{NE}}$, which in the absence of systematic errors would be given by $\omega^{\mathcal{NE}} = -d_e \mathcal{E}_{\mathrm{eff}}$ independent of j.

From here on we will drop the j subscript that denotes a grouping of n adjacent asymmetry points about a particular time after ablation t_j; it is implicit that independent phase measurements were computed from many separate groups of data, each with different values of t_j across the duration of the molecule pulse. At the end of the analysis, and whenever it was convenient to do so, we implicitly performed weighted averaging across the j subscript.

Other phase channels could be used to search for and monitor systematic errors, discussed in detail in sections 3 and 4, or to measure properties of ThO, as is the case with

$\omega^{\mathcal{NB}}$. The dominant contribution to this channel comes from $\tilde{\mathcal{N}}$ dependent modification to the $g-$factor that comes from rotational Stark mixing [21, 86, 135], discussed in section 4.4. This channel,

$$\omega^{\mathcal{NB}} = -\mu_B \eta_{H.J=1} |\mathcal{E}| \mathcal{B}_z,$$

provided a measure of $\eta_{H,J=1} = -0.79 \pm 0.01$ nm/V, since $|\mathcal{E}|$ and $\mathcal{B}_z$ were well characterized.

2.3.3 Varying the analysis method

Three primary data cuts were applied as part of the analysis: fluorescence rate threshold, polarization bin, and contrast threshold. These cuts made sure that we only used data taken under appropriate experimental conditions (e.g. only when lasers remained locked etc.) and thus ensured a high signal to noise ratio for the data used to extract the electron EDM value. We thoroughly investigated how each of these cuts affected the calculated electron EDM mean and uncertainty.

As previously mentioned, a fluorescence threshold cut of about $F_{\text{cut}} \approx 3 \times 10^5$ s^{-1}, was applied to each trace (average of 25 molecule pulses) to ensure that the fluorescence rate would always be larger than the background rate. This threshold was chosen to include the maximum number of asymmetry points in our measurement while also excluding low signal-to-noise asymmetry measurements that would increase the overall electron EDM uncertainty, as described below. We also removed entire blocks (complete sets of $\tilde{\mathcal{N}}$,$\tilde{\mathcal{E}}$,$\tilde{\mathcal{B}}$,$\tilde{\theta}$) of data from the analysis if any of the block's experiment states had < 0.5 ms of fluorescence data above F_{cut}.

The count rates of uncorrelated fluorescence photo-electrons exhibit Poissonian statistics. In each block we averaged together four traces with the same experimental configuration. After such averaging, the number of detected photo-electrons within a pair of laser polarization bins was > 50, which was large enough that the photo-electron number distribution closely resembled a normal distribution. Because the asymmetry was defined as a ratio of two approximately normally distributed random variables ($F_X - F_Y$ and $F_X + F_Y$), its distribution was not necessarily normal. Rather, it approached a normal distribution in the limit of large $F_X + F_Y$ [86]. The same followed for all quantities computed from the asymmetry, including the electron EDM. The fluorescence threshold cut therefore ensured

that the distribution of electron EDM measurements was very nearly normally distributed. Including low-signal data would have caused the distribution to deviate from normal and increase the overall uncertainty. To check that this signal size cut did not lead to a systematic error in our determination of $\omega^{\mathcal{NE}}$ we routinely varied this cut-point in the analysis. If the cut was increased above 6×10^5 s^{-1} the mean value was seen to move slightly, but within the computed uncertainties, and the uncertainty to increased as expected. However, for all plausible values of the cuts the resulting value of $\omega^{\mathcal{NE}}$ was consistent, within uncertainties, with our final stated value.

As described in section 2.3.1, data points within a polarization bin were averaged together when calculating the asymmetry (cf. figure 2.5A). These data points were separated by 200 ns. Numbering these points from when the readout laser beam polarization is switched, I binned points 0–25, but others performing the analysis [86, 158] used fewer points, 5–20. I made this choice to minimize the statistical uncertainty in the result given the lack of evidence for systematic errors that depended on time within the polarization switching cycle. As shown in figure 2.3.4, we checked for systematic errors associated with this choice by also using several different polarization bins to compute the electron EDM. The uncertainty increased, as expected, for polarization bins that cut out data with significant fluorescence levels, but the mean values were routinely consistent with each other within their respective uncertainties.

In order for a block of data to be included in our final measurement, we also required that each of the 8 $(\tilde{\mathcal{N}}, \tilde{\mathcal{E}}, \tilde{\mathcal{B}})$ experiment states had a measured fringe contrast above 80%. The primary cause of blocks failing to meet this requirement was the state preparation laser becoming unlocked. This cut resulted in less than 1% of blocks being discarded. If the contrast cut was lowered, or not applied at all, the electron EDM mean and uncertainty change by less than 3% of our statistical uncertainty. As with the signal threshold, if this cut threshold was increased to 90%, close to the average value of contrast, $\mathcal{C}$, then a larger fraction of data was neglected and the electron EDM uncertainty was seen to increase.

For all the cuts discussed, we significantly varied the associated cut and in some cases removed it entirely. The electron EDM mean and uncertainty were very robust against significant variation of each of these cuts, and the cuts were chosen before the blind offset applied to the electron EDM channel was removed.

As a mentioned, three of us [86, 158] performed independent analyses of the data. We

each followed the general analysis method described above, but varied some of the small details such as background subtraction method, cut thresholds, numbers of points grouped together to compute asymmetry, polarization bin choice, etc. The analyses differed in the polynomial order of the fits applied to both the contrast $\mathcal{C}$ and the precession time τ vs. time after ablation t. The analyses also differed in the inclusion of a subset of the electron EDM data that featured a particularly large unexplained signal in the $\omega^{\mathcal{N}}$ channel. Having multiple analyses frequently proved useful in finding sign-errors and bugs in our respective code, as we would frequently compare the results of data runs and flag instances where we significantly disagreed.

Each of the three analyses independently computed the electron EDM channel and the systematic error in the electron EDM channel. The uncertainties for all three routines were nearly identical, and the means agreed to within $\Delta\omega^{\mathcal{NE}} < 3$ mrad/s, which is within the statistical uncertainty of the measurement $\delta\omega^{\mathcal{NE}} = \pm 4.8$ mrad/s. The electron EDM mean and uncertainty were averaged over the three analyses to produce the final result.

2.3.4 EDM Mean and Statistical Uncertainty

The final data set used to report our result is shown in figure 2.7. It consisted of $\sim 10^4$ blocks of data taken over the course of $\sim$2 weeks (figure 2.7B); each block contains ≈ 20 separate electron EDM measurements distributed over the duration of the molecule pulse (Figure 2.7A). All $\approx 2 \times 10^5$ measurements were combined with standard Gaussian error propagation to obtain the reported mean and uncertainty. Figure 2.7C,D shows histograms of all measurements on a linear (C) and log (D) scale, showing the distribution agrees extremely well with a Gaussian fit. The resulting uncertainty was about 1.2 times that expected from the photo-electron shot-noise limit, taking into account the photo-electron rate from molecule fluorescence, background light, and PMT dark current. When the electron EDM measurements were fit to a constant value, the reduced χ^2 was 0.996 ± 0.006 where this uncertainty represents the 1σ width of the χ^2 distribution for the appropriate number of degrees of freedom.

When computing the electron EDM result, data from superblocks were averaged together. The mean could be either weighted or unweighted by the statistical uncertainty in each superblock state. Weighted averaging minimized the resulting statistical uncertainty, but unweighted averaging could suppress systematic errors that have well-defined

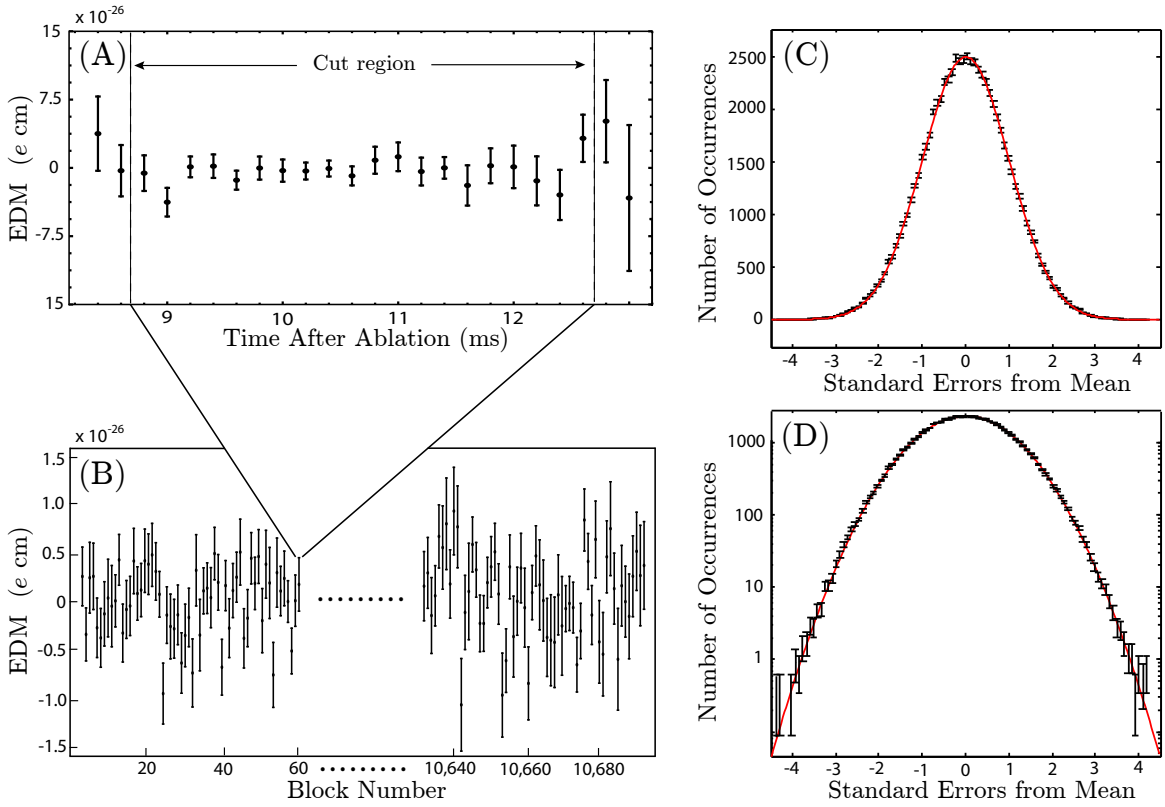

Figure 2.7: The data set associated with our reported electron EDM limit. **(A)** Variations in the extracted electron EDM as a function of position within the molecular pulse. **(B)** Over 10,000 blocks of data were taken over a combined period of about two weeks. **(C)**-**(D)** The distribution of ∼200,000 separate electron EDM measurements (black) matches very well with a Gaussian fit (red). The same data is plotted with both a linear and a log scale. In these histograms the mean of each individual measurement was normalized to its corresponding error bar.

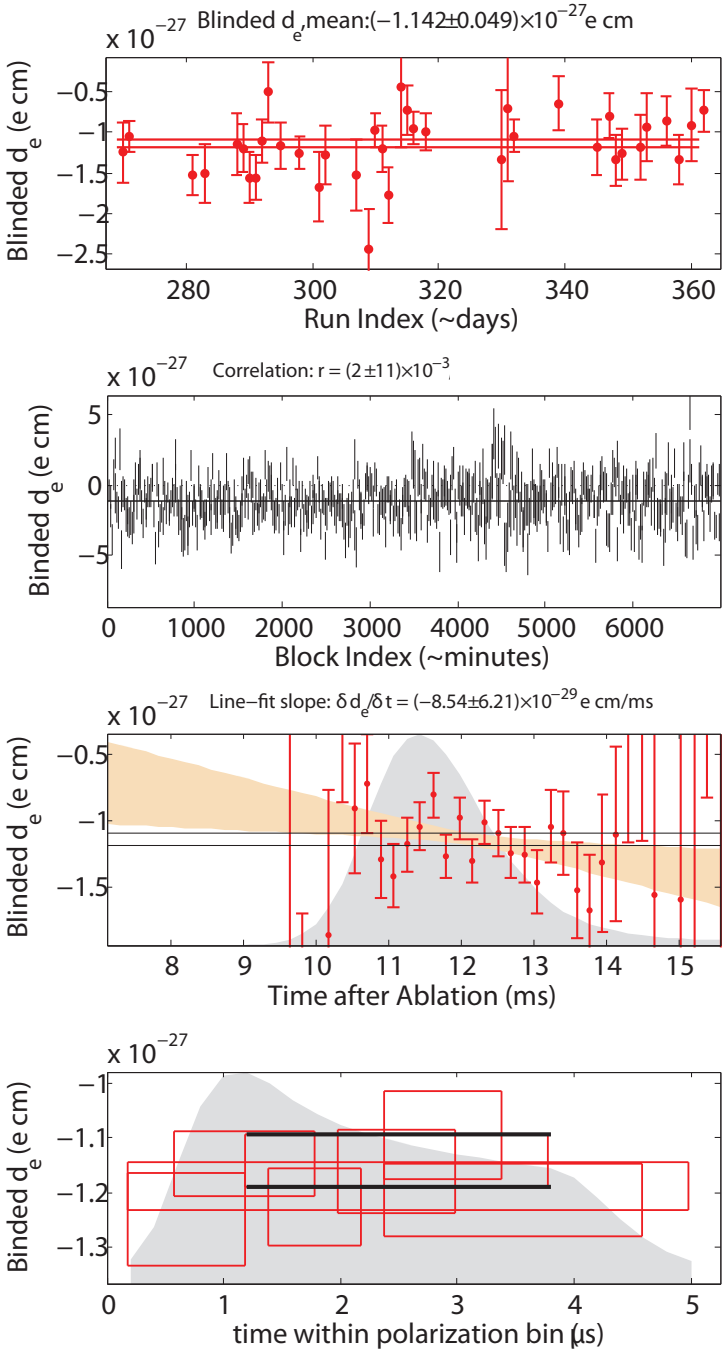

Figure 2.8: Searches for variation of $\omega^{\mathcal{NE}}$ over many timescales spanning from μs to months during the course of a large set of runs that constituted the searches for systematic errors. This data includes the blind offset that had been applied to the measurement of d_e and is presented in units of $e \cdot \text{cm}$ assuming a $\mathcal{E}_{\text{eff}} \approx 100\,\text{GV/cm}$. Bottom: variation with choice of polarization bin (μs timescale). Bottom Middle: variation with time within the molecule pulse (ms timescale). Top Middle: variation with time between blocks (minute timescale). Top: variation with time between systematic error search data runs (day timescale).

superblock parity from entering into the extracted value for $\omega^{\mathcal{NE}}$.

Due to molecule number fluctuations, each block of data had a different associated uncertainty. However, roughly equal amounts of data were gathered for the 2^4 superblock states defined by the state readout parity $\tilde{\mathcal{P}}$, field plate lead configuration $\tilde{\mathcal{L}}$, state readout laser polarization $\tilde{\mathcal{R}}$, and global laser polarization $\tilde{\mathcal{G}}$. For the reported electron EDM value, unweighted averaging (or to be precise, performing the basis change prescribed by equation 2.16) was used to combine data from the different $\tilde{\mathcal{P}}$, $\tilde{\mathcal{R}}$, $\tilde{\mathcal{L}}$, $\tilde{\mathcal{G}}$ experiment states, since there were known systematic errors with well-defined superblock parity that were suppressed by these switches. Note, however, that figure 3.5 shows that these systematic errors produced no significant electron EDM shift, and that the overall uncertainty was comparable (within 10%) when the data was combined with weighted or unweighted averaging.

Unequal amounts of data were collected for the $\mathcal{B}_z$, $\mathcal{E}$, and $\hat{k}\cdot\hat{z}$ experimental states. For example, 40% (60%) of data were gathered with the state preparation and readout laser beams pointing east (west), $\hat{k}\cdot\hat{z} = -1(+1)$. To account for this, we performed state-by-state analysis of the systematic errors: the primary systematic errors (described in section 3) were allowed to depend on the magnitude of the magnetic field (though $\mathcal{B}_z = 1, 40$ mG were grouped together), and the pointing direction, and separate systematic error subtractions were performed for each ($\mathcal{B}_z$, $\hat{k}\cdot\hat{z}$) state. After this subtraction, the systematic uncertainties were added in quadrature with the statistical uncertainties for each state, and the data from each state was averaged together weighted by the resulting combined statistical and systematic uncertainties.

The reported statistical uncertainty was obtained via the method above assuming no systematic uncertainty. The reported systematic uncertainty was defined such that the quadrature sum of the reported statistical and systematic uncertainties gives the same value as when incorporating the state-by-state analysis. A description of the methods used to evaluate the systematic error and the systematic uncertainty in the measurement is provided in section 3.6.1. To prevent experimental bias we performed a blind analysis by adding an unknown offset to the mean of the electron EDM channel, $\omega^{\mathcal{NE}}$. This blind offset can be seen in a sample set of data that we took during our systematic error search data runs in figure 2.3.4; the blind allows us to examine possible variations of the measurement without knowing whether the actual measurement is consistent with zero or not. The offset was randomly generated in software from a Gaussian distribution with standard deviation

$\sigma = 150$ mrad/s and mean zero. The mean, statistical error, procedure for calculating the systematic error, and procedure for computing the reported confidence interval were all determined before revealing and subtracting the blind offset.

Chapter 3

Systematic Error Search and Characterization

> "It is what you don't expect," he'd said, "that most needs looking for."
>
> Neal Stephenson, Anathem

According to Sozzi [157], "The best way to handle systematic effects is not to have any...". This is good advice, and we designed the ACME experiment to be very resilient to the systematic errors that had impacted electron EDM experiments in the past [164, 165]. However, we cannot ensure that those systematic errors that we are protected against are the only ones that could appear in our experiment, so we performed an extensive search for unforeseen systematic errors. After observing some, we developed models to understand them, which are described primarily in section 4, and carefully quantified them in auxiliary measurements. In this chapter I describe the search for and characterization of these systematic errors. Note that additional details regarding this process may also be found in these theses, [77, 86, 158].

A true electron EDM should contribute to the $\tilde{\mathcal{N}}\tilde{\mathcal{E}}$-correlated spin precession frequency, $\omega^{\mathcal{N}\mathcal{E}}$, with a signal $\omega_T^{\mathcal{N}\mathcal{E}}$ that does not vary with any experimental parameter. To discriminate between a systematic error in $\omega^{\mathcal{N}\mathcal{E}}$ and $\omega_T^{\mathcal{N}\mathcal{E}}$, we pursued a strategy to vary a large number of experimental parameters and imperfections while closely monitoring $\omega^{\mathcal{N}\mathcal{E}}$. If $\omega^{\mathcal{N}\mathcal{E}}$ changes then there must be a systematic error correlated with that varied parameter. During our search for systematic errors we varied parameters including applied electric and magnetic fields, magnetic field gradients, molecule beam pointing, and laser beam shape,

pointing, detuning, and polarization. In addition to monitoring $\omega^{\mathcal{NE}}$, we monitored the spin precession frequency ω, contrast $\mathcal{C}$, fluorescence signal F, and a number of additional experimental conditions such as molecule beam velocity, vacuum pressure and room temperature. We examined the correlations of these quantities with the experiment switches to determine whether there are any spurious signals that might point to unforeseen systematic errors, or a gap in our understanding of the experiment.

3.1 Systematic error search

We varied more than 40 parameters during our systematic error search, and most of these have been listed in table 3.1. These fall into two categories. Category I consists of parameters P which are zero in the idealized measurement scheme described in section 2.1. We choose parameterizations such that $P \neq 0$ represents an experimental imperfection. We were able to use experimental data to put a direct limit on the size of possible systematic errors proportional to these parameters. Category II contains parameters that have no optimum value and which we could vary significantly without affecting the nature of the spin precession measurement. The variation of these parameters could reveal systematic errors and serve as a check that we understood the response of our system to those parameters, but no quantitative bounds on the associated systematic errors were derived.

For each Category I parameter P, we exaggerated the size of the imperfection by a factor greater than $10\times$, if possible, relative to the residual size of the imperfection under normal operating conditions, $\bar{P}$, which was obtained from auxiliary measurements or based on estimation. Following previous work [68, 82, 141], we assumed a linear relationship between $\omega^{\mathcal{NE}}$ and P, and extracted the sensitivity of the $\omega^{\mathcal{NE}}$ to parameter P, $\partial\omega^{\mathcal{NE}}/\partial P$. The systematic error under normal operating conditions was computed as $\omega_P^{\mathcal{NE}} = (\partial\omega^{\mathcal{NE}}/\partial P)\bar{P}$. The statistical uncertainty in the systematic error, referred to as the systematic uncertainty, $\delta\omega_P^{\mathcal{NE}}$ was obtained from linear error propagation of uncorrelated random variables,

$$\delta\omega_P^{\mathcal{NE}} = \sqrt{\left(\frac{\partial\omega^{\mathcal{NE}}}{\partial P}\,\delta\bar{P}\right)^2 + \left(\bar{P}\,\delta\frac{\partial\omega^{\mathcal{NE}}}{\partial P}\right)^2}, \tag{3.1}$$

where $\delta\bar{P}$ is the uncertainty in $\bar{P}$ and $\delta\partial\omega^{\mathcal{NE}}/\partial P$ is the uncertainty in $\partial\omega^{\mathcal{NE}}/\partial P$.

For parameters that had been observed to produce statistically significant shifts in $\omega^{\mathcal{NE}}$,

Table 3.1: Parameters varied during our systematic error search. Left: Category I Parameters — These are ideally zero under normal experimental running conditions and we were able to vary them significantly relative to the residual size of the imperfection. For each of these parameters direct measurements or limits were placed on possible systematic errors. Right: Category II Parameters — These had no single ideal value. Although direct limits on these systematic errors could not be derived, they served as checks for the presence of unanticipated systematic errors. See the main text for more details on all the systematic errors referenced.

Category I Parameters	Category II Parameters
Magnetic Fields	**Laser Powers**
- Non-reversing $\mathcal{B}$-field: $\mathcal{B}_z^{\mathrm{nr}}$	- Power of prep./read lasers
- Transverse $\mathcal{B}$-fields: $\mathcal{B}_x, \mathcal{B}_y$	**Experiment Timing**
(both even and odd under $\tilde{\mathcal{B}}$)	- $\hat{X}/\hat{Y}$ polarization switching rate
- $\mathcal{B}$-field gradients:	- Number of molecule pulses averaged
$\frac{\partial \mathcal{B}_x}{\partial x}, \frac{\partial \mathcal{B}_y}{\partial x}, \frac{\partial \mathcal{B}_y}{\partial y}, \frac{\partial \mathcal{B}_y}{\partial z}, \frac{\partial \mathcal{B}_z}{\partial x}, \frac{\partial \mathcal{B}_z}{\partial z}$	per experiment trace
(both even and odd under $\tilde{\mathcal{B}}$)	**Analysis**
- $\tilde{\mathcal{E}}$ correlated $\mathcal{B}$-field: $\mathcal{B}^{\mathcal{E}}$	- Signal size cuts, asymmetry size cuts,
(to simulate$\vec{v} \times \vec{\mathcal{E}}$/geometric phase	contrast cuts
/leakage current)	- Difference between two PMT detectors
Electric Fields	- Variation with time within molecule
- Non-reversing $\mathcal{E}$-field: $\mathcal{E}^{\mathrm{nr}}$	pulse (serves to check v_x dependence)
- $\mathcal{E}$-field ground offset	- Variation with time within polarization
Laser Detunings	switching cycle
- State preparation/readout	- Variation with time throughout the
lasers: $\Delta_{\mathrm{prep}}^{\mathrm{nr}}$, $\Delta_{\mathrm{read}}^{\mathrm{nr}}$	full data set (autocorrelation)
- $\tilde{\mathcal{P}}$ correlated detuning, $\Delta^{\mathcal{P}}$	- Search for correlations between
- $\tilde{\mathcal{N}}$ correlated detunings: $\Delta^{\mathcal{N}}$	all channels of phase, contrast and
Laser Pointings	fluorescence signal
- Change in pointing of prep./read lasers	- Correlations with auxiliary
- State readout laser $\hat{X}/\hat{Y}$	measurements of $\mathcal{B}$-fields, laser powers,
dependent pointing	vacuum pressure, and temperature
- $\tilde{\mathcal{N}}$ correlated laser pointing	- 3 independent data analysis routines
- $\tilde{\mathcal{N}}$ and $\hat{X}/\hat{Y}$ dependent	
laser pointing	
Laser Powers	
- $\tilde{\mathcal{N}}\tilde{\mathcal{E}}$ correlated power $\Omega_{\mathrm{r}}^{\mathcal{N}\mathcal{E}}$	
- $\tilde{\mathcal{N}}$ correlated power $\Omega_{\mathrm{r}}^{\mathcal{N}}$	
- $\hat{X}/\hat{Y}$ dependent state readout	
laser power, Ω_{r}^{XY}	
Laser polarization	
- Preparation laser ellipticity, S_{prep}	
Molecular Beam Clipping	
- Molecule beam clipping along $\hat{y}$ and $\hat{z}$	
($\langle v_y \rangle$,$\langle v_z \rangle$,$\langle y \rangle$,$\langle z \rangle$ of molecule beam)	

such as the non-reversing electric field, $\mathcal{E}^{\mathrm{nr}}$, we monitored the size of the systematic error throughout the reported data set during *Intentional Parameter Variations* (described in section 2.2) and deducted this quantity from $\omega^{\mathcal{NE}}$ to give a value of the spin precession frequency due to T-odd interactions in the H state of ThO, $\omega_T^{\mathcal{NE}} = \omega^{\mathcal{NE}} - \sum_P \omega_P^{\mathcal{NE}}$. Most Category I parameters did not cause a statistically significant $\omega_P^{\mathcal{NE}}$ and were not monitored. For these parameters, we did not subtract $\omega_P^{\mathcal{NE}}$ from $\omega^{\mathcal{NE}}$, but rather included an upper limit of $\left[(\omega_P^{\mathcal{NE}})^2 + (\delta\omega_P^{\mathcal{NE}})^2\right]^{1/2}$ in the systematic uncertainty on $\omega_T^{\mathcal{NE}}$, or chose to omit this parameter from the systematic error budget altogether based on the criteria described in section 3.6.1.

Where applicable, we also fit higher-order polynomial functions to $\omega^{\mathcal{NE}}$ with respect to P during the systematic error searches. No significant increase in the systematic uncertainty was observed using such fits and hence the contributions to the systematic error budget in Table 3.2 were all estimated from linear fits. We note, however, that certain non-linear dependences of $\omega^{\mathcal{NE}}$ on P could lead to underestimates of the systematic uncertainty, for example if $\omega^{\mathcal{NE}}$ has a small (large) nonzero value for large (small) values of P. In efforts to avoid this, data were taken over as wide a range as possible, it is, however, always possible that such non-linear dependence is present between the parameter values for which we took data. Our models indicated that over the range in which the parameters were varied, no significant non-linearity should be manifest, so we believe the procedure outlined above produced accurate estimates of the systematic errors.

Most of the searches for systematic errors related to the parameters listed in table 3.1 did not produce any statistically significant shift in the $\omega^{\mathcal{NE}}$ measurement. Since we performed so many checks, we can look at the distribution of the measured parameter slopes, $\partial\omega^{\mathcal{NE}}/\partial P$, which are presented in figure . This distribution does not have any clear outliers and the χ^2 value for the fit of the resulting distribution to the expected normal distribution is measured to be consistent with 1, which gives us added confidence that we did not overlook any possible systematic error during this search.

3.2 Systematic errors due to correlated laser parameters

The dominant contributions to the systematic error in ACME I were derived the use of lasers for state preparation and state read-out in the phase precession measurement. Correlations

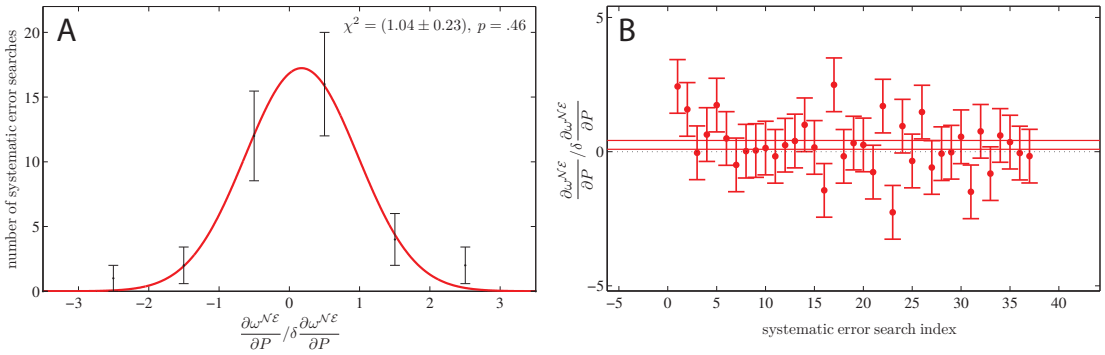

Figure 3.1: Left: Distribution of the measured sensitivity of $\omega^{\mathcal{NE}}$ to various parameters P during our search for systematic errors, for parameters that were not observed to produce a significant systematic error. The χ^2 value for the fit of the distribution to the expected normal distribution is consistent with 1. Right: All of the data points that contributed to the histogram on the left are shown. The mean of all of these data points is reasonably consistent with zero.

between the laser detuning from resonance Δ and the transition Rabi frequency Ω_r and the expected EDM signal were able to mimic the EDM signal by entering the phase measurement through a dependence of the measured phase on these parameters, $\Phi = \Phi(\Delta, \Omega_\mathrm{r})$, with an empirically determined functional behavior,

$$d\Phi(\Delta, \Omega_\mathrm{r}) = \sum_i \left[\alpha_{\Delta,i}\Delta_i + \alpha_{\Delta^2,i}\Delta_i^2 + \beta_{d\Omega_\mathrm{r},i}(d\Omega_{\mathrm{r},i}/\Omega_{\mathrm{r},i}) + \dots\right], \tag{3.2}$$

where $i \in \{\mathrm{prep}, \mathrm{read}\}$ indexes the state preparation and read-out lasers. We determined that this phase dependence can come from mixing between bright and dark states due to a small non-adiabatic laser polarization rotation during the optical pumping that is performed to prepare the coherent spin state and then later read it out. The mixed bright and dark states differ in energy by the A.C. Stark shift that leads to a relative phase accumulation that depends on the laser parameters Δ and Ω_r. In this section we describe the observed correlated laser parameters $\Delta^{\mathcal{NE}}$ and $\Omega_\mathrm{r}^{\mathcal{NE}}$ and we described the characterization of the resulting systematic errors. In section 4.3 we explore an array of mechanisms by which these AC Stark shift phases may be produced.

3.2.1 Laser parameter correlations

In the state preparation and state read-out regions we optically pumped on the $|H, J = 1, M, \tilde{\mathcal{N}}\rangle \rightarrow |C, J = 1, M = 0, \tilde{\mathcal{P}}\rangle$ transition to first prepare an initial spin state, and then

later to read-out how the spin state changed in the spin precession region. The transition frequency can be described by,

$$\omega_{HC,i} = \omega_{HC}^{\mathrm{nr}} - \frac{1}{2}\tilde{\mathcal{P}}_i \Delta_{C,J=1} + \tilde{\mathcal{N}} D_{H,J=1} |\vec{\mathcal{E}}(x_i) \cdot \hat{z}|, \tag{3.3}$$

where $\omega_{HC}^{\mathrm{nr}}$ is the optical transition frequency between the line centers of the $|H, J=1\rangle$ and $|C, J=1\rangle$ manifolds, $\Delta_{C,J=1}$ is the omega-doublet splitting in $|C, J=1\rangle$, and $-\tilde{\mathcal{N}} D_{H.J=1} |\mathcal{E}|$ is the Stark shift in $|H, J=1\rangle$. The index $i \in \{\mathrm{prep}, X, Y\}$ denotes the laser that is addressing the molecules, and we note that we fix parity of the excited state addressed by the state preparation laser, $\tilde{\mathcal{P}}_{\mathrm{prep}} = +1$, and we switch the excited state addressed by the two state read-out lasers $\tilde{\mathcal{P}} = \tilde{\mathcal{P}}_X = \tilde{\mathcal{P}}_Y$. We can parameterize imperfections in the electric field as,

$$\vec{\mathcal{E}}(x) \cdot \hat{z} = \mathcal{E}(x)\tilde{\mathcal{E}} + \mathcal{E}^{\mathrm{nr}}(x) + \mathcal{E}^{\mathcal{L}}\tilde{\mathcal{L}} + \ldots, \tag{3.4}$$

where $\tilde{\mathcal{L}}$ represents the binary state of the physical leads connecting the voltage supply to the field plates, $\mathcal{E}\tilde{\mathcal{E}}$ is the intentionally applied electric field component, $\mathcal{E}^{\mathrm{nr}}$ is a non-reversing component of the electric field, and $\mathcal{E}^{\mathcal{L}}$ is a non-reversing electric field component from the power supply that can be reversed by switching $\tilde{\mathcal{L}}$. In order to switch the molecule orientation, $\tilde{\mathcal{N}}$, and excited state parity, $\tilde{\mathcal{P}}$, that we address in the experiment, we use an array of Acousto-optic modulators (AOMs) to shift the laser frequency $\omega_{\mathrm{L},i}^{\mathrm{nr}} \rightarrow \omega_{\mathrm{L},i}$ into resonance with the desired transition, $\omega_{HC,i}$. Hence, we can parameterize the laser frequency as

$$\omega_{\mathrm{L},i} = \omega_{\mathrm{L},i}^{\mathrm{nr}} + \tilde{\mathcal{N}}\omega_{\mathrm{L}}^{\mathcal{N}} + \tilde{\mathcal{P}}\omega_{\mathrm{L}}^{\mathcal{P}}\delta_{i,\{X,Y\}}, \tag{3.5}$$

where $\omega_{\mathrm{L}}^{\mathcal{N}}$ and $\omega_{\mathrm{L}}^{\mathcal{P}}$ are RF frequency shifts applied to the laser frequency $\omega_{\mathrm{L},i}^{\mathrm{nr}}$ by AOMs. Note that we use the same laser for both the state preparation and state readout laser beams, but we can apply independent laser detuning shifts to these two beam paths using AOM frequency shifts so that ω_i^{nr} can depend on index i as suggested in equation 3.5.

Given the expression in equations 3.3, 3.4, and 3.5, The laser detuning from resonance and its correlations can be expressed as

$$\Delta_i = \omega_{HC,i} - \omega_{\mathrm{L},i} \tag{3.6}$$

$$\approx \Delta_i^{\mathrm{nr}} + \tilde{\mathcal{N}}\Delta_i^{\mathcal{N}} + \tilde{\mathcal{N}}\tilde{\mathcal{E}}\Delta_i^{\mathcal{NE}} + \tilde{\mathcal{P}}\Delta_i^{\mathcal{P}}\delta_{i,\{X,Y\}} + \ldots, \tag{3.7}$$

Here, $\Delta_i^{\mathcal{N}} = (D_{H,J=1}\mathcal{E}(x_i) - \omega_{\mathrm{L}}^{\mathcal{N}})$ is the mismatch between the Stark shift and the AOM frequency $\omega_{\mathrm{L}}^{\mathcal{N}}$ used to switch between resonantly addressing the two $\tilde{\mathcal{N}}$ states, where x_i is the x position of laser beam i. $\Delta_i^{\mathcal{NE}} = D_{H,J=1}\mathcal{E}^{\mathrm{nr}}(x_i)$ is a detuning component correlated like an electron EDM signal which is due to a non-reversing component of the applied electric field. $\Delta_i^{\mathcal{P}} = (-\frac{1}{2}\Delta_{C,J=1} - \omega_{\mathrm{L},i}^{\mathcal{P}})$ is the mismatch between the omega doublet splitting and the AOM frequency used to switch between resonantly addressing the two $\tilde{\mathcal{P}}$ states in the state readout region. We observed that $\Delta^{\mathcal{N}}$ ($\Delta^{\mathcal{P}}$) was typically less than $2\pi \times 20$ kHz ($2\pi \times 50$ kHz). Although we could measure $\Delta^{\mathcal{N}}$ with $\sim 2\pi \times 1$ kHz precision, fluctuations in the Stark splitting, likely caused by thermally-induced fluctuations of the field plate spacing, or a drifting voltage supply output, limited our ability to zero out this correlated detuning [158]. The overall detuning Δ^{nr}, defined as $\Delta^{\mathrm{nr}} = (\Delta_{\mathrm{prep}}^{\mathrm{nr}} + (1/2)(\Delta_X^{\mathrm{nr}} + \Delta_Y^{\mathrm{nr}}))/2$, typically fluctuated by $\sim 2\pi \times 0.1$ MHz over several hours. Every 30–60 minutes the detuning of the state read-out laser was scanned across resonance using an AOM and was set to the value where the fluorescence signal was maximum. This ensured that the average detuning of the state read-out laser beams, $(\Delta_X^{\mathrm{nr}} + \Delta_Y^{\mathrm{nr}})/2$, was close to zero, however, if the three laser beams are not quite parallel, there could be a difference between in the detunings of these beams due to the resulting difference in Doppler shifts. Additionally, each day we scanned the frequency of the preparation laser across the molecule resonance while monitoring the contrast of our fluorescence signal to ensure $\Delta_{\mathrm{prep}}^{\mathrm{nr}}$ was kept below $2\pi \times 0.2$ MHz (an example scan is shown in figure 2.6). The $\tilde{\mathcal{N}}\tilde{\mathcal{E}}$ correlated detuning $\Delta^{\mathcal{NE}} \sim -2\pi \cdot 5\,\mathrm{kHz}$, caused by a non-reversing component of the electric field, was characterized by a number of methods that are described in section 6.2. It was found to vary significantly spatially, but was not found to drift significantly in time. This detuning correlation can couple to the AC Stark shift phase in equation 3.2 to result in a systematic error, $\omega_{\mathcal{E}^{\mathrm{nr}}}^{\mathcal{NE}} \approx (1/\tau)\sum_i \alpha_{\Delta,i}^{\mathrm{nr}}\Delta^{\mathcal{NE}}$.

In an entirely analogous manner, the Rabi frequency magnitude Ω_{r} of the $H \rightarrow C$

transition exhibited correlations,

$$\Omega_{\mathrm{r},i} = \Omega_{\mathrm{r},i}^{\mathrm{nr}} + \tilde{\mathcal{N}}\Omega_{\mathrm{r},i}^{\mathcal{N}} + \tilde{\mathcal{N}}\tilde{\mathcal{P}}\Omega_{\mathrm{r},i}^{\mathcal{NP}} + \tilde{\mathcal{N}}\tilde{\mathcal{E}}\Omega_{\mathrm{r},i}^{\mathcal{NE}} + \dots \tag{3.8}$$

Here, $\Omega_{\mathrm{r},i}^{\mathrm{nr}}$ is the dominant component of the Rabi frequency for laser $i \in \{\mathrm{prep}, X, Y\}$, which could fluctuate in time on the order of 5% due to laser power instability. $\Omega_{\mathrm{r},i}^{\mathcal{N}}$ is generated by a laser power difference between the $\tilde{\mathcal{N}}$ states. This arose because we routed the laser light along different paths through a series of AOMs for each state. We measured this effect with photodiodes and found that the largest fractional power correlation was $\Omega_{\mathrm{r}}^{\mathcal{N}}/\Omega_{\mathrm{r}}^{\mathrm{nr}} \approx 2.5 \times 10^{-3}$. An additional contribution to $\Omega_{\mathrm{r},i}^{\mathcal{N}}$, and a contribution to $\Omega_{\mathrm{r},i}^{\mathcal{NP}}$ on the same order, arises due to Stark mixing between rotational levels in H and C, and is derived in section 4.2.3.

Although we did not observe a laser power correlation with $\tilde{\mathcal{N}}\tilde{\mathcal{E}}$ we did observe signals consistent with a Rabi frequency correlation, $\Omega_{\mathrm{r}}^{\mathcal{NE}}$. A nonzero $\tilde{\mathcal{N}}\tilde{\mathcal{E}}$-correlated fluorescence signal (as defined in section 2.3.1) that also reversed with the laser propagation direction $\hat{k}\cdot\hat{z}$, $F^{\mathcal{NE}}/F^{\mathrm{nr}} \approx -(2.4\times10^{-3})(\hat{k}\cdot\hat{z})$, together with a nonzero $\omega^{\mathcal{NEB}} \approx (2.5\,\mathrm{mrad/s})(\mathcal{B}_z/\mathrm{mG})(\hat{k}\cdot\hat{z})$, provided the first evidence that a nonzero $\Omega_{\mathrm{r}}^{\mathcal{NE}}$ existed in our system. We believe that this fluorescence correlation arises from a linear dependence of the fluorescence signal size on Rabi frequency, $F^{\mathcal{NE}} = (\partial F/\partial\Omega_{\mathrm{r}}^{\mathrm{nr}})\Omega_{\mathrm{r}}^{\mathcal{NE}}$, which is nonzero since the state readout transitions were not fully saturated. Although the measurements are consistent with an $\Omega_{\mathrm{r}}^{\mathcal{NE}}$, the origin of this correlation is still not fully understood, and we are continuing to explore models to understand this effect, as discussed in section 4.2.4.

We believe that the signal in $\omega^{\mathcal{NEB}}$ was caused by a coupling between the Rabi frequency correlation and the $\mathcal{B}$-odd AC Stark shift phase, $\omega^{\mathcal{NEB}} = \frac{1}{\tau}\sum_i \beta_{d\Omega_{\mathrm{r}},i}^{\mathcal{B}}(d\Omega_{\mathrm{r}}^{\mathcal{NE}}/\Omega_{\mathrm{r}}^{\mathrm{nr}})$, where $\beta_{d\Omega_{\mathrm{r}},i}^{\mathcal{B}}$ is an AC Stark shift phase factor from equation 3.2. We were able to verify a linear dependence of both of these channels on $\Omega_{\mathrm{r}}^{\mathcal{NE}}$ by intentionally correlating the laser intensity with $\tilde{\mathcal{N}}\tilde{\mathcal{E}}$ using AOMs; this is shown for the $\Phi^{\mathcal{NEB}}$ channel in Figure 3.2. Varying the size of this artificial $\Omega_{\mathrm{r}}^{\mathcal{NE}}$ allowed us to measure the value present in the experiment under normal operating conditions, $\Omega_{\mathrm{r}}^{\mathcal{NE}}/\Omega_{\mathrm{r}}^{\mathrm{nr}} = (-8.0 \pm 0.8)\times10^{-3}(\hat{k}\cdot\hat{z})$. $\Omega_{\mathrm{r}}^{\mathcal{NE}}$ can couple to $\beta_{d\Omega_{\mathrm{r}},i}^{\mathrm{nr}}$ as per equation 3.2 to result in a systematic error in $\omega_{d\Omega_{\mathrm{r}}}^{\mathcal{NE}} = \frac{1}{\tau}\sum_i \beta_{d\Omega_{\mathrm{r}},i}^{\mathrm{nr}}(d\Omega_{\mathrm{r}}^{\mathcal{NE}}/\Omega_{\mathrm{r}}^{\mathrm{nr}})$. A nonzero $\beta_{d\Omega_{\mathrm{r}},i}^{\mathrm{nr}}$ can be produced by a linear polarization angle gradient (not observed in the experiment) or by a non-reversing Zeeman shift component, $g_{H,J=1}\mu_{\mathrm{B}}\mathcal{B}_z^{\mathrm{nr}}$.

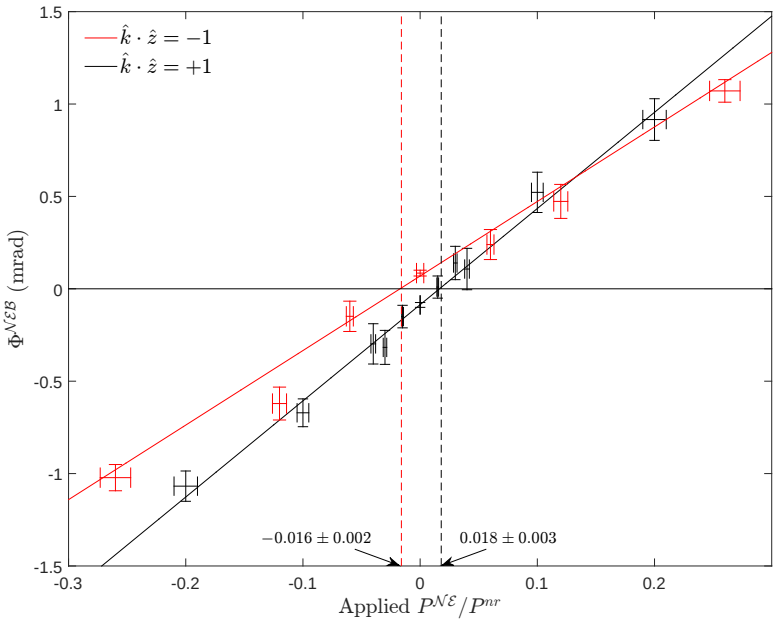

Figure 3.2: $\Phi^{\mathcal{NEB}}$ as a function of applied $\tilde{\mathcal{N}}\tilde{\mathcal{E}}$-correlated laser power, $P^{\mathcal{NE}}$, for both directions of laser pointing, $\hat{k}\cdot\hat{z}$. The artificial $\Omega_{\mathrm{r}}^{\mathcal{NE}}$ resulting from correlated power $P^{\mathcal{NE}}$ systematically shifts $\omega^{\mathcal{NEB}}$ in accordance with equation 4.62. $\Phi^{\mathcal{NEB}}$ is zero when the applied $P^{\mathcal{NE}}$ is such that there is no net $\tilde{\mathcal{N}}\tilde{\mathcal{E}}$-correlated Rabi frequency. The intrinsic $\Omega_{\mathrm{r}}^{\mathcal{NE}}$ (i.e. that inferred when $P^{\mathcal{NE}}=0$) changed sign with $\hat{k}\cdot\hat{z}$ within the resolution of the measurement. The slopes between the two measurements differ due to differences in the AC Stark shift phase, believed to be due to differences in the spatial intensity profile and polarization structure between the two measurements.

Given the empirical AC Stark shift phase model in equation 3.2, the resulting systematic errors in the frequency measurement are given by

$$\omega^{\mathcal{NE}}_{\mathcal{E}^{\rm nr}} = \frac{1}{\tau} \sum_{i\in\{\rm prep,X,Y\}} \alpha^{\rm nr}_{\Delta,i} D_{H,J=1} \mathcal{E}^{\rm nr}(x_i) \tag{3.9}$$

$$\omega^{\mathcal{NE}}_{\Omega^{\mathcal{NE}}_{\rm r}} = \frac{1}{\tau} \sum_{i\in\{\rm prep,X,Y\}} \beta^{\rm nr}_{d\Omega_{\rm r},i} (\Omega^{\mathcal{NE}}_{\rm r}/\Omega^{\rm nr}_{\rm r}). \tag{3.10}$$

Early in the experiment, we observed a nonzero systematic shift $\omega^{\mathcal{NE}}_{\mathcal{E}^{\rm nr}}$ and took steps discussed in reference [158] to suppress it. To verify that the steps taken were effective, we examined $\omega^{\mathcal{NE}}$ as a function of an intentionally applied non-reversing electric field. The resulting data are shown in figure 3.3. The original slope, $\partial\omega^{\mathcal{NE}}/\partial\mathcal{E}^{\rm nr} = (6.7 \pm 0.4)$(rad/s)/(V/cm), corresponded to a systematic shift of $\omega^{\mathcal{NE}}_{\mathcal{E}^{\rm nr}} \approx -34$ mrad/s when combined with the measured $\mathcal{E}^{\rm nr} \approx -5$ mV/cm. Following the modifications described above, the $\partial\omega^{\mathcal{NE}}/\partial\mathcal{E}^{\rm nr}$ slope was greatly suppressed, reducing the systematic error to $\omega^{\mathcal{NE}}_{\mathcal{E}^{\rm nr}} < 1$ mrad/s, well below the statistical uncertainty in the measurement of $\omega^{\mathcal{NE}}$.

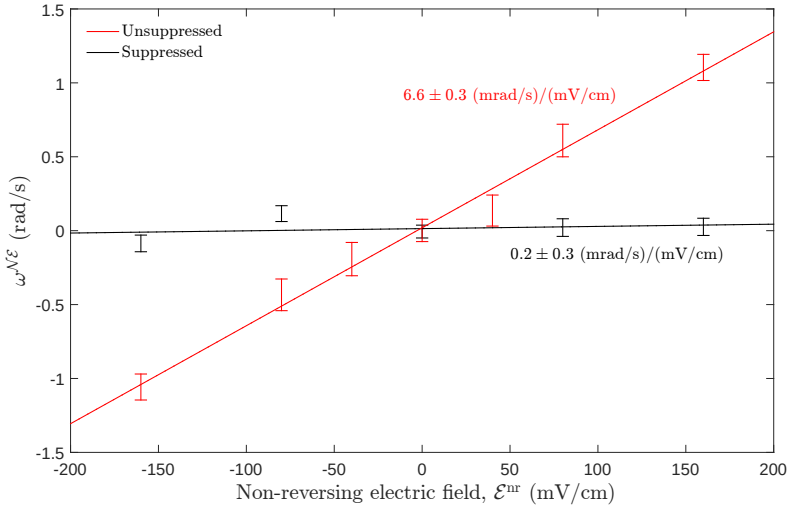

Figure 3.3: Linear dependence of the $\omega^{\mathcal{NE}}$ channel on an applied non-reversing electric field observed before (red) and after (black) we suppressed the known AC Stark shift phase by optimizing the preparation laser beam shape, time-averaged power and polarization.

Because we observed that the parameters $\mathcal{E}^{\rm nr}$ and $\Omega^{\mathcal{NE}}_{\rm r}$ caused systematic errors in $\omega^{\mathcal{NE}}$, we intermittently measured the size of the associated systematic errors throughout the data sets that were used for our reported result. We measured $\partial\omega^{\mathcal{NE}}/\partial\mathcal{E}^{\rm nr}$ by applying a range of large non-reversing electric fields, up to around 70 times that present under normal running

conditions. The value of $\partial\omega^{\mathcal{NE}}/\partial\Omega_{\mathrm{r}}^{\mathcal{NE}}$ was measured by applying a correlated laser power $P^{\mathcal{NE}}$ in the state preparation and state readout beams with a magnitude corresponding to an applied $\Omega_{\mathrm{r}}^{\mathcal{NE}}$ that was up to 20 times that measured under normal operating conditions. These parameters were measured for multiple values of the magnetic field magnitude, $\mathcal{B}_z$, for which different state readout laser beam polarizations were required. Due to known birefringent behavior of the AC stark shift phases, we allowed for this possibility for all AC stark shift phase systematic errors. We measured $\partial\omega^{\mathcal{NE}}/\partial\mathcal{E}^{\mathrm{nr}}$ for both $\hat{k}\cdot\hat{z}=\pm1$, but the $\Omega_{\mathrm{r}}^{\mathcal{NE}}$ systematic error was only discovered after the $\hat{k}\cdot\hat{z}=+1$ dataset and hence $\partial\omega^{\mathcal{NE}}/\partial\Omega_{\mathrm{r}}^{\mathcal{NE}}$ was only monitored during the $\hat{k}\cdot\hat{z}=-1$ dataset. The $\Omega_{\mathrm{r}}^{\mathcal{NE}}$ systematic error during the $\hat{k}\cdot\hat{z}=+1$ dataset was determined from auxiliary measurements of the AC Stark shift phase. As described in section 6.2, $\mathcal{E}^{\mathrm{nr}}(x)$ exhibits significant spatial variation along the beam-line axis, x. However the $\mathcal{E}^{\mathrm{nr}}$ that was intentionally applied to determine $\partial\omega^{\mathcal{NE}}/\partial\mathcal{E}^{\mathrm{nr}}$ was spatially uniform, and hence these measurements were insensitive to the difference $(\mathcal{E}^{\mathrm{nr}}(x_{\mathrm{prep}})-\mathcal{E}^{\mathrm{nr}}(x_{\mathrm{read}}))$ between the state preparation laser beam at x_{prep} and the state readout beam at x_{read}. For this reason, we deduced the systematic error proportional to the difference $(\mathcal{E}^{\mathrm{nr}}(x_{\mathrm{prep}})-\mathcal{E}^{\mathrm{nr}}(x_{\mathrm{read}}))$ from auxiliary measurements of the AC Stark shift phase parameters, $\alpha_{\Delta,i}^{\mathrm{nr}}$.

In summary, the systematic errors proportional to $\mathcal{E}^{\mathrm{nr}}$ and $\Omega_{\mathrm{r}}^{\mathcal{NE}}$ that were evaluated and subtracted from $\omega^{\mathcal{NE}}$ to report a measured value of $\omega_T^{\mathcal{NE}}$ can be expressed as

$$\begin{aligned}\omega_{\mathcal{E}^{\mathrm{nr}}}^{\mathcal{NE}} &= \left(\frac{\partial\omega^{\mathcal{NE}}}{\partial\mathcal{E}^{\mathrm{nr}}}\right)\frac{1}{2}(\mathcal{E}^{\mathrm{nr}}(x_{\mathrm{prep}})+\mathcal{E}^{\mathrm{nr}}(x_{\mathrm{read}})) \\ &\quad+\frac{1}{\tau}(\alpha_{\Delta,\mathrm{prep}}^{\mathrm{nr}}-\alpha_{\Delta,X}^{\mathrm{nr}}-\alpha_{\Delta,Y}^{\mathrm{nr}})\frac{1}{2}(\mathcal{E}^{\mathrm{nr}}(x_{\mathrm{prep}})-\mathcal{E}^{\mathrm{nr}}(x_{\mathrm{read}})) \qquad (3.11)\end{aligned}$$

$$\omega_{\Omega_{\mathrm{r}}^{\mathcal{NE}}}^{\mathcal{NE}} = \begin{cases}\frac{1}{\tau}\sum_{i\in\{\mathrm{prep},X,Y\}}\beta_{d\Omega_{\mathrm{r}},i}^{\mathrm{nr}}\left(\frac{\Omega_{\mathrm{r}}^{\mathcal{NE}}}{\Omega_{\mathrm{r}}^{\mathrm{nr}}}\right) & (\hat{k}\cdot\hat{z})=+1 \\ \left(\frac{\partial\omega^{\mathcal{NE}}}{\partial\Omega_{\mathrm{r}}^{\mathcal{NE}}}\right)\Omega_{\mathrm{r}}^{\mathcal{NE}} & (\hat{k}\cdot\hat{z})=-1\end{cases} \qquad (3.12)$$

where $(\partial\omega^{\mathcal{NE}}/\partial\mathcal{E}^{\mathrm{nr}})$ and $(\partial\omega^{\mathcal{NE}}/\partial\Omega_{\mathrm{r}}^{\mathcal{NE}})$ were monitored by *Intentional Parameter Variations* (see section 2.2) throughout the dataset used for our reported result, and $\mathcal{E}^{\mathrm{nr}}(x_{\mathrm{prep}})$, $\mathcal{E}^{\mathrm{nr}}(x_{\mathrm{read}})$, $d\Omega_{\mathrm{r}}^{\mathcal{NE}}$, $\alpha_{\Delta,i}^{\mathrm{nr}}$, and $\beta_{d\Omega_{\mathrm{r}},i}^{\mathrm{nr}}$ were obtained from auxiliary measurements. These two systematic errors account for almost all of the systematic offset that was subtracted from $\omega^{\mathcal{NE}}$ to obtain $\omega_T^{\mathcal{NE}}$ as described in section 3.6.1.

3.3 Zeeman spin precession systematic errors

Previous electron EDM measurements have often been limited by a variety of systematic errors that would have produced an $\tilde{\mathcal{E}}$-correlated phase precession frequency in our experiment, $\omega^{\mathcal{E}}$ [49, 92, 118, 141], such as $\tilde{\mathcal{E}}$-correlated leakage currents, geometric phases, and motional magnetic fields. Our ability to spectroscopically reverse the molecular orientation through a choice of $\tilde{\mathcal{N}}$ distinguished these effects from an electron EDM-generated phase. In addition, the aforementioned effects scale with the magnitude of the applied electric field, which was orders of magnitude smaller in our experiment than previous similar electron EDM experiments due to the high polarizability of ThO [141]. Also, because the molecular polarization was saturated, the electron EDM phase should have been independent of the magnitude of the applied field. We also note that any shifts from leakage currents and motional magnetic fields coupled through the magnetic dipole moment, which is near-zero in the H-state of ThO. Thus we expected $\omega^{\mathcal{E}}$ to be substantially suppressed, and that it should not enter $\omega^{\mathcal{N}\mathcal{E}}$ at any significant level.

The reversal of $\tilde{\mathcal{N}}$ did not, however, entirely eliminate an electron EDM-like phase due to $\omega^{\mathcal{E}}$. As discussed in section 2.3.2, there was a small and $\mathcal{E}$-field dependent difference between the g-factors of the two $\tilde{\mathcal{N}}$ levels [21, 135], which meant that a systematic error in the $\omega^{\mathcal{E}}$ channel showing up in $\omega^{\mathcal{N}\mathcal{E}}$ at a level given by $\omega^{\mathcal{N}\mathcal{E}}_{\omega^{\mathcal{E}}} = (\eta\mathcal{E}/g_1)\omega^{\mathcal{E}}$. verified this relation by intentionally correlating a 1.4 mG component of our applied magnetic field with $\tilde{\mathcal{E}}$. This deliberate $\mathcal{B}^{\mathcal{E}}$ resulted in a large shift in the value of $\omega^{\mathcal{E}}$ and a $\sim$1000-times smaller offset of $\omega^{\mathcal{N}\mathcal{E}}$, as illustrated in figure 3.4.

The intentionally applied $\mathcal{B}^{\mathcal{E}}$ was the only experimental parameter that was observed to produce a measurable shift in $\omega^{\mathcal{E}}$. Even large ($\sim$20 mG) magnetic fields components along $\hat{x}$ and $\hat{y}$, which exaggerate the effect of motional magnetic fields, did not shift $\omega^{\mathcal{E}}$ (this is expected, since the large tensor Stark shift in $|H, J = 1\rangle$ dramatically suppresses the effect of motional magnetic fields [136]). For our electron EDM data set, $\omega^{\mathcal{E}}$ was consistent with zero. We included a contribution from $\omega^{\mathcal{E}}$ in our error budget for $\omega^{\mathcal{N}\mathcal{E}}$ by multiplying the mean and uncertainty of the extracted $\omega^{\mathcal{E}}$ by our measured $|\mathcal{E}|$-dependent suppression factors $\eta\mathcal{E}/g_1$.

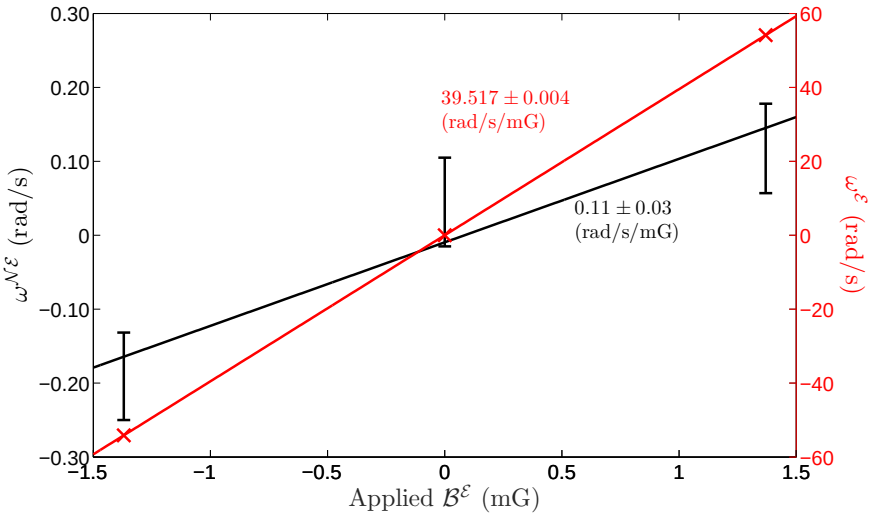

Figure 3.4: Illustration of the ∼1000-fold suppression of systematic errors associated with $\omega^{\mathcal{E}}$ provided by the $\tilde{\mathcal{N}}$ switch. Large values of $\omega^{\mathcal{E}}$ occur when there is a component of $\mathcal{B}_z$ correlated with $\tilde{\mathcal{E}}$, $\mathcal{B}^{\mathcal{E}}$. In previous electron EDM experiments, this would have corresponded to a systematic error. In our experiment a much smaller shift in $\omega^{\mathcal{N}\mathcal{E}}$ results from the small difference in magnetic moments between the two $\tilde{\mathcal{N}}$ levels. Error bars for the $\omega^{\mathcal{E}}$ data are significantly smaller than the data points. Data were taken with $\mathcal{E} = 142$ V/cm and the measured ratio of the slopes, $(\partial\omega^{\mathcal{N}\mathcal{E}}/\partial\mathcal{B}^{\mathcal{E}})/(\partial\omega^{\mathcal{E}}/\partial\mathcal{B}^{\mathcal{E}}) = (2.8 \pm 0.8) \times 10^{-3}$ is consistent with the expected value $\eta\mathcal{E}/g_1 = (2.5 \pm 0.1) \times 10^{-3}$.

3.4 Searching for correlations in the electron EDM data set

In addition to performing systematic error checks for possible variations of $\omega^{\mathcal{NE}}$ with various experimental parameters, we searched for statistically nonzero values within the set of 1536 possible correlations with the block and superblock switches. This analysis was performed for our primary measured quantities ω, $\mathcal{C}$, and F and for a wide range of auxiliary measurements such as laser powers, magnetic field, room temperature, etc. We also examined the switch-parity channels of ω, $\mathcal{C}$, and F as a function of time within the molecule beam pulse, and as a function of time within the polarization switching cycle. We used the Pearson correlation coefficient to look for correlations between the aforementioned switch-parity channels and used the autocorrelation function to look for signs of time variation of the mean within those channels. Figure 3.5 illustrates data from such a search with a subset of the previously described quantities.

In this search, we looked at 4390 quantities and we set the significance threshold at 4σ which corresponds to a probability of $p \approx 0.25$ that there will be one or more false positives above that threshold. We represented the significance of each of these quantities with a gray scale pixel. Each pixel that was significant at the 4σ level is marked with a symbol corresponding to a known explanatory physical model, or a red dot if the signal is not yet explained. The fact that we understand most of the significant signals present in our experiment, combined with the fact that the statistical distribution of the remaining signals below the significance threshold is consistent with a normal distribution, gives us added confidence in our models of the experiment and our reported electron EDM result.

Channels/correlations marked with symbols are significantly nonzero due to known mechanisms as follows:

- Green stars: Correlations due to the nonzero and drifting signal in the $\omega^{\mathcal{N}}$ channel described in section 3.5.
- Light blue squares: Signals in $\omega^{\mathcal{NEB}}$ channels due to the $\tilde{\mathcal{B}}$-odd AC stark shift phase coupling to $\Omega_{\mathrm{r}}^{\mathcal{NE}}$ as described in section 3.2.
- Orange triangles: Correlations due to contrast or asymmetry coupling to $\Omega_{\mathrm{r}}^{\mathcal{NE}}$. Contrast correlations arise simply because there is a linear dependence of total contrast on Rabi frequency, and the asymmetry correlation is described in section 4.3.6.

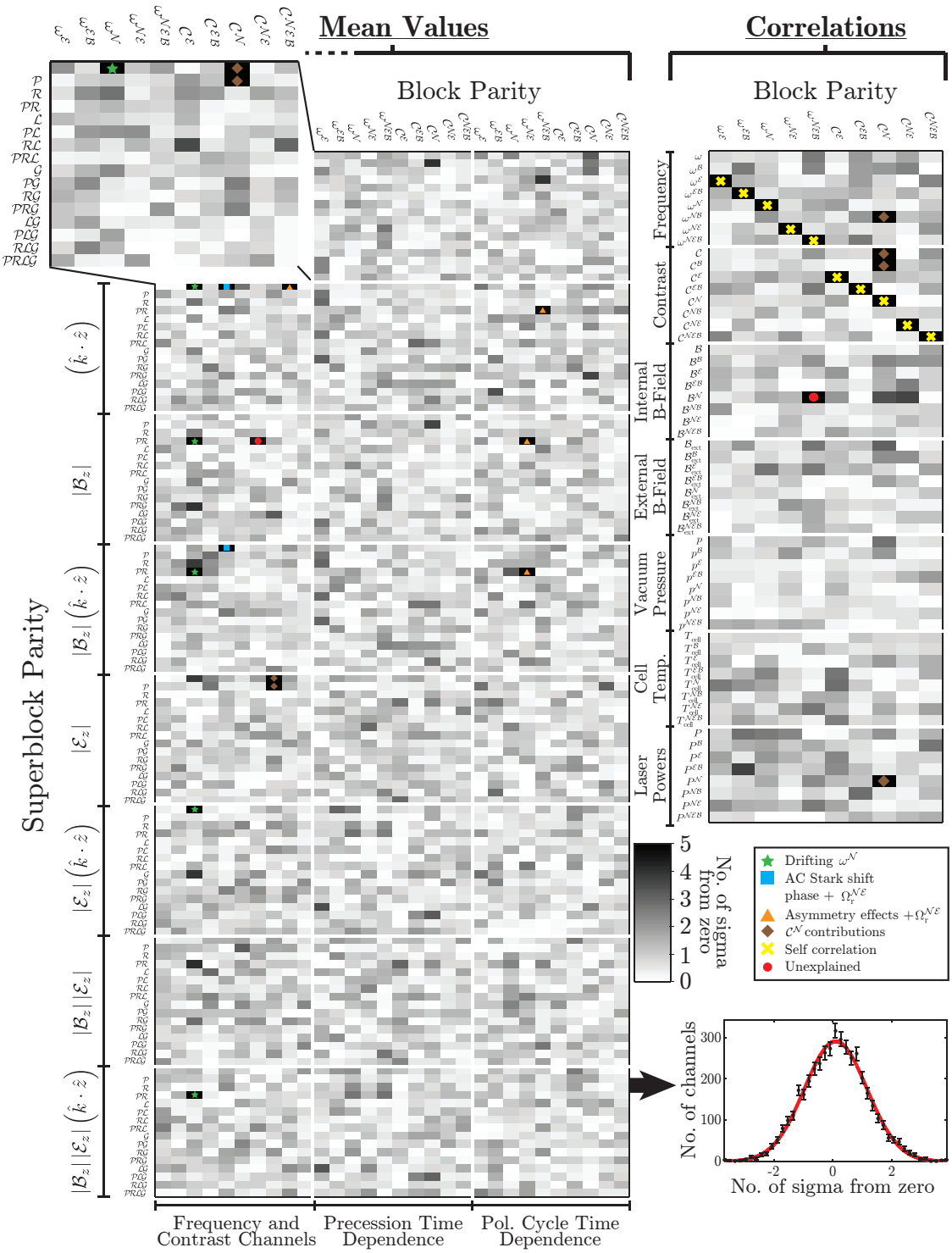

Figure 3.5: Over 4,000 switch-parity channels (left) and correlations between switch parity channels (upper right) computed from the electron EDM data set. The deviation of each quantity from zero in units of the statistical uncertainty is indicated by the gray scale shading. We set a significance threshold of 4σ above which there is a probability of $p = 25\%$ of finding at least 1 false positive. We mark each significant channel/correlation with a symbol corresponding to a model known to produce a signal in that channel. The quantities below this threshold exhibit a normal distribution, shown in the lower right.

- Brown diamond: Correlations in $\mathcal{C}^{\mathcal{N}}$ and related contrast channels due to nonzero Rabi frequency correlations $\Omega_{\mathrm{r}}^{\mathcal{N}}$ and $\Omega_{\mathrm{r}}^{\mathcal{NP}}$. These arise due to laser power correlations with the $\tilde{\mathcal{N}}$ and $\tilde{\mathcal{P}}$ switches and due to Stark mixing between rotational levels in H and C, which create $\tilde{\mathcal{N}}$- and $\tilde{\mathcal{P}}$-correlated transition amplitudes on the $H \rightarrow C$ transition as described in section 4.2.3.

- Red dot: Signals above our significance threshold for which we have been unable to find a plausible explanation. Even if these quantities arise from real physical effects, they would need to couple to other correlated quantities to contribute to $\omega^{\mathcal{NE}}$ and there is no evidence for this in the electron EDM dataset.

3.5 Loose ends and peculiarities

Correlations due to experimental switch configuration

Early during ACME I we measured a large correlation of the magnetic field with our $\tilde{\mathcal{N}}$ reversal, $\mathcal{B}^{\mathcal{BN}}$ using the fluxgate magnetometers that were embedded in the experiment. We were able to determine that we were observing this correlation because at the beginning of each block, the magnetic field had not yet finished settling after the first experiment state. Given that we began each block with the same $\tilde{\mathcal{N}} = +1$ state, this state repeatably experienced a smaller magnetic field magnitude compared to the following state $\tilde{\mathcal{N}} = -1$ resulting in a systematic error shift in the $\omega^{\mathcal{NB}}$ measurement. After making this observation we modified the switching sequence such that the first $\tilde{\mathcal{N}}$ state during a given block is randomly selected. This selection of which $\tilde{\mathcal{N}}$ state was selected first could also be treated as a switch in the analysis to identify what kind of systematic errors may be resulting from this effect. This anecdote serves as a cautionary tale regarding the choice of the experiment switching sequence. The more randomness that is introduced into the switching sequence, the less likely it is that fluctuations in parameters over time will manifest themselves as apparent correlations with experiment switches. This was the motivation for the creation of a new software program that could generate more randomness in the experimental switch sequences in ACME II compared to that used in ACME I [77]

Unexplained $\omega^{\mathcal{N}}$ and what we learned

We discovered a nonzero, time-dependent signal in $\omega^{\mathcal{N}}$ which was associated with an $\tilde{\mathcal{N}}$-correlated laser pointing, $\hat{k}^{\mathcal{N}} \approx 5$ μrad. An investigation into the mechanism behind this effect was inconclusive. We found that the pointing correlation appeared downstream of the AOMs that created the rapid polarization switching and improved alignment was able to reduce the effect. We also found that the observed pointing was in some way correlated with the seed power and input angle of incidence into the high-power fiber amplifier immediately upstream of the polarization switching, despite the fact that pointing out of the amplifier did not fluctuate. Since we used four different sets of AOMs to perform the $\tilde{\mathcal{N}}$ and $\tilde{\mathcal{P}}$ switches before the amplifier, we observed laser pointing correlated with both of these switches. By matching the characteristics of these four beam paths we were able to suppress $\hat{k}^{\mathcal{N}}$ to < 1 μrad.

The effect of $\hat{k}^{\mathcal{N}}$ on $\omega^{\mathcal{N}}$ was studied by exaggerating the former with piezoelectrically actuated mirrors. Examining $\partial\omega^{\mathcal{N}}/\partial\hat{k}^{\mathcal{N}}$ showed significant fluctuations in its value. We were unable to identify the mechanism by which $\hat{k}^{\mathcal{N}}$ affected $\omega^{\mathcal{N}}$.

We had no evidence that the effect causing the observed variation in $\omega^{\mathcal{N}}$ also caused a systematic error in $\omega^{\mathcal{NE}}$, but to be cautious we included an associated systematic uncertainty in our systematic error budget (section 3.6.1). Assuming a linear relationship between $\omega^{\mathcal{NE}}$ and $\omega^{\mathcal{N}}$, we extracted $\partial\omega^{\mathcal{NE}}/\partial\omega^{N}$ from a combination of data taken under normal conditions and with an exaggerated $\omega^{\mathcal{N}}$ induced by an exaggerated $\hat{k}^{\mathcal{N}}$. We then placed an upper limit on a possible systematic error $\omega^{\mathcal{NE}}_{\omega^{\mathcal{N}}}$ based on the value of $\omega^{\mathcal{N}}$ obtained under normal running conditions. The resulting systematic uncertainty was four times smaller than our statistical uncertainty.

Unexplained correlation between $\mathcal{B}^{\mathcal{N}}$ and $\omega^{\mathcal{NEB}}$

In section 3.4, we examined a large array of quantities correlated with the experiment switches and correlations between these measurements as they vary over time . One of the few unexplained signals that was observed to be significantly non-zero was a correlation coefficient of about $r(\mathcal{B}^{\mathcal{N}}, \omega^{\mathcal{NEB}}) \approx .04$. If this is indicative of a linear relationship between these two parameters, then it could be characterized by a slope $\partial\omega^{\mathcal{NEB}}/\partial\mathcal{B}^{\mathcal{N}} \approx 15\,\mathrm{mrad/s}/\mu\mathrm{G}$. Additionally, from the monitoring magnetometers, we have measurements

of $\mathcal{B}^{\mathcal{N}} \approx .1 - .4\,\mu G$ that is unexplained, consistently non-zero, large, drifting in time, and appears to be vary with electric field magnitude. However, it is not clear what is causing this fluxgate reading correlation. If this were a magnetic field component it should have induced Zeeman spin precession $\omega^{\mathcal{N}} \approx \mu_B g_{H,J=1} B^{\mathcal{N}} \approx 4 - 16\,\mathrm{mrad}/s$ and should have dominantly resulted in a large correlation between $\omega^{\mathcal{N}}$ and $\mathcal{B}^{\mathcal{N}}$ which was not observed to be non-zero. As discussed in section 3.5, we did observe an unexplained and large drifting $\omega^{\mathcal{N}}$ whose value varied with $\hat{k} \cdot \hat{z}$ and $|\mathcal{E}|$, and it is possible that these two phenomena are related, but the data does not seem to support a simple relationship between the two phenomena at this time. If $\mathcal{B}^{\mathcal{N}}$ is not caused by a magnetic field, then what could it be caused by? One plausible explanation is pick-up in the magnetometers from the RF radiated into the room from the AOMs that do the $\tilde{\mathcal{N}}$ switching. That RF amplitude and frequency is correlated both with $\tilde{\mathcal{N}}$ and $|\mathcal{E}|$, and could maybe be picked up by the magnetometers and converted to DC, and could plausibly be interacting with the molecules resulting in fluctuations in the $\omega^{\mathcal{N}\mathcal{E}\mathcal{B}}$ measurement.

Given the measured correlation between $\mathcal{B}^{\mathcal{N}}$ and $\omega^{\mathcal{N}\mathcal{E}\mathcal{B}}$ with the magnitude described above, then the existence of a non-zero $\mathcal{B}^{\mathcal{N}\mathcal{B}}$ (by which I mean a signal from the same source as $\mathcal{B}^{\mathcal{N}}$ which has opposite parity with respect to $\tilde{\mathcal{B}}$) could couple to this relationship to lead to a non-zero systematic error in the electron EDM channel, $\omega^{\mathcal{N}\mathcal{E}}$, with approximate magnitude given by,

$$\omega^{\mathcal{N}\mathcal{E}}_{\mathcal{B}^{\mathcal{N}\mathcal{B}}} = \frac{\partial \omega^{\mathcal{N}\mathcal{E}\mathcal{B}}}{\partial \mathcal{B}^{\mathcal{N}}} \mathcal{B}^{\mathcal{N}\mathcal{B}}. \tag{3.13}$$

Note that a contribution to $\mathcal{B}^{\mathcal{N}\mathcal{B}}$ from the same source as the $\mathcal{B}^{\mathcal{N}}$ is not hard to imagine because we know that $\mathcal{B}^{\mathcal{N}}$ is drifting fairly significantly in time, and if it is drifting significantly over the course of a block, we can obtain a contribution to $\mathcal{B}^{\mathcal{N}\mathcal{B}}$ since $\tilde{\mathcal{B}}$ is the longest timescale switch within a block. Indeed, we did at one point measure a non-zero $\mathcal{B}^{\mathcal{N}\mathcal{B}} \approx .02\mu G$ which was marginally statistically significant, which could result in a systematic error of $\omega^{\mathcal{N}\mathcal{E}}_{\mathcal{B}^{\mathcal{N}\mathcal{B}}} \sim .3\,\mathrm{mrad/s}$. This is small compared to our statistical uncertainty in ACME I, but is not small compared to our individual contributions to the systematic uncertainty in ACME I, and is comparable to the projected statistical sensitivity of the ACME II measurement. However, $\mathcal{B}^{\mathcal{N}\mathcal{B}}$ appears to have been consistent with zero for the electron EDM run overall, suggesting that this systematic error, if present, is significantly

smaller than the previous estimate.

3.6 ACME I result

3.6.1 Systematic Error Budget

Table 3.2: Systematic shifts and uncertainties for $\omega^{\mathcal{NE}}$, in units of mrad/s. Total uncertainties are calculated by summing the individual contributions in quadrature. Note that $\omega^{\mathcal{NE}} \approx 1.3$ mrad/s corresponds roughly to $1 \times 10^{-29}\ e \cdot \text{cm}$ for our experiment.

Class	Parameter	Shift	Uncertainty
A	$\mathcal{E}^{\text{nr}}$ correction	-0.81	0.66
A	$\Omega_{\text{r}}^{\mathcal{NE}}$ correction	-0.03	1.58
A	$\omega^{\mathcal{E}}$ correlated effects	-0.01	0.01
B	$\omega^{\mathcal{N}}$ correlation		1.25
C	Non-reversing $\mathcal{B}$-field ($\mathcal{B}_z^{\text{nr}}$)		0.86
C	Transverse $\mathcal{B}$-fields $\left(\mathcal{B}_x^{\text{nr}}, \mathcal{B}_y^{\text{nr}}\right)$		0.85
C	$\mathcal{B}$-field gradients		1.24
C	Prep./read laser detunings		1.31
C	$\tilde{\mathcal{N}}$ correlated detuning		0.90
C	$\mathcal{E}$-field ground offset		0.16
	Total Systematic	-0.85	3.24
	Statistical Uncertainty		4.80
	Total Uncertainty		5.79

The method used for construction of a systematic uncertainty varies from experiment to experiment (see for example [14,152]), and it is ultimately a subjective quantity. Even if individual contributions are derived from objective measurements, their inclusion or exclusion in the systematic uncertainty is subjective. Furthermore, the systematic uncertainty cannot possibly be a measure of the uncertainty in all systematic errors in the experiment, but rather only those which were identified and searched for. Although we work hard to identify all significant systematic errors in the measurement, we cannot rule out the possibility that some were missed.

Our criteria for including a given quantity in the systematic uncertainty consist of three classes of systematic errors in order of decreasing importance of inclusion:

A If we measured a nonzero correlation between $\omega^{\mathcal{NE}}$ and some parameter which had an ideal value in the experiment, we performed auxiliary measurements to evaluate the corresponding systematic error and subtract that error from $\omega^{\mathcal{NE}}$ to obtain $\omega_T^{\mathcal{NE}}$.

The statistical uncertainty in the shift made to $\omega^{\mathcal{NE}}$ contributed to the systematic uncertainty.

B If we observed a signal in a channel that we deemed important to understand, and it was not understood, but was not observed to be correlated with $\omega^{\mathcal{NE}}$, we set an upper limit on the shift in $\omega^{\mathcal{NE}}$ due to a possible correlation between the two channels. Since such a signal represented a gap in our understanding of the experiment, we added this upper limit as a contribution to the systematic uncertainty.

C If a similar experiment saw a nonzero, not understood correlation between their measurement channel and some parameter with an ideal experimental value, but we did not observe an analogous correlation, we set an upper limit on the shift in $\omega^{\mathcal{NE}}$ due to this imperfection. Since this signal may have signified a gap in our understanding of our experiment, we added this upper limit as a contribution to the systematic uncertainty.

Table 3.2 contains a list of the contributions to our systematic error, grouped by inclusion class, with the corresponding shifts and/or uncertainties. Accounting for class A systematic errors was obligatory, and the removal of these errors from $\omega^{\mathcal{NE}}$ can be viewed as a redefinition of the measurement channel to $\omega_T^{\mathcal{NE}}$ which does not contain those unwanted effects. These systematic errors consisted of those that depended on the parameters $\mathcal{E}^{\mathrm{nr}}$, $\Omega_{\mathrm{r}}^{\mathcal{NE}}$, and $\omega^{\mathcal{E}}$ as described in sections 3.2 and 3.3, and as such our reported measurement of the T-odd spin precession frequency is defined as $\omega_T^{\mathcal{NE}} = \omega^{\mathcal{NE}} - \omega_{\mathcal{E}^{\mathrm{nr}}}^{\mathcal{NE}} - \omega_{\Omega_{\mathrm{r}}^{\mathcal{NE}}}^{\mathcal{NE}} - \omega_{\omega^{\mathcal{E}}}^{\mathcal{NE}}$. The class B and class C systematic errors were included in the systematic uncertainty to lend credence to our result despite unexplained signals and unexplained systematic errors in experiments similar to ours. All uncertainties in the contributions to the systematic error were added in quadrature to obtain the systematic uncertainty.

With reference to the class B criterion, we deemed the following channels as important to understand: $\omega^{\mathcal{N}}$, $\omega^{\mathcal{E}}$, $\omega^{\mathcal{EB}}$, and $\omega^{\mathcal{NEB}}$. Signals were initially not expected in any of these channels and could be measured with the same precision as $\omega^{\mathcal{NE}}$. The ω^{nr}, $\omega^{\mathcal{B}}$ and $\omega^{\mathcal{NB}}$ channels were not included in our systematic error since the Zeeman spin precession signals present in these channels had non-stationary means and additional noise due to drift in the molecule beam velocity. Only one of these channels, $\omega^{\mathcal{N}}$, described in section 3.5, met the class B inclusion criterion.

With reference to the class C criterion, we defined the set of experiments similar to ours to include other electron EDM experiments performed in molecules: the YbF experiment [82] and the PbO experiment [49]. The PbO experiment observed unexplained systematic errors coupling to stray magnetic fields and magnetic field gradients , and the YbF experiment observed unexplained systematic errors proportional to detunings and a field plate ground voltage offset . Thus we included the systematic uncertainty associated with the aforementioned effects in our budget.

After having accounted for the systematic errors and systematic uncertainty, we reported $\omega_T^{\mathcal{NE}}$, the contribution to the channel $\omega^{\mathcal{NE}}$ induced by T-odd interactions present in the H state of ThO, as

$$\omega_T^{\mathcal{NE}} = 2.6 \pm 4.8_{\text{stat}} \pm 3.2_{\text{syst}} \text{ mrad/s} \tag{3.14}$$

$$= 2.6 \pm 5.8 \text{ mrad/s} \tag{3.15}$$

where the combined uncertainty is defined as the quadrature sum of the statistical and systematic uncertainties, $\sigma^2 = \sigma_{\text{stat}}^2 + \sigma_{\text{syst}}^2$. This result is consistent with zero within 1σ. Since σ_{syst} is to some extent a subjective quantity, its inclusion should be borne in mind when interpreting confidence intervals based on σ. Nevertheless, this inclusion decision does not have a large impact on the meaning of the resulting confidence intervals since σ is only about 20% larger than σ_{stat}.

3.6.2 Confidence interval construction

In ACME I, we chose to present the result of the experiment as a Feldman-Cousins confidence interval [58], at a 90% confidence level, for the absolute value of the electron's EDM. This is a frequentist confidence interval insofar as its interpretation - that given a fixed true value of the electron's EDM, $\mu = |\omega_{T,\text{true}}^{\mathcal{NE}}|$, if we were to repeat our measurement of $x = |\omega_{T,\text{meas}}^{\mathcal{NE}}|$ a large number of times and the confidence interval were constructed in the same way, then the confidence interval would contain the true value a fraction of the time equivalent to the stated confidence level p. If the probability distribution governing the observation of x given a true value μ is $P(x|\mu)$, then the frequentist confidence band

$(x_1(\mu),\, x_2(\mu))$ (this is the inverse of the confidence interval $(\mu_1(x),\, \mu_2(x))$), must satisfy

$$p = \int_{x_1(\mu)}^{x_2(\mu)} P(x|\mu)dx, \tag{3.16}$$

for all μ. As described in section 2.3.4 the measurements of $\omega_{T,\mathrm{meas}}^{\mathcal{NE}}$ were consistent with being normally distributed, so we model its absolute value, x, with the folded normal distribution. However, the Feldman-Cousins approach is not strictly a Neyman frequentist confidence interval construction because it uses an ordering principle for which values of x with a higher likelihood ratio $\mathcal{L}(\mu|x)/\mathcal{L}(\mu_{\max}(x)|x)$, where $\mathcal{L}(\mu|x) = P(x|\mu)$ and $\mu_{\max}(x) = \mathrm{argmax}_\mu \mathcal{L}(\mu|x)$, are preferentially included in the confidence band; the Neyman construction strictly forbids such a comparison between alternate hypotheses for μ [22].

Since no statistically significant electron EDM has yet been observed, the recent custom has been for experiments to report an upper limit at the $p = 90\%$ confidence level [82, 141]. However, before we had unblinded our result, we imagined that if we observed a non-zero electron EDM, we would have liked to present a two-sided confidence interval. If we had naively decided to change our confidence interval construction method contingent on the result, the resulting confidence intervals would under-cover the stated confidence level (the fraction of time that the constructed confidence interval contains the true value would be less than p). Hence, we selected the Feldman-Cousins confidence interval construction because it produces the desired behavior with appropriate coverage (i.e. the frequentist confidence interval interpretation is still valid); it produces an upper limit if x is close to zero and produces a two sided confidence interval if x is far from zero.

However, there are several possible confidence interval constructions that could have been used that would have produced the desired behavior. Figure 3.6.2 shows a comparison of several Neyman confidence interval constructions and the Feldman-Cousins construction for the folded normal distribution at 90% confidence. This includes an upper limit, a lower limit, a symmetric area interval (defined such that $\int_{x_1(\mu)}^{x_m(\mu)} P(x|\mu)dx = \int_{x_m(\mu)}^{x_2(\mu)} P(x|\mu)dx = p/2$, where $x_m(\mu)$ is the median of the distribution), and a symmetric likelihood interval (defined by $P(x_1(\mu)|\mu) = P(x_2(\mu)|\mu)$). Indeed, we can see that the Feldman-Cousins, the symmetric likelihood, and the symmetric area intervals all produce the desired behavior of transitioning from one-sided to two sided confidence intervals with increasing x. One downside to using frequentist confidence interval constructions is that they can frequently

produce empty set confidence intervals, in which case you can be sure that your reported confidence interval does not contain the true value. For the folded normal distribution, the symmetric area construction always produces empty set intervals for sufficiently small values of x, for all confidence levels; the Feldman-Cousins construction produces empty set intervals for sufficiently small values of x, for confidence levels $p < 68\%$; and the symmetric likelihood construction does not produce empty set intervals. For this reason, if we were to choose our confidence interval construction method today, I would choose the symmetric likelihood construction. However, for frequentist constructions, we should choose the confidence interval construction method before making the measurement so that we may ensure that the outcome of the measurement does not affect how we made that decision. In ACME I we chose to present our result using the Feldman-Cousins construction before unblinding the result. Furthermore, we may not want to switch confidence interval constructions between ACME I and ACME II so that we may make a more direct comparison between our results.

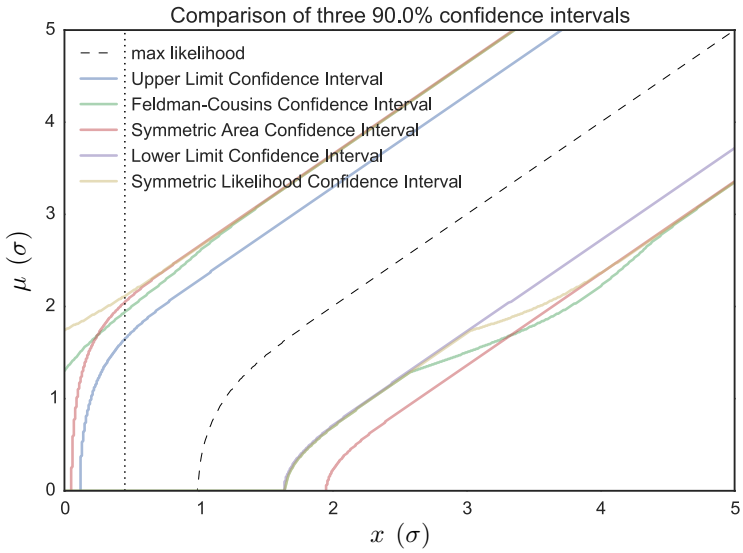

Figure 3.6: Comparisons of different frequentist confidence interval constructions for the folded normal distribution at a 90% confidence level. Here x is the measurement value in units of the statistical uncertainty σ, and y is the true value in units of the statistical uncertainty σ. The constructions include the upper limit, lower limit, symmetric area, symmetric likelihood, and Feldman-Cousins. The vertical dotted line shows the ACME I measurement.

From equation (3.15), we find $x = 0.46\sigma$ with $\sigma = 5.79$ mrad/s. For this measurement, our confidence interval construction produces an upper bound of $|\omega_T^{\mathcal{NE}}| < 1.9\sigma = 11$ mrad/s

at a 90% confidence level. We believe that the confidence intervals that were presented for previous electron EDM measurements [68, 82, 141] were likely Bayesian credible intervals conditioned on a uniform prior for μ, rather than the frequentist upper limit presented in figure 3.6.2 . These intervals do not satisfy equation 3.16, but rather over-cover for small values of μ [58]. The Feldman-Cousins confidence interval that we are presenting here produces a 7% larger limit than the limit than the limit that we would have produced if we had used the Bayesian credible interval upper limit approach.

3.6.3 Interpretation of the result

Under the most general interpretation, our experiment is sensitive to any P- and T-violating interaction that produces an energy shift $\omega_T^{\mathcal{NE}}$. The electron EDM is not the only such predicted interaction for diatomic molecules [98], and in particular a P- and T-odd electron-nucleon interaction would also manifest as a $\tilde{\mathcal{N}}\tilde{\mathcal{E}}$-odd spin precession frequency in our measurement. Thus, we interpret the measurement as having possible contributions from these two effects,

$$\omega_T^{\mathcal{NE}} = -d_e \mathcal{E}_{\text{eff}} - W_{\text{S}} C_{\text{S}}, \tag{3.17}$$

where W_{S} is a calculated molecule specific constant [47, 48, 153, 154] and C_{S} is the constant characterizing the strength of the T-violating electron-nucleon coupling.

We can use our measurement to set an upper limit on d_e by assuming that $C_{\text{S}} = 0$ and that $\omega_T^{\mathcal{NE}}$ is therefore entirely attributable to the electron EDM. Taking the effective electric field to be the unweighted mean of the two most recent calculations of this quantity [61,154], $\mathcal{E}_{\text{eff}} = 78.4$ GV/cm, we can interpret our result in equation (3.15) as:

$$d_e = (-2.2 \pm 4.8) \times 10^{-29}\ e \cdot \text{cm} \tag{3.18}$$

$$\Rightarrow |d_e| < 9.3 \times 10^{-29}\ e \cdot \text{cm}\ (90\%\,\text{C.L.}), \tag{3.19}$$

where the second line is obtained by appropriately scaling the upper bound on $|\omega_T^{\mathcal{NE}}|$ derived above.

If, instead, we assume that $d_e = 0$, our measurement of $\omega_T^{\mathcal{NE}}$ in ThO can be restated as a measurement of C_{S}. Using the most recent calculation of the interaction coefficient,

$W_S = 1.81 \times 10^6$ rad/s [47, 154], we obtain:

$$C_S = (-1.4 \pm 3.2) \times 10^{-9} \tag{3.20}$$

$$\Rightarrow |C_S| < 6.1 \times 10^{-9}\,(90\%\,\text{C.L.}), \tag{3.21}$$

which, at the time, was an order of magnitude smaller than the existing best limit set by the ^{199}Hg EDM experiment [161], and is still a factor of 2 smaller than the recently improved limit from the same group [67].

Chapter 4

Models for Understanding Systematic Errors

> Most people don't believe something can happen until it already has. That's not stupidity or weakness, that's just human nature.
>
> Max Brooks, World War Z

In the process of understanding and interpreting the data that we took during the ACME I systematic error search, and in anticipation of possible new systematic errors that might appear when we operate with improved sensitivity in ACME II, we have developed a library of analytic models that serve to describe and estimate the size of possible systematic errors in the experiment. In this chapter, I will focus less on the experiments that were performed to understand and characterize the systematic errors that we previously observed, and focus more on compiling a theoretical framework for understanding systematic errors that we both have and have not yet experimentally observed. My hope is that this chapter will serve as a reference for understanding signals observed in the experiment in the future, and I hope that others will add to this library as our understanding of our system becomes even more detailed.

In section 4.1 I provide a framework within which we can describe changes in the molecule state and derive how these changes in the molecule state contribute the spin precession measurement signals. In section 4.2 I explore an array of mechanisms by which interference in the state preparation and state read-out transitions can result in correlations in the Rabi frequency describing the strength of the coupling and correlations in the

molecule state that is prepared or read-out in the spin precession measurement. In section 4.3 I provide a list of mechanisms that can result in changes to the measured phase $\Phi(\Delta, \Omega_r)$ that depend on the laser detuning Δ or Rabi frequency Ω_r while the molecule state evolves in the state preparation and read-out lasers. Finally, in section 4.4 we explore how electromagnetic fields in the spin precession region can affect the molecule state. In each section I discuss how these various effects could result in systematic errors in the electron EDM measurement channel, $\omega^{\mathcal{NE}}$, and provide order of magnitude estimates of the size of these effects that we might expect. This chapter also includes interwoven discussions on how these various systematic errors may manifest themselves in ACME II and efforts that we have made to suppress them. To the set the scale for the estimates of the systematic errors to come, the statistical resolution of the phase measurement ACME I was approximately 5 μrad and ACME II is projected to have a sensitivity of $.1 - .5\,\mu$rad.

4.1 Phase measurement with polarization offsets

4.1.1 Idealized Measurement Scheme with Polarization Offsets

As described in section 2.1, in the ACME I experiment the molecules initially enter the state preparation laser beam in an incoherent mixture of the two states $|\pm, \tilde{\mathcal{N}}\rangle$. The bright state $|B(\hat{\epsilon}_{\text{prep}}), \tilde{\mathcal{N}}, \tilde{\mathcal{P}}_{\text{prep}}\rangle$ is then optically pumped away through $|C, \tilde{\mathcal{P}}_{\text{prep}}\rangle$ leaving behind the dark state $|D(\hat{\epsilon}_{\text{prep}}), \tilde{\mathcal{N}}, \tilde{\mathcal{P}}_{\text{prep}}\rangle$ as the initial state for the spin precession. The molecules then undergo spin precession by angle ϕ evolving to a final state $|\psi_f\rangle = U(\phi)|D(\hat{\epsilon}_{\text{prep}}), \tilde{\mathcal{N}}, \tilde{\mathcal{P}}_{\text{prep}}\rangle$ where $U(\phi) = \sum_{\pm} e^{\mp i\phi}|\pm, \tilde{\mathcal{N}}\rangle\langle\pm, \tilde{\mathcal{N}}|$ is the spin precession operator. The molecules then enter the state readout laser that optically pumps the molecules with alternating polarizations $\hat{\epsilon}_X$ and $\hat{\epsilon}_Y$ (which are nominally linearly polarized and orthogonal) between $|\pm, \tilde{\mathcal{N}}\rangle$ and $|C, \tilde{\mathcal{P}}_{\text{read}}\rangle$. For each polarization, the optical pumping results in a fluorescence count rate proportional to the projection of the state onto the bright state, $F_{X,Y} = fN_0|\langle B(\hat{\epsilon}_{X,Y}), \tilde{\mathcal{N}}, \tilde{\mathcal{P}}_{\text{read}}|\psi_f\rangle|^2$ where f is the photon detection efficiency, and N_0 is the number of molecules in the addressed $\tilde{\mathcal{N}}$ level. We then compute the asymmetry, $\mathcal{A} = (F_X - F_Y)/(F_X + F_Y)$, dither the linear polarization angles in the state readout laser beams to evaluate the fringe contrast, $\mathcal{C} = (\partial\mathcal{A}/\partial\phi)/2 \approx -(\partial\mathcal{A}/\partial\theta_{\text{read}})/2$, and extract the

measured phase, $\Phi = \mathcal{A}/(2\mathcal{C}) + q\pi/4$.[1] We then report the result of the measurement in terms of an equivalent phase precession frequency $\omega = \Phi/\tau$ where $\tau \approx 1\,\text{ms}$ is the spin precession time, which was measured for each block as described in section 2.3.2. This description of the phase measurement pertains to ACME I. In ACME II, as described in section 2.20 we changed the state preparation scheme such that a pair of STIRAP laser beams prepare an initial spin state and then a refinement laser beam reprojects the initial spin state to suppress systematic errors caused by the STIRAP state transfer scheme. For the purpose of this discussion, the refinement laser beam in ACME II plays the same role as the state preparation laser beam in ACME I apart from effects discussed in section 4.3.5.

Let us first consider the idealized case in which all laser polarizations are exactly linear, $\Theta_i = \pi/4$ for each laser $i \in \{\text{prep}, X, Y\}$, the angle between the state preparation laser polarization (prep) and state readout basis (X, Y) is $\pi/4$, $\theta_{\text{read}} - \theta_{\text{prep}} = -\pi/4$, and the accumulated phase is small, $|\phi| \ll 1$ (i.e. no magnetic field is applied). Under these conditions, the measured phase Φ is equal to the accumulated phase ϕ. Now consider the effect of adding polarization offsets $d\vec{\epsilon}_i$ to each of the three laser beams such that $\hat{\epsilon}_i \to \hat{\epsilon}_i + \lambda d\vec{\epsilon}_i$, where $\lambda = 1$ is a perturbation parameter. It is useful to cast the polarization imperfections in terms of linear angle imperfections, $\theta_i \to \theta_i + \lambda d\theta_i$ and ellipticity imperfections, $\Theta_i \to \Theta_i + \lambda d\Theta_i$ where $S_i = -2d\Theta_i$ is the laser ellipticity Stokes parameter; these are related by

$$\frac{\hat{z} \cdot (\hat{\epsilon}_i \times d\vec{\epsilon}_i)}{\hat{\epsilon}_i \cdot \hat{\epsilon}_i} = d\theta_i - i d\Theta_i. \tag{4.1}$$

Note that laser polarizations can have a nonzero projection in the $\hat{z}$ direction, but we assume in the discussion above that $\hat{\epsilon}_i$ represents a normalized projection of the laser polarization onto the xy plane.[2] With these polarization imperfections in place, the measured phase Φ gains additional terms:

$$\Phi = \phi + \lambda(d\theta_{\text{prep}} - \frac{1}{2}(d\theta_X + d\theta_Y)) - \lambda^2 \tilde{\mathcal{P}}_{\text{prep}} \tilde{\mathcal{P}}_{\text{read}} d\Theta_{\text{prep}} (d\Theta_X - d\Theta_Y) + O\left(\lambda^3\right), \tag{4.2}$$

up to second order in λ. In the electron EDM measurement, we switch between two values

1. Recall q is chosen to be an integer which depends on the size of the applied magnetic field as mentioned in section 2.20

2. The z-component of the polarization can only drive $\Delta M = 0$ transitions, which are far off resonance from the state preparation/readout lasers.

of $\tilde{\mathcal{P}} \equiv \tilde{\mathcal{P}}_{\rm read}$, the parity of the excited state addressed during state readout, and we set $\tilde{\mathcal{P}}_{\rm prep} = +1$, the parity of the excited state addressed during state preparation. It is worth dwelling on equation 4.2 for a moment. A rotation of all polarizations by the same angle leaves the measured phase unchanged: $d\theta_i \to d\theta_i + d\theta \implies \Phi \to \Phi$, as expected. A deviation in the relative angle between the state preparation and readout beams, $d\theta_{\rm prep} \to d\theta_{\rm prep} + d\theta$ and $d\theta_{X,Y} \to d\theta_{X,Y} - d\theta$, enters into the phase measurement as $\Phi \to \Phi + 2d\theta$, but is benign so long as $d\theta$ is uncorrelated with the expected electron EDM signal. The laser ellipticities affect the phase measurement only when the state readout beams differ in ellipticity, and this contribution to the phase can be distinguished from the others by switching the excited state parity, $\tilde{\mathcal{P}}$. This last term is particularly interesting because it allows for multiplicative couplings between polarization imperfections in the state preparation and state readout beams to contribute to the measured phase.

Although the polarization imperfection terms in equation 4.2 are uncorrelated with the $\tilde{\mathcal{N}}\tilde{\mathcal{E}}$ and hence do not contribute to the systematic error, we will see in later sections that additional imperfections can lead to changes in the molecule state that is prepared or read-out that are equivalent to correlations $d\theta_i^{\mathcal{NE}}$ and $d\Theta_i^{\mathcal{NE}}$. The framework of equation 4.2 is useful for understanding how these correlations result in systematic errors in the measurement of $\Phi^{\mathcal{NE}}$,

$$\begin{aligned}\Phi^{\mathcal{NE}} =& \phi^{\mathcal{NE}} + \lambda(d\theta_{\rm prep}^{\mathcal{NE}} - \frac{1}{2}(d\theta_X^{\mathcal{NE}} + d\theta_Y^{\mathcal{NE}})) \\ &- \lambda^2 \tilde{\mathcal{P}}_{\rm prep}\tilde{\mathcal{P}}_{\rm read}\left\{d\Theta_{\rm prep}^{\rm nr}(d\Theta_X^{\mathcal{NE}} - d\Theta_Y^{\mathcal{NE}}) + d\Theta_{\rm prep}^{\mathcal{NE}}(d\Theta_X^{\rm nr} - d\Theta_Y^{\rm nr}) + \dots\right\} + \dots \quad (4.3)\end{aligned}$$

In this expression for $\Phi^{\mathcal{NE}}$, I have included the second order terms of the form $d\Theta_i^{\rm nr} d\Theta_j^{\mathcal{NE}}$, which consist of a multiplicative coupling between the ellipticity of the light in laser i and an $\tilde{\mathcal{N}}\tilde{\mathcal{E}}$ correlated spin ellipticity generated in laser j, but I have not explicitly written other possible second order terms, for example ones like $d\Theta_i^{\mathcal{N}} d\Theta_j^{\mathcal{E}}$ or $d\Theta_j^{\mathcal{B}} d\Theta_j^{\mathcal{NEB}}$, that can also, in principle, generate electron EDM systematic errors.

4.1.2 Suppressing Second Order Phase Shifts with Polarization Control

In the following sections, we discuss several mechanisms that can generate a correlated spin state rotation, $d\theta_i^{\mathcal{NE}}$, or a correlated spin state ellipticity, $d\Theta^{\mathcal{NE}}$ during the state preparation or state read-out processes and both correlations can contribute to systematic errors in the

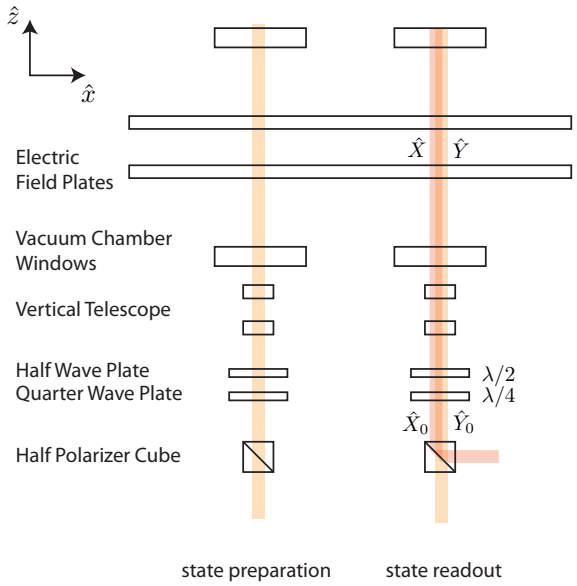

Figure 4.1: Schematic of state preparation and state readout optics set-up with improved polarization control relative to ACME I. A $\lambda/2$ and $\lambda/4$ waveplate on a rotate-able stepper motor mount is present on each beam path to finely tune the polarization to eliminate ellipticity in the region where the molecules interact with the laser beam.

electron EDM experiment as in equation 4.3. For some of these mechanisms, $d\theta_i^{\mathcal{NE}}$ is proportional to the ellipticity $d\Theta_i^{\mathrm{nr}}$ in that laser beam. As in equation 4.3, $d\Theta_i^{\mathcal{NE}}$ couples to the ellipticity in a different laser beam, $d\Theta_j^{\mathrm{nr}}$, to result in a systematic error. Hence, both of these classes of systematic errors could be suppressed if the ellipticities of all of the laser beams were suppressed.

During ACME I we believe that the ellipticities of the state preparation and state read-out laser beams were on the order of $S \sim 2\%$[3]and the linear polarization angle offsets were around $d\theta \sim 1$ mrad. In this section we explore the possibility of suppressing the ellipticities further in ACME II by adding additional polarization control to aid in suppressing a large group of systematic errors that can depend on these quantities. In particular, we consider fine tuning of the angles of a $\lambda/4$ waveplate and a $\lambda/2$ waveplate that the beams could be sent through before entering into the apparatus in order to minimize the ellipticity.

Lets assume that in the state read-out region, we start with polarizations $\hat{X}_0$ and $\hat{Y}_0$ that are combined on a polarizing beamsplitter (PBS). Recall that the state read-out scheme

3. We do not have direct measurements of the ellipticity during ACME I because our polarimetry was limited by systematic errors in measuring ellipticity more precisely than about $|S| < 2\%$ [77]. During a spin precession experiment in which we varied S_{prep} we were able to estimate that $S_X - S_Y \approx 4\%$ from a measurement of $\partial\Phi^{\mathcal{P}}/\partial S_{\mathrm{prep}} \approx -4(S_X - S_Y)$.

consists of alternating between addressing the molecules with nominally orthogonal and linearly polarized laser beams, so only one of these beams is incident on the PBS at a time. Here, $\hat{X}_0$ and $\hat{Y}_0$ correspond closely to the laboratory axes, $\hat{x}$ and $\hat{y}$ and only deviate to the extent that the PBS lets polarization imperfections through or generates new polarization imperfections. Then we send these laser beams through a $\lambda/4$ waveplate with fast-axis angle $\theta_{\lambda/4}$ with a possible small retardance error $\Gamma_{\lambda/4}$. Then the light passes through a $\lambda/2$ waveplate with fast axis at angle $\theta_{\text{read}}/2$ (where θ_{read} is the nominal read-out polarization basis angle), with a possible small retardance error $\Gamma_{\lambda/2}$. Then the light travels into the vacuum chamber and some of the glass that the light travels through may be slightly birefringent with small retardance Γ_g and fast axis θ_g. These operations result in polarizations $\hat{X}$ and $\hat{Y}$ in the detection region that interact with the molecules,

$$\begin{aligned}\begin{pmatrix}\hat{X}\\ \hat{Y}\end{pmatrix} =& M\left(\lambda\Gamma_g, \theta_g\right) M\left(\frac{\pi}{2}+\lambda\Gamma_{\lambda/2}, \frac{\theta_{\text{read}}}{2}\right)\\ &\times M\left(\frac{\pi}{4}+\lambda\Gamma_{\lambda/4}, \lambda\theta_{\lambda/4}\right)\begin{pmatrix}\hat{X}_0\\ \hat{Y}_0\end{pmatrix},\end{aligned} \tag{4.4}$$

where I use the notation $M\left(\Gamma, \theta\right)$ to denote phase retarder operation with retardance Γ and fast axis angle θ with respect to the xy plane. Here $\lambda = 1$ is a label that I use to mark small quantities and can be used as a parameter in a perturbative expansion. The resulting polarizations have imperfections at first order in λ given by:

$$\frac{1}{2}\left(d\theta_X + d\theta_Y\right) = -\frac{1}{2}\left(d\Theta_{X0} - d\Theta_{Y0}\right) - \theta_{\lambda/4} \tag{4.5}$$

$$\frac{1}{2}\left(d\theta_X - d\theta_Y\right) = -\frac{1}{2}\left(d\Theta_{X0} + d\Theta_{Y0}\right) \tag{4.6}$$

$$\frac{1}{2}\left(d\Theta_X + d\Theta_Y\right) = -\frac{1}{2}\left(d\theta_{X0} - d\theta_{Y0}\right) \tag{4.7}$$

$$\begin{aligned}\frac{1}{2}\left(d\Theta_X - d\Theta_Y\right) =& -\frac{1}{2}\left(d\theta_{X0} + d\theta_{Y0}\right) + \theta_{\lambda/4}\\ &+ \Gamma_{\lambda/2}\sin\theta_{\text{read}} + \Gamma_{\text{g}}\sin(2(\theta_{\text{read}} - \theta_g))\end{aligned} \tag{4.8}$$

Equation 4.8 indicates that by tuning the angle $\theta_{\lambda/4}$ of the $\lambda/4$ waveplate we can compensate for excess birefringence from the $\lambda/2$ waveplate or from birefringent elements down-

stream and tune the difference in ellipticity in the state readout region, $d\Theta_X - d\Theta_Y$, to zero. In practice this tuning can be performed by varying the ellipticity in the state preparation region, performing the spin precession measurement to extract the phase sensitivity to ellipticity $d\Phi^{\mathcal{P}}/\partial d\Theta_{\text{prep}} = -(d\Theta_X - d\Theta_Y)$, and feeding back on the angle of the $\lambda/4$ waveplate angle in the state readout laser beam path, $\theta_{\lambda/4,\,\text{read}} \to \theta_{\lambda/4,\,\text{read}} + \frac{1}{2}\partial\Phi^{\mathcal{P}}/\partial S_{\text{prep}}$. The ellipticity in the state preparation region can be varied by rotating the $\lambda/4$ waveplate that is placed in that laser beam's path. In a completely analogous way, we can feedback on the ellipticity in the state readout region by varying the $\lambda/4$ waveplate angle in the state read-out laser path, measuring the phase sensitivity to ellipticity $d\Phi^{\mathcal{P}}/(d\Theta_X - d\Theta_Y) = -d\Theta_{\text{prep}}$, and rotating the state preparation $\lambda/4$ waveplate by $\theta_{\lambda/4,\,\text{prep}} \to \theta_{\lambda/4,\,\text{prep}} + \frac{1}{2}\partial\Phi^{\mathcal{P}}/\partial S_{\text{read}}$. However after optimizing the $\lambda/4$ waveplate angles in the state preparation and state readout beam paths to tune $d\Theta_{\text{prep}}$ and $\frac{1}{2}(d\Theta_X - d\Theta_Y)$ to zero, the average ellipticity, $\frac{1}{2}(d\Theta_X + d\Theta_Y)$ remains – the size of this experimental imperfection depends only on the non-orthogonality of the linear polarizations on the output of the beamsplitter as indicated by equation 4.7.

To get an idea of what kind of polarization imperfections we might expect on the output of a polarizing beamsplitter, lets consider a very simple model of a PBS in which it passes light of $\hat{x}$ polarization and suppresses and phase shifts light of $\hat{y}$ polarization by a factor $\sqrt{\xi}e^{i\psi}$, where ψ is some phase shift and $\xi \approx 10^{-5}$ is the extinction ratio[4]. Assuming linearly polarized input light at angle θ with respect to the xy plane, the output polarization imperfections from ideal are given by $d\theta - id\Theta \approx \sqrt{\xi}e^{i\psi}\tan\theta$. So depending on the phase shift ψ and the input polarization θ, which is likely close to zero, the polarization imperfections could be in the range of $d\theta_0 \sim d\Theta_0 \sim 3 \times \left(10^{-4} - 10^{-3}\right)$. If the phase shift is small $\psi \ll 1$ such that $d\theta_0 \ll d\Theta_0$, then adding the $\lambda/4$ along the beam path can swap imperfections between $d\Theta$ and $d\theta$ as specified in equations 4.6 and 4.7 to improve the average ellipticity between the two state read-out lasers and hence reduce systematic errors, such as those in section 4.3.4 that are proportional to that particular combination of ellipticities.

4. Polarizing beamsplitters are specified by an "extinction ratio" which is the ratio of the lowest intensity to the highest intensity of light observed on the output while varying the polarization on the input. Typical extinction ratios for a commercial PBS fall in the range of $10^{-3} - 10^{-5}$. In ACME I we used a Glan-Laser PBS with an extinction ratio of about 10^{-5}.

4.1.3 Three level Hamiltonian and useful basis expansions

In the next few sections, we will skip between a few representations of the three level system that we address on in the state preparation and state read-out regions. In this section we define the dressed state eigenvectors and the dressed state Hamiltonian for future convenience in description of various mechanisms that result in shifts in the measured phase Φ.

Consider a three level system consisting of the bright $|B(\hat{\varepsilon}), \tilde{\mathcal{N}}, \tilde{\mathcal{P}}\rangle$ and dark $|D(\hat{\varepsilon}), \tilde{\mathcal{N}}, \tilde{\mathcal{P}}\rangle$ states and the lossy excited state $|C, \tilde{\mathcal{P}}\rangle$ with decay rate γ_C. For simplicity, assume that there is no applied magnetic field for the time being. In this system, the instantaneous eigenvectors (depicted in figure 4.2C) are

$$|B_\pm\rangle \equiv \pm\, \kappa_\pm |C, \tilde{\mathcal{P}}\rangle + \kappa_\mp |B(\hat{\varepsilon}), \tilde{\mathcal{N}}, \tilde{\mathcal{P}}\rangle, \;\; |D\rangle \equiv |D(\hat{\varepsilon}), \tilde{\mathcal{N}}, \tilde{\mathcal{P}}\rangle, \tag{4.9}$$

and the instantaneous eigenvalues are

$$E_{B\pm} = \frac{1}{2}\left(\Delta \pm \sqrt{\Delta^2 + \Omega_{\mathrm{r}}^2}\right), \; E_D = 0, \tag{4.10}$$

such that the mixing amplitudes $\kappa_\pm$ are given by

$$\kappa_\pm = \frac{1}{\sqrt{2}} \sqrt{1 \pm \frac{\Delta}{\sqrt{\Delta^2 + \Omega_{\mathrm{r}}^2}}}. \tag{4.11}$$

The effect of the decay of the excited state (which occurs almost entirely to states outside of the three level system) may be taken into account by adding an anti-Hermitian operator term in the Schrodinger equation, $|\dot{\psi}\rangle = -i(H - i\frac{1}{2}\Gamma)|\psi\rangle$, where $\Gamma = \gamma_C |C, \tilde{\mathcal{P}}\rangle\langle C, \tilde{\mathcal{P}}|$ is the decay operator. This formulation is equivalent to the Lindblad master equation,

$$\dot{\rho} = -\, i\,[H, \rho] - \frac{1}{2}\,\{\Gamma, \rho\}\,, \tag{4.12}$$

that governs the time evolution of the density matrix $\rho = |\psi\rangle\langle\psi|$. In practice, we implement this decay term by calculating the time evolution of the system according to H, and then making the substitution $\Delta \to \Delta - i\gamma_C/2$ before calculating squares of amplitudes.

It is useful to work in the dressed state basis, $|D\rangle$, $|B_\pm\rangle$, (basis C in figure 4.2) because these are nearly stationary states and have simple time evolution in the case that laser

polarization and Rabi frequency are stationary. If we allow the laser polarization to vary in time, then the dressed state basis varies in time, and the system evolves according to the Hamiltonian,

$$\tilde{H} = UHU^{\dagger} - iU\dot{U}^{\dagger}, \tag{4.13}$$

where U is the transformation from time independent basis A to time dependent basis C (from figure 4.2), $UHU^{\dagger}$ is diagonal, and $-iU\dot{U}^{\dagger}$ is a fictitious force term that arises because we are working in a non-inertial frame when the laser polarization is time dependent [28].

Assuming that the polarization is nearly linear, $\Theta \approx \pi/4$, but allowing the polarization to rotate slightly, and allowing for a nonzero two photon detuning due to the Zeeman shift $\delta = -\mu_{\mathrm{B}} g_{H,J=1} \mathcal{B}_z \tilde{\mathcal{B}}$, the Hamiltonian in the dressed state picture is:

$$\tilde{H} = \begin{pmatrix} 0 & -i\dot{\chi}^{*}\kappa_{+} & -i\dot{\chi}^{*}\kappa_{-} \\ i\dot{\chi}\kappa_{+} & E_{B-} & -\frac{i}{2}\frac{\dot{\Omega}_{\mathrm{r}}\Delta - \Omega_{\mathrm{r}}\dot{\Delta}}{\Delta^2+\Omega^2} \\ i\dot{\chi}\kappa_{-} & \frac{i}{2}\frac{\dot{\Omega}_{\mathrm{r}}\Delta - \Omega_{\mathrm{r}}\dot{\Delta}}{\Delta^2+\Omega_{\mathrm{r}}^2} & E_{B+} \end{pmatrix} \begin{matrix} |D\rangle \\ |B_-\rangle \\ |B_+\rangle \end{matrix} \tag{4.14}$$

where $\dot{\chi} = \dot{\Theta} - i(\dot{\theta} + \delta)$ can be considered to be a complex polarization rotation rate, $\dot{\Omega}_{\mathrm{r}}$ is the rate of change of the Rabi frequency, and $\dot{\Delta}$ is the rate of change of the detuning. Note that this Hamiltonian implies that the effect of a two photon detuning arising from the Zeeman shift is equivalent to that of a linear polarization rotating at a constant rate.

4.2 Interference in state preparation and read-out

4.2.1 Stark interference between plane wave multipole transition amplitudes

In an applied electric field, opposite parity levels are mixed, allowing both odd parity (E1, M2,...) and even parity (M1, E2,...) electromagnetic multipole amplitudes to contribute when driving an optical transition. These amplitudes depend on the orientation of the electric field relative to the light polarization $\hat{\epsilon}$ and the laser pointing direction $\hat{k}$. This Stark interference (S.I.) effect forms the basis of precise measurements of weak interactions through parity non-conserving amplitudes in atoms and molecules [26, 43, 175]. However, it can also generate a systematic error in searches for permanent electric dipole moments which

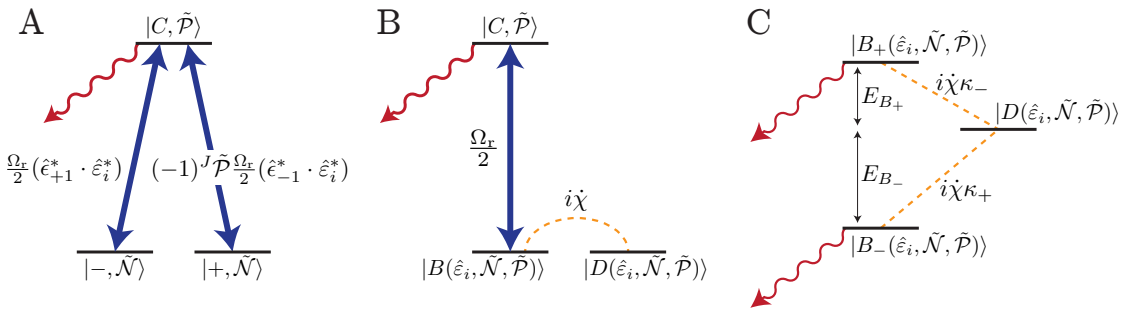

Figure 4.2: Energy level diagrams depicting the Hamiltonian when the three-level $H \to C$ transition is addressed by the state preparation or readout lasers in three different bases. Solid double-sided blue arrows denote strong laser couplings between H and C. Wiggly red arrows denote spontaneous emission from C to states outside of the three level system. Dashed orange lines denote weak couplings induced by laser polarization rotation. Basis A is useful for describing the spin precession phase induced by the Zeeman and electron EDM Hamiltonians. Basis B is useful for describing the states that are prepared and read-out in the spin precession measurement. Basis C is useful for evaluating the AC Stark Shift phases induced by laser polarization rotations.

look for spin precession correlated with the orientation of an applied electric field. These Stark interference amplitudes have been calculated and measured for optical transitions in Rb [31,79] and Hg [100,107], and have been included in the systematic error analysis in the Hg EDM experiment [68,161].

In this section, we consider Stark interference as a source of systematic errors in the ACME experiment. There are two important differences between molecular and atomic systems. First, molecular states such as the $H^3\Delta_1$ state in ThO can be highly polarizable and opposite parity states can be completely mixed by the application of a modest laboratory electric field. Second, molecular selection rules can be much weaker than atomic selection rules: the $H^3\Delta_1 \to C^3\Pi_1$ transition that we drive is nominally an E1 forbidden spin-flip transition ($\Delta\Sigma = 1$, where Σ is the projection of the total electron spin $S = 1$ onto the intermolecular axis), but these states have significant subdominant contributions from other spin-orbit terms [133], between some of which the E1 transition is allowed. Both of these effects significantly amplify the effect of Stark interference in molecules relative to atoms. In this section we will derive the effect of Stark interference on the measured phase Φ in ACME I and make anticipate the effect in ACME II.

Multipole matrix elements on the $H \to C$ transition

Consider a plane wave vector potential $\vec{A}$ with real amplitude A_0, oscillating at frequency ω, that is resonant with a molecular optical transition $|g\rangle \to |e\rangle$, with wave vector $\vec{k} = (\omega/c)\,\hat{k}$, and complex polarization $\hat{\epsilon}$:

$$\vec{A}\,(\vec{r},t) = A_0\hat{\epsilon}e^{i\vec{k}\cdot\vec{r}-i\omega t} + \text{c.c.} \tag{4.15}$$

The interaction Hamiltonian H_{int} between this classical light field and the molecular system is given by:

$$H_{\text{int}}\,(t) = -\sum_a \frac{e^a}{m^a}\vec{A}\,(\vec{r}^a,t)\cdot\vec{p}^a \tag{4.16}$$

where a indexes a sum over all of the particles in the system with charge e^a, mass m^a, position $\vec{r}^a$ and momentum $\vec{p}^a$. Typically we apply the multipole expansion on the transition matrix element between states $|g\rangle$ and $|e\rangle$; the matrix element can then be written as

$$\mathcal{M} \equiv \langle e|H_{\text{int}}|g\rangle = iA_0\omega_{eg}\sum_{\lambda=1}^{\infty}\langle e|\hat{\epsilon}\cdot\vec{E}_\lambda + (\hat{k}\times\hat{\epsilon})\cdot\vec{M}_\lambda|g\rangle, \tag{4.17}$$

where $\vec{E}_\lambda$ describes the electric interaction of order $O((\vec{k}\cdot\vec{r})^{\lambda-1})$ and $\vec{M}_\lambda$ describes the magnetic interaction of order $O(\alpha(\vec{k}\cdot\vec{r})^{\lambda-1})$ (where α is the fine structure constant) such that

$$\begin{aligned}
\vec{E}_\lambda =& \frac{(i)^{\lambda-1}}{\lambda!}\sum_a e^a\vec{r}^a\left(\vec{k}\cdot\vec{r}^a\right)^{\lambda-1}, \qquad (4.18)\\
\vec{M}_\lambda =& \frac{(i)^{\lambda-1}}{(\lambda-1)!}\sum_a\left(\frac{e^a}{2m^a}\right)\\
&\times\left[\left(\vec{k}\cdot\vec{r}^a\right)^{\lambda-1}\left(\frac{1}{\lambda+1}\vec{L}^a+\frac{1}{2}g^a\vec{S}^a\right)+\left(\frac{1}{\lambda+1}\vec{L}^a+\frac{1}{2}g^a\vec{S}^a\right)\left(\vec{k}\cdot\vec{r}^a\right)^{\lambda-1}\right],
\end{aligned}$$

where L^a is the orbital angular momentum, S^a is the spin angular momentum, and g^a is the spin g-factor for particle of index a (see e.g. [143]). For typical atomic or molecular optical transitions, if all moments are allowed, we expect the dominant corrections to the leading order E1 transition moment to be on the order of M1/E1 $\sim \alpha \sim 10^{-2}$–10^{-3} and E2/E1$\sim ka_0 \sim 10^{-3}$–10^{-4}, where a_0 is the Bohr radius. In this work we neglect the higher

order contributions beyond E2, though the effects may by evaluated by using the expansion above.

$$\left\langle e\left|H_{\text{int}}\left(O^{\lambda}\right)\right|g\right\rangle = iA_0\omega_{eg}\left[\hat{\epsilon}^*_{+1}\left\langle e\left|T^{\lambda}_{+1}\left(O^{\lambda}\right)\right|g\right\rangle + \hat{\epsilon}^*_{-1}\left\langle e\left|T^{\lambda}_{-1}\left(O^{\lambda}\right)\right|g\right\rangle\right]\cdot\vec{V}\left(O^{\lambda}\right)+\ldots$$

Term	Tensor rank, λ	Molecular Operator, O^{λ}	Light Vector, $\vec{V}\left(O^{\lambda}\right)$
E1	1	$\Sigma_a e^a r_i^a$	$\hat{\epsilon}$
M1	1	$\Sigma_a \frac{e^a}{2m^a}\left(L_i^a + g^a S_i^a\right)$	$\hat{k}\times\hat{\epsilon}$
E2	2	$\frac{\omega}{2c}\sum_a e^a r_i^a r_j^a$	$\frac{i}{\sqrt{2}}\left[\hat{\epsilon}(\hat{k}\cdot\hat{z}) + \hat{k}(\hat{\epsilon}\cdot\hat{z})\right]$
M2	2	$\frac{\omega}{c}\Sigma_a\frac{e^a}{2m^a}\left\{r_i^a, \frac{1}{3}L_j^a + \frac{1}{2}g^a S_j\right\}$	$\frac{i}{\sqrt{2}}\left[\hat{k}((\hat{k}\times\hat{\epsilon})\cdot\hat{z}) + (\hat{k}\times\hat{\epsilon})(\hat{k}\cdot\hat{z})\right]$

Table 4.1: Only spherical tensor operators T^{λ}_q with projection $q = \pm 1$ contribute to the $|H\rangle \rightarrow |C\rangle$ transition amplitude. With this simplifying assumption, we can write the matrix element for each multipole operator in the form shown at the top of this table, which factors the molecule properties and the light properties (where $\hat{\epsilon}_{\pm} = \mp(\hat{x} \pm i\hat{y})/\sqrt{2}$ are the spherical basis vectors, and $\hat{z}$ is the direction of the electric field). Here, the molecular operators O^{λ} and the corresponding light vectors $\vec{V}\left(O^{\lambda}\right)$ are listed for the E1, M1, E2, and M2 operators.

During the state preparation and readout of the molecule state, transitions are driven between the state $|g\rangle = \sum_{\pm} d_{\pm}|\pm,\tilde{\mathcal{N}}\rangle$ and $|e\rangle = |C,\tilde{\mathcal{P}}\rangle$, where $d_{\pm}$ are state amplitudes that denote the particular superposition in $|H\rangle$ that is being interrogated. The particular $d_{\pm}$ combination that results in $\mathcal{M} = 0$ describes the state that is dark, and the orthogonal state is bright and is optically pumped away.

It is convenient to expand the Hamiltonian H_{int} in terms of spherical tensor operators. Furthermore, the laser is only resonant with $\Delta M = \pm 1$ transitions, so the spherical tensor operators with angular momentum projections other than ± 1 can be reasonably omitted. In table 4.1, we factor the first 4 multipole operators into products of molecule and light field operators and express the molecular operators in terms of spherical tensors $T^{\lambda}_{\pm 1}$ of rank $\lambda = 1, 2$. The E1 and M1 terms consist of vector operators with $\lambda = 1$. The E2 and M2 operators are rank 2 Cartesian operators which can have spherical tensor operator contributions for $\lambda = 0, 1, 2$. The rank $\lambda = 0$ components of the E2 and M2 operators, and the $\lambda = 1$ component of the E2 operator, vanish. The rank $\lambda = 1$ component of the M2 operator does not vanish, but the light field angular dependence of this operator is

equivalent to E1, so we may treat it as such.

Using well-known properties of angular momentum matrix elements [27], we may write the transition matrix element in the following form,

$$\mathcal{M} = iA_0\omega_{eg}c_{\mathrm{E1}}\frac{1}{\sqrt{2}}\left[(-1)^{J+1}\tilde{\mathcal{P}}\right]^{(1-\tilde{\mathcal{N}}\tilde{\mathcal{E}})/2}\left(\hat{\epsilon}^*_{-1}d_+ + \tilde{\mathcal{P}}\,(-1)^{J'}\,\hat{\epsilon}^*_{+1}d_-\right)\cdot\vec{\varepsilon}_{\mathrm{eff}}, \tag{4.19}$$

such that $\vec{\varepsilon}_{\mathrm{eff}}$ is the "effective E1 polarization" (i.e. including the effects of interference between multipole transition matrix elements is equivalent to an E1 transition with this polarization) with the form

$$\vec{\varepsilon}_{\mathrm{eff}} = \hat{\epsilon} - a_{\mathrm{M1}}i\hat{n}\times(\hat{k}\times\hat{\epsilon}) + a_{\mathrm{E2}}(\tilde{\mathcal{P}})i(\hat{k}(\hat{\epsilon}\cdot\hat{n}) + \hat{\epsilon}(\hat{k}\cdot\hat{n})) + \ldots \tag{4.20}$$

where $\hat{n} = \tilde{\mathcal{N}}\tilde{\mathcal{E}}\hat{z}$ is the orientation of the internuclear axis in the laboratory frame, $a_{\mathrm{E2}}(\tilde{\mathcal{P}}) = c_{\mathrm{E2}}(\tilde{\mathcal{P}})/(\sqrt{2}c_{\mathrm{E1}})$ and $a_{\mathrm{M1}} = c_{\mathrm{M1}}/c_{\mathrm{E1}}$ are real dimensionless ratios describing the strength of the M1 and E2 matrix elements relative to E1, and the c coefficients are matrix elements,

$$c_{\mathrm{E1}} = \left\langle C, J, M=0, \Omega=1\,|\mathrm{E1}|\,H, J', M=1, \Omega=1\right\rangle \tag{4.21}$$

$$c_{\mathrm{M1}} = \left\langle C, J, M=0, \Omega=1\,|\mathrm{M1}|\,H, J', M=1, \Omega=1\right\rangle \tag{4.22}$$

$$\begin{aligned} c_{\mathrm{E2}}(\tilde{\mathcal{P}}) = &\left\langle C, J, M=0, \Omega=1\,|\mathrm{E2}|\,H, J', M=1, \Omega=1\right\rangle + \\ &\tilde{\mathcal{P}}\,(-1)^J\left\langle C, J, M=0, \Omega=1\,|\mathrm{E2}|\,H, J', M=1, \Omega=-1\right\rangle, \end{aligned} \tag{4.23}$$

where 'E1, M1, E2' refer to the corresponding molecular operators in table 4.1. It is useful to define the Rabi frequency $\Omega_{\mathrm{r}} = |\mathcal{M}| \propto \sqrt{|\vec{\varepsilon}|^2 - |\vec{\varepsilon}\cdot\hat{z}|^2}$ as the magnitude of the amplitude connecting to the bright state, and the unit vector $\hat{\varepsilon}_{\mathrm{eff}}$ corresponding to the projection of $\vec{\varepsilon}_{\mathrm{eff}}$ onto the xy plane,

$$\hat{\varepsilon}_{\mathrm{eff}} = \frac{\vec{\varepsilon}_{\mathrm{eff}} - (\vec{\varepsilon}_{\mathrm{eff}}\cdot\hat{z})\hat{z}}{\sqrt{|\vec{\varepsilon}_{\mathrm{eff}}|^2 - |\vec{\varepsilon}_{\mathrm{eff}}\cdot\hat{z}|^2}}. \tag{4.24}$$

This completely determines the bright and dark states, which have been previously defined in equations 2.5 and 2.6 for solely E1 transition matrix elements.

The odd parity E1 and even parity M1 and E2 contributions to the effective polarization differ by a factor of $\tilde{\mathcal{N}}\tilde{\mathcal{E}}$, which is correlated with the expected electron EDM signal. Expanding the effective E1 polarization in terms of switch parity components, $\hat{\varepsilon}_{\mathrm{eff}} = \hat{\varepsilon}^{\mathrm{nr}}_{\mathrm{eff}} + \tilde{\mathcal{N}}\tilde{\mathcal{E}}d\vec{\varepsilon}^{\mathcal{NE}}_{\mathrm{eff}}$,

and evaluating the effective $\tilde{\mathcal{N}}\tilde{\mathcal{E}}$ correlated polarization imperfections using equation 4.1, we find that the bright and dark states have effective polarization correlations given by:

$$\frac{\hat{z}\cdot(\hat{\varepsilon}_{\text{eff}}^{\text{nr}}\times d\vec{\varepsilon}_{\text{eff}}^{\mathcal{N}\mathcal{E}})}{\hat{\varepsilon}_{\text{eff}}^{\text{nr}}\cdot\hat{\varepsilon}_{\text{eff}}^{\text{nr}}} \approx d\theta_{\text{eff}}^{\mathcal{N}\mathcal{E}} - id\Theta_{\text{eff}}^{\mathcal{N}\mathcal{E}} \tag{4.25}$$

$$\approx -i(a_{M1}-a_{E2}(\tilde{\mathcal{P}}))(\hat{\epsilon}\cdot\hat{z})((\hat{k}\times\hat{\epsilon})\cdot\hat{z}). \tag{4.26}$$

Analogously, the correlated component of the Rabi frequency that results from this interference is given by

$$\frac{\Omega_{\text{r}}^{\mathcal{N}\mathcal{E}}}{\Omega_{\text{r}}^{\text{nr}}} = \text{Re}\left(\vec{\epsilon}_{\text{eff}}^{*}\cdot\delta\vec{\epsilon}_{\text{eff}}^{\mathcal{N}\mathcal{E}}\right) = 0, \tag{4.27}$$

which vanishes for plane wave multiple interference.

Estimate of the Size of the Interference Coefficients

Given the Stark Interference systematic error mechanism that has been expressed in equation 4.26, we would like to estimate the size of the interference coefficients a_{M1} and a_{E2} so that we may estimate the size of the resulting systematic error. At the most coarse level of approximation, we might generally assume that if E1, M1, and E2 transitions are all allowed, then the coefficients would be on the order of $a_{\text{M1}} \sim \alpha \sim 10^{-2}$, where α is the fine structure constant, and $a_{\text{E2}} \sim ka_0 \sim 5\times10^{-4}$ where a_0 is the Bohr radius and k is the wave-vector for an optical transition. Since we would expect that $a_{\text{M1}} \gg a_{\text{E2}}$, we prioritize estimating the size of a_{M1} over a_{E2}.

At a slightly better level of approximation we can make use of measured transition electric dipole moments, D_{ij}, extracted from measurements in combination with crudely estimated transition magnetic dipole moments $\mu_B g_{ij}$ based on calculated spin orbit contributions to the electronic states in ThO provided in references [99,133], which are reproduced in table 4.2.1 for convenience. These transition dipole matrix element estimates are provided in table 4.2.1.

The estimate for the $H \to C$ transition electric dipole moment comes from optical pumping saturation measurements in ACME I in the state preparation and state readout region [158]. The estimate for the $X \to C$ transition electric dipole moment comes from a combination of estimates of the branching ratio b_{XC} which is discussed in section 5.2 in

combination with the measured lifetime of the C state, $\gamma \approx 1/(500\,\text{ns})$ [77], assuming that the entirety of the $X \to C$ decay occurs via E1, $b_{XC}\gamma = \frac{4}{3}\alpha\frac{\omega_{XC}^3}{c^2}D_{XC}^2$. Estimates of the $I \to H$ transition electric dipole moment were measured indirectly in reference [96] and more directly in an optical pumping saturation measurement in section 5.5.2.

The estimates for the E1/M1 interference coefficients, a_{M1}, that result from the estimates in table 4.2.1 indicate that the $H \to C$ transition likely has the largest coefficient and it could be as large as $a_{\text{M1}} \lesssim .1$ and that this interference coefficient is likely to be smaller by $10\times - 100\times$ smaller on the $H \to I$ transition.

State	Spin Orbit Make-up
X	$(0.999,\ 0.995)^1\,\Sigma_0^+ + (0,\ .002)^3\,\Pi_0 + \ldots$
H	$(.005,\ .001)^1\Pi_1 + (.011,\ .006)^3\,\Pi_1 + (.984,\ .989)^3\,\Delta_1 + \ldots$
C	$(.775,\ .679)^1\,\Pi_1 + (.195,\ .132)^3\,\Pi_1 + (.015,\ .002)^3\,\Delta_1 + \ldots$
I	?

Table 4.2: Spin-orbit contributions to electronic states in ThO from calculations in references [99, 133]. These are squares of amplitudes and signs are omitted.

	$H \to C$	$X \to C$	$H \to I$
D	$(.01 - .02)\ ea_0$	$(.4 - .5)\,ea_0$	$(.28 - .38)\ ea_0$
g	$(.05 - .10)$	$(.7 - 1.0)$	$(.03 - .12)$
$a_{\text{M1}} = \alpha e a_0 g/D$	$(20 - 70) \times 10^{-3}$	$(10 - 20) \times 10^{-3}$	$(.6 - 3) \times 10^{-3}$

Table 4.3: Estimates for the molecule frame transition electric dipole moment D_{AB}, transition magnetic dipole moment $\mu_B g_{AB}$, and ratios of the magnetic to electric dipole moments $a_{\text{M1}}$for electronic transitions $A \to B$ for states A, B of interest for the experiment.

Stark Interference in ACME I

It is useful to use a particular parameterization of the laser pointing $\hat{k}$ and polarization $\hat{\epsilon}$ to expand the expression in equation 4.26 in terms of pointing and polarization imperfections. The state preparation laser $\hat{k}$-vector is aligned along (or against) the $\hat{z}$ direction in the laboratory, so it is convenient to parameterize the pointing deviation from normal by spherical angle ϑ_k, and the direction of this pointing imperfection by polar angle φ_k in the xy plane, such that:

$$\hat{k} = \cos\varphi_k \sin\vartheta_k \hat{x} + \sin\varphi_k \sin\vartheta_k \hat{y} + \cos\vartheta_k \hat{z}. \tag{4.28}$$

We may use a parameterization for the polarization $\hat{\epsilon}$ that is similar to that in equation 2.7, but a slight modification is required to ensure that $\hat{k} \cdot \hat{\epsilon} = 0$:

$$\hat{\epsilon} = N_\epsilon \left(-e^{-i\theta} \cos\Theta \hat{\epsilon}_{+1} + e^{i\theta} \sin\Theta \hat{\epsilon}_{-1} + \epsilon_z \hat{z} \right) \tag{4.29}$$

$$\epsilon_z = -\frac{1}{\sqrt{2}} \tan\theta_k \left(e^{-i(\theta-\varphi_k)} \cos\Theta + e^{i(\theta-\varphi_k)} \sin\Theta \right) \tag{4.30}$$

where N_ϵ is a normalization constant that ensures that $\hat{\epsilon}^* \cdot \hat{\epsilon} = 1$. With these parameterizations in place, and expanding about small ellipticities $d\Theta$ such that $\Theta = \pi/4 + d\Theta$, and small laser pointing deviation, $\vartheta_k \ll 1$, we find that the $\tilde{\mathcal{N}}\tilde{\mathcal{E}}$-correlated effective laser polarization imperfections are given by:

$$d\theta_{\text{eff}}^{\mathcal{NE}} \approx -\frac{1}{2}(a_{M1} - a_{E2}(\tilde{\mathcal{P}}))\vartheta_k^2 \, S \, \cos(2(\theta - \varphi_k)) \tag{4.31}$$

$$d\Theta_{\text{eff}}^{\mathcal{NE}} \approx -\frac{1}{2}(a_{M1} - a_{E2}(\tilde{\mathcal{P}}))\vartheta_k^2 \, \sin(2(\theta - \varphi_k)) \tag{4.32}$$

where $S_i = -2d\Theta_i$ describe the laser ellipticities. Hence, following equation 4.2, there is a systematic error in $\omega^{\mathcal{NE}}$,

$$= \frac{1}{\tau}\frac{1}{4}\left(a_{M1} - a_{E2}\left(\tilde{\mathcal{P}}\right)\right) \times \tag{4.33}$$

$$\Big[\vartheta_{k,\text{prep}}^2 \left(-2S_{\text{prep}} c_{\text{prep}} + \tilde{\mathcal{P}} s_{\text{prep}} \left(S_X - S_Y \right) \right) + \tag{4.34}$$

$$\vartheta_{k,X}^2 \left(S_X c_X + \tilde{\mathcal{P}} S_{\text{prep}} s_X \right) + \vartheta_{k,Y}^2 \left(S_Y c_Y - \tilde{\mathcal{P}} S_{\text{prep}} s_Y \right) \Big] \tag{4.35}$$

where $c_i \equiv \cos\left(2(\theta_i - \varphi_{i,k})\right)$ and $s_i \equiv \sin\left(2(\theta_i - \varphi_{i,k})\right)$ describe the dependence of the systematic error on the difference between the linear polarization angle θ_i and the pointing angle $\varphi_{i,k}$ in the xy plane. Note that, in this particular case, the first and second order terms in equation 4.3, have roughly the same size contributions to this systematic error because $d\theta_{\text{eff}}^{\mathcal{NE}}$ is smaller than $d\Theta_{\text{eff}}^{\mathcal{NE}}$ by an ellipticity factor.

The electron EDM channel, $\omega^{\mathcal{NE}}$, was defined in ACME I to be even under the superblock switches (including $\tilde{\mathcal{P}}$), hence those terms proportional to $\tilde{\mathcal{P}}$ in the equation above do not contribute to our reported result. Additionally, the $\tilde{\mathcal{G}}$ and $\tilde{\mathcal{R}}$ switches rotate the polarization angles for each laser by roughly $\theta_i \to \theta_i + \pi/2$ periodically and the resulting $\omega^{\mathcal{NE}}$ signal is averaged over these states. Provided that the pointing drift is much slower than the timescale of these switches, and to the extent that the laser polarizations consti-

tuting the $\tilde{\mathcal{R}}$ and $\tilde{\mathcal{G}}$ states are orthogonal, then these systematic errors should dominantly contribute to the $\omega^{\mathcal{NEG}}$ and $\omega^{\mathcal{NER}}$ channels which were found to be consistent with zero (see Figure 3.5).

An indirect limit on the size of the systematic error due to Stark interference, $\omega_{\text{S.I.}}^{\mathcal{NE}}$, may be estimated by assuming a reasonable suppression factor by which the effects in $\omega^{\mathcal{NER}}$ and $\omega^{\mathcal{NEG}}$ may "leak" into $\omega^{\mathcal{NE}}$. We monitored the pointing drift on a beam profiler and observed pointing drifts up to $d\vartheta_k \sim 50$ μrad throughout a full set of superblock states. The absolute pointing misalignment angle was not well known but was estimated to be larger than $\vartheta_k \gtrsim 0.5$ mrad. Hence we may estimate a conservative suppression factor $d\vartheta_k/\vartheta_k \lesssim 1/10$ by which pointing drift may contaminate $\omega^{\mathcal{NE}}$ from $\omega^{\mathcal{NER}}$ and $\omega^{\mathcal{NEG}}$. The two $\tilde{\mathcal{R}}$ states are very nearly orthogonal, but the $\tilde{\mathcal{G}}$ states deviate sufficiently from orthogonal such that the leakage from $\omega^{\mathcal{NEG}} \to \omega^{\mathcal{NE}}$ will dominate the systematic error; we estimate a suppression factor of about $c_p^{\text{nr}}/c_p^{\mathcal{G}} \sim s_p^{\text{nr}}/s_p^{\mathcal{G}} \sim 1/5$. Based on the upper limits on the measured values for $\omega^{\mathcal{NER}}$ and $\omega^{\mathcal{NEG}}$ combined with leakage from $\omega^{\mathcal{NER}}$ and $\omega^{\mathcal{NEG}}$ into $\omega^{\mathcal{NE}}$ due to pointing drift, and leakage from $\omega^{\mathcal{NEG}}$ into $\omega^{\mathcal{NE}}$ due to non-orthogonality of the two $\tilde{\mathcal{G}}$ states, we estimate the possible size of the systematic error to be $\omega_{\text{S.I.}}^{\mathcal{NE}} \lesssim 1\,\text{mrad/s}$, corresponding to $\Phi_{\text{S.I.}}^{\mathcal{NE}} \lesssim 10^{-6}\,\text{rad}$.

Note that the mechanism for this systematic error was not discovered until after the publication of our result [6] and hence was not included in our systematic error analysis there. Furthermore, since we did not observe this effect, this systematic error does not match any of the inclusion criteria outlined in section 3.6.1 and hence is not included in the systematic error budget in the result publication. Since we did not understand the mechanism for this systematic error while running the apparatus, we were not able to place direct limits on the size of this systematic error. We estimate that the absolute pointing deviation from ideal was at most 5 mrad and the ellipticity of each laser was no more than $S_i \approx 5\%$. The E1/M1 interference coefficient is estimated to be $a_{M1} \lesssim 0.1$ for the $H \to C$ transition as estimated in table 4.2.1. This gives an estimate of $\omega_{\text{S.I.}}^{\mathcal{NE}} \lesssim 0.1\,\text{mrad/s}$ before suppression due to the $\tilde{\mathcal{R}}$ and $\tilde{\mathcal{G}}$ switches. Hence, we do not believe that this systematic error significantly shifted the result of our measurement.

This estimated upper limit on the size of the systematic error in ACME I was well below that measurements sensitivity, but is comparable to the projected ACME II sensitivity. However, we have made a few modifications to the ACME II apparatus that should suppress

this systematic error even further. First, we plan to optically pump on the $H \to I$ transition with the refinement beam and the state read-out beams, for which we have estimated that the coefficient a_{M1} is likely at least a factor of $10\times$ smaller relative to that on the $H \to C$ transition. Also, the procedure described in section 4.1.2 should aid in suppressing the ellipticity of the laser light by effectively making polarization measurements with the molecules.

Furthermore, we have introduced a new scheme for aligning the laser pointing with the electric field direction [170]. In this scheme, we assume that the normal vector to electric field plate ITO surface is parallel with the electric field. The laser reflection off of that surface is sent back into the optical fiber from which that light came, and is separated from the rest of the laser light on the other side of that fiber by the rejection port of an optical isolator. The pointing of the beam can be varied to maximize the intensity of light propagating back into the fiber, and the spatial filtering provided by the fiber offers improved precision in alignment. The combination of these three improvements in ACME II will likely suppress the effect of this systematic error in the refinement beam and state read-out beams such that its size will be below the resolution of the experiment.

Enhanced sensitivity to Stark interference with STIRAP lasers

In ACME II we are using a pair of laser beams that are propagating along the $\hat{y}$ direction to perform state preparation from $|X, J = 0, M = 0\rangle$ to $|H, J = 1, M, \tilde{\mathcal{N}}\rangle$ via the excited state $|C, J = 1\rangle$ using a STIRAP process. There are two reasonable schemes by which we can perform this transfer that are depicted in figure 4.2.1:

1. $\hat{z}$ polarized $X \to C$ laser, $\hat{x}$ polarized $C \to H$ laser, connecting via $|C, J = 1, M = 0, \tilde{\mathcal{P}} = -1\rangle$ state

2. $\hat{x}$ polarized $X \to C$ laser, $\hat{z}$ polarized $C \to H$ laser, connecting via $|C, J = 1, M, \tilde{\mathcal{N}}\rangle$ states

Whereas in the ACME I state preparation scheme the initial spin precession state was determined by the polarization of the state preparation laser, in ACME II, the state prepared by STIRAP is determined by the polarization of the laser with nominal $\hat{x}$ polarization.

Lets assume that the laser with nominal $\hat{x}$ polarization is propagating along $\hat{k} = \hat{y}$ and has polarization,

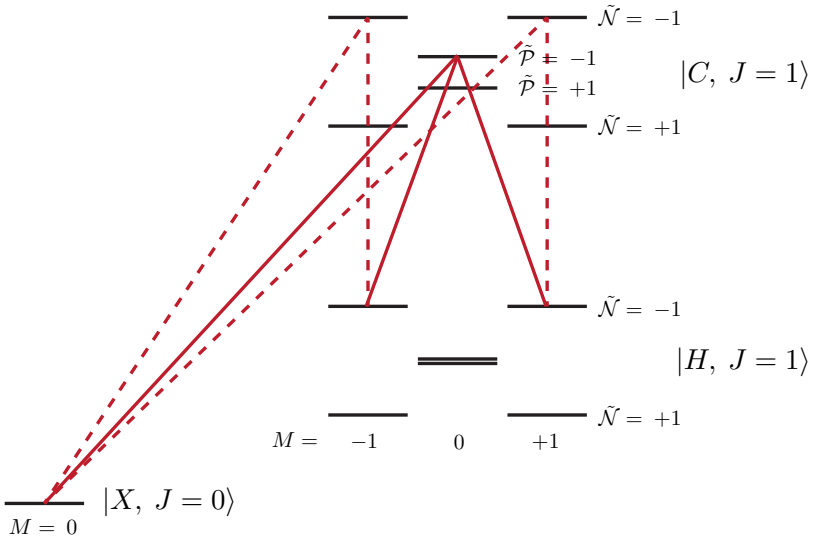

Figure 4.3: Illustration of two possible schemes for performing STIRAP on the $|X, J = 0, M = 0\rangle \rightarrow |C, J = 1\rangle \rightarrow |H, J = 1, M, \tilde{\mathcal{N}}\rangle$ transition. Here, the dotted red lines illustrate scheme 1, and the solid red lines illustrated scheme 2, referring to STIRAP schemes defined in the text.

$$\hat{\epsilon} = \frac{1}{\sqrt{2}} \left\{ e^{-i\theta} \cos\Theta \left[\hat{x} - i\hat{z}\right] + e^{+i\theta} \sin\Theta \left[\hat{x} + i\hat{z}\right] \right\}, \tag{4.36}$$

which is expressed in analogy to equations 2.7 and 4.29, where θ is the linear polarization angle in the xz plane, where $\theta = 0$ corresponds to $\hat{x}$ polarization, and $\Theta \approx \pi/4 + d\Theta$ where $S \approx -2d\Theta$ is the ellipticity of the light in the xz plane. With this parameterization of the polarization, the Stark interference systematic error given in equation 4.26 can be expressed as

$$d\theta^{\mathcal{NE}} - id\Theta^{\mathcal{NE}} \approx -i(a_{\mathrm{M1}} - a_{\mathrm{E2}})(d\theta - id\Theta), \tag{4.37}$$

where we have expanded to first order in the polarization imperfections $d\theta$ and $d\Theta$. Here we see that ellipticity of this STIRAP laser beam with nominal $\hat{x}$ polarization results in a spin alignment correlation $d\theta^{\mathcal{NE}}$ which is a systematic error in the measurement of the electron's EDM. Assuming an ellipticity of this laser beam of about $S \approx 2\%$ and using estimated a_{M1} coefficients from table 4.2.1 we would expect a systematic error of $d\theta^{\mathcal{NE}} \sim$

1 mrad in scheme 1 in which the spin state is being set on the $H \rightarrow C$ transition or $d\theta^{\mathcal{NE}} \sim .3$ mrad in scheme 2 in which the spin state is being set on the $X \rightarrow C$ transition. This possible systematic error is more than a factor of $10^3\times$ the sensitivity of the ACME II measurement and would obstruct an improved measurement of the electron's EDM if this issue were not directly addressed. To suppress this systematic error we decided to introduce the refinement laser beam which is sent with laser propagation direction $\hat{k} \approx \hat{z}$ immediately after the STIRAP state preparation and serves to reproject the spin state so that the Stark interference that occurs in the STIRAP beams does not significantly affect the spin precession measurement. Estimates of the attenuation of this systematic error by the refinement laser beam are provided in section 4.3.5, and measurements presented there are consistent with a suppression factor $\lesssim 10^{-3}$ as required.

We might consider which of these two schemes is preferable for use in the experiment. In terms of the size of the likely Stark interference systematic error, scheme 2 may be preferable. In terms of the technical implementation, however, scheme 2 requires frequency switching of both STIRAP lasers synchronously to perform the $\tilde{\mathcal{N}}$ switch, whereas scheme 1 requires only the $H \rightarrow C$ laser to undergo frequency switching. For this reason, we have implemented STIRAP with scheme 1, but if the Stark interference systematic error becomes an issue, scheme 2 may be explored in the future. Another factor to keep in mind is that in scheme 2, the transition matrix element is larger on the $H \rightarrow C$ transition; since the STIRAP efficiency is limited by the available laser power in the $H \rightarrow C$ laser beam [129], better inefficiencies may be possible with scheme 2.

Given that the effect of Stark interference is greatly enhanced when the laser propagation direction is perpendicular to the electric field compared to the case in which they are nominally parallel, we should be able to reconfigure the spin precession measurement to precisely measure the interference coefficients, $(a_{\mathrm{M1}} - a_{\mathrm{E2}})$, that we estimated in table 4.2.1. Such measurements would enable us to make more accurate estimates of the Stark interference systematic error in the electron EDM experiment, and could serve as an additional benchmark for assessing the validity and accuracy of calculations of molecular wavefunctions in ThO. Such comparisons between theory and experiment could aid in improving the computational methods required to make even more precise calculations of the electron EDM sensitivity, $\mathcal{E}_{\mathrm{eff}}$ in molecules with heavy nuclei.

This experiment could be performed rather simply to assess these coefficients for the $H \rightarrow C$ and $X \rightarrow C$ transitions by implementing either STIRAP scheme 1 or scheme 2 respectively, blocking the refinement beam, and then performing the electron EDM measurement while dithering the ellipticity for the laser that is nominally $\hat{x}$ polarized. For this measurement, the interference coefficient is given by $\partial\Phi^{\mathcal{NE}}/\partial d\Theta \approx -(a_{\mathrm{E1}} - a_{\mathrm{E2}})$. A measurement of the Stark interference coefficient on the $H \rightarrow I$ transition may also be assessed by moving the refinement beam such that it is propagating along the $\hat{y}$ direction, and performing the same measurement as previously described except with the ellipticity dither on the refinement beam. To reduce the complexity of this second proposed experiment, and to eliminate possible systematic errors due to reprojection phases, discussed in section 4.3.5, the H-state could alternatively be populated with the 943 nm $H \rightarrow A$ state transfer laser that was used in ACME I before being addressed by the refinement beam.

4.2.2 Interference Due to Opposite Parity Excited State

In the previous section we modeled the state preparation and state read-out with a 3-level Λ system resonantly addressed with a laser field. In this section, we include the off-resonant opposite parity excited state, $|C'\rangle \equiv |C, J = 1, M = 0, -\tilde{\mathcal{P}}\rangle$, as part of a 4-level system in combination with multipole Stark interference. Since the bright ground state superpositions that correspond to each of the two opposite parity states are not orthogonal when the ellipticity of the laser beam is non-zero, the off-resonant coupling can mix the bright and dark ground states leading to a phase shift in the electron EDM measurement.

Lets first consider the case where we have a time independent Hamiltonian, H, while the laser is on (a flat top intensity beam). Including the opposite parity state $|C'\rangle$ modifies the dark state $|D\rangle$ to $|D'\rangle$ which is no longer completely dark, but is nevertheless the "darkest" system eigenstate (i.e. it's decay rate is much slower than the other system eigenstates during optical pumping and is not significantly pumped away while the laser is on). At second order in time-independent perturbation theory, the darkest state $|D'\rangle$ is given by

$$|D'\rangle = |D\rangle + \sum_{\pm} a_{B_\pm} |B_\pm\rangle, \tag{4.38}$$

where the bright state amplitudes, $a_{B\pm}$ are given by

$$a_{B\pm} = \frac{\langle B_\pm | H | C' \rangle \langle C' | H | D \rangle}{(E_D - E_{B_\pm})(E_D - E_{C'})}. \tag{4.39}$$

Here, $|B_\pm\rangle$ are the bright state eigenstates given in equation 4.9 and $E_{C'} = -\tilde{\mathcal{P}}\Delta_{C,J=1}$ is the detuning of the opposite parity state, where $\Delta_{C,J=1}$ is the omega doublet splitting in $|C, J = 1\rangle$.

If the laser then turns off non-adiabatically, the remaining population in the excited state will decay away leaving behind the state:

$$\left|D\left(\hat{\varepsilon}'\right)\right\rangle = |D\left(\hat{\varepsilon}\right)\rangle + a\,|B\left(\hat{\varepsilon}\right)\rangle \tag{4.40}$$

$$\hat{\varepsilon}' = \hat{\varepsilon} + ai\hat{z} \times \hat{\varepsilon}^* \tag{4.41}$$

where the coefficient a is given by

$$a = \Sigma_\pm \kappa_\mp a_{B\pm} = \tilde{\mathcal{P}} \left(\frac{i\gamma - 2\Delta}{\Delta_C} \right) (\hat{\varepsilon}_- \cdot \hat{\varepsilon}_+)(i\hat{z} \cdot (\hat{\varepsilon}_-^* \times \hat{\varepsilon}_+)), \tag{4.42}$$

where $\hat{\varepsilon}_+ \equiv \hat{\varepsilon}(\tilde{\mathcal{P}})$ is the on-resonant effective E1 polarization and $\hat{\varepsilon}_- \equiv \hat{\varepsilon}(-\tilde{\mathcal{P}})$ is the off-resonant effective E1 polarization. The distinction is fairly minor because only rank 2 tensor operators and higher can contribute is such a way that depends on $\tilde{\mathcal{P}}$, so in most cases we can approximate $\hat{\varepsilon}_+ = \hat{\varepsilon}_- = \hat{\varepsilon}$. Under this approximation, and assuming laser beams approximately propagating along $\hat{z}$, this effect results in a change in the state that is prepared or read out as

$$d\theta' - id\Theta' \approx -\tilde{\mathcal{P}} \left(\frac{\gamma + 2i\Delta}{\Delta_C} \right) (2d\Theta) \tag{4.43}$$

where $d\Theta'$ is the shift to the ellipticity of the state, and $d\Theta$ is the ellipticity of the laser. Here, systematic errors can arise from a non-reversing electric field,$\Delta^{\mathcal{NE}}$ and an ellipticity in both the state preparation and readout lasers. Given ellipticity $S \sim 2\%$ and a non reversing electric field, $\Delta^{\mathcal{NE}} \sim 2\pi \times 5\,\text{kHz}$, this systematic error is likely to be smaller than the resolution of both ACME I and ACME II, $\Phi^{\mathcal{NE}} \sim 5 \times 10^{-8}$.

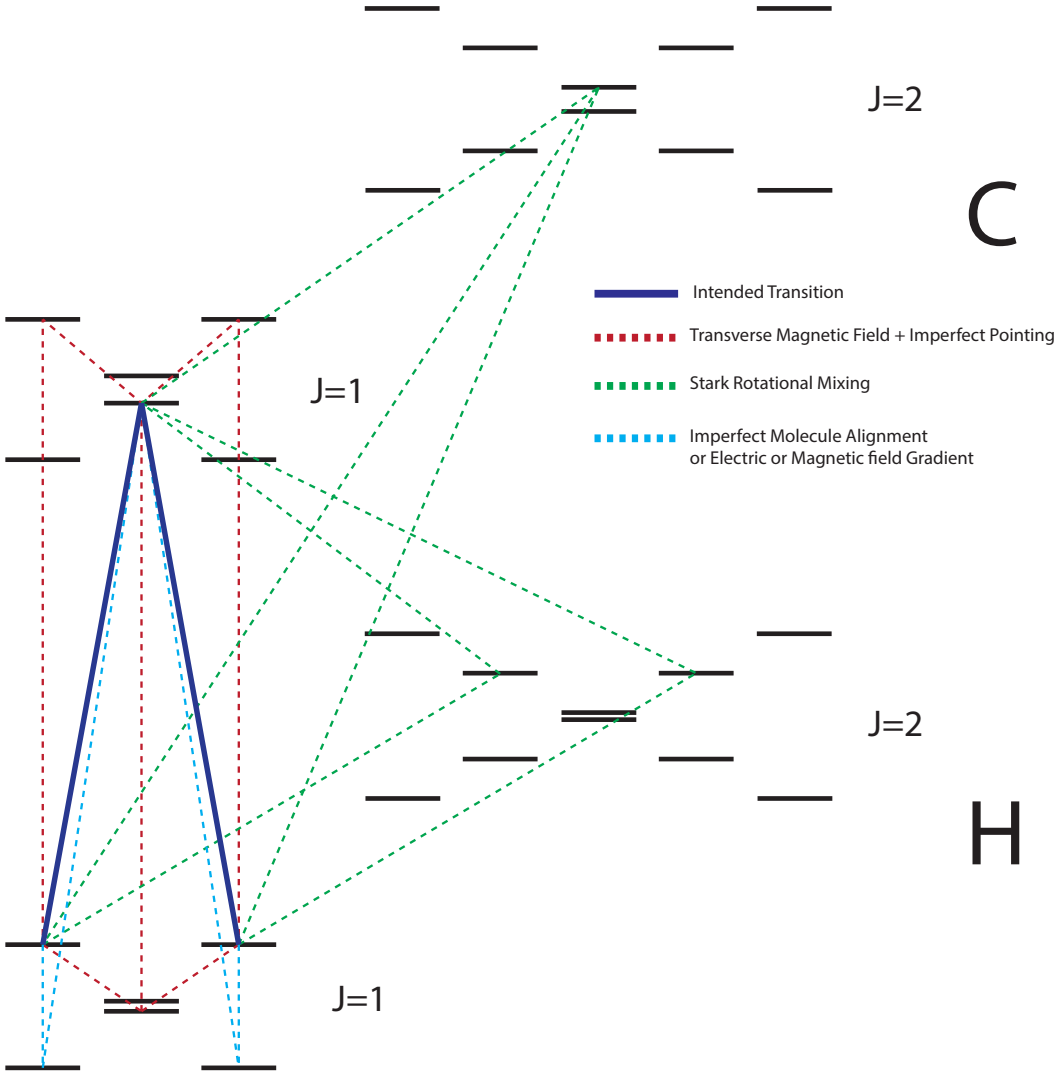

Figure 4.4: Energy level diagram showing interference mechanisms on the $H \rightarrow C$ transition in the presence of electric and magnetic fields. The transition that we intend to drive is depicted with solid dark blue lines. Unintended pathways that can interfere with the intended transition are depicted with dashed lines. The red dashed lines account for first order transverse magnetic field mixing, the light blue dashed lines account for first order Coriolis (omega doublet) mixing. The green dashed lines account for first order rotational Stark mixing.

4.2.3 Interference due to first order Stark and Zeeman mixing

In the previous sections we describe the mechanism by which interference between the first few plane wave multipoles and multipole couplings can result in correlations in the state that is either prepared or read-out. In this section, we explore how the inclusion of other states beyond the three-state model and the inclusion of Stark and Zeeman mixing between these levels can result in additional correlations that we can detect in the spin precession measurements. Figure 4.4 illustrates these additional interference mechanisms which include Zeeman mixing with a magnetic field component perpendicular to the electric field, Coriolis mixing accounting for the extent to which the molecule is not fully aligned in the laboratory frame, and rotational Stark mixing. Before accounting for these interactions, the energy of each of these states can reasonably be approximated by

$$E\left(A, J, M \neq 0, \tilde{\mathcal{N}}\right) = B_{R,\,A} J\left(J+1\right) - \tilde{\mathcal{N}} \frac{|M D_A \mathcal{E}|}{J\left(J+1\right)} \tag{4.44}$$

$$E\left(A, J, M = 0, \tilde{\mathcal{P}}\right) = \left(B_{R,\,A} + (-1)^J \frac{1}{2} \tilde{\mathcal{P}} \Delta_A\right) J\left(J+1\right) \tag{4.45}$$

where $B_{R,\,A}$ is the rotational constant, D_A is the molecule fixed electric dipole moment, and Δ_A is the omega-doubling constant for electronic state A^5. The $E1$ transition dipole matrix element on the $H \rightarrow C$ transition is then modified at first order in perturbation theory to the following expression,

5. Sometimes we refer instead to the omega doublet splitting given by $\Delta_{A,J} = \Delta_A J\left(J+1\right)$, or the electric dipole moment for the state $|A, J\rangle$, given by $D_{A,\,J} = D_A / J\left(J+1\right)$.

$$\left\langle C, J=1, \tilde{\mathcal{P}} \left| \hat{\epsilon} \cdot \hat{r} \right| H, J=1, M, \tilde{\mathcal{N}} \right\rangle \approx \tag{4.46}$$

$$+ \left\langle C, J=1, M=0, \tilde{\mathcal{P}} \left| \hat{\epsilon} \cdot \hat{r} \right| H, J=1, M, \Omega \right\rangle \tag{4.47}$$

$$+ \frac{\left\langle C, J=1, M=0, \tilde{\mathcal{P}} \left| \hat{\epsilon} \cdot \hat{r} \right| H, J=1, M, \Omega \right\rangle \left\langle H, J=1, M, -\Omega \left| H_{\Delta} \right| H, J=1, M, \Omega \right\rangle}{E\left(H, J=1, M, \tilde{\mathcal{N}}\right) - E\left(H, J=1, M, -\tilde{\mathcal{N}}\right)} \tag{4.48}$$

$$+ \frac{\left\langle C, J=1, M=0, \tilde{\mathcal{P}} \left| \hat{\epsilon} \cdot \hat{r} \right| H, J=2, M, \Omega \right\rangle \left\langle H, J=2, M, \Omega \left| -D \cdot \mathcal{E} \right| H, J=1, M, \Omega \right\rangle}{E\left(H, J=1, M, \tilde{\mathcal{N}}\right) - E\left(H, J=2, M, \tilde{\mathcal{N}}\right)} \tag{4.49}$$

$$+ \frac{\left\langle C, J=1, M=0, \tilde{\mathcal{P}} \left| -D \cdot \mathcal{E} \right| C, J=2, M=0, -\tilde{\mathcal{P}} \right\rangle \left\langle C, J=2, M=0, -\tilde{\mathcal{P}} \left| \hat{\epsilon} \cdot \hat{r} \right| H, J=1, M, \Omega \right\rangle}{E\left(C, J=1, M=0, \tilde{\mathcal{P}}\right) - E\left(C, J=2, M=0, -\tilde{\mathcal{P}}\right)} \tag{4.50}$$

$$+ \frac{\left\langle C, J=1, M=0, \tilde{\mathcal{P}} \left| -\mu \cdot \mathcal{B} \right| C, J=1, M, \Omega \right\rangle \left\langle C, J=1M, \Omega \left| \hat{\epsilon} \cdot \hat{r} \right| H, J=1, M, \Omega \right\rangle}{E\left(C, J=1, M=0, \tilde{\mathcal{P}}\right) - E\left(C, J=1, M, \tilde{\mathcal{N}}\right)} \tag{4.51}$$

$$+ \ldots \tag{4.52}$$

As we did previously, we can then reinterpret this matrix element in terms of an effective $E1$ polarization vector $\vec{\varepsilon}_{\text{eff}}$ which describes the $E1$ polarization that would be needed, in the absence of the perturbations to the states due to Coriolis, Zeeman and Stark mixing, to simulate those effects. This effective $E1$ polarization is given approximately by,

$$\vec{\varepsilon}_{\text{eff}} \approx \left[1 - \tilde{\mathcal{N}}\tilde{\mathcal{P}}\frac{\Delta_H}{D_H \left|\mathcal{E}\right|} + \tilde{\mathcal{N}} \left|\mathcal{E}\right| \frac{1}{20}\left(\frac{D_C}{B_{R,\,C}} - \frac{3}{2}\frac{D_H}{B_{R,\,H}}\right)\right]\hat{\epsilon} - i\tilde{\mathcal{N}}\left(\frac{\mu_C \mathcal{B}}{D_C \left|\mathcal{E}\right|}\right)(\hat{n}\cdot\hat{\epsilon})\left(\hat{n}\times\hat{\mathcal{B}}\right). \tag{4.53}$$

Note that the Coriolis mixing and the rotational Stark mixing simply varies the size of the Rabi frequency, and the transverse magnetic field mixing can contribute both to the size of the Rabi frequency and to spin state that is prepared or read-out, in the case that the laser pointing deviates from ideal. The Rabi frequency is proportional to the magnitude of the effective E1 polarization,

$$\Omega_{\mathrm{r}} \propto \sqrt{\vec{\epsilon}^{*}_{\mathrm{eff}} \cdot \vec{\epsilon}_{\mathrm{eff}}} = 1 - \tilde{\mathcal{N}}\tilde{\mathcal{P}}\frac{\Delta_H}{2D_H\left|\mathcal{E}\right|} + \tilde{\mathcal{N}}\left|\mathcal{E}\right|\frac{1}{20}\left(\frac{D_C}{B_{R,\,C}} - \frac{3}{2}\frac{D_H}{B_{R,\,H}}\right) \tag{4.54}$$

$$+ \frac{1}{2}\tilde{\mathcal{N}}\frac{\mu_C\left[i(\hat{\epsilon}\times\hat{\epsilon}^{*})\cdot\left(\hat{\mathcal{B}} - \left(\hat{\mathcal{B}}\cdot\hat{n}\right)\hat{n}\right)\right]}{D_C\left|\mathcal{E}\right|} + \ldots \tag{4.55}$$

Note that $i(\hat{\epsilon}\times\hat{\epsilon}^{*})$ is real and is the ellipticity of the laser light measured relative to the propagation axis $\hat{k}$ which is slightly different from S, which we have previously defined as the ellipticity measured with respect to the $\hat{z}$ laboratory axis. Hence, we expect that the Rabi frequency has correlations of approximate size,

$$\frac{\Omega_{\mathrm{r}}^{\mathcal{N}}}{\Omega_{\mathrm{r}}^{\mathrm{nr}}} \approx \frac{1}{20}\left(\frac{D_C\left|\mathcal{E}\right|}{B_{R,\,C}} - \frac{3}{2}\frac{D_H\left|\mathcal{E}\right|}{B_{R,\,H}}\right) \sim \begin{cases} -3.5\times10^{-4} & \left|\mathcal{E}\right| \approx 36\ \frac{\mathrm{V}}{\mathrm{cm}} \\ -1.5\times10^{-3} & \left|\mathcal{E}\right| \approx 141\ \frac{\mathrm{V}}{\mathrm{cm}} \end{cases} \tag{4.56}$$

$$\frac{\Omega_{\mathrm{r}}^{\mathcal{NP}}}{\Omega_{\mathrm{r}}^{\mathrm{nr}}} \approx -\frac{\Delta_H}{D_H\left|\mathcal{E}\right|} \sim \begin{cases} -2.5\times10^{-3} & \left|\mathcal{E}\right| \approx 36\ \frac{\mathrm{V}}{\mathrm{cm}} \\ -6.5\times10^{-4} & \left|\mathcal{E}\right| \approx 141\ \frac{\mathrm{V}}{\mathrm{cm}} \end{cases} \tag{4.57}$$

Both of these correlations were observed in ACME I and contributed to the correlated contrast, $\mathcal{C}^{\mathcal{N}}$ and $\mathcal{C}^{\mathcal{NP}}$, as can be seen in figure 3.5. The transverse magnetic field mixing term also contributes to $\Omega_{\mathrm{r}}^{\mathcal{N}}$ when interfering with E1 and can contribute to $\Omega_{\mathrm{r}}^{\mathcal{E}}$ when interfering with $M1$, but both of these contributions are estimated to be incredibly small, $< 10^{-9}$ and hence were neglected in the above calculation.

The additional interference terms in equation 4.53 also introduces the possibility of correlations in the prepared spin state. Just as one example, there are contributions to $\Phi^{\mathcal{N}}$ with spin spate imperfections,

$$d\theta^{\mathcal{N}} - id\Theta^{\mathcal{N}} \approx -i\left(\frac{\mu_C\mathcal{B}}{D_C|\mathcal{E}|}\right)\left(\hat{z}\cdot\left(\hat{\epsilon}\times\left(\hat{z}\times\hat{\mathcal{B}}\right)\right)\right)(\hat{\epsilon}\cdot\hat{n}) \tag{4.58}$$

which could have plausibly been as large as $\sim 10^{-7}$ rad, below the level of sensitivity of the ACME I experiment, and well below the size of the not-understood signal in the $\omega^{\mathcal{N}}$ channel described in section 3.5.

4.2.4 The persistent $\Omega_{\mathrm{r}}^{\mathcal{NE}}$ mystery

As described in section 3.2, during the course of ACME I, we observed a couple pieces of evidence that pointed to the existence of a Rabi frequency correlation $\Omega_{\mathrm{r}}^{\mathcal{NE}}/\Omega_{\mathrm{r}}^{\mathrm{nr}} \approx (-8.0 \pm 0.8) \times 10^{-3}(\hat{k} \cdot \hat{z})$ that reversed with the propagation direction of the laser beams, $\hat{k} \cdot \hat{z}$, and there was no strong evidence for $\Omega_{\mathrm{r}}^{\mathcal{NE}}$ varying with any of the other experiment parameters that we routinely varied, within the resolution of the experiment. These observations motivated the development of the Stark interference model described in section 4.2.1. If we allow for the coefficients a_{M1} and a_{E2} to be complex, then the Stark interference results in a Rabi frequency correlation,

$$\frac{\Omega_{\mathrm{r}}^{\mathcal{NE}}}{\Omega_{\mathrm{r}}^{\mathrm{nr}}} \approx -\operatorname{Im}\left[a_{\mathrm{M1}} + a_{\mathrm{E2}}\right](\hat{k} \cdot \hat{n}), \tag{4.59}$$

which provides the same functional behavior as that observed in the experiment. Furthermore, the estimates for a_{M1} in table 4.2.1 suggest that it may be as small as the measured $\Omega_{\mathrm{r}}^{\mathcal{NE}}/\Omega_{\mathrm{r}}^{\mathrm{nr}}$ (in magnitude), and on the higher end it could plausibly be up to a factor $10\times$ larger. Despite the apparent similarities between the Stark interference model and the observed Rabi frequency correlation, for a single plane wave a_{M1} is distinctly real which implies that the Rabi frequency correlation vanishes, as stated in equation 4.27. Nevertheless, this model still seems plausibly viable for explaining the measurement if an additional complication is introduced that effectively applies a phase shift of the M1 amplitude relative to E1.

As a proof of principle of my claim that we can conceive of some effect that mimics an imaginary component of a_{M1}, consider the interaction of the molecule with both a plane wave propagating in the forward $\hat{k} \approx \hat{z}$ direction, and its reflection off of the far electric field plate with reflection amplitude r and backward propagation direction $\hat{k}' \approx -\hat{k}$. The amplitudes of these two plane waves add resulting in an effective E1 polarization that takes into account both waves and the E1 and M1 transitions,

$$\vec{\varepsilon}_{\mathrm{eff}} = (e^{ikz} + re^{-ikz})\hat{\epsilon} - ia_{\mathrm{M1}}(e^{ikz} - re^{-ikz})\hat{n} \times (\hat{k} \times \hat{\epsilon}), \tag{4.60}$$

which results in a correlated Rabi frequency,

$$\frac{\Omega_{\mathrm{r}}^{\mathcal{NE}}}{\Omega_{\mathrm{r}}^{\mathrm{nr}}} \approx -\, a_{\mathrm{M1}} \mathrm{Im}\left[\frac{1 - re^{-2ikz}}{1 + re^{-2ikz}}\right](\hat{k}\cdot\hat{z}), \tag{4.61}$$

Given that the reflectivity off of the field plates is about $|r|^2 \sim 0.1$, the magnitude of the Rabi frequency correlation would be around $\sim 10^{-2}$, comparable to that which we observed in the experiment. However, the value oscillates spatially over the scale of the wavelength of the light, which is much smaller than the scale of the molecule beam, and hence should average out to zero in the spin precession measurement. So, although this mechanism does not explain the measured $\Omega_{\mathrm{r}}^{\mathcal{NE}}/\Omega_{\mathrm{r}}^{\mathrm{nr}}$, it lends credence to the possibility that the Stark interference could still be part of the generating mechanism.

4.3 AC Stark shift phases

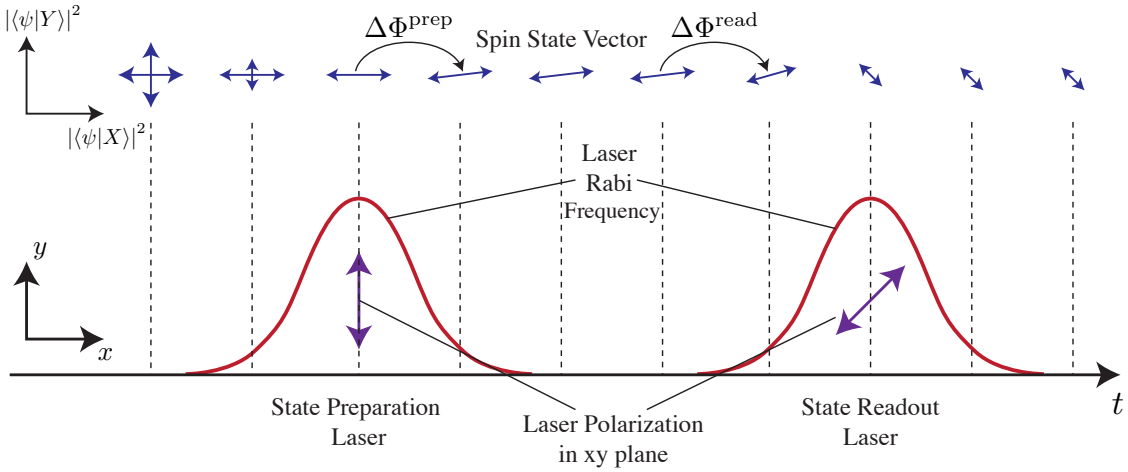

Figure 4.5: Schematic of the EDM spin precession measurement including effects from AC Stark induced phases $\Delta\Phi_{\mathrm{prep}}$ and $\Delta\Phi_{\mathrm{read}}$ from non-adiabatic polarization rotations after the state preparation and before the state read-out lasers respectively. Top: illustration of the spin state evolution in time by plotting the relative phase between $|\tilde{\mathcal{N}}, M = \pm 1\rangle$ as an angle in 2d space, and by illustrating the state norm by the length of the line segment. The spin state is initially incoherent in ACME I, but the state preparation laser depletes half of the molecules resulting in a coherent state. Bottom: The Rabi frequency as seen by the molecules as a function of time is shown in red, and the polarizations of these laser beams in the xy plane is shown in purple.

4.3.1 Polarization gradients and Zeeman mixing

In this section we describe contributions to the measured phase Φ that depend on the AC Stark shift induced by the state preparation and readout lasers. We describe mechanisms by which such phase contributions may arise, and we describe mechanisms by which $\tilde{\mathcal{N}}\tilde{\mathcal{E}}$ correlated experimental imperfections may couple to these phases to result in electron EDM-mimicking phases. Concise descriptions of some of the effects described here can be also be found in [77, 86, 158].

During our search for systematic errors as described in section 3.1, we empirically found that there was a contribution to the measured phase $d\Phi(\Delta, \Omega_\mathrm{r})$ that had an unexpected linear dependence on the laser detuning, Δ, a quadratic dependence on laser detuning Δ in the presence of a nonzero magnetic field, and a linear dependence on small changes to the magnitude of the Rabi frequency, $d\Omega_\mathrm{r}/\Omega_\mathrm{r}$, in the presence of a nonzero magnetic field,

$$d\Phi\left(\Delta, \Omega_\mathrm{r}\right) = \sum_i \left[\alpha_{\Delta,i}\Delta_i + \alpha_{\Delta^2,i}\Delta_i^2 + \beta_{d\Omega_{\mathrm{r},i}}(d\Omega_{\mathrm{r},i}/\Omega_{\mathrm{r},i}) + \dots\right]. \tag{4.62}$$

where $i \in \{\mathrm{prep}, X, Y\}$ indexes the state preparation and readout lasers. The coefficients we measured were $\alpha_\Delta \sim 1\,\mathrm{mrad}/(2\pi \times \mathrm{MHz})$, $\alpha_{\Delta^2} \sim 1\,\mathrm{mrad}/\left(2\pi \times \mathrm{MHz}\right)^2$ and $\beta_{d\Omega_\mathrm{r}} \sim 10^{-3}$. We performed these measurements by independently varying the laser detunings Δ_i across resonance using AOMs or modulating the laser power using AOMs and extracting the measured phase Φ. Examples of such measurements are given in figure 4.3.1. Such phases can couple to observed correlations in the detuning, $\Delta^{\mathcal{N}\mathcal{E}} \approx 2\pi \cdot 5\,\mathrm{kHz}$, and the Rabi frequency, $\Omega_\mathrm{r}^{\mathcal{N}\mathcal{E}}/\Omega_\mathrm{r}^{\mathcal{N}\mathcal{E}} \approx 8 \times 10^{-3}$, to result in systematic errors that are expressed in equations 3.9 and 3.10.

We determined that this behavior can be caused by mixing between bright and dark states, due to a small non-adiabatic laser polarization rotation or Zeeman interaction present during the optical pumping used to prepare and read out the spin state. The mixed bright and dark states differ in energy by the AC Stark shift, which leads to a relative phase accumulation between the bright and dark state components that depends on the laser parameters Δ and Ω_r. We shall now derive an AC Stark shift phase that reproduces the behavior described in equation 4.62, under simplifying assumptions amenable to analytic calculations.

We may apply first order time-dependent perturbation theory in this picture to deter-

mine the extent of bright/dark state mixing due to $\dot{\chi}$ in the time evolution of the three level system under the Hamiltonian in equation 4.14. If we parameterize the time-dependent state as

$$|\psi(t)\rangle = c_D(t)|D\rangle + c_{B+}(t)|B_+\rangle + c_{B-}(t)|B_-\rangle, \tag{4.63}$$

then in the case of a uniform laser field $\dot{\Omega}_\mathrm{r} = 0$, of duration t and with a constant detuning $\dot{\Delta} = 0$, the time evolution of the coefficients is given at first order by:

$$c_D(t) = c_D(0) - \sum_{\pm}\int_0^t \dot{\chi}^*\left(t'\right)\kappa_{\mp}\left(t'\right)e^{-iE_{B\pm}t'}c_{B\pm}(0)\ \ dt' \tag{4.64}$$

$$c_{B\pm}(t) = e^{-iE_{B\pm}t}c_{B\pm}(0) + e^{-iE_{B\pm}t}\int_0^t \dot{\chi}\left(t'\right)\kappa_{\mp}\left(t'\right)e^{iE_{B\pm}t'}c_D(0)\ \ dt'. \tag{4.65}$$

In ACME I the molecules begin in an incoherent mixture of the states $|B(\hat{\varepsilon}_\mathrm{prep}), \tilde{\mathcal{N}}, \tilde{\mathcal{P}}\rangle$ and $|D(\hat{\varepsilon}_\mathrm{prep}), \tilde{\mathcal{N}}, \tilde{\mathcal{P}}\rangle$ and then enter the state preparation laser beam. In the ideal case of uniform laser polarization, molecules that were in the bright state are optically pumped out of the three level system, and molecules that are in the dark state remain there; this results in a pure state, $|D(\hat{\varepsilon}_\mathrm{prep}), \tilde{\mathcal{N}}, \tilde{\mathcal{P}}\rangle$. However, if there is a small polarization rotation by amount $d\chi \equiv \int_0^t \dot{\chi}(t')\,dt' \equiv d\Theta - i(d\theta - g_{H,J=1}\mu_\mathrm{B}\tilde{\mathcal{B}}\mathcal{B}_z t)$, such that $|d\chi| \ll 1$, then the dark state obtains a bright state admixture that may not be completely optically pumped away before leaving the laser beam.[6] In this case, the final state can be written as

$$|D(\hat{\varepsilon}'_\mathrm{prep}), \tilde{\mathcal{N}}, \tilde{\mathcal{P}}\rangle = |D(\hat{\varepsilon}_\mathrm{prep}), \tilde{\mathcal{N}}, \tilde{\mathcal{P}}\rangle + d\chi\Pi|B(\hat{\varepsilon}_\mathrm{prep}), \tilde{\mathcal{N}}, \tilde{\mathcal{P}}\rangle \tag{4.66}$$

where $\hat{\varepsilon}'_\mathrm{prep}$ is the effective polarization that parameterizes the initial state in the spin precession region,

$$\hat{\varepsilon}'_\mathrm{prep} = \hat{\varepsilon}_\mathrm{prep} + d\chi\Pi i\hat{z}\times\hat{\varepsilon}^*_\mathrm{prep}, \tag{4.67}$$

and Π is a complex amplitude that accounts for the AC Stark shift phase and the time

6. This is most liable to occur just before a molecule leaves the laser beam, such that complete optical pumping does not occur.

dependent dynamics of the non-adiabatic mixing during the polarization rotation,

$$\Pi = \sum_{\pm} (\kappa_{\mp})^2 e^{-iE_{B\pm}t} \int_0^t dt' \, \frac{\dot{\chi}\,(t')}{d\chi} e^{iE_{B\pm}t'}. \tag{4.68}$$

The deviations between the effective polarization and the actual laser polarization can be viewed as effective polarization imperfections,

$$d\theta_{\text{prep,eff}} = -\, d\Theta_{\text{prep}} \text{Im}\Pi + (d\theta_{\text{prep}} - g_1 \mu_{\text{B}} \mathcal{B}_z \tilde{\mathcal{B}} t) \text{Re}\Pi, \tag{4.69}$$

$$d\Theta_{\text{prep, eff}} = -\, d\Theta_{\text{prep}} \text{Re}\Pi - (d\theta_{\text{prep}} - g_1 \mu_{\text{B}} \mathcal{B}_z \tilde{\mathcal{B}} t) \text{Im}\Pi, \tag{4.70}$$

that lead to shifts in the measured phase Φ as described in equation 4.2. For definiteness, consider the simple case in which the polarization rotation rate $\dot{\chi}(t') = (d\chi/t)(0 \leq t' \leq t)$ is a constant for the duration of the optical pumping pulse t. In this case,

$$\Pi = \sum_{\pm} (\kappa_{\mp})^2 e^{-iE_{B\pm}t/2} \text{sinc}(E_{B\pm}t/2). \tag{4.71}$$

This function has the property that $\text{Im}\Pi$ is an odd function in Δ that can take on values up to order unity across resonance (a frequency range that spans the larger of the excited state decay rate, γ_C, and the Doppler width, Δ_D) and is exactly zero on resonance. $\text{Re}\Pi$ is an even function, quadratic in Δ about resonance, and depends linearly on small changes in the Rabi frequency on resonance. If the laser beam intensity reduces quickly as the molecule leaves the laser beam then most of the AC Stark shift phase arises from the last Rabi flopping period before the molecule exits the laser beam (provided that $\dot{\chi}$ is nonzero during that time). If the intensity reduces slowly, the AC Stark shift phase can be exacerbated since the bright state amplitude is not as effectively optically pumped away while $\Omega_{\text{r}} < \gamma_C$. Nevertheless, beam shaping tests [158] and numerical simulations indicate that Π is not very sensitive to the shape of the spatial intensity profile of the laser beam or the shape of the spatial variation of the polarization.

If we consider only the first order contribution to the shift in the measured phase in equation 4.2, $d\theta_{\text{prep,eff}}$, and neglect the second order shift that arises due to $d\Theta_{\text{prep,eff}}$, then we can relate the parameters in equation 4.62 to the amplitude Π accounting for the AC

Stark shift phase and the complex polarization rotation $d\chi$, by

$$\alpha_{\Delta,\mathrm{prep}} \approx -\frac{\partial \mathrm{Im}\Pi}{\partial \Delta_{\mathrm{prep}}} d\Theta_{\mathrm{prep}} \tag{4.72}$$

$$\alpha_{\Delta^2,\mathrm{prep}} \approx \frac{\partial^2 \mathrm{Re}\Pi}{\partial \Delta_{\mathrm{prep}}^2} \left(d\theta_{\mathrm{prep}} - g\mu_{\mathrm{B}} \mathcal{B}_z \tilde{\mathcal{B}} t \right) \tag{4.73}$$

$$\beta_{d\Omega_{\mathrm{r}},\mathrm{prep}} \approx \Omega_{\mathrm{r}} \frac{\partial \mathrm{Re}\Pi}{\partial \Omega_{\mathrm{r}}} \left(d\theta_{\mathrm{prep}} - g\mu_{\mathrm{B}} \mathcal{B}_z \tilde{\mathcal{B}} t \right). \tag{4.74}$$

We can interpret these results as follows. The linear dependence of the measured phase on detuning, $\alpha_{\Delta,\mathrm{prep}}$, comes from a spatially varying ellipticity in the x direction coupling to the AC Stark shift phase. Similarly, the quadratic dependence of Φ on Δ, $\alpha_{\Delta^2,\mathrm{prep}}$, and the dependence of Φ on a relative change in Ω_{r}, $\beta_{d\Omega_{\mathrm{r}},\mathrm{prep}}$, come from either a spatially varying linear polarization in the x direction or a Zeeman shift, each coupling to the AC Stark shift phase.

Here, we only analyzed the phase shift that results from AC Stark shift effects in the state preparation laser beam, but there is an analogous phase shift in the state readout beam, which is approximately given as the average phase shift measured by the $\hat{\epsilon}_X$ and $\hat{\epsilon}_Y$ read-out laser beams. Since these two laser beams are nominally orthogonal, if the polarization gradients in the laser beams are generated by a birefringent mechanism, such at that described in section 4.3.3, then the contributions to the phase shifts in the $\hat{\epsilon}_X$ and $\hat{\epsilon}_Y$ laser beams have opposite signs resulting in cancellation of the effect in the spin precession signal.

There are several other subdominant effects that also contribute to the AC Stark shift phase behavior described in equation 4.2 in the presence of polarization imperfections. The opposite parity excited state $|C, -\tilde{\mathcal{P}}\rangle$ couples strongly to the dark state, but the mixing between these two states is weak because the transition frequency is off-resonant by a detuning $\Delta_{\Omega,C,J=1} \approx 2\pi \times 51$ MHz $\gg \gamma_C$. In the case that an optical pumping laser has nonzero ellipticity, the bright state gains a weak coupling to the opposite-parity excited state proportional to this ellipticity. Then, two-photon bright-dark state mixing ensues in such a way that the mixing amplitude, and hence the measured phase, depends on the laser detuning. This mechanism is described in detail in section 4.2.2 above.

The rapid polarization switching of the state readout beam can also introduce AC Stark shift-induced phases in the absence of a polarization gradient, if the average ellipticity

between the two polarizations is non-zero. Suppose a particular molecule is first excited by the $\hat{\epsilon}_X$ polarized beam. The two bright eigenstates $|B_\pm\rangle$ are mostly optically pumped away, resulting in a fluorescence signal F_X. The population remaining in the bright eigenstates acquires a phase relative to the dark state, due to the AC Stark shift. Then the molecules are optically pumped by the $\hat{\epsilon}_Y$ polarized beam. If there is a nonzero average ellipticity, $\hat{\epsilon}_Y$ is not quite orthogonal to $\hat{\epsilon}_X$ and the new bright eigenstates that give rise to the fluorescence signal F_Y are superpositions of the former bright and dark states that acquired a relative AC Stark shift phase. This results in a fluorescence signal, and hence measured phase component, that depends linearly on laser detuning Δ. This mechanism is described in detail in section 4.3.4.

In ACME I, we used Acousto-optic modulators in both the state preparation and state read-out beam paths to independently vary the detuning and laser intensity of each beam. We then performed spin precession measurements while scanning across several values of Δ and Ω_r, allowing us to measure the phase dependence $\Phi(\Delta, \Omega_\mathrm{r})$. We would switch the magnetic field direction, $\tilde{\mathcal{B}}$, so that we could distinguish between AC Stark shift phases caused by polarization imperfections and the Zeeman interaction. We also switched $\tilde{\mathcal{P}}$, $\tilde{\mathcal{R}}$ so that we could distinguish phases from contributions to the asymmetry induced by differences in power, laser intensity profile, pointing, or polarization imperfections of the two state read-out beams. These "asymmetry effects" are described in more detail in section 4.3.6

Example data, taken between the two $\hat{k} \cdot \hat{z} = \pm 1$ measurements in ACME I, of the AC Stark shift phases is presented in figure 4.3.1. This data clearly shows a non-zero $\alpha_\Delta^\mathrm{nr}$ in both the state preparation and state read-out region of approximately the same magnitude but opposite sign, which could have been caused by an ellipticity gradient, amongst other possible causes. Nonzero $\alpha_{\Delta^2}^\mathrm{nr}$ and $\beta_{d\Omega_\mathrm{r}}^\mathrm{nr}$ were not observed within the resolution of these experiments, which indicates the absence of a significant linear polarization gradient. AC Stark shift phases due to the Zeeman interaction, $\alpha_{\Delta^2}^\mathcal{B}$ and $\beta_{d\Omega_\mathrm{r}}^\mathcal{B}$, were observed and had coefficients that are roughly consistent with those which are expected.

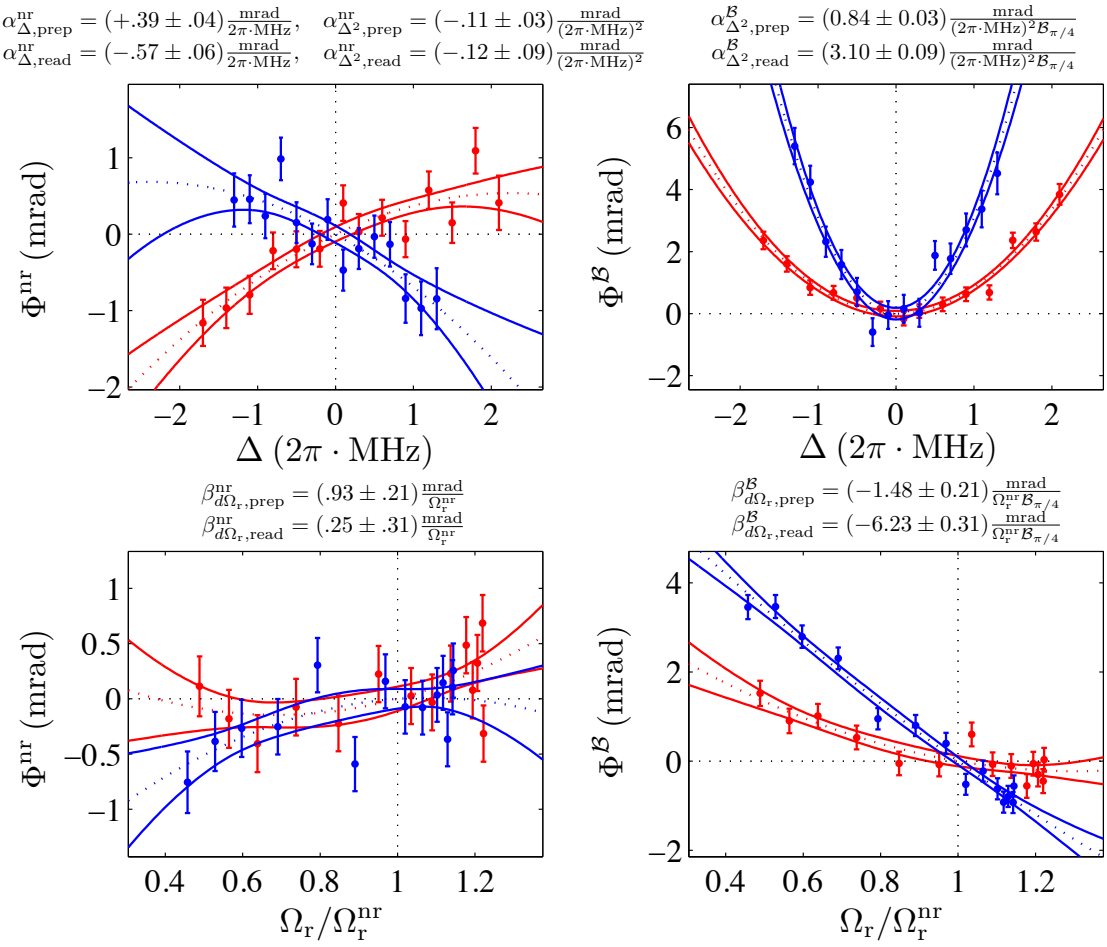

Figure 4.6: Measured AC Stark shift phases $\Phi(\Delta, \Omega_r) = \Phi^{\rm nr} + \tilde{\mathcal{B}}\Phi^{\mathcal{B}}$ and their dependence on the laser parameters Δ and Ω_r for both the State Preparation beam (red) and the State Read-out beam (blue), obtained from laser detuning and power scans. The points with 1σ errorbars are data taken from the experiment and the solid lines are $\pm 1\sigma$ confidence intervals for quadratic fits to the measurements. For each of these plots the offset phase under normal operating conditions, $\Delta = 0$, $\Omega_r/\Omega^{\rm nr}_r = 1$, has been subtracted.

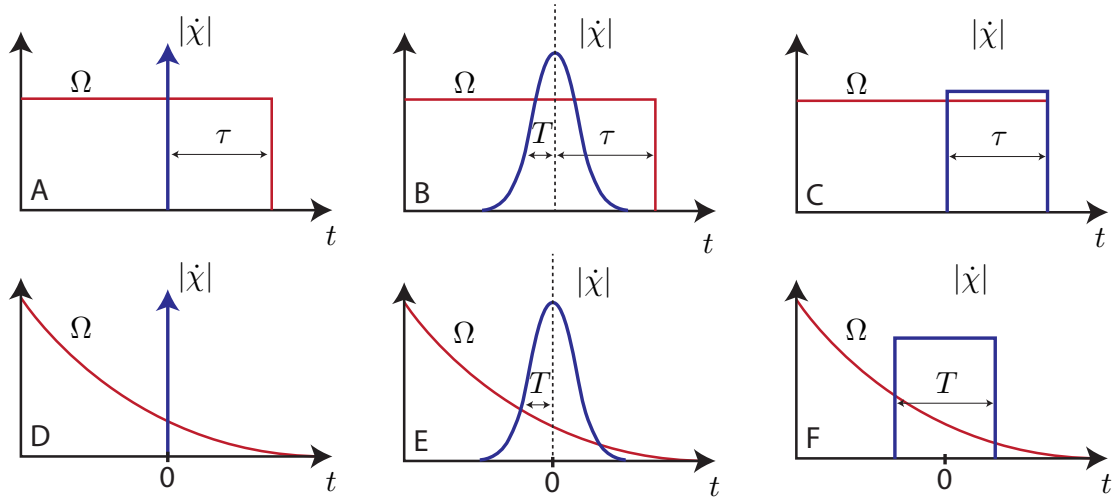

Figure 4.7: Here is an illustration of the 6 models that are considered analytically for evaluating the AC stark shift induced phase shifts in the state preparation laser beam for different spatial profiles of the Rabi frequency, $\Omega_r(t)$, and polarization rotation rate, $\dot{\chi}$. The top row illustrates models with a uniform intensity laser beam, $\Omega_r(t) = \Omega_r(t < \tau)$, and the bottom row illustrates models with an exponentially decaying intensity laser beam, $\Omega_r(t) = \Omega_r e^{-t/\tau}$. The columns correspond to the 3 models for the polarization rotation rate function $\dot{\chi}(t)$, the Dirac impulse, the Gaussian impulse, and the constant rotation rate.

4.3.2 Comparison of analytic models for the AC Stark shift phase factor Π

Uniform Rabi frequency

In the previous section, we derived the dependence of the phase on the AC Stark shift phase factor, which we parameterized as Π in equation 4.68 in the case of a uniform Rabi frequency. I stated previously, without proof, that Π is not very sensitive to the shape of the spatial intensity profile of the laser beam or the shape of the spatial variation of the polarization. In this section, we will explore a few analytic models of the AC Stark shift phase from polarization gradients for different functional forms of the spatial variation of the polarization gradient and the Rabi frequency to justify this claim.

In the case that the laser Rabi frequency is uniform and shuts off non-adiabatically at time $t = \tau$, $\Omega_r(t) = \Omega_r(t \leq \tau)$, we can evaluate the function Π using equation 4.68. Lets consider 3 spatial profiles of the polarization rotation $\dot{\chi}(t)$,

1. Dirac impulse: an instantaneous polarization rotation at $t = 0$, $\dot{\chi}(t) = d\chi\, \delta(t)$.

2. Gaussian impulse: a slightly more gradual polarization rotation (possibly a reasonable

model of effects from two overlapping laser beams with slightly different polarization). The polarization occurs around $t = 0$ with a timescale of T such that $T < \tau$, $\dot{\chi}(t) = d\chi\, e^{-t^2/2T^2}/\sqrt{2\pi T^2}$.

3. Constant: a uniform polarization rotation rate from time $t = 0$ to $t = \tau$ when the laser beam shuts off, $\dot{\chi}(t) = (d\chi/\tau)\,(0 \le t \le \tau)$.

These three models are illustrated at the top of figure 4.3.2. Table 4.3.2 shows explicit expressions for the Π function for each of the three model $\dot{\chi}$ functions described above in terms of $\kappa_\pm$, $E_{B\pm}$, and τ. Recall that the effect of the decay is included in this function by making the substitution $\Delta \to \Delta - i\gamma/2$ in the definitions of $E_{B\pm}$ and $\kappa_\pm$ in equations 4.11 and 4.9. As described earlier, the bright state admixture $d\chi\Pi$ will be exponentially suppressed by $\sim \exp(-\gamma t/2)$ if polarization rotation mostly occurs in the center of the laser beam where the optical pumping is taking place such that $\Omega_r\tau \gg 1$ and $\gamma\tau \gg 1$. Since the AC Stark shift phase will be dominated by polarization rotation near the falling tail of the spatial intensity profile, we do not explicitly consider this limit. We also do not consider the limit in which optical pumping does not significantly take place, $\Omega_r\tau \gg 1$ and $\gamma\tau \ll 1$, because optical pumping is required for the measurement scheme. The dominant contributions to Π come from polarization rotation that occurs during the last Rabi flop such that $\Omega\tau \le \pi$, in which case Π approaches 1. Hence there are two limits that we would like to understand well, which are:

1. $\Omega_r\tau \ll 1$, $\gamma\tau \ll 1$, this is the case where the polarization rotation occurs very close to the edge of a laser beam with a spatial intensity profile that falls off very abruptly.

2. $\Omega_r\tau \ll 1$, $\gamma\tau \gg 1$, this is the case where the polarization rotation occurs within a weak field tail of a laser beam with a spatial intensity profile that falls of gradually so that the Rabi flopping is slow, but the decay of the excited state is still rapid.

In both of these limits, it will be useful to express Π as a Taylor expansion in $\Delta\tau$ and $\Omega_r\tau$ for easier comparison between measured experiment coefficients in equation 4.62. In the limit that $\Omega_r\tau \ll 1$, $\gamma\tau \ll 1$, it is useful to use an expansion in $\Omega_r\tau$ and $i\Delta\tau$,

$$\Pi = \sum_{n,m=0}^{\infty} \alpha_{nm} \left(i\Delta\tau\right)^n \left(\Omega_{\mathrm{r}}\tau\right)^m \tag{4.75}$$

$$= 1 + \alpha_{02} \left(\Omega_{\mathrm{r}}\tau\right)^2 + i\alpha_{12} \left(\Delta\tau\right) \left(\Omega_{\mathrm{r}}\tau\right)^2 - \alpha_{22} \left(\Delta\tau\right)^2 \left(\Omega_{\mathrm{r}}\tau\right)^2 + \ldots \tag{4.76}$$

which is practically useful up to around $\Omega_{\mathrm{r}}\tau \sim \pi$. It is also notable that the largest sensitivity of Π to Ω_{r} and Δ occurs in the regime of $\gamma\tau \ll 1$ with $\Omega_{\mathrm{r}}\tau \sim \pi$ and $\Delta\tau \sim \pi$. In the limit of $\Omega_{\mathrm{r}}\tau \ll 1$, $\gamma\tau \gg 1$, it is illustrative to express Π as a Taylor expansion in $\Omega_{\mathrm{r}}\tau$ and $1/\left(i\Delta\tau + \gamma/2\right)$ which shows explicitly the resonant behavior of the Π function as a function of detuning in this limit,

$$\Pi = \sum_{n,m=0}^{\infty} \beta_{nm} \frac{\left(\Omega_{\mathrm{r}}\tau\right)^m}{\left(i\Delta\tau + \gamma\tau/2\right)^n} \tag{4.77}$$

$$= 1 - i\beta_{12} \frac{\left(\Omega_{\mathrm{r}}\tau\right)^2}{\left(\Delta\tau - i\gamma\tau/2\right)} - \beta_{22} \frac{\left(\Omega_{\mathrm{r}}\tau\right)^2}{\left(\Delta\tau - i\gamma\tau/2\right)^2} + \ldots \tag{4.78}$$

Table 4.3.2 lists the first three nontrivial α_{nm} coefficients for the three models described in both the $\Omega_{\mathrm{r}}\tau \ll 1, \gamma\tau \ll 1$ limit the first 2 nontrivial β_{nm} coefficients in the $\Omega_{\mathrm{r}}\tau \ll 1$ and $\gamma\tau \gg 1$ limit. Notice that the model coefficients vary with respect to each other by factors of about $1\times -4\times$ and that the coefficients typically decrease in size (as required for convergence) with higher order.

		Dirac Impulse	Gaussian Impulse	Constant
$\dot{\chi}\left(t\right) =$		$d\chi\delta\left(t\right)$	$\frac{d\chi}{\sqrt{2\pi T^2}}\exp\left(-\frac{1}{2}\frac{t^2}{T^2}\right)$	$\left(d\chi/\tau\right)\Theta\left(t\right)\Theta\left(\tau - t\right)$
$\Pi =$		$\sum_{\pm}\kappa_{\mp}^2 e^{-iE_{B\pm}\tau}$	$\sum_{\pm}\kappa_{\mp}^2 e^{-\frac{1}{2}E_{B\pm}^2 T^2 - iE_{B\pm}\tau}$	$\sum_{\pm}\kappa_{\mp}^2 e^{-i\frac{1}{2}E_{B\pm}\tau}\mathrm{sinc}\left(\frac{1}{2}E_{B\pm}\tau\right)$
$\gamma\tau \ll 1$	α_{02}	$-1/8$	$-\frac{1}{8}\left(1 + \left(\frac{T}{\tau}\right)^2 + \ldots\right)$	$-1/24$
	α_{12}	$+1/24$	$+\frac{1}{24}\left(1 + 3\left(\frac{T}{\tau}\right)^2 + \ldots\right)$	$+1/96$
	α_{22}	$-1/96$	$-\frac{1}{96}\left(1 + 6\left(\frac{T}{\tau}\right)^2 + \ldots\right)$	$-1/480$
$\gamma\tau \gg 1$	β_{02}	$-1/4$	$-1/4 + \ldots$	$-1/8$
	β_{22}	$+1/4$	$+1/4 + \ldots$	$+1/4$

Table 4.4: Analytic models for the AC Stark shift phase accumulation in the tail of the State Preparation laser, $\Delta\Phi_{\mathrm{prep}} \equiv d\chi\Pi$, in the case of a uniform Rabi frequency, $\Omega_{\mathrm{r}}\left(t\right) = \Omega_{\mathrm{r}}(t \leq \tau)$. The top shows the analytic expressions for the $\dot{\chi}\left(t\right)$ functions that are assumed and the Π functions that are derived. The bottom shows the expansion coefficients corresponding to the definitions in equation 4.76 for the Π functions in the limit that $\Omega_{\mathrm{r}}\tau \ll 1$ for both both $\gamma\tau \gg 1$ and $\gamma\tau \ll 1$ limits.

Exponentially decreasing Rabi frequency

In reality laser beams almost always have low intensity tails that fall off gradually. Since we expect that the AC Stark shift phase comes dominantly from non-adiabatic polarization rotation in these low intensity tails, we would prefer a model that takes this behavior into account. However, a significant gradient in Rabi frequency can lead to non-perturbative mixing between the two bright states in the dressed state picture which makes the adiabatic perturbation theory approach, that we have used up to this point, impractical. In this section we will explore a model in which can accommodate such a time varying Rabi frequency.

For this model, we work in a quasi dressed state picture with a basis set consisting of the$|D\rangle$, $|B\rangle$, and $|C\rangle$ states for which the Hamiltonian can be written as

$$\tilde{H} = \begin{pmatrix} \Delta & \frac{1}{2}\Omega_{\mathrm{r}} & 0 \\ \frac{1}{2}\Omega_{\mathrm{r}} & 0 & i\dot{\chi} \\ 0 & -i\dot{\chi}^* & 0 \end{pmatrix} \begin{matrix} |C\rangle \\ |B\rangle \\ |D\rangle \end{matrix} \tag{4.79}$$

where $\dot{\chi} = (\dot{\Theta} - i(\dot{\theta} - \mu_B g_{H,J=1}\tilde{\mathcal{B}}\mathcal{B}_z))$ and Ω_{r} and $\dot{\chi}$ are possibly time dependent. The state $|\psi\rangle = c_D\,|D\rangle + c_B\,|B\rangle + c_C\,|C\rangle$ evolves according to the Schrodinger equation, and assuming that the effect of the polarization rotation results in a small change to the dark state amplitude, then to a good approximation, we can evaluate $|\psi\rangle$ up to first order in $\dot{\chi}$. If we perturbatively expand the state coefficients in powers of $d\chi$, $c_i = \sum_{n=0}^{\infty} d\chi^n c_i^{(n)}$, then to zeroth order the state coefficients are stationary and equal to the initial conditions, $c_D^{(0)} = 1$ and $c_B^{(0)} = c_C^{(0)} = 0$. The first order coefficient for the dark state vanishes, $c_D^{(1)} = 0$, and the coefficients $c_B^{(1)}$ and $c_C^{(1)}$ are determined by a two state Schrodinger equation that is externally driven by polarization rotation from the dark state,

$$\begin{pmatrix} \dot{c}_C^{(1)} \\ \dot{c}_B^{(1)} \end{pmatrix} = -\,i \begin{pmatrix} \Delta & \frac{1}{2}\Omega_{\mathrm{r}} \\ \frac{1}{2}\Omega_{\mathrm{r}} & 0 \end{pmatrix} \begin{pmatrix} c_C^{(1)} \\ c_B^{(1)} \end{pmatrix} + \begin{pmatrix} 0 \\ \dot{\chi}/d\chi \end{pmatrix}, \tag{4.80}$$

with the initial condition that $c_B^{(1)}(-\infty) = 0, c_e^{(1)}(-\infty) = 0$. Since we would only like to evaluate $d\chi\, c_B^{(1)}(\infty) = d\chi\,\Pi$, then it is useful to convert this into a second order differential

equation for only $c_B^{(1)}(t)$,

$$\ddot{c}_B^{(1)} + \dot{c}_B^{(1)}\left(i\Delta - \frac{\dot{\Omega}_\mathrm{r}}{\Omega_\mathrm{r}}\right) + c_B^{(1)}\left(\frac{1}{4}\Omega_\mathrm{r}^2\right) = \frac{\dot{\chi}}{d\chi}\left(i\Delta - \frac{\dot{\Omega}_\mathrm{r}}{\Omega_\mathrm{r}}\right) + \frac{\ddot{\chi}}{d\chi}, \tag{4.81}$$

with the initial conditions $c_B^{(1)}(-\infty) = \dot{c}_B^{(1)}(-\infty) = 0$. This is a differential equation that is rather difficult to solve with a general time dependent Rabi frequency, $\Omega_\mathrm{r}(t)$. However, there is an analytic solution for the Greens function of the homogeneous differential operator in the case of a Rabi frequency that decreases exponentially with time, $\Omega_\mathrm{r}(t) = \Omega_\mathrm{r} e^{-t/\tau}$. This laser intensity model should be fairly good for determining the effects of a polarization rotation in the weak field laser tail. In this case, we can derive the Π function as an integral over the analytic Green's function and the polarization rotation function,

$$\Pi = \int dt\, {}_0F_1\left(;\frac{3}{2} + i\frac{\Delta\tau}{2} + \frac{\gamma\tau}{4}; -\left(\frac{\Omega_\mathrm{r}\tau}{4}\right)^2 e^{-2t/\tau}\right)\frac{1}{d\chi}\left[\dot{\chi}(t) + \frac{\ddot{\chi}(t)\,\tau}{1 + i\Delta\tau + \frac{1}{2}\gamma\tau}\right] \tag{4.82}$$

$$\approx 1 - \frac{1}{24}\frac{(\Omega_\mathrm{r}\tau)^2}{1 + \frac{1}{3}i\Delta\tau + \frac{1}{6}\gamma\tau}\int dt\, e^{-2t/\tau}\frac{1}{d\chi}\left(\dot{\chi}(t) + \frac{\ddot{\chi}(t)}{1 + i\Delta\tau + \frac{1}{2}\gamma\tau}\right) + O(\Omega_\mathrm{r}\tau)^4 \tag{4.83}$$

where ${}_0F_1(;a;z)$ is a hypergeometric function. Performing an integral analytically over this hypergeometric function is probably not possible for must functions $\dot{\chi}(t)$ (except for the special case where $\dot{\chi}(t) = 2d\chi\, e^{-2t/\tau}/\tau$), but this integral reduces to a nice exponential integral in the limit of $\Omega_\mathrm{r}\tau \ll 1$ which can be analytically integrated over for all of our $\dot{\chi}(t)$ model functions shown in the bottom of figure 4.3.2. The resulting coefficients for these models corresponding the expansions in equations 4.76 and 4.78 are listed in table 4.3.2. Notice that the coefficients in the exponentially decreasing Rabi frequency model are of a similar order of magnitude to those from the class of models with a uniform Rabi frequency, and the effect of a polarization rotation that lasts for time that is comparable to or longer than the decay time of the laser leads to an exponential enhancement of the expansion coefficients.

In figure 4.3.2, we compare the functional form of the AC Stark shift phase factor $\Pi(\Delta, \Omega_\mathrm{r})$ for two fairly different models that we have considered, 1.) the model with a uniform Rabi frequency and constant polarization rotation rate is shown in blue and 2.) a model with an exponentially decreasing Rabi frequency an instantaneous polarization impulse, $\dot{\chi} = d\chi\delta(t)$ is shown in red. These plots show that the AC Stark shift phase model

does not qualitatively depend too much on the details of the spatial profile of $\dot{\chi}$ and Ω_r. These plots also show how the AC Stark shift phases oscillate and are slowly suppressed by improved optical pumping with larger $\Omega_r\tau$.

		Dirac Impulse	Gaussian Impulse	Constant
$\dot{\chi}(t) =$		$d\chi\delta(t)$	$\frac{d\chi}{\sqrt{2\pi T^2}}\exp\left(-\frac{1}{2}\frac{t^2}{T^2}\right)$	$\frac{d\chi}{T}\left(-\frac{T}{2}\leq t\leq\frac{T}{2}\right)$
$\Pi\approx$		${}_0F_1\left(;\frac{3}{2}+i\frac{\Delta\tau}{2}+\frac{\gamma\tau}{4};-\left(\frac{\Omega_r\tau}{4}\right)^2\right)$	$1-\frac{1}{24}\frac{(\Omega_r\tau)^2}{1+i\Delta\tau+\frac{\gamma\tau}{2}}e^{2\left(\frac{T}{\tau}\right)^2}$	$1-\frac{1}{24}\frac{(\Omega_r\tau)^2}{1+\frac{1}{3}i\Delta\tau+\frac{1}{6}\gamma\tau}\mathrm{sinch}\left(\frac{T}{\tau}\right)$
$\gamma\tau\ll1$	α_{02}	$-1/24$	$-(1/24)\,e^{2\left(\frac{T}{\tau}\right)^2}$	$-(1/24)\,\mathrm{sinch}\left(\frac{T}{\tau}\right)$
	α_{12}	$+1/72$	$+(1/24)\,e^{2\left(\frac{T}{\tau}\right)^2}$	$+(1/72)\,\mathrm{sinch}\left(\frac{T}{\tau}\right)$
	α_{22}	$-1/216$	$-(1/24)\,e^{2\left(\frac{T}{\tau}\right)^2}$	$-(1/216)\,\mathrm{sinch}\left(\frac{T}{\tau}\right)$
$\gamma\tau\gg1$	β_{02}	$-1/8$	$-(1/24)\,e^{2\left(\frac{T}{\tau}\right)^2}$	$-(1/8)\,\mathrm{sinch}\left(\frac{T}{\tau}\right)$
	β_{22}	$+3/8$	$+(1/24)\,e^{2\left(\frac{T}{\tau}\right)^2}$	$+(3/8)\,\mathrm{sinch}\left(\frac{T}{\tau}\right)$

Table 4.5: Analytic models for the A.C. Stark shift phase accumulation in the tail of the State Preparation laser, $\Delta\Phi_{\mathrm{prep}}\equiv d\chi\Pi$, in the case of an exponentially decreasing Rabi frequency, $\Omega_r(t)=\Omega_r e^{-t/\tau}$. The top shows the analytic expressions for the $\dot{\chi}(t)$ functions that are assumed and the Π functions that are derived. The bottom shows the expansion coefficients corresponding to the definitions in equation 4.76 for the Π functions in the limit that $\Omega_r\tau\ll1$ for both both $\gamma\tau\gg1$ and $\gamma\tau\ll1$ limits. Here, I am defining $\mathrm{sinch}(x)=\sinh(\mathrm{x})/\mathrm{x}$ in analog to the $\mathrm{sinc}(x)=\sin(x)/x$ function.

4.3.3 Sources of polarization gradients

Thermal stress-induced birefringence

The AC Stark shift phases described in the previous sections can be induced by polarization gradients in $\hat{x}$ across the state preparation and readout laser beams. In this section we describe a known mechanism by which these arose in ACME I. Recall that these laser beams passed through transparent, ITO-coated electric field plates. For an absorbance α and laser intensity I, the rate of heat deposition into the plates is $\dot{Q}(x,y)=\alpha\,I(x,y)$. The laser beam profile is stretched in the y direction to ensure that all molecules are addressed. For simplicity we assume that the heating distribution, $\dot{Q}(x,y)=\dot{Q}(x)$, is completely uniform in the y direction. We also assume that there are no shear stresses, i.e. local expansion of the glass is isotropic. Under these assumptions, the relationship between the heating rate, $\dot{Q}$, and the internal stress tensor σ_{ij} (where i,j are Cartesian indices) is

$$\frac{\partial^2\sigma_{yy}}{\partial x^2}=\frac{E\alpha_V}{\kappa}\dot{Q}(x)\,, \tag{4.84}$$

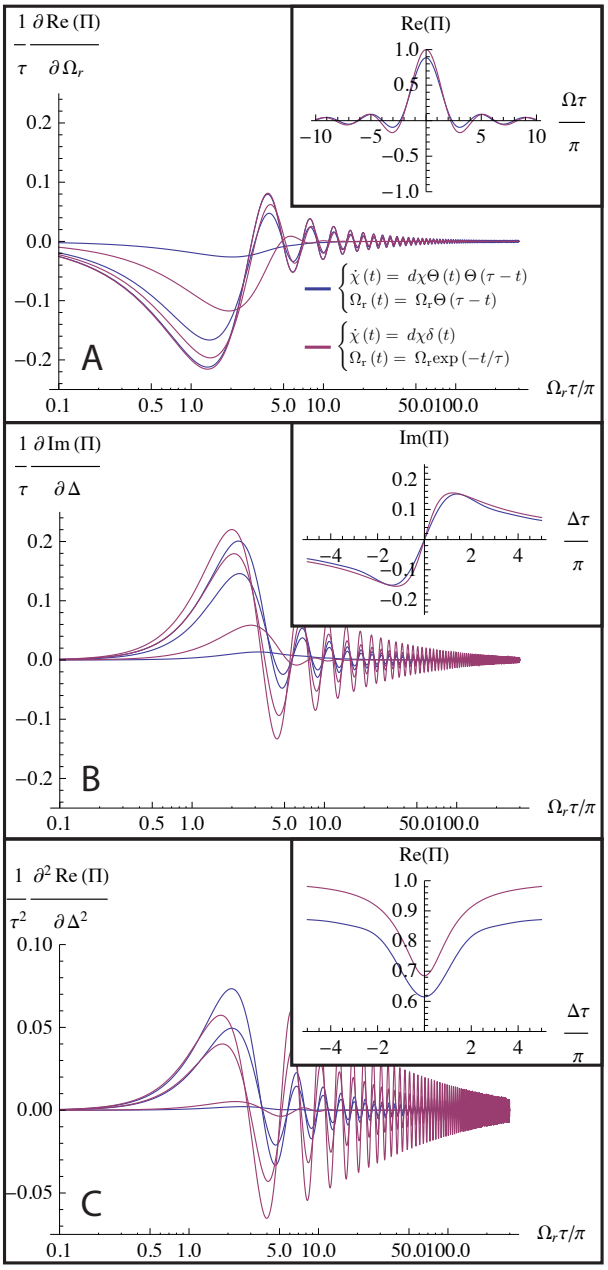

Figure 4.8: Illustration of the $\Pi(\Delta, \Omega)$ behavior for two of the analytic models considered in the text. In blue: A uniform Rabi frequency, $\Omega_r(t) = \Omega_r(t \leq \tau)$ and a constant polarization rotation rate, $\dot{\chi}(t) = (d\chi/\tau)(0 \leq t \leq \tau)$. In red: An exponentially decreasing Rabi frequency, $\Omega_r(t) = \Omega_r e^{-t/\tau}$ and an instantaneous polarization impulse, $\dot{\chi} = d\chi\delta(t)$. Each of the large plots has three curves of the same color which correspond to $\gamma\tau = .1, 1, 10$ with the curve of the largest magnitude corresponding to $\gamma\tau = .1$, and the curve of the smallest magnitude corresponding to $\gamma\tau = 10$. Each of small inset plots have a single curve of each color corresponding to $\gamma\tau = 1$ (and $\Omega_r\tau = \pi$ and $\Delta\tau = 0$ where when those parameters are not varied). The small insets show the behavior of the Π function, and the large plots show the behavior of derivatives of the Π function.

where E, α_V and κ are the Young's modulus, coefficient of thermal expansion, and thermal conductivity, respectively [12]. Unit vectors $\hat{x}$ and $\hat{y}$ correspond to the principal axes of the stress tensor due to the symmetry of the heating function, hence the off-diagonal (shear) elements are zero, $\sigma_{xy} = 0$, in this basis. The other diagonal component, σ_{xx}, is uniform across the plates, and equal to σ_{yy} far away from the laser. The stress-optical law states that the birefringence and stress are linearly proportional along the principal axes of the stress tensor [38]. The difference between the indices of refraction in the x and y directions is then $\Delta n = K(\sigma_{xx} - \sigma_{yy})$, where $K \approx 4 \times 10^{-6}\,\mathrm{MPa}^{-1}$ is the stress-optical coefficient for Borofloat glass [150]. The retardance of an incident laser beam of index i is $\Gamma_i = 2\pi\Delta n\,(t/\lambda)$, where t is the thickness of the field plates (in the z direction), and λ is the wavelength of light. Hence, in this limit, the retardance due to thermal stress-induced birefringence is related to the laser intensity by

$$\frac{\partial^2 \Gamma}{\partial x^2} = \eta \frac{t}{\lambda} I\,(x)\,, \tag{4.85}$$

where $\eta = 2\pi K E \alpha_V \alpha/\kappa \approx 26 \times 10^{-6}\ \mathrm{W}^{-1}$ is a material constant of Borofloat glass [150]. The ellipticity imprinted on the nominally linearly polarized laser beam is given by

$$S_i = \Gamma_i(x) \sin(2(\theta_i - \phi_{\Gamma,i})), \tag{4.86}$$

where θ_i is the linear polarization angle and $\phi_{\Gamma,i}$ is the orientation of the fast axis of the birefringent material (nominally $\hat{x}$ in our case).

Assuming the laser has total power P, a Gaussian profile in x with 1σ intensity with w_x, and a top-hat profile in y with half width w_y, the intensity is given by

$$I\,(x) = \frac{P}{\sqrt{8\pi} w_x w_y} e^{-\frac{x^2}{2w_x^2}} (-w_y \leq y \leq w_y), \tag{4.87}$$

where we assume that $2w_y \gg w_x$. There is then an analytic solution to equation 4.85 from which we extracted a retardance gradient in the laser tail, $x \approx w_x$, of

$$\frac{\partial \Gamma}{\partial x}\,(x = w_x) \approx \frac{\mathrm{erf}(1/\sqrt{2}) P \kappa t}{4 w_y \lambda} \approx 0.03\ \mathrm{rad/mm} \tag{4.88}$$

for a nominal laser power of ≈ 2 W. Similar results were obtained from numerical finite element analysis. Thermal stress-induced birefringence has been observed in similar systems such as in UHV vacuum windows [155], laser output windows [53], and Nd:YAG rods [95].

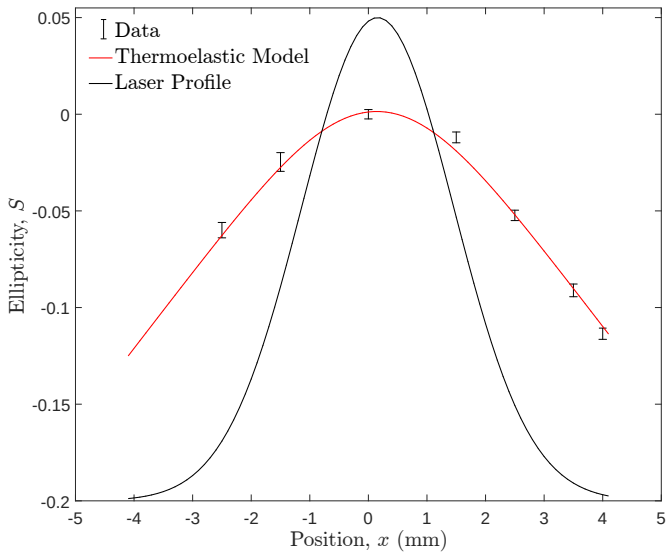

Figure 4.9: Measurement of the ellipticity, S, as a function of position along x within the state readout laser beam. A fit to the thermo-elastic model, which assumes a Gaussian laser profile and has the amplitude and offset in S as free parameters, is overlaid.

The estimates of the ellipticity gradient agree well with measurements of the polarization of the beam, as shown in figure 4.9. These polarimetry measurements were adapted from the procedure described in [19]; a polarimeter was constructed consisting of a rotating quarter-wave plate, fixed polarizer, and fast photodiode. The use of a fast photodetector allows for polarimetry of the probe beam during the 100 kHz polarization switching. The resolution of the system was such that we could quickly measure the normalized circular Stokes parameter, S, to a few percent, which is sufficient to measure typical birefringence gradients of $\sim 10\%$ across the beam. Additional details regarding the polarimetry that was done during ACME I can be found in reference [77].

A couple changes to the apparatus in ACME II to reduce the size of the thermal stress-induced birefringence have been implemented. We replaced the ACME I Borofloat electric field plates with 200 nm conductive ITO coating, with Corning 7980 electric field plates with 20 nm conductive ITO coating. The Corning 7980 has a $5\times$ smaller thermal expansion coefficient than Borofloat [37, 86, 150] and similar other material properties, resulting in a significant reduction in the thermal stress-induced birefringence in the bulk glass. Additionally, we believe that a significant fraction of the light absorbed by the electric field plates in ACME I was caused by the 200 nm ITO coating. We reduced the thickness of

this coating on the ACME II plates by a factor of 10× relative to ACME I to reduce the absorption of light by the electric field plates. Polarimetry that was performed on both sets of electric field plates with the same incident laser power, beam shape, and wavelength indicated that the thermal stress-birefringence is smaller by more than a factor of 10× in the ACME II electric field plates relative to the ACME I electric field plates [11]. Furthermore, we have changed out detection transition from the $H \rightarrow C$ to the $H \rightarrow I$, which has a much stronger transition electric dipole moment (see table 4.2.1) and hence requires much less laser power incident on the electric field plates. Whereas we used about 2 W of 1090 nm laser light incident on the electric field plates in ACME I, we plan to use up to around 100 mW of 703 laser light incident in the ACME II refinement and state read-out laser beams.

Guoy phase in a focused Gaussian laser beam

We were able to reduce the size of polarization gradients from technical effects such as those discussed in the previous section. However Maxwell's equations require that all Maxwell-Gaussian laser beams have polarization gradients [55, 62] at some level. Lets suppose that we have a Maxwell-Gaussian laser beam with nominal $\hat{x}$ polarization that is propagating in the $\hat{z}$ direction with Raleigh range z_R, such as the state preparation and state read-out laser beams in ACME I. The field strength for such a beam is

$$u\left(x,y,z\right) = \frac{1}{\sqrt{q_x\left(z\right)q_y\left(z\right)}}\exp\left(-\frac{1}{2}ik\left(\frac{x^2}{q_x\left(z\right)}+\frac{y^2}{q_y\left(z\right)}\right)\right), \tag{4.89}$$

where the complex beam parameters for the x and y directions are given by $q_i\left(z\right) = z + iz_{R,i}$ where $z_{R,i}$ is the Raleigh range for direction i. The Raleigh range is set by the width of the 1σ intensity width of the laser beam at the focus, w_i, given by $z_{R,i} = 2\pi w_i^2/\lambda$, where λ is the wavelength of the light and can be different for the two orthogonal transverse directions. The spatial profile of the amplitude for the electric field vector across this laser beam is then given by

$$\vec{\mathcal{E}} \propto u\left(x,y,z\right)\hat{x} + \frac{1}{2k^2}\frac{\partial^2 u}{\partial x \partial y}\hat{y} + i\frac{1}{k}\frac{\partial u}{\partial x}\hat{z}, \tag{4.90}$$

which results in a polarization structure given by

$$\hat{\epsilon} = \hat{x} - \frac{xy}{q_x(z)\, q_y(z)}\hat{y} + \frac{x}{q_x(z)}\hat{z}. \tag{4.91}$$

If the location of interaction between the molecules and the laser beam occurs at a position that is at the beam waist, $z \ll z_{R,i}$, then the polarization gradient at up to second order in quantities like $(r\lambda/w^2)$ is

$$\hat{\epsilon} \approx \hat{x} + \left(\frac{\lambda}{2\pi}\right)^2 \frac{xy}{w_x^2 w_y^2}\hat{y} - i\left(\frac{\lambda}{2\pi}\right)\frac{x}{w_x^2}\left(1 - \frac{\lambda z}{2\pi w_x^2}\right)\hat{z} + \ldots \tag{4.92}$$

For laser beam parameters like those used for state preparation and state readout in ACME I, $\lambda = 1090\,\text{nm}$, $w_y \sim 1\,\text{cm}$, $w_x \sim 2\,\text{mm}$, there is a linear polarization rotation in the xy plane that varies across the molecule beam in the y direction,

$$\frac{\partial\theta}{\partial x} \approx \left(\frac{\lambda}{2\pi}\right)^2 \frac{y}{w_x^2 w_y^2} \sim 10^{-9}\left(\frac{\text{rad}}{\text{mm}}\right)\left(\frac{y}{\text{cm}}\right), \tag{4.93}$$

which is incredibly small and would not have significantly contributed to the AC Stark shift phases that we observed in ACME I.

On the other hand, in ACME II, we have implemented highly focused STIRAP laser beams with which we can perform state preparation, and these have a laser propagation direction along $\hat{y}$ instead of $\hat{z}$. Hence in the STIRAP $H \to C$ laser, with $\lambda = 1090\,\text{nm}$, $w_x \approx 150\,\mu\text{m}$, $w_y \approx 2\,\text{cm}$, we would expect polarization gradients in the xy plane given approximately by

$$\frac{\partial\Theta}{\partial x} \approx \frac{\lambda}{2\pi w_x^2} \approx 8\,\frac{\text{mrad}}{\text{mm}} \tag{4.94}$$

$$\frac{\partial\theta}{\partial x} \approx \left(\frac{\lambda}{2\pi}\right)^2 \frac{y}{w_x^4} \approx .5\,\left(\frac{\text{mrad}}{\text{mm}}\right)\left(\frac{y}{\text{cm}}\right). \tag{4.95}$$

which are larger than any polarization gradients that we observed in ACME I and could generate substantial AC Stark shift phases. This is one of the reasons that we decided to implement the refinement beam in ACME II which reprojects the spin state to remove variations in the spin state that is prepared by the STIRAP beams.

4.3.4 AC Stark shift phases from polarization switching

In the discussion above we have considered various effects that can modify the molecule state and then ideal perfect read-out of the spin angle of that state as described in section 4.1.1. However, there are a number of observable effects in the experiment that result from deviations from ideal in the state read-out laser beams that cannot be analyzed in this way. The state read-out scheme consists of two nominally linearly polarized laser beams with orthogonal polarizations $\hat{\epsilon}_X$ and $\hat{\epsilon}_Y$ that have the same spatial intensity profile, laser power, and laser pointing. These lasers alternate in addressing the molecules by rapidly turning these laser beams on and off with AOMs. A particular molecule arriving in the detection region may first see that the $\hat{\epsilon}_X$ laser beam is turned on for a time $t = 3.8\,\mu s$ during which optical pumping occurs, then both lasers are kept off for a dead-time of $\delta t = 1.2\,\mu s$ during which population remaining in the excited state decays away, and then the $\hat{\epsilon}_Y$ laser beam is turned on for a time t during which optical pumping of the molecule state is for the most part completed, followed by another dead-time of duration δt. This pulse train continues indefinitely and depending on the time of arrival of molecules in the detection region they have approximately equal likelihood of encountering an $\hat{\epsilon}_X$ or $\hat{\epsilon}_Y$ pulse first. This polarization switching read-out scheme serves to normalize the measurement to molecule number fluctuations and to boost the signal size by a factor of 2 relative to an alternative measurement scheme in which only one of these lasers is used.

This polarization switching read-out scheme can also introduce AC Stark shift phases in the absence of a polarization gradient, if the two read-out polarizations are not quite orthogonal. In particular suppose a molecule is first optically pumped by the $\hat{\epsilon}_X$ beam – the projection of the input state onto the bright eigenstate is mostly optically pumped away resulting in a fluorescence signal F_X and the remaining bright amplitude acquires a phase due to the A.C. Stark shift. Then the molecules are then optically pumped by the $\hat{\epsilon}_Y$ beam. If $\hat{\epsilon}_Y$ is not quite orthogonal to $\hat{\epsilon}_X$, then the new bright eigenstate that is optically pumped away, resulting in fluorescence signal F_Y, is a superposition of the former bright and dark states that acquired a relative AC Stark shift phase. In this section, we work out a simple analytic model to describe this phenomenon.

The initial state that is prepared by the state preparation laser is $|\psi(t=0)\rangle = |D(\hat{\epsilon}_p), \tilde{\mathcal{N}}, \tilde{\mathcal{P}}\rangle \equiv |D_p\rangle$. After entering into the $\hat{\epsilon}_X$ polarized state readout beam in the state readout region,

with bright and dark states $|B_X\rangle, |D_X\rangle$, the laser turns on non-adiabatically and the projection of the initial state onto the bright state undergoes optical pumping for a time t. The laser then turns off non-adiabatically, and during a dead-time period of duration δt, the population in the excited state decays away out of the three level system leaving behind the state

$$|\psi\left(t=\tau+\delta\tau\right)\rangle \approx \langle D_X|D_p\rangle|D_X\rangle + \Pi_X\langle B_X|D_p\rangle|B_X\rangle, \tag{4.96}$$

where $\Pi_X = \sum_{X\pm}(\kappa_{X\mp})^2 e^{-iE_{BX\pm}t}$ is an optical pumping factor. Then, the process repeats, but this time with a different laser with $\hat{\epsilon}_Y$ polarization. To a reasonable approximation, assuming that optical pumping goes nearly to completion during each of the two optical pumping pulses, the laser induced fluorescence that is detected during the $\hat{\epsilon}_i$ polarized laser pulse is proportional to the square of the projection of the bright state onto the state that enters the optical pumping beam,

$$\begin{aligned}
F_X \approx& |\langle B_X|\psi(t=0)\rangle|^2 && (4.97)\\
\approx& |\langle B_X|D_p\rangle|^2 && (4.98)\\
F_Y \approx& |\langle B_Y|\psi(t=\tau+\delta t)\rangle|^2 && (4.99)\\
\approx& |\langle D_X|D_p\rangle\langle B_Y|D_X\rangle|^2 + 2\mathrm{Re}\left[\Pi_X\langle D_p|D_X\rangle\langle D_X|B_Y\rangle\langle B_Y|B_X\rangle\langle B_X|D_p\rangle\right]. && (4.100)
\end{aligned}$$

Since molecules have an equal chance of seeing either the $\hat{\epsilon}_X$ or $\hat{\epsilon}_Y$ pulses first, then we can obtain a better approximation to the measured signal by symmetrizing the signals in this regard (e.g. $F_X\left(X,Y\right) \rightarrow F_X\left(X,Y\right) + F_Y\left(Y,X\right)$),

$$F_X \approx \frac{1}{2}\left\{|\langle B_X|D_p\rangle|^2 + |\langle D_Y|D_p\rangle\langle B_X|D_Y\rangle|^2 + 2\mathrm{Re}\left[\Pi\langle D_p|D_Y\rangle\langle D_Y|B_X\rangle\langle B_X|B_Y\rangle\langle B_Y|D_p\rangle\right]\right\} \tag{4.101}$$

$$F_Y \approx \frac{1}{2}\left\{|\langle B_Y|D_p\rangle|^2 + |\langle D_X|D_p\rangle\langle B_Y|D_X\rangle|^2 + 2\mathrm{Re}\left[\Pi\langle D_p|D_X\rangle\langle D_X|B_Y\rangle\langle B_Y|B_X\rangle\langle B_X|D_p\rangle\right]\right\}, \tag{4.102}$$

where I have made the approximation that $\Pi = \Pi_X \approx \Pi_Y$.

In actuality, the molecules see varying pulse durations depending on when they enter the laser beam with respect to the pulse sequence, the molecules see different Rabi frequencies

since the spatial intensity profile of the laser beams is not flat, and the detunings are significantly different amongst the molecules due to the transverse Doppler shift. In a more realistic model of the AC Stark shifts, we might want to average over probability distributions for each of these parameters to extract F_X and F_Y. However, for our purposes, the expressions above should be sufficient for extracting the general behavior of this AC Stark shift phase.

In data analysis we construct the asymmetry, $\mathcal{A} = (F_X - F_Y)/(F_X + F_Y)$, and then we measure the sensitivity of the measurement to phase, $\mathcal{C} = -(1/2)\partial\mathcal{A}/\partial\theta_{\text{read}}$, and extract the measured phase, $\Phi = \mathcal{A}/2\mathcal{C}$ under conditions in which state preparation laser polarization is at about 45 degrees with respect to the readout polarization. In this case the measured phase is approximately,

$$\Phi \approx d\theta_{\text{prep}} - \frac{1}{2}\left(d\theta_X + d\theta_Y\right) - \lambda^2\tilde{\mathcal{P}}d\Theta_{\text{prep}}\left(d\Theta_X - d\Theta_Y\right) \tag{4.103}$$

$$+ \text{Im}(\Pi)\frac{1}{2}\left(d\Theta_X + d\Theta_Y\right) + \tilde{\mathcal{P}}\text{Im}(\Pi)d\Theta_{\text{prep}}\left(d\theta_X - d\theta_Y\right) + \ldots, \tag{4.104}$$

and the contrast is

$$\mathcal{C} = \tilde{\mathcal{P}}\left[1 + \tilde{\mathcal{P}}\lambda\text{Re}(\Pi)\left(d\phi_X - d\phi_Y\right) - \lambda^2\left(2d\Theta_{\text{prep}}^2 + d\Theta_X^2 + d\Theta_Y^2 + \ldots\right) + \ldots\right], \tag{4.105}$$

where I defined $\tilde{\mathcal{P}} \equiv \tilde{\mathcal{P}}_{\text{prep}}\tilde{\mathcal{P}}_{\text{read}}$ is the relative parity of the excited states that are used to prepare and read-out the state. This indicates that the AC Stark shift phase factor $\text{Im}\,(\Pi)$ contributes to the measured phase Φ when the two readout laser polarizations are not orthogonal, coupling either to the average ellipticity between the two beams, $d\Theta_X + d\Theta_Y$, or the deviation in the difference in the linear polarization angles from $\pi/2$, $d\theta_X - d\theta_Y$. Just as the AC Stark shift phase factors in the section 4.3.1, $\text{Im}\Pi$ is of order unity across resonance and is linearly proportional to detuning, Δ. Note that $\text{Re}\Pi$ does not contribute to the measured phase, but rather enters into the contrast. This means that although this effect can contribute to the $\mathcal{E}^{\text{nr}}$ systematic error, it does not contribute to the $\Omega_{\text{r}}^{\mathcal{NE}}$ systematic error. Note that if we did not make the assumption that the population in the excited state decays away entirely during the dead-time, then we can obtain an additional AC Stark shift phase term which couples to input state ellipticity [122].

4.3.5 Refinement beam suppression and phases

As previously discussed in sections 4.2.1 and 4.3.3, we anticipate that the AC Stark shift phases and the effect of Stark interference could have a larger effect in the STIRAP state preparation beams in ACME II compared to those effects in the state preparation or state read-out beams present in ACME I. For that reason, in ACME II we decided to add an optical pumping beam called the *refinement beam*, which serves to reproject the molecule state immediately after STIRAP state preparation and serves a similar role to state preparation laser that was present in ACME I – provided that the suppression of input state imperfections is great enough, then the systematic errors that are caused in the refinement beam in ACME II should be equivalent to the systematic errors caused in the state preparation beam in ACME I. In this section, we derive an analytic expression for the refinement beam suppression factor in a simplified system and show that if the refinement beam does not drive optical pumping to completion and the suppression factor is poor, then the refinement beam serves as a new source of AC Stark shift phases. We also show some experimental data that was taken immediately following ACME I in which we demonstrate reprojection of a spin state misalignment.

After the molecules leave the STIRAP laser beam, the molecules are prepared in the state $|D_s\rangle = |D(\hat{\epsilon}_s), \tilde{\mathcal{N}}, \tilde{\mathcal{P}}\rangle$ which is equivalent to the state that would have been prepared in ACME I using a state preparation laser polarization $\hat{\epsilon}_s$[7]. We approximate the refinement laser as a square optical pumping pulse of Rabi frequency Ω_r and duration t, which is amenable to simple analytical calculations. The molecule state evolves in this laser pulse to the state $|D'_r\rangle = |D(\hat{\epsilon}'_r)\rangle$ where $\hat{\epsilon}'_r$ is the effective polarization of the refinement beam which is equivalent to the actual polarization in the case of perfect input state reprojection, and where $|D_r\rangle = |D(\hat{\epsilon}_r)\rangle$ and $|B_r\rangle = |B(\hat{\epsilon}_r)\rangle$ are the dark/bright state eigenstates in the refinement beam with actual polarization $\hat{\epsilon}_r$. The molecule state is assumed to undergo non-adiabatic transfer into the refinement beam, undergoes optical pumping, and then exits the laser beam non-adiabatically. The remaining population in the excited state decays out of

7. If the polarization of the $H \rightarrow C$ STIRAP laser is $\hat{\epsilon}_\mathrm{STIRAP}$, then the prepared state is approximately $|B(\hat{\epsilon}_\mathrm{STIRAP})\rangle = |D(\hat{z} \times \hat{\epsilon}^*_{STIRAP})\rangle$, so the equivalent polarization that I defined is related to the actual polarization by $\hat{\epsilon}_s = \hat{z} \times \hat{\epsilon}^*_\mathrm{STIRAP}$.

the three level system, leaving behind the state

$$|D(\hat{\epsilon}_r')\rangle \approx \langle D_r|D_s\rangle \left\{ |D_r\rangle + \Pi \frac{\langle B_r|D_s\rangle}{\langle D_r|D_s\rangle} |B_r\rangle \right\}, \tag{4.106}$$

where Π is a factor that depends on the details of the time evolution of the optical pumping, and in this simple case,

$$\Pi = \sum_{\pm} (\kappa_{\mp})^2 e^{-iE_{B\pm}t}. \tag{4.107}$$

The effective polarization $\hat{\epsilon}_r'$ deviates from $\hat{\epsilon}_r$ by the misalignment between $\hat{\epsilon}_r$ and $\hat{\epsilon}_s$, suppressed by the complex optical pumping factor Π,

$$\hat{\epsilon}_r' = \hat{\epsilon}_r + \Pi \left[\frac{\hat{z} \cdot (\hat{\epsilon}_r \times \hat{\epsilon}_s)}{\hat{\epsilon}_r^* \cdot \hat{\epsilon}_s} \right] \hat{z} \times \hat{\epsilon}_r^*. \tag{4.108}$$

If we assume that $\hat{\epsilon}_p$ and $\hat{\epsilon}_s$ are linearly polarized and in the xy plane, but can deviate slightly from each other by their angles in the xy plane, then we can reasonably define a suppression factor A of the misalignment angle of the initial state given by the ratio of the misalignment angle between $\hat{\epsilon}_r'$ and $\hat{\epsilon}_r$ over the misalignment angle between $\hat{\epsilon}_s$ and $\hat{\epsilon}_r$,

$$A = \mathrm{Re}\left[\frac{\hat{z} \cdot (\hat{\epsilon}_r' \times \hat{\epsilon}_r)}{\hat{\epsilon}_r' \cdot \hat{\epsilon}_r} \right] / \mathrm{Re}\left[\frac{z \cdot (\hat{\epsilon}_s \times \hat{\epsilon}_r)}{\hat{\epsilon}_r \cdot \hat{\epsilon}_r} \right] \approx \mathrm{Re}\left[\Pi\right]. \tag{4.109}$$

Additionally, the refinement beam contributes AC Stark shift phases if the optical pumping is not driven to completion, given by

$$d\theta_r' - i d\Theta_r' = \Pi \left[(d\theta_s - d\theta_r) - i(d\Theta_s - d\Theta_r) \right]. \tag{4.110}$$

Note that these AC Stark shift phases provide expressions that are nearly equivalent to those derived in equations 4.69 and 4.70 in the case where we analyzed the effects of a continuously rotating polarization. The way in which we treated this problem is nearly equivalent to a rapid polarization rotation in the middle of a single optical pumping pulse. Also, note that the molecule state may undergo Zeeman precession between the STIRAP and refinement lasers and so we may require a different refinement laser polarization to be

set for each magnetic field value at which we operate the experiment in order to minimize the effect of AC Stark shift phases. Note that this means that we will likely want intentionally correlate the refinement beam polarization with $\tilde{\mathcal{B}}$, which will result in a systematic error in the measurement of the overall Zeeman precession frequency.

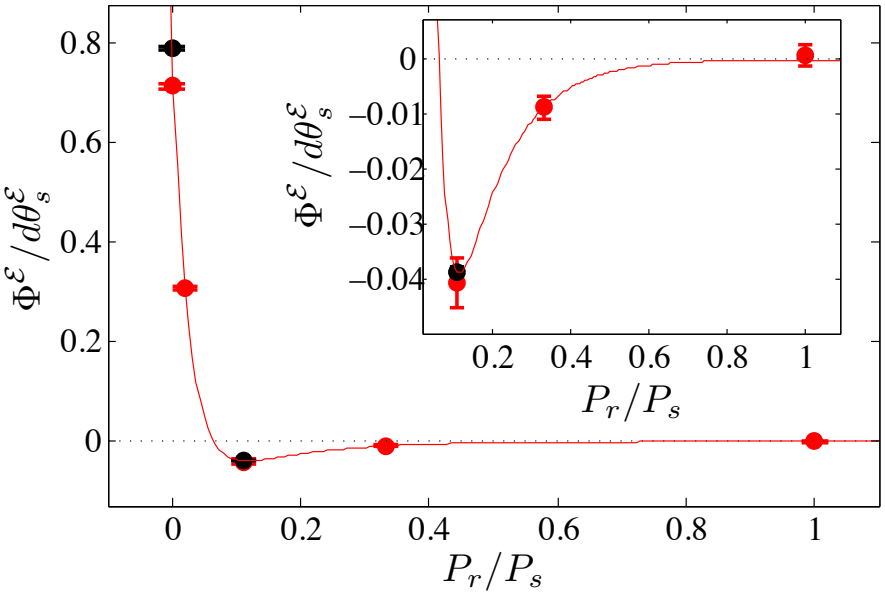

Figure 4.10: Demonstration of suppression of molecule state imperfections by optical pumping with a refinement beam. We measured the suppression factor A of an intentionally applied $d\theta_s^{\mathcal{E}}$ by looking at the ratio $A = \Phi^{\mathcal{E}}/d\theta_s^{\mathcal{E}}$. We observe that as we increase the power of the clean-up beam, the attenuation factor changes sign, and appears to approach zero from below as the power in the clean-up beam increases. For equal powers in the state preparation and clean-up beams, we were able to put an upper limit of about $A < 1/300$ on observed the attenuation factor, which is consistent with zero. The red lines is a fit to the data consisting of the sum of two exponential functions which was empirically motivated. The red points were taken with $d\theta_s^{\mathcal{E}} \approx 35$ mrad, and the black points were taken with $d\theta_s^{\mathcal{E}} \approx 105$ mrad.

Immediately after the ACME I experiment, we performed a test to ensure that we could achieve reasonable suppression of a spin state misalignment using a refinement beam. In this test, we split the state preparation beam into two beam paths using a half-wave plate followed by a polarizing beamsplitter so that we could control the fraction of power appropriated to each laser beam. The upstream beam performed state preparation that was equivalent to ACME I, except a half waveplate was placed in the beam path enabling us to apply an intentional correlated spin state misalignment, $d\theta_s^{\mathcal{E}}$. We chose to correlate the misalignment with $\tilde{\mathcal{E}}$ solely because the measurement channel $\omega^{\mathcal{E}}$ did not have any detected

background facilitating a high signal to noise measurement. The downstream beam played the role of the refinement beam. Both of these lasers had widths in the x direction of about $\delta x = 5\,\mathrm{mm}$, were separated by about 1 cm and were stretched in the y direction by about 1.5 cm. The maximum intensity, achieved when all of the power was in one of the beams, was about $4\,\mathrm{W/cm^2}$.

We then performed the spin precession measurement while varying the fraction of power allocated to the state preparation beam and the refinement beam. We observed that as we increased the laser power in the refinement beam, the measured suppression factor of the initial misalignment, $A = \Phi^{\mathcal{E}}/d\theta_s^{\mathcal{E}}$, decreased, then crossed zero, and then approached zero from the negative side, as displayed in figure 4.3.5. The reversal of sign of the suppression factor A with increasing power is a signature of the AC Stark shift phase in the refinement beam. When the refinement beam is weak, the misaligned component of the molecule state undergoes Rabi flopping which can result in a reversal of the sign of that state component relative to the aligned component as observed in the experiment.

4.3.6 Asymmetry effects

In addition to the dependence of the measured phase on laser detuning and Rabi frequency, we observed dependence of the asymmetry $\mathcal{A}$ (as defined in section 2.3.1) on the laser parameters Δ_{read} and $\Omega_{\mathrm{r,read}}$, due to differences between the properties of the X and Y readout laser beams. The laser-induced fluorescence signal $F(\Delta, \Omega_{\mathrm{r}})$ varies quadratically with detuning (for small detuning) and linearly with Rabi frequency. Under normal conditions, the signal sizes from X and Y are comparable, $F_X \approx F_Y \approx F$. If the X and Y beams have different wavevectors, $\vec{k}_{X,Y} = \vec{k}^{\mathrm{nr}} \pm \vec{k}^{XY}$, and $\vec{k}^{XY}$ has some component along $\hat{x}$, then the two beams will acquire different Doppler shifts. This leads to a linear dependence of the asymmetry on detuning, which in turn can couple to $\Delta^{\mathcal{NE}}$ to result in a contribution to $\mathcal{A}^{\mathcal{NE}}$,

$$\mathcal{A}^{\mathcal{NE}} \approx \frac{1}{F}\frac{\partial^2 F}{\partial \Delta_{\mathrm{read}}^2}(\vec{k}^{XY} \cdot \langle \vec{v} \rangle)\Delta^{\mathcal{NE}}. \tag{4.111}$$

Similarly, if the two readout beams differ in Rabi frequency, $\Omega_{r,X/Y} \approx \Omega_{\mathrm{r}}^{\mathrm{nr}} \pm \Omega_{\mathrm{r}}^{XY}$, the asymmetry becomes linearly dependent on Rabi frequency, which in turn can couple to

$\Omega_{\mathrm{r}}^{\mathcal{NE}}$ to result in a contribution to $\mathcal{A}^{\mathcal{NE}}$,

$$\mathcal{A}^{\mathcal{NE}} \approx -\left(\frac{1}{F}\frac{\partial F}{\partial \Omega_{\mathrm{r}}}\right)^2 \Omega_{\mathrm{r}}^{XY}\Omega_{\mathrm{r}}^{\mathcal{NE}}. \tag{4.112}$$

However, these asymmetry effects are very distinguishable from spin precession phases and polarization misalignments. Since the $\tilde{\mathcal{P}}$ and $\tilde{\mathcal{R}}$ switches effectively swap the role of the X and Y readout beams, the $\mathcal{A}^{\mathcal{NE}}$ effects described above do not contribute to $\omega^{\mathcal{NE}}$ when averaged over these switches. Additionally, asymmetry effects, once converted to an equivalent frequency or phase, depend on the sign of the contrast, $\mathcal{C}$, unlike true phases. In the $\mathcal{B}_z \approx 20$ mG configuration, $\mathrm{sgn}(\mathcal{C}) = \mathrm{sgn}(\mathcal{B}_z)$, but $\mathrm{sgn}(\mathcal{C})$ is independent of $\mathrm{sgn}(\mathcal{B}_z)$ for $\mathcal{B}_z \approx 1,\ 40$ mG. Hence asymmetry correlations $\mathcal{A}^{\mathcal{NE}}$ are mapped onto frequency correlations $\omega^{\mathcal{NEPR}}$ or $\omega^{\mathcal{NEBPR}}$ depending on the magnetic field magnitude.

If the pointing or Rabi frequency differences between the X and Y beams drift on timescales comparable to or shorter than the $\tilde{\mathcal{P}}$ or $\tilde{\mathcal{R}}$ switches, these effects can occasionally "leak" into the "adjacent" channels $\omega^{\mathcal{NEP}}$, $\omega^{\mathcal{NER}}$, $\omega^{\mathcal{NEBP}}$, $\omega^{\mathcal{NEBR}}$; however, we have not seen any evidence of these effects contributing to the $\omega^{\mathcal{NE}}$ channel itself, and hence did not include systematic error contributions due to these effects in our systematic error budget in ACME I.

A simple and frequently useful model of the optical pumping lineshape $F(\Delta, \Omega_{\mathrm{r}})$ is to consider the bright and excited states as a two level system which is driven by a flat laser pulse with Rabi frequency Ω_{r}, detuning Δ, and duration t. In this case, the optical pumping lineshape takes the form

$$F(\Delta, \Omega_{\mathrm{r}}) = 1 - |\sum_{\pm} (\kappa_{\mp})^2 e^{-iE_{B\pm}t}|^2. \tag{4.113}$$

This lineshape can be convolved with the distribution of Doppler shifts to obtain a more realistic shape, or the Schrodinger equation or Master equation may be integrated with a more realistic spatial intensity profile of the lasers and those numeral solutions may be convolved with the distribution of Doppler shifts to obtain an even more realistic optical pumping lineshape. However, equation 4.113 provides a very convenient analytic expression for modeling the lineshape.

4.4 Zeeman spin precession

4.4.1 Static electric and magnetic fields

The Zeeman shifts $\Delta E(M,\tilde{\mathcal{N}})$ imparted on the state $|H, J=1, M, \tilde{\mathcal{N}}\rangle$ can be fairly well described by the following effects that have been well studied:

- Assuming that the molecule is fully aligned by an applied electric field, $\Delta_{H,J=1} \ll D_{H,J=1}\mathcal{E} \ll B_{R,H}$, the magnetic field along the electric field axis, $\mathcal{B}_z$ can contribute to a linear Zeeman shift. The H state of ThO is nearly entirely described by the $^3\Delta_1$ spin orbit term for which the g-factor contributions from the spin and orbital angular momenta nearly perfectly cancel. The residual $g-$factor in $|H, J=1, M, \tilde{\mathcal{N}}\rangle$ has been measured to be about $g_{H,J=1} = .0044 \pm .0001$ [93, 164, 166] .

- The Zeeman interaction is modified by first order rotational Stark mixing which depends on the molecule orientation, $\tilde{\mathcal{N}}$ [70, 71]. Measurements that we performed in ACME I, described in reference [135], revealed that the spin-uncoupling interaction leads to an admixture of $^3\Delta_2$ character in $|H, J=2, M, \tilde{\mathcal{N}}\rangle$ that contributes significantly to this effect due to the relatively large $^3\Delta_2$ g-factor, despite the small mixing coefficient. This effect is described by an electric field dependent $g-$factor, $\eta_{H,J=1} = -0.79 \pm .01\,\mathrm{nm/V}$.

- Magnetic fields transverse the axis of the applied electric field, $\mathcal{B}_\perp$, can also contribute to the energy shifts in $|H, J=1, M, \tilde{\mathcal{N}}\rangle$. However, this effect enters in second order in perturbation theory suppressed by the relatively large Stark shift. Additionally, the transverse magnetic fields only contribute to the relative Zeeman shift between the $M = \pm 1$ levels if there is also a magnetic field component along the electric field axis, $\mathcal{B}_z$.

These three effects contribute to the Zeeman energy shifts $\Delta E(M,\tilde{\mathcal{N}})$ to the state $|H, J=1, M, \tilde{\mathcal{N}}\rangle$ (where I have dropped terms that do not depend on the sign of M),

$$\Delta E(M,\tilde{\mathcal{N}}) = -M\mu_B g_{H,J=1}\tilde{\mathcal{B}}\mathcal{B}_z \left\{1 + \tilde{\mathcal{N}}\frac{\eta_{H,J=1}}{g_{H,J=1}}|\mathcal{E}| - \frac{1}{2}\left(\frac{\mu_B g_{H,J=1}\mathcal{B}_\perp}{D_{H,J=1}\mathcal{E}}\right)^2 + \dots\right\}, \tag{4.114}$$

which can lead to contributions to the $\omega^{\mathcal{NE}}$ and $\omega^{\mathcal{E}}$ spin precession frequency measurements,

$$\begin{aligned} \omega^{\mathcal{NE}} &= -\mu_B \eta_{H,J=1} \left(\mathcal{E}^{\mathrm{nr}} \mathcal{B}_z^{\mathrm{nr}} + |\mathcal{E}| \mathcal{B}_z^{\mathcal{E}} \right) \\ \omega^{\mathcal{E}} &= -\mu_B g_{H,J=1} \mathcal{B}_z^{\mathcal{E}}. \end{aligned} \tag{4.115}$$

The first systematic error term in $\omega^{\mathcal{NE}}$ above is well below the resolution of ACME I or ACME II, contributing to phase accumulation of around 5×10^{-11} rad, assuming $\mathcal{B}_z^{\mathrm{nr}} \sim .1\,\mathrm{mG}$, $\mathcal{E}^{\mathrm{nr}} \sim 10\,\mathrm{mV/cm}$, $\tau \approx 1\,\mathrm{ms}$, and is accounted for when we characterize systematic errors proportional to $\mathcal{B}^{\mathrm{nr}}$ and $\mathcal{E}^{\mathrm{nr}}$.

The second term requires the existence of a component of the magnetic field that molecules experience that is correlated with the applied electric field, $\mathcal{B}^{\mathcal{E}}$. Such a quantity can arise due to the motional magnetic field due to the molecule moving through applied electric field, $\mathcal{B}_{\perp}^{\vec{\mathcal{E}}} = \vec{v} \times \vec{\mathcal{E}} \approx .3\,\mu\mathrm{G}\,\hat{y}$. However, this quantity is strictly orthogonal to the electric field and hence contributions to the overall Zeeman shift are highly suppressed by the relatively large Stark shift. A $\mathcal{B}_z^{\mathcal{E}}$ can also arise due to leakage current between the two electric field plates, if this current changes with the reversal of the electric field. Such leakage currents measured in ACME I were very small, around 1.2 pA [158], capable of generating $\mathcal{B}_z^{\mathcal{E}} \lesssim 1\,\mathrm{pG}$. Regardless of the source of a $\mathcal{B}_z^{\mathcal{E}}$, it should contribute to Zeeman spin precession in the $\omega^{\mathcal{E}}$ measurement at a level that is a factor of $g_{H,J=1}/\eta_{H,J=1}\,|\mathcal{E}| \approx 10^2 - 10^3$ times larger than the contribution to the $\omega^{\mathcal{NE}}$ measurement. Hence the systematic error can be precisely characterized using the measurement of $\omega^{\mathcal{E}}$ and can be subtracted from the from the EDM measurement channel, $\omega^{\mathcal{NE}}$.

4.4.2 Time varying electric and magnetic fields

Just as static electric and magnetic fields can lead to Stark and Zeeman shifts as discussed in the previous section, oscillatory electric and magnetic fields can also contribute to time average energy shifts, commonly referred to as AC Stark and AC Zeeman shifts. These effects are completely analogous to the static effects, described in the previous section, in a rotating reference frame. These effects, also referred to as *geometric phases,* are also documented in references [134,163,164], but I have included this discussion for completeness of this systematic error model compilation.

Lets suppose that a system is described by the sum of a time dependent and time

independent Hamiltonian, $H = H_0 + H_1(t)$, and states $|a\rangle$ and $|b\rangle$ are eigenstates of H_0 with energies E_a and E_b respectively. $H_1(t)$ can couple these two states and is purely oscillatory such that the matrix element can take the form $\langle b|H_1(t)|a\rangle = h_{ba}e^{-i\omega t}$. Assuming that ω is far off resonant with the transition $\Delta_{ba} = E_b - E_a$, then the state $|a\rangle$ time evolves to state $|\tilde{a}\rangle$ which is given at first order in perturbation theory by

$$|\tilde{a}\rangle = |a\rangle - ie^{-i\Delta_{ba}t}|b\rangle \int_0^t h_{ba}e^{+i(\Delta_{ba}-\omega)t'}dt', \tag{4.116}$$

resulting in a first order energy shift of this state $|a\rangle$ due to $H_1(t)$ given by

$$\langle a|H_1(t)|\tilde{a}\rangle \approx -\frac{|h_{ba}|^2}{\Delta_{ba}-\omega} + O\left(e^{i\omega t}\right). \tag{4.117}$$

Here, we are neglecting oscillatory terms that may average out over the phase measurement if the duration of the phase measurement is long compared to the period of oscillation, $\omega\tau \gg 1$.

Given the result in equation 4.117, we may evaluate the energy shift due to different types of oscillating fields on the states $|H, J=1, M, \tilde{\mathcal{N}}\rangle$ in which we perform the spin precession measurement. Lets first consider a rather perverse scenario in which there are components of the electric and magnetic field that are parallel with each other, perpendicular to the applied static electric field, and rotating with the same frequency in phase. This scenario is described by the Stark and Zeeman interactions in the time dependent Hamiltonian,

$$H_1(t) = -\left(D\cdot\mathcal{E}_\perp + \mu\cdot\mathcal{B}_\perp\right)\left(\hat{x}\cos\omega t + \hat{y}\sin\omega t\right) \tag{4.118}$$

$$= \frac{1}{\sqrt{2}}\left(D\cdot\mathcal{E}_\perp + \mu\cdot\mathcal{B}_\perp\right)\sum_{q=\pm1} q\hat{\epsilon}_q e^{-iq\omega t} \tag{4.119}$$

This Hamiltonian couples the states $|H, J=1, M, \tilde{\mathcal{N}}\rangle$ with the $|H, J=1, M=0, \tilde{\mathcal{P}}\rangle$ states with matrix element

$$\left\langle H, J=1, M, \tilde{\mathcal{N}}\right|H_1(t)\left|H, J=1, M=0, \tilde{\mathcal{P}}\right\rangle = \frac{1}{4}\left(\delta_{\Omega+} - \tilde{\mathcal{P}}\delta_{\Omega-}\right)\left(\Omega D_H\mathcal{E}_\perp + \mu_H\mathcal{B}_\perp\right)e^{+iM\omega t}, \tag{4.120}$$

where $\Omega = M\tilde{\mathcal{N}}\tilde{\mathcal{E}}$ as usual. Following equation 4.117, and summing over the interactions with both $\tilde{\mathcal{P}} = \pm1$ states, the energy shift due to these oscillating fields, $\omega_{\mathrm{AC}}(M, \tilde{\mathcal{N}})$ in the

state $|H, J = 1, M, \tilde{\mathcal{N}}\rangle$ is approximately,

$$\omega_{\mathrm{AC}}(M, \tilde{\mathcal{N}}) \approx \frac{1}{4} \frac{(D_H \mathcal{E}_\perp)^2 + 2M\tilde{\mathcal{N}}\tilde{\mathcal{E}} D_H \mathcal{E}_\perp \mu_H \mathcal{B}_\perp + (\mu_H \mathcal{B}_\perp)^2}{\tilde{\mathcal{N}} D_H |\mathcal{E}| + M(\mu_H \mathcal{B}_z - \omega)}. \tag{4.121}$$

There are not any clear systematic error terms that are proportional to $M\tilde{\mathcal{N}}\tilde{\mathcal{E}}$, as most of the terms contribute to the energy shift correlated with $\tilde{\mathcal{N}}$, like the Stark shift, or to the energy shift correlated with M, like the Zeeman shift. Amar had done a calculation like this one and concluded that the omega doublet structure of ThO affords us protection from geometric phase effects that have contributed to electron EDM experiments in the past [163, 164].

Similarly, we may also consider the case in which we have electric and magnetic fields that are oscillating with the same frequency ω, and the same phase, along the electric field direction, which is described by the Stark and Zeeman Hamiltonian,

$$H_1(t) = -(D \cdot \mathcal{E}_= + \mu \cdot \mathcal{B}_=) \cos(\omega t)\, \hat{z}. \tag{4.122}$$

This Hamiltonian can couple adjacent rotational levels, mixing $|H, J = 1, M, \tilde{\mathcal{N}}\rangle$ with $|H, J = 2, M, \tilde{\mathcal{N}}\rangle$ with matrix element,

$$\left\langle H, J = 2, M, \tilde{\mathcal{N}} \left| H_1(t) \right| H, J = 1, M, \tilde{\mathcal{N}} \right\rangle = -\sqrt{\frac{3}{20}} (D_H \mathcal{E}_= + \mu_H \Omega \mathcal{B}_=) \frac{1}{2} \left(e^{i\omega t} + e^{-i\omega t}\right). \tag{4.123}$$

This mixing consists of two waves with different frequencies $\pm\omega$, which can both contribute the energy shift,

$$\omega_{\mathrm{AC}}(M, \tilde{\mathcal{N}}) = -\frac{3}{160 B_{R,H}} \left[(D_H \mathcal{E}_=)^2 + 2M\tilde{\mathcal{N}}\tilde{\mathcal{E}} \mu_H \mathcal{B}_= D_H \mathcal{E}_= + (\mu_H \mathcal{B}_=)^2\right] + O\left(\frac{\omega}{B_{R,H}}\right)^2, \tag{4.124}$$

where I have expanded about small oscillation frequency with respect to the rotational splitting, $\omega \ll B_{R,H}$. Here there is a term that contributes directly to a systematic error,

$$\omega_{\mathrm{AC}}^{\mathcal{NE}} = -\frac{3}{80 B_{R,H}} \mu_H \mathcal{B}_=^{\mathrm{nr}} D_H \mathcal{E}_=^{\mathrm{nr}} = -\frac{1}{2} \mu_B \eta_{H,J=1} \mathcal{E}_=^{\mathrm{nr}} \mathcal{B}_=^{\mathrm{nr}}, \tag{4.125}$$

which is directly analogous to the first term in equation 4.115 in an off-resonant the rotating frame, and is estimated to be similarly negligible in size. Here, I have substituted $\eta_{H,J=1} = (3/40)\, g_H D_H / B_{R,H}$ so that we may directly compare this result with equation 4.115. However, as we discovered in ACME I, the estimate of $\eta^{\text{est}}_{H,J=1} = -1.4\,\text{nm/V}$ that is obtained from this expression does not agree well with the measured value, $\eta^{\text{meas}}_{H,J=1} = -.79\,\text{nm/V}$. The value for $\eta_{H,J=1}$ is significantly modified by the spin-uncoupling interaction between the ${}^3\Delta_1$ and ${}^3\Delta_2$ states in the $|H, J = 2, M, \tilde{\mathcal{N}}\rangle$ states which is described in detail in references [86, 135].

Chapter 5

Statistical Upgrades to the Apparatus

> She pressed her tongue hard against her lower front teeth. One moved slightly, activating her microchannel amps; the random bounce of photons through the darkness was converted to a pulse of electrons, the concrete around her coming up ghost-pale and grainy. "Okay, honey. Now go out to play."
>
> William Gibson, Neuromancer

5.1 Overview

Although the ACME I experiment achieved its goal of making a measurement of the electron's EDM with greater precision than previous experiments, we determined that significant improvements could be made to the apparatus and the measurement scheme that could enable a subsequent measurement, that we denote by ACME II, which could have more than a factor of 10× more sensitivity to the electron's EDM. In this chapter, I will provide descriptions of the experimental apparatus used in ACME I and ACME II, which are shown in figure 5.1 with an emphasis on those aspects that changed between the two. For more complete descriptions of the ACME I apparatus, I refer the reader to the following references [77, 86, 158, 164].

The upgrades that we implemented in order to increase the statistical sensitivity of the

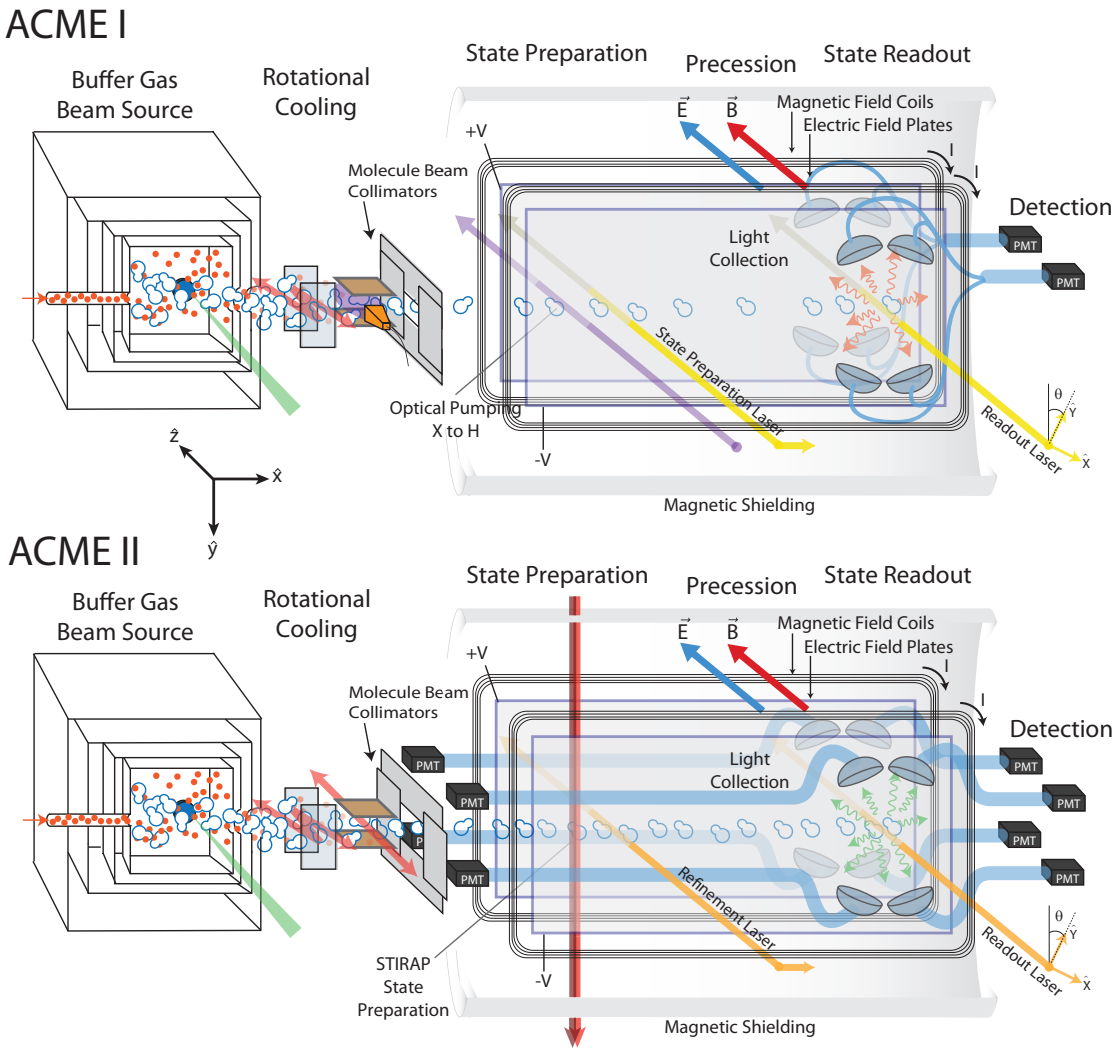

Figure 5.1: Schematic of the experimental apparatus that was used in ACME I (top) and ACME II (bottom), provided in the same figure so that the upgrades may be easily identifiable.

measurement include:

1. **Beamline Geometry Optimization:** By reducing the length of the molecule beam line between the beam source and the detection region and by widening the collimators that select the molecules that enter the spin precession region we were able to increase the detected flux of molecules by a factor of $8\times$.

2. **Efficient Spin State Preparation:** ACME I transferred molecules from the ground state into the initial spin state in H via a lossy two stage optical pumping scheme. By switching to a STImulated Rapid Adiabatic Passage (STIRAP) state transfer scheme by which molecules are adiabatically transferred between two quantum states we were able to increase the number of molecules in the detected state by a factor of $12\times$.

3. **Improved Molecule Detection:** We changed our detection transition to one that provides more emitted photons per molecule and these emitted photons are at a different wavelength at which we were able to find higher quantum efficiency PMTs. Additionally, improvements were made to the collection optics so that more of the emitted photons would arrive at the PMTs. These improvements increased the number of detected molecules by a factor of $5\times$.

In total, based on the demonstrated improvements made to ACME II, we anticipate that the number of detected molecule signal will be a factor of $250 - 800\times$ larger than that observed in ACME I. Assuming that the measurement is still photo-electron shot-noise limited, we anticipate that these improvements will enable a $15 \times -30\times$ improvement in sensitivity to the electron's EDM. Assuming that we do not encounter any unforseen systematic errors, this improved sensitivity should enable a measurement of the electron's EDM with better than a factor of ten improvement in precision relative to ACME I. Additionally, in chapter 4, we discussed methods to reduce the size of known systematic errors in ACME II.

5.2 Beam Source and Rotational Cooling

ThO molecules are produced via pulsed laser ablation of a ThO_2 ceramic target. This takes place in a cryogenic neon buffer gas cell, held at a temperature of $\approx 16\,\mathrm{K}$, at a repetition rate of 50 Hz. The resulting molecular beam is collimated and has a forward velocity $v_{\parallel} \approx 200\,\mathrm{m/s}$. In the state readout region the molecular pulses have a temporal (spatial)

Improvement	Signal Gain	Section
Rotational Cooling	$1-1.5\times$	5.2
Beamline Optimization	$7-9\times$	5.4.1
Efficient State Preparation	$10-13\times$	5.3
Detection Improvements	$3.5-4.5\times$	5.5
All Improvements	$250-750\times$	
Initial Observation [127]	$\sim 300\times$	

Table 5.1: Summary of anticipated detected molecule gain compared with initial measurements of the actual signal gain from the statistical upgrades made for the ACME II experiment.

length of around 2 ms (40 cm). As I neither specialized in work on the buffer gas beam source and since the source is not planned to change during ACME II, I refer the reader to detailed descriptions of the beam source in the following references [86–88].

After leaving the buffer gas source, the molecules have a velocity distribution and rotational level populations that are reasonably consistent with a Maxwell-Boltzmann distribution at a temperature of ≈ 4 K. This was lower than the cell temperature, and the cooling is attributed to isentropic expansion of the gas into the high vacuum region, which enhances the number of usable ThO molecules in the relevant rotational states. At this temperature the resulting fractions of molecules in the $J = 0 - 3$ levels were estimated to be 0.1, 0.3, 0.3 and 0.2 respectively. Further rotational cooling was provided via optical pumping (and additionally microwave mixing in ACME I) in order to condense the population in X before transfer of molecules from $X \to H$ to increase the population of molecules in H.

As described in section 2.1, in ACME I we sought to transfer as much of the initial ground state population as possible into $|H, J = 1\rangle$ which is populated via spontaneous emission when optical pumping on the $|X, J = 1, M = \pm 1\rangle \to |A, J = 0\rangle$. To enhance the population which was transferred, we accumulated population in a single rotational level $|X, J = 1\rangle$ of the ground state before state preparation. The scheme used to achieve this, which we refer to as rotational cooling, is illustrated schematically at the top of figure 5.2 and is discussed in detail in [158].

The first stage of the process, which is common to ACME I and ACME II was the optical pumping of molecules out of $|X, J = 2, 3\rangle$ via $|C, J = 1, 2\rangle$ from which spontaneous emission preferentially populates the $|X, J = 0, 1\rangle$ states respectively using laser light at 690 nm. Since these $J \to J - 1$ optical pumping schemes have more states in the ground state compared to the excited state, dark states that are not optically pumped are present

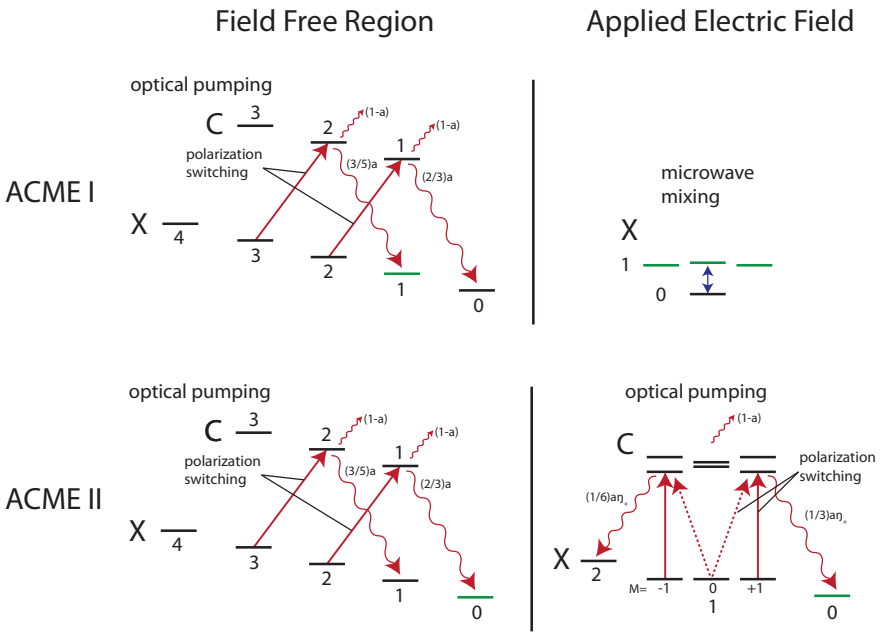

Figure 5.2: Schematic of ACME I and ACME II rotational cooling schemes with target states highlighted in green. Both schemes begin with polarization switched optical pumping on the $|X, J = 3\rangle \rightarrow |C, J = 2\rangle$ and $|X, J = 2\rangle \rightarrow |C, J = 1\rangle$ transitions in the absence of an electric field to increase the population in $|X, J = 0, 1\rangle$. The ACME I scheme then equalizes the populations between $|X, J = 0, M = 0\rangle$, $|X, J = 1, M = 0\rangle$ using a long microwave pulse in an applied electric field to enhance the population in the target state $|X, J = 1\rangle$. The ACME II scheme then performs polarization switched optical pumping on the $|X, J = 1\rangle \rightarrow |C, J = 1\rangle$ transition in an applied electric field to enhance the population in the target state $|X, J = 0\rangle$.

in the ground state. This situation is similar to that encountered when laser cooling and slowing of molecules [85]. In order to ensure that all molecules in the ground state are optically pumped, we non-adiabatically alternate the polarization of light so that states that are dark with respect to a given polarization of light are optically pumped by the following polarization of light. Laser beams with linear polarization alternating between $\hat{x}$ and $\hat{y}$ were achieved by directing around 10 passes of the beam, offset in x, through the vacuum chamber, passing through a quarter-wave plate twice in each pass, over a distance of around 2 cm.

The natural linewidth of the $X \to C$ transition is $\approx 2\pi \times 0.3$ MHz, however the usable molecules had a ≈ 0.7 m/s transverse velocity spread, corresponding to a 1σ Doppler width of $\approx 2\pi \times 1.5$ MHz at 690 nm. Because the lasers linewidths ($\lesssim 1$ MHz) and natural linewidth were less than the Doppler width, driving optical pumping to completion required a combination of power broadening and extended interaction time compared to the C state lifetime. Optical pumping occurred in a magnetically unshielded region where a background field $\mathcal{B} \sim 500$ mG was present; however, the magnetic moment of X and C states are $\sim \mu_N$ and $\approx \mu_B/J\,(J+1)$ respectively, where μ_N is the nuclear magneton and μ_B is the Bohr magneton, which led to a Zeeman shift of $\sim 2\pi \times 400$ Hz and $2\pi \times 400$ kHz such that the M sublevels were not resolved by the optical pumping. The $|C, J=1\rangle$ state has an $\Omega-$doublet splitting of $\Delta_{C,J=1} \approx 2\pi \times 51$ MHz [52]. This splitting scales as $\Delta_{C,J} \propto J\,(J+1)$, which implies that we can spectroscopically resolve the opposite parity states for all $|C, J\rangle$ states that we addressed. In addition, having no $\mathcal{E}$-field present meant that the M-sublevels of C and X remained unresolved and the energy eigenstates remained parity eigenstates.

The lasers used rotational cooling, and for all other applications unless otherwise noted, are extended cavity diode lasers (ECDLs) and are frequency-stabilized using a scanning transfer cavity with a computer-controlled servo [69]. Frequency-doubled light at 1064 nm from a frequency-stabilized Nd:YAG laser, locked to a molecular iodine line via modulation transfer spectroscopy [57], provides the reference for the transfer cavity.

For an approximate calculation of the transfer efficiency of this first rotational cooling step, lets assume an initial Maxwell-Boltzmann distribution of the rotational population in X,

$$P_J^0 = \frac{1}{Z}\,(2J+1)\exp\left(-J\,(J+1)\,\frac{B_R}{k_B T}\right) \tag{5.1}$$

where Z is the partition function that ensures that $\sum_J P_J^0 = 1$, $T \approx 4\,\mathrm{K}$ is the rotational temperature, and B_R is the rotational constant for the X state. Here the subscript is an index that denotes the stage of rotational cooling and the subscript denotes the rotational level. Assuming that optical pumping is driven to completion, a simple calculation of the populations P_0^1 and P_1^1 in $|X, J = 0, 1\rangle$ after optical pumping respectively shows

$$P_0^1 = P_0^0 + P_2^0 \left(\frac{\frac{3}{5}b}{1 - \frac{2}{5}b} \right) \approx .3 \tag{5.2}$$

$$P_1^1 = P_1^0 + P_3^0 \left(\frac{\frac{2}{3}b}{1 - \frac{1}{3}b} \right) \approx .4 \tag{5.3}$$

where $b \approx .7$ is the branching ratio from $|C, \nu = 0\rangle \rightarrow |C, \nu = 1\rangle$ [1]

In ACME I we sought to concentrate the population in the $|X, J = 1, M\rangle$ states from which we later drove optical pumping on $|X, J = 1, M = \pm 1\rangle \rightarrow |A, J = 0\rangle$ resulting in spontaneous decay to the target state $|H, J = 1\rangle$. Hence, since there was considerably more population in $|X, J = 0\rangle$ after the first round of optical pumping compared to any of the individual states in $|X, J = 1\rangle$, we applied a continuous microwave field, resonant with the $|X, J = 0, M = 0\rangle \rightarrow |X, J = 1, M = 0\rangle$ transition; a sufficiently high microwave power combined with the inherent velocity dispersion of the molecule beam led to an equilibration of population between the coupled levels [158]. In this second stage of rotational cooling it was empirically observed that applying an electric field to lift the M sublevel degeneracy was necessary to obtain the increased population in $|X, J = 1\rangle$. Also note that the state to which we drove population, $|X, J = 1, M = 0\rangle$ is not adiabatically connected to the states from which we later drove the population, $|X, J = 1, M = \pm 1\rangle$, however, we empirically observed that the population was scrambled amongst the M-sublevels by some non-adiabatic process between the rotational cooling region and the interaction region – this was likely caused by large electric field gradients that the molecules see as they approach the sharp conducting blades of the fixed collimator at the start of the interaction region. Hence the population in the target rotational state after rotational cooling P_1^2, the population that was addressed

1. This branching ratio number is fairly uncertain but current estimates suggest that the branching from $|C, \nu = 0\rangle \rightarrow |X, \nu = 0\rangle$ is in the range of $.65 - .8$. The bulk of the remaining population likely decays to $|X, \nu \neq 0\rangle$ and $|Q\rangle$ with branching ratios to these states in the range of $.1 - .15$. Estimates of these branching ratios come from a combination of crude evidence from optical pumping experiments, measured [169] and estimated [120] Franck-Condon factors, and estimates of the spin-orbit state contributions [109] to the various relevant electronic states.

by the state transfer scheme in the interaction region after optical pumping $P^{\text{ACME I}}$, and the molecule gain achieved by using rotational cooling $g_{\text{RC}}^{\text{ACME I}}$ are approximately:

$$P_1^2 \approx \frac{1}{2}P_0^1 + \frac{5}{6}P_1^1 \approx .45 \tag{5.4}$$

$$P_{\text{RC}}^{\text{ACME I}} \approx \frac{2}{3}P_1^2 \approx .3 \tag{5.5}$$

$$g_{\text{RC}}^{\text{ACME I}} \approx \frac{P_1^2}{P_1^0} \approx 1.7\times \tag{5.6}$$

Indeed, these calculations are reasonably consistent with the observed factor $1.5 - 2.0\times$ increase in the molecule fluorescence signal F in the state readout region when including rotational cooling. This gain factor was observed to vary slowly over time, possibly due to variations in the rotational temperature of the molecule beam, with significant changes sometimes observed when the ablation target was changed, and also with slow drift in the rotational cooling laser frequencies which were periodically tuned to maximize the signal in the detection region.

In ACME II, as described in section 5.3 below, we changed the state transfer and preparation scheme from an optical pumping scheme to an adiabatic state transfer scheme using the STIRAP scheme between $|X, J\rangle \rightarrow |C, J\rangle \rightarrow |H, J = 1\rangle$. We had some choice of rotational levels from which and via which we could perform the state transfer. We decided to perform STIRAP starting from the $|X, J = 0, M = 0\rangle$ with $\left|C, J = 1, M = 0, \tilde{\mathcal{P}} = -1\right\rangle$ as the intermediate state so that we could maximize the transition dipole moments to maximize our chances of satisfying adiabaticity.

So, prior to ACME II we investigated alternative rotational cooling schemes that will maximize the population in the new target state $|X, J = 0, M = 0\rangle$ and we implemented the scheme shown in the bottom of figure 5.2. This scheme has the same first step as in ACME I, but has a different second step in which the population is optically pumped on the $|X, J = 1\rangle \rightarrow \left|C, J = 1, M = \pm 1, \tilde{\mathcal{N}}\right\rangle$ transition in the presence of a small electric field, which results primarily in spontaneous decay to the target state $|X, J = 0\rangle$, but also results in some lost population to $|X, J = 2\rangle$. The electric field is used to mix the parities of the excited states such that the E1 transition dipole matrix element on the driving transition is sufficiently large that we can drive optical pumping to completion. However, this mixing should be minimized so as to prevent too much unwanted spontaneous emission on the

$\left|C, J=1, M=\pm 1, \tilde{\mathcal{N}}\right\rangle \rightarrow |X, J=1\rangle$ transition. Population that decays here has more chances to be lost to states other than the target state, and hence has lower efficiency of transfer. So, we can express the population $|X, J=1\rangle$ after this second stage of rotational cooling as:

$$P_{\mathrm{RC}}^{\mathrm{ACME}\ II} = P_0^2 = P_0^1 + P_1^1 \left(\frac{\frac{2}{3} a \eta_+}{1 - a\,(1 - \eta_+)} \right) \approx .3 - .45 \tag{5.7}$$

$$g_{\mathrm{RC}}^{\mathrm{ACME}\ II} = \frac{P_0^2}{P_0^0} = 2.5 - 4\times \tag{5.8}$$

where $\eta_\pm = \frac{1}{2}\left(1 \pm 1/\sqrt{1 + \left(\frac{2 D_C \mathcal{E}}{\Delta_C}\right)^2}\right) \in (0,1)$ describes the degree of polarization of the C state where $\eta_+ = 1$ is unpolarized (perfect parity eigenstates) and $\eta_+ = 0$ is fully polarized, D_C is the electric dipole moment of $|C, J=1\rangle$, and Δ_C is the parity doublet splitting in $|C, J=1\rangle$. This is in reasonable agreement with measured rotational cooling gains of about $g_{\mathrm{RC}}^{\mathrm{ACME}\ II} \approx 2.7\times$ [103].

Although the use of rotational cooling is more critical in ACME II since $g_{\mathrm{RC}}^{\mathrm{ACME}\ II} > g_{\mathrm{RC}}^{\mathrm{ACME}\ I}$, the gain in number of detected molecules, g_{RC} from implementing this rotational cooling scheme is of order unity,

$$g_{\mathrm{RC}} = \frac{P_{\mathrm{RC}}^{\mathrm{ACME}\ II}}{P_{RC}^{\mathrm{ACME\ I}}} \approx 1 - 1.5 \times . \tag{5.9}$$

However, it is notable that if we were to replace some of the 690 nm rotational cooling lasers resonant with the $X \rightarrow C$ transition with 512 nm lasers resonant with the $X \rightarrow I$ transition, we could achieve an improvement in g_{RC} since the branching ratio a from $|I, \nu=0\rangle \rightarrow |X, \nu=0\rangle$ has been measured to be larger, $a \approx .91$ [96] which suggests that if all three rotational cooling lasers were replaced, we could achieve populations on the order of $P_{\mathrm{RC}}^{\mathrm{ACME}\ II} \approx .35 - .6$ and gains relative to ACME I on the order of $g_{\mathrm{RC}} \approx 1.2 - 2.0\times$. Such a laser has been under development and could be implemented for this purpose in the future.

5.3 Efficient State Preparation

One of the primary ways in which we significantly increased our detected molecule signal in the ACME II apparatus relative to ACME I was a change in the method of populating the initial state prepared for the spin precession measurement in $|H, J = 1, M, \tilde{\mathcal{N}}\rangle$ given a rotationally cooled beam of ground state molecules in $|X, J = 0, M = 0\rangle$. ACME I used two stages of optical pumping to prepare this state, with an efficiency of approximately 6%. Using the technique of STImulated Raman Adiabatic Passage (STIRAP), we demonstrated an increase in the population of the desired state by a factor of 12 ± 1, corresponding to a state transfer efficiency of $75 \pm 5\%$. The measurements of this first demonstration of STIRAP are detailed in reference [129]. In this section I describe some of the formalism that we used in order to model the STIRAP state transfer and then later to understand the peculiarities in the STIRAP signals that we observed.

5.3.1 STIRAP Hamiltonian

For the discussion here, we will consider the three level system consisting of the states $|X\rangle \equiv |X, J = 0, M = 0\rangle$, $|C\rangle \equiv |C, J = 1, M = 0, \tilde{\mathcal{P}} = -1\rangle$, and $|H\rangle \equiv |B(\hat{\varepsilon}_s), \tilde{\mathcal{N}}, \tilde{\mathcal{P}} = -1\rangle$, where $|H\rangle$ is a superposition of the $|H, J = 1, M, \tilde{\mathcal{N}}\rangle$ states which is determined by the polarization $\hat{\varepsilon}_s$ of the $H \rightarrow C$ laser beam as per equation 2.5. In the STIRAP state preparation scheme, the goal is to transfer all of the population from $|X\rangle$ to $|H\rangle$, and this population transfer occurs as follows:

- We first turn on a laser coupling on the $|H\rangle \rightarrow |C\rangle$ transition such that in the dressed state picture the dark state in this three level system is $|X\rangle$.
- We adiabatically turn on a laser coupling between $|X\rangle \rightarrow |C\rangle$ while adiabatically turning off the coupling between $|H\rangle \rightarrow |C\rangle$, such that the dark state adiabatically evolves from $|X\rangle$ to $|H\rangle$ [17].
- We turn off the $|X\rangle \rightarrow |C\rangle$ coupling, and the population that was initially in $|X\rangle$ is now in $|H\rangle$.

If we parameterize the two transition Rabi frequencies as

$$\begin{aligned}\Omega_{\mathrm{HC}} =& \Omega_{\mathrm{r}} e^{-i\theta} \cos\Theta \\ \Omega_{\mathrm{XC}} =& \Omega_{\mathrm{r}} e^{+i\theta} \sin\Theta,\end{aligned}$$

then the STIRAP state transfer takes place while the angle Θ adiabatically evolves from 0 to $\pi/2$. $\Omega_{\mathrm{r}} = \sqrt{|\Omega_{\mathrm{HC}}|^2 + |\Omega_{\mathrm{XC}}|^2}$ is the total Rabi frequency, and θ is a relative phase between the two laser couplings; laser phase noise can contribute to a time dependent phase θ. Each of these two couplings can also have different detunings, which we can parameterize as

$$\begin{aligned}\Delta_{\mathrm{HC}} =& \Delta + \delta \\ \Delta_{\mathrm{XC}} =& \Delta - \delta\end{aligned}$$

where Δ is referred to as the "one-photon detuning", and δ is referred to as the "two-photon detuning". With these definitions in place, the Hamiltonian describing the time evolution of this three level system can be expressed as,

$$H = \begin{pmatrix} \Delta & \frac{1}{2}\Omega_{\mathrm{r}} e^{+i\theta} \cos\Theta & \frac{1}{2}\Omega_{\mathrm{r}} e^{-i\theta} \sin\Theta \\ \frac{1}{2}\Omega_{\mathrm{r}} e^{-i\theta} \cos\Theta & -\delta & 0 \\ \frac{1}{2}\Omega_{\mathrm{r}} e^{+i\theta} \sin\Theta & 0 & +\delta \end{pmatrix} \begin{matrix} |C\rangle \\ |H\rangle \\ |X\rangle \end{matrix} .$$

However, it is usually more useful to work in the dressed state basis $|D\rangle, |B_{\pm}\rangle$, described previously in equation 4.9 in a different context, where we can then treat the effects of the two photon detuning δ, and the time derivatives of the coupling angles $\dot{\theta}$, $\dot{\Theta}$ as perturbations to this system under the assumption that these quantities are small compared to the AC Stark shifts $E_{B\pm}$ which are on the order of the Rabi frequency, Ω_{r}. In this frame, the Hamiltonian can be re-expressed as,

$$\tilde{H} = \begin{pmatrix} \xi & -i\kappa_+\dot{\chi^*} & -i\kappa_-\dot{\chi^*} \\ i\kappa_+\dot{\chi} & E_{B-} - \xi\kappa_+^2 & -\kappa_+\kappa_-\xi \\ i\kappa_-\dot{\chi} & -\kappa_+\kappa_-\xi & E_{B+} - \kappa_-^2\xi \end{pmatrix} \begin{matrix} |D\rangle \\ |B_-\rangle \\ |B_+\rangle \end{matrix} \tag{5.10}$$

where, $E_{B\pm}$ and $\kappa_{\pm}$ are defined in equations 4.10 and 4.11 respectively, the phase angle rotation rate is given by $\dot{\chi} = i\dot{\Theta} - i(\dot{\theta} + \delta)\sin 2\Theta$, and I have defined a new quantity, $\xi = (\delta + \dot{\theta})\cos 2\Theta$. It is worthwhile noting that this Hamiltonian is the same as that which we used to described systematic errors in section 4.1.3, the only difference being that I have not made the assumption here that $\Theta \approx \pi/4$, and I have called the quantities Θ, θ, and δ by different names.

This Hamiltonian indicates that if the population transfer rate $\dot{\Theta}$, phase noise frequency $\dot{\theta}$, or two photon detuning δ is comparable to Ω_{r}, then there will be significant mixing between the dark state and the bright states, leading to population lost from the dark state resulting in inefficiency in the STIRAP state transfer process. Note that the system is most vulnerable to such mixing due to the two photon detuning or phase noise when the state transfer is about half completed, $\Theta \approx \pi/4$.

5.3.2 Constraints on STIRAP laser spatial intensity profile width

Although STIRAP has been performed in a number of atomic and molecular-beam experiments [39, 64, 74, 119, 130, 156], performing efficient STIRAP state transfer in our apparatus is particularly challenging because we must efficiently transfer population with a large distribution of two photon Doppler shifts, $\delta_D = (k_{\mathrm{HC}} - k_{\mathrm{XC}})\sigma_{v_y}/2 \approx 2\pi \cdot 0.3\,\mathrm{MHz}$ (where $\sigma_{v_y} \approx 1.2\,\mathrm{m/s}$ is the transverse velocity distribution width as specified in section 5.4.1 below) and a large spatial distribution of molecules spanning about 25 mm, with a finite amount of laser power available for the notably weak $H \rightarrow C$ transition (with estimated transition dipole matrix element in table 4.2.1). The STIRAP laser beams were sent through the apparatus along the $\hat{y}$ direction for technical reasons discussed in section 5.4.2. Lets consider that we have a spatial intensity profile $I(x, z)$ that is Gaussian along the $\hat{x}$ direction with 1σ width of w_x, and flat-topped along the $\hat{z}$ direction with a half width of w_z, with laser power P,

$$I_i(x, z) = \frac{P_i}{\sqrt{8\pi} w_x w_z} \exp\left(-\frac{(x - x_i)^2}{2w_x^2}\right) (-w_z \leq z \leq w_z),$$

where x_i is the x position of laser beam with index $i \in \{\mathrm{HC}, \mathrm{XC}\}$. The Rabi frequency is then given by

$$\Omega_i = D_i \sqrt{\frac{2I_i(x,z)}{c\epsilon_0}}$$

where D_i is the transition dipole matrix element, ϵ_0 is the electrical constant, and c is the speed of light.

Given that we have about 10 W available at 1090 nm for the $H \to C$ transition, and given that the transition dipole matrix element is about $D_{\mathrm{HC}} \approx .005\, e\, a_0$ and the laser beam must be stretched to address all the molecules, $w_z \approx 1.5$ cm, then the maximum Rabi frequency available for the $H \to C$ transition is about $\Omega_{\mathrm{HC}} \approx 2\pi \cdot 2\,\mathrm{MHz}\,\sqrt{100\,\mu\mathrm{m}/w_x}$. In order to efficiently transfer the full two photon Doppler width of molecules, we require that $\Omega_{\mathrm{r}} \gg \delta_D$, which sets an upper bound on the laser intensity width of roughly $w_x \ll 1$ mm, which implies that we must focus these laser beams in the x direction.

On the other hand, if the laser intensity profiles have a width of about w_x in the $\hat{x}$ direction, and the molecules are traveling through these beams at $v_x \approx 180$ m/s, then the full state transfer must be completed within a time period of w_x/v_x. In other words, the state transfer rate is approximately $\dot{\theta} \sim (\pi/2)(v_x/w_x)$, and in order to maintain adiabatic transfer of the molecules we require that $\Omega_{\mathrm{r}} \gg \dot{\theta}$, which sets a lower bound on the laser intensity width of roughly $w_x \gg 20\,\mu$m. Ultimately we observed efficient state transfer with $w_x \approx 160\mu$m, which is consistent with the two photon Doppler width and adiabaticity conditions.

5.3.3 Effect of laser phase noise

We had to ensure that the integrated power spectral density of the phase noise with $\dot{\phi} \sim \Omega_{\mathrm{r}}$ was sufficiently low so that it would not significantly resonantly drive population from the dark to the bright states in the dressed state picture. The light for these two lasers was derived from commercial external cavity diode laser systems (ECDLs) at 1090 nm (resonant with $H \to C$) and 690 nm (resonant with $C \to X$) and these systems typically have noise spectral density linewidths on the order of $\sim 2\pi \cdot 1$ MHz. By performing active frequency stabilization with respect to ultra-low expansion (ULE) glass cavities with a finesse of about 30,000 using the Pound Drever Hall (PDH) locking method [46], the laser power

spectral densities were significantly narrowed. Measurements of the power spectral density of the beat-note between two 690 nm lasers locked to separate cavities indicated a narrow ($\approx 2\pi \times 150\,\mathrm{Hz}$) peak on top of a much broader pedestal, suppressed by about a factor of $100\times$ in power with respect to the peak, with a $\approx 2\pi \times 1\,\mathrm{MHz}$ linewidth that is typical of the unlocked laser.

With these power spectral densities we observed STIRAP state transfer efficiencies in the range of $30 - 40\%$. This behavior is consistent with recently reported detrimental effects on STIRAP transfer efficiency due to broad pedestals in the spectral line shape that are common to stabilized ECDLs [177]. Furthermore, we performed simulations of the STIRAP efficiency by integrating the Lindblad master equation with random sampling over the spatial and velocity distributions within the molecular beam. The simulations were run with a phase model consistent with the measured power spectral density of the lasers, varying phase noise parameters such as pedestal amplitude, width, and position of noise features within the uncertainty of the measurement.

In this model, the relative phase between the Stokes and Pump STIRAP lasers are is given by a random waveform, $\phi\,(t)$, given by

$$\phi\,(t) = \delta\phi \int_0^\infty \phi\,(\omega)\sin(\omega t)\,d\omega, \tag{5.11}$$

such that $\delta\phi$ is the phase noise amplitude, and $\phi(\omega)$ is a normally distributed random variable with zero mean, $\langle\phi(\omega)\rangle = 0$ and a diagonal covariance with a Lorentzian spectral shape,

$$\langle\phi(\omega)\phi(\omega')\rangle = \delta(\omega - \omega')\frac{(\gamma/2)^2}{\omega^2 + (\gamma/2)^2}. \tag{5.12}$$

Here, $\delta\phi$ is the phase noise amplitude for which the noise pedestal in the power spectral density is suppressed by about $10\log_{10}(\delta\phi^2)$ dB relative to the power at the carrier frequency. γ is the width of the phase noise pedestal.

The results of these simulations are consistent with the observed behavior, i.e., they showed a typical STIRAP saturation with laser power of the transfer efficiency at only 30%–40% in a parameter range similar to that of our system.

To reduce the laser phase noise in the pedestals, the off-the-shelf diodes were replaced with AR-coated diodes, which yield a narrower linewidth in an ECDL configuration before

locking ($2\pi \times 200\,\text{kHz}$ compared to $2\pi \times 1.5\,\text{MHz}$). The power spectrum of the beat note from locked ECDLs with the new diodes displays a much-suppressed pedestal ($10^3\times$ instead of $10^2\times$) with approximately the same pedestal linewidth ($\sim 2\pi \times 1\,\text{MHz}$). Simulations using a phase noise model consistent with the improved power spectrum predict near-unity STIRAP efficiency.

5.3.4 Peculiarities in the Observed STIRAP

As expected, the STIRAP efficiency was observed to be very sensitive to two-photon detunings $\delta \neq 0$, but quite robust to one-photon detunings $\Delta \neq 0$. Unlike many other STIRAP systems, we obtain higher efficiency when running at one-photon detunings that are large compared to the Doppler linewidths on the two transitions. Transfer efficiency decreases by about 10–20% when on one-photon resonance – we believe that this is due to excess light in the spatial intensity profiles of the laser beams outside of the region where the STIRAP state transfer takes place. On resonance, this excess laser intensity in the wings of the spatial intensity profiles (due, e.g., to scatter or diffraction from apertures in the laser beam paths) can drive optical pumping, depleting the population of the initial state before it is transferred or the final state after it the population had already been transferred.

Simulations of the molecule ensemble, when integrating the Schrodinger equation of the three-level system, show similar behavior when including Airy-like wings in the tails of the spatial intensity profiles of the lasers with amplitudes at the level of 10–20% of the maximum intensity, comparable to the ones observed in our laser beams.

We also observed that at one-photon detunings that are large compared to the one-photon Doppler linewidths of the pump and Stokes lasers, the two-photon lineshape is very asymmetric. This is a fairly generic signature of STIRAP that exhibited when at one-photon detunings that are large compared to $\Delta \gg \Omega_\text{r}$ and when the peak Rabi frequencies are not equal [25]. In our case, $\Omega_\text{XC}/\Omega_\text{HC} \approx 1.5\times$.

5.4 Interaction Region

In the ACME apparatus, we refer to the large rectangular vacuum chamber in which the spin precession region takes place as the *interaction region.* This vacuum chamber houses the electric field plate assembly that is used to apply a uniform electric field in the $\hat{z}$ direction

to the molecules, the fixed collimator that selects the solid angle of the molecular beam that is detected, and the optics assembly used to collect the laser induce fluorescence as the experiment signal. This chamber includes a number of windows, ports, and feedthroughs to enable laser access, molecular beam access, and electrical access to the spin precession region.

Several modifications were made to this vacuum chamber for the ACME II apparatus including:

- a shortening of the beamline between the beam source and the interaction region, widening the fixed molecule beam collimators, and widening the distance between the electric field plates to enable detection of a larger solid angle of the molecular beam.
- changes in the vacuum chamber to accommodate a larger area of optical access along the $\hat{z}$ direction, and new optical access along the $\hat{y}$ direction for STIRAP lasers.
- the addition of vacuum ports to accommodate magnetometry with fluxgate magnetometers at positions closer to the molecules, and with the ability to vary the position and orientation of the magnetometers from outside the apparatus.
- a modification to the support structure for the electric field plate assembly, and a modification to the trunk connection port for increased rigidity of the system.
- the addition of vacuum ports to accommodate more light pipe feedthroughs for the improved light collection system.

In this section and the following section, I will elaborate on each of these improvements and the considerations that were required in making these design decisions.

5.4.1 Beam Geometry and Collimation

The design of the molecule beamline and collimation geometry in ACME I was not highly optimized to maximize detected molecule flux, so there was a significant opportunity to increase the molecule signal in the interaction region in ACME II with a beamline redesign[2].

2. Early in the development of ACME II, we explored the possibility of and constructed an electrostatic lens for the purpose of focusing molecules in either the low field seeking $|X, J = 1, M = 0\rangle$ or $|X, J = 2, M = 0\rangle$ states with a transverse velocity capture range larger than the transverse velocity distribution in the detection region in ACME I which could significantly increase the detected molecule flux. After we observed X-rays being emitted from the device (see this reference for a more detailed description: [171]), in combination with

Our efforts can be decomposed into two fairly separable efforts: the reduction in the length of the beamline between the output conical aperture in the molecule beam source, and the increase in the size of the fixed collimator and the field plate separation in the interaction region.

Beamline length optimization

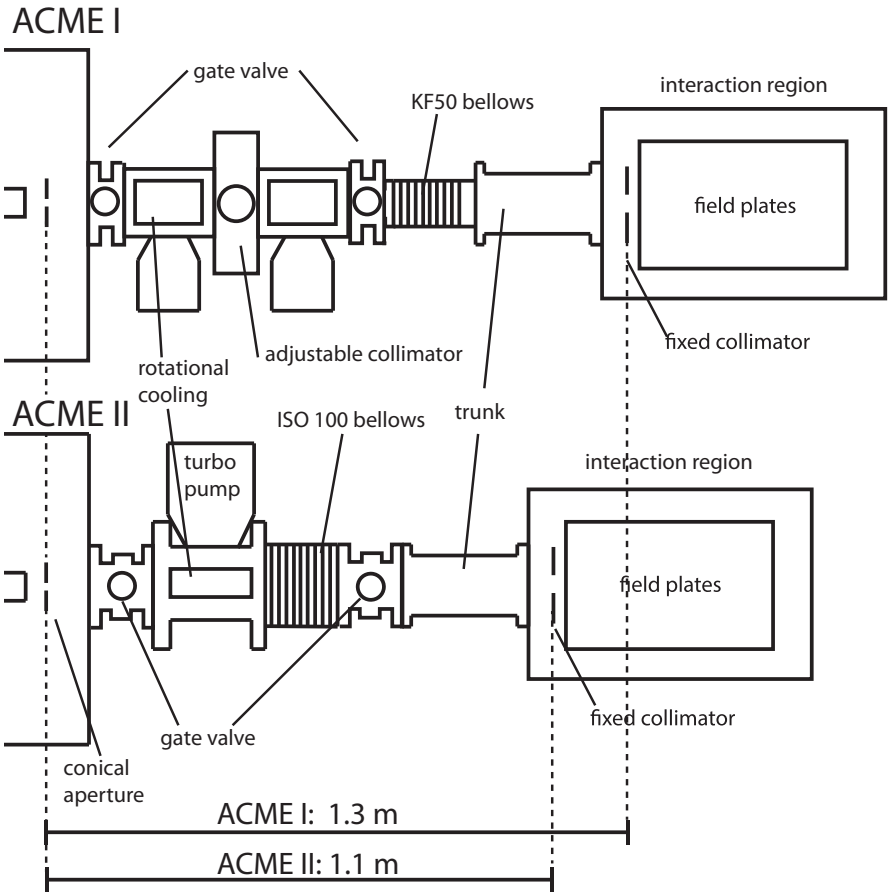

Figure 5.3: A comparison of the contributions to the length of the beamline in the ACME I (top) and ACME II (bottom) configurations. Note that the ACME I apparatus included a second vacuum chamber that had been originally included only for diagnostic purposes and it was not replicated in the ACME II beamline. Additionally, ACME I included a module containing adjustable collimators, that enabled searches for systematic errors that varied throughout the molecule beam spatially in the transverse direction that was also not replicated in ACME to aid in reducing beamline length.

concerns regarding the increase in complexity of the experiment, we explored obtaining a detected molecule flux increase from a modification of the beamline and collimation geometry in place of the electrostatic lens. We found that an electrostatic lens could provide only perhaps a few times larger signal gain compared to simply optimizing the beam geometry and so we decided to put the lens project on hold.

Figure 5.3 shows the contributions to the beamline in both ACME I and ACME II which have lengths of 1.3 m and 1.1 m respectively between the conical output aperture in the beam source and the square fixed collimator in the interaction region, resulting in a gain in detected molecule flux of roughly $(\ell^{\mathrm{ACME}\,I}/\ell^{\mathrm{ACME}\,II})^2 \approx 1.4\times$ due to the increase in solid angle subtended by the detection region. The ACME I apparatus included two small vacuum chambers with KF50 ports along the beamline, one of which was used for the rotational cooling scheme discussed above in section 5.2 and another that had been originally included only for diagnostic purposes. In ACME II we redesigned the beamline to accommodate ISO100 connections so that we could improve conductance along the beamline to reduce the effects of molecule beam attenuation by background gas [172], and we did not include a second diagnostic chamber. Additionally, ACME I included a module containing adjustable collimators, that enabled searches for systematic errors that varied throughout the molecule beam spatially in the transverse direction. Since systematic errors that would exhibit this signature are not well theoretically motivated and since these systematic error runs were not sensitive enough to put a strong empirical limit on any systematic error that might have this behavior, we decided not to include the adjustable collimators in ACME II to aid in reducing the beamline length. We decided to keep the rotational cooling region since the increase in molecule signal provided by the cooling is not offset by the gain in detected solid angle from shortening the beamline further. However, future iterations of this experiment might benefit from performing some rotational cooling immediately before or after the conical aperture within the beam source vacuum chamber, if effective[3], while eliminating all components of the beamline other than the trunk, a bellows, and a gate valve.

Optimizing the fixed collimator aperture size and field plate separation

In ACME I, it is not clear why the electric field plate spacing was set to $d_{FP} = 2.5\,\mathrm{cm}$ – the motivation for that decision seems to be lost to history. Nevertheless, the fixed collimator aperture size d_c was selected to satisfy a design requirement that no geometric trajectory of a molecule can be incident on the electric field plates and those trajectories that come closest

3. We currently do not know the J-changing collision rate between molecules and the background buffer gas in the vicinity of the conical aperture - if this rate is faster than the rotational cooling rate, then rotational cooling may not be possible in this region. Further experiments would be required to determine if this is a viable path forward for the experiment.

come no closer than $d_o = 3\,\text{mm}$ away to account for various uncertainties in the relative alignment of components that define the beamline. This was satisfied by a rectangular collimating aperture with a $d_c = 1\,\text{cm}$ width along the $\hat{z}$ direction [173]. The height of the collimating aperture was constrained by the requirement that the full distribution of molecules be addressed by the state preparation and read-out lasers which were limited in height to 2.5 cm by the chosen viewports on the interaction region vacuum chamber. So the fixed collimator size was chosen to be a 1 cm square.

In ACME II, we decided to change the spacing d_{FP} between the electric field plates while using the same trajectory constraint as used in ACME I to set the largest acceptable fixed collimator size d_c, to increase the detected solid angle of the molecular beam, given by

$$d_{FP} = 2d_o + d_c + (d_c + d_s)\,\frac{\ell_{FP}}{\ell}, \tag{5.13}$$

where $\ell \approx 1.1\,\text{m}$ is the length of the beamline between the conical aperture beam source output of diameter $d_s \approx 7\,\text{mm}$ and the fixed collimator, and $\ell_{\text{FP}} \approx 48\,\text{cm}$ is the length of the field plate assembly in the interaction region. Since this optimization was done after the vacuum chamber modifications described in section 5.4.2 and magnetic shield and coil modifications were implemented, the field plate spacing was limited to be less 5 cm for a number of technical reasons – for instance, that is the size of the available optical access for the STIRAP lasers along the $\hat{z}$ direction. Additionally simulations indicate [126] that with our existing collection optics system [86] the total gain in detected molecule signal levels off and begins decreasing as the field plate spacing reaches and begins to exceed 5 cm due to decreased light collection efficiency resulting from a decreased solid angle subtended by the collection optics, and decreased light transmission due to the larger phase space distribution of light being emitted from the larger cloud of molecules in the detection region.

Additional considerations in selecting a field plate spacing include ensuring that the STIRAP state transfer, and the state read-out optical pumping can continue to be efficient in performing their functions with the increased Doppler widths and increased molecule cloud sizes that accompany the larger solid angle of the molecular beam in the detection region. In order to estimate these quantities, we can model the beam source as a probabilistic emitter an emission probability $P(\vec{x}, \vec{v})$ with a uniform distribution of emission within a

circle defined by the conical aperture with radius d_s, with a fixed longitudinal velocity $v_\parallel$, and a normally distributed transverse velocity with variance δv^2. The number of molecules N admitted by the fixed collimator (perturbatively expanding about $\delta v/v_\parallel \ll 1$) is

$$N = \frac{1}{2\pi}\left(\frac{d_c^2 v_\parallel^2}{\ell^2 \delta v^2}\right)\left[1 - \frac{1}{48}\frac{\left(4d_c^2 + 3d_s^2\right)}{\ell^2}\left(\frac{v_\parallel}{\delta v}\right)^2 + \ldots\right]. \tag{5.14}$$

Then the variance of the velocities in the z direction of the molecules admitted by the square collimator δv_z^2, and the variance in z positions of the admitted molecules as a function of position x from the fixed collimator aperture, $\delta z^2(x)$, are given by

$$\delta v_z^2 \approx \frac{1}{12} v_\parallel^2 \left(\frac{d_c}{\ell}\right)^2 \left(1 + \frac{3}{4}\left(\frac{d_s}{d_c}\right)^2\right) + \ldots \tag{5.15}$$

$$\delta z^2(x) \approx \frac{1}{12} d_c^2 \left\{\left(1 + \frac{3}{4}\left(\frac{d_s}{d_c}\right)^2\right)\left(1 + \frac{x}{\ell}\right)^2 + \frac{3}{4}\left(\frac{d_s}{d_c}\right)^2\right\} + \ldots \tag{5.16}$$

With these considerations taken into account, we decided to set the field plate spacing to $d_{FP} = 4.5\,\text{cm}$ and to set the fixed collimating aperture to $d_c = 24\,\text{mm}$. Using equation 5.14, we anticipated an improvement of molecule flux in the detection region in ACME II of $g_{\text{geo}} \approx N^{\text{ACME II}}/N^{\text{ACME I}} \approx 8\times$ which is reasonably consistent with that which is observed in the experiment. With this geometry, the variance in the transverse velocity distribution is about 1.2 m/s corresponding to a Doppler width in the state read-out region of $2\pi \times 1.7\,\text{MHz}$ on the $|H, J = 1\rangle \rightarrow |I, J = 1\rangle$ transition. Since this Doppler width is not too much larger than the natural linewidth of the I state, $\gamma_I \approx 2\pi \times 1.0\,\text{MHz}$ [96], it is reasonable to expect that driving optical pumping to completion for molecules on the tail of the distribution should not be too much of a problem provided that we have enough laser power to achieve a reasonable Rabi frequency on the order of $\Omega_\text{r} \approx \gamma_I$. Indeed, after simulations described in section 5.5.2 indicate that we will be able to drive optical pumping to completion with the available laser power in the state read-out region in ACME II.

5.4.2 Interaction Region Design

Modifications for STIRAP

Most of the components in the interaction region required either modification or redesign for the ACME II apparatus. The major modifications are highlighted in a cut-away CAD

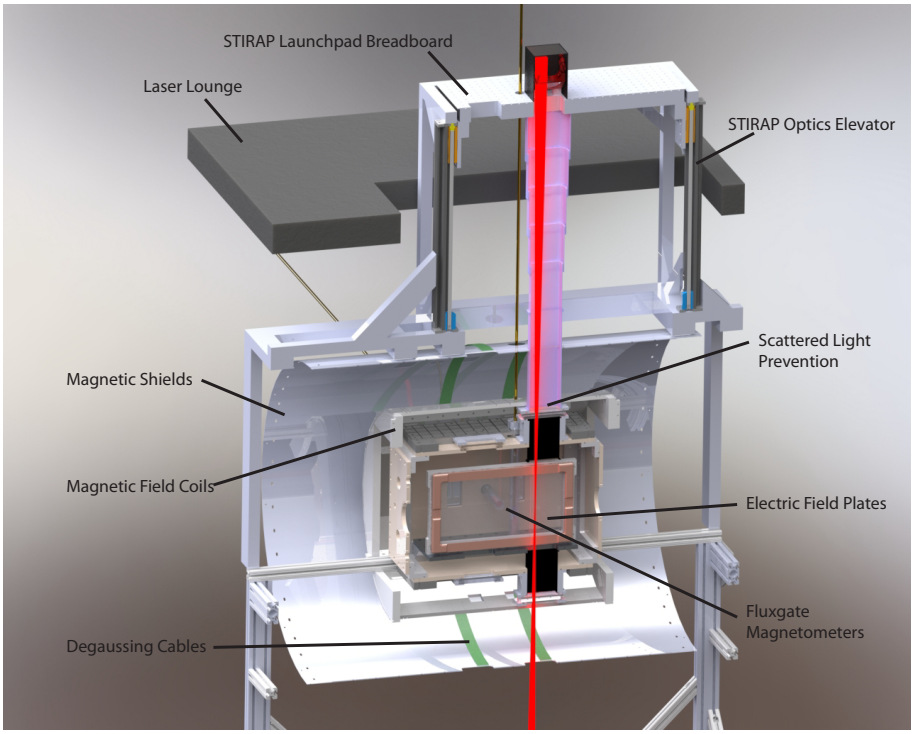

Figure 5.4: A cut-away view of a CAD model of the ACME II interaction region design

drawing of the interaction region in figure 5.4.2. The dominant reason for these changes was to enable vertical optical access through the apparatus along the $\hat{y}$ direction that was not previously available to accommodate the STIRAP lasers for efficient state transfer from $|X\rangle \rightarrow |H\rangle$. This required a redesign of the vacuum chamber flanges, a redesign of the auxiliary magnetic field coils that generate $\mathcal{B}_y$ and gradients thereof, a modification to the primary magnetic field coils that generate $\mathcal{B}_z$ and gradients thereof, new holes in the magnetic shields, and a modification to the electric field plate assembly.

In principle we could have sent the STIRAP lasers along the $\hat{z}$ direction using optical access previously available for the state preparation lasers, but we decided that this was not a viable option for several reasons. When the design choices were being made, we had not yet considered changing the detection transition in ACME II, so we were concerned about the possibility of significant scattered light in the detection region from the 690 nm STIRAP laser introducing a large background in the 690 nm laser-induced fluorescence signal from $|C\rangle \rightarrow |X\rangle$ decay thereby introducing a new significant source of noise that could reduce the experimental sensitivity to the electron's EDM. If the STIRAP lasers passed along $\hat{z}$ they would have passed through the field plates, which we empirically determined would result

in a scattered light signal that would completely dominate the laser-induced fluorescence signal. Additionally, the STIRAP laser beams are high power (>1 W) lasers that need to be highly focused to obtain sufficient laser intensity to ensure adiabatic transfer of the molecules, as described in section 5.3. These high intensities could be sufficient to damage ITO coating and possibly induce a large $\mathcal{E}^{\mathrm{nr}}$ or a significant inhomogeneity in $\mathcal{E}(x)$ that could lead to systematic errors as previously described in section 3.2. Furthermore, if the STIRAP laser passes through the two electric field plates, the molecules would interact also with the defocused back-reflection off of the second electric field plate, which could result in significant optical pumping before or after the STIRAP state transfer is intended to take place resulting in a low efficiency of transfer.

The size of the vertical optical access along the $\hat{z}$ direction, 5 cm, was chosen such that the required holes in the magnetic shields would be as large as we would be comfortable with when considering both structural integrity of the shields and penetration of external magnetic fields into the spin precession region. The size of the optical access along the $\hat{x}$ direction, 10 cm, was chosen such that the aspect ratio of the windows was about 2 : 1 so as to ensure high probability of success with window vacuum seals given that there was some difficulty with a large aspect ratio window seal during the development of ACME I on the same vacuum chamber. When making these design decisions, we had not yet considered the beam geometry optimization that was discussed in section 5.4.1 and this decision impacted the choice of the field plate spacing.

We also made a series of design decisions that resulted from our concern regarding a large background of scattered light at 690 nm within the chamber caused by the $|X\rangle \rightarrow |C\rangle$ STIRAP laser. In order to minimize scattered light we carefully chose the material for the vacuum chamber windows[4]. We also recessed the windows away from the interaction region as far as possible using custom vacuum nipples so that the point where the laser is incident on the window does not have a line of sight to the light collection optics in the detection region. Additionally, since the STIRAP lasers are highly focused in the interaction region, pulling the windows away from the beamline reduces the intensity of light on the windows

4. These windows are Corning 7980 Grade 0F Fused Silica. These have dimensions 5.5" × 3.5" × .75" ± .01" with the clear aperture being the center 4" × 2" of the glass face. These were specified to have a 10 − 5 Scratch-Dig rating, $\lambda/8$ total wavefront distortion (TWD) at 690 nm, and were custom manufactured by Custom Scientific. Calculations indicate that the deflection of the surface will be on the order of $\sim \lambda/10$. These windows were AR coated by Spectrum Thin Films on both sides with a specified reflectivity of ¡1% for the relevant wavelengths - 512 nm, 690 nm, 703 nm, 1090 nm.

which decreases the likelihood of damaging the anti-reflection (AR) coatings which could have lead to increased scattered light. Additionally, we enclosed the beam path so that dust, which could serve as laser scatterers, would more slowly accumulate on the surface of the window. This enclosed beam path consists of a blackened rectangular aluminum tube connected that extends outside the magnetic shields and a flexible duct coupling connected to a box that sits on an optics table with a right angle wedge mirror and another window through which the STIRAP lasers pass.

A platform, known as the *Laser Lounge*, was built above the experiment to enable us to set-up optics required for the shaping, focusing, and launching of the STIRAP lasers into the apparatus. This platform is supported from above by two aluminum I-beams that are connected to supports in the walls of the lab. A separate support structure, supported by the floor, was built around the existing interaction region structure, while maintaining structural independence from both that structure and from the Laser Lounge. This structure supports an optics breadboard right above the interaction region vacuum chamber that includes the STIRAP optics in a location where the optics can be easily manipulated by a lab member who is on the Laser Lounge. The optics breadboard is attached to 4 steel rails that surround it, which enables the optics breadboard to be raised or lowered with the aid of a crane that is built into the lab. This degree of freedom included in the design so that the optics may be manipulated when the optics breadboard is in the raised position, but the optics breadboard may be lowered to reduce the lever arm between where the STIRAP lasers are launched and the molecules in case fluctuations in the laser positions are leading to noticeably drifting STIRAP efficiencies over time.

Pockets for Magnetometer Access and Reversal

During ACME I we monitored the magnetic field near the spin precession region by mounting 4 fluxgate magnetometers on the interaction region vacuum chamber. This allowed us to characterize the approximate size of the applied $\mathcal{B}$-field and other contributions to the $\mathcal{B}$-field that were correlated with other experimental switches. However our fluxgate magnetometers have an electronic offset that varies over time that necessitates reversal of the magnetometer to subtract of this electronic offset to measure a background $\mathcal{B}^{\mathrm{nr}}$ field. As a result, we were unaware of the unexpectedly large $\vec{\mathcal{B}}^{\mathrm{nr}} \approx .7\hat{y}\,\mathrm{mG}$ residual magnetic field that we discovered when performing magnetometry on the system after the ACME I

experiments were completed.

We decided to modify the way in which we monitor the magnetic fields during ACME II by moving the magnetometers closer to the spin precession region so that the measured $\mathcal{B}$-field will be closer to that which the molecules feel, and by enabling the rotation of the magnetometers while they are inside the apparatus from outside, we can we can measure the residual magnetic field $\vec{\mathcal{B}}^{\mathrm{nr}}$. To achieve this, we built "magnetometer pockets" which are Aluminum flanges that attach to a KF40 port on the interaction region chamber, which extend *into* the vacuum chamber. These pockets are cylindrical and match the outer diameter of a Teflon magnetometer holder that we designed to enable the connection of the fluxgate magnetometer to the end of a rod for rotation and translation, and provides a low coefficient of friction between the pocket and the magnetometer. There are four pockets, two that extend in the $\hat{y}$ direction and two that extend in $\pm\hat{x}$ on either side of the electric field plates. This magnetometry scheme required that we add access through the magnetic shields, the main magnetic field coils, and the auxiliary magnetic field coils into the experiment for each of the manipulation rods that are attached to the magnetometers. Since all of these components already required modification or redesign necessitated by the STIRAP scheme, ensuring magnetometer access in each of these components did not require too much additional work. The magnetometers that sit in the $\hat{y}$ magnetometer ports are connected to rotation stages and a translation stage that are mounted on the Laser Lounge. The translation stage enables mapping of the magnetic field and extraction of magnetic field gradients along the $\hat{y}$ direction. The magnetometers that sit in the $\hat{x}$ magnetometer ports are connected to rotation stages that are mounted to the magnetic shields.

Additional Modifications

There were a series of additional modifications to the apparatus that were not motivated by either the introduction of the STIRAP state transfer process or improved magnetometry.

- We increased the optical access for the state preparation and state readout lasers along the $\hat{z}$ direction, which was limited mostly by the size of the existing holes in the magnetic shields, and by existing cable positions on the main magnetic field coil. Since the access area available was similar to the target for the STIRAP, the same set of windows were used for $\hat{z}$ and $\hat{y}$ optical access.

- We modified the vacuum chamber flanges on the $\pm\hat{x}$ sides of the vacuum chamber to enable a more rigid connection between the interaction region vacuum chamber and the beamline trunk, and we added ports so that we could accommodate 8 light pipe feedthroughs for an improved light collection scheme.

- The connection between the electric field plate assembly and the interaction region vacuum chamber was redesign to provide increased rigidity and to improve the positioning tolerance of the electric field plates with respect to the vacuum chamber.

Materials Selection and Vacuum Composition

As was previously described during the construction of the ACME I apparatus [164], during ACME II all components within the magnetic shields in the interaction region were constructed with careful regard for the materials selection. So as to minimize residual magnetic fields and gradients that contribute to $\mathcal{B}^{\mathrm{nr}}$, all materials in this region were chosen to be non-ferrous and non-magnetic. Some common materials that are found in this region include Al6061, brass, copper, titanium, ceramics, plastics, phosphor bronze, berrilium copper, glass, etc. Materials that were explicitly excluded include iron, steel, and nickel. Before inserting each component into the apparatus each one was tested for magnetization by passing it over a fluxgate magnetometer and looking for detected magnetic fields down to the sensitivity of about $.1\mu$G.

Materials inside the vacuum chamber were subject to further scrutiny to ensure that all materials are UHV compatible such that outgassing would be reduced in the chamber. All materials in the vacuum system underwent cleaning in a series of solvents: detergent, water, hexane, acetone, and then isopropanol, followed by drying and baking in a vacuum oven if the parts were small enough to fit in our oven. Solvents were only excluded for parts with materials that react chemically or dissolve in the solvents. After the interaction region vacuum chamber was assembled in its near final form, the chamber was baked with all parts, except for the optical components, for several days at around $100^{\circ}C$.

In a first round of vacuum baking, as we increased the temperature, we observed the appearance of a strong signature of phthalate molecules at a mass to charge ratio of about 149 amu in a mass spectrum taken with our residual gas analyzer (RGA) . We identified that these phthalates were originating from a Viton component in the electric field plate

assembly that is used in the clamping mechanism to distribute more evenly an asymmetric force profile from the copper clamp on the glass field plate to try to prevent bending of the field plate . We later learned that "commercial Viton" includes a large fraction of plasticizers such as phtalates that is not contained in "virgin Viton" which is UHV compatible and used in O-ring construction. After we replaced the offending part with another one made from this better material, we baked the vacuum chamber again for several days at $100°C$ and the phthalate signal in the vacuum chamber did not reappear.

The vacuum pressure after baking reached about 1×10^{-7} torr which is sufficiently low that the attenuation of the molecule beam by the background gas should not be significant. A mass spectrum and an analysis of the gas components in this spectrum are presented in figure 5.4.2. This analysis consists of fit of the mass spectrum peak amplitudes to a small library of mass spectra for a series of compounds acquired from the following NIST mass spectrum database [121]. Since a mass spectrometer detects molecule fragments, many large molecules show similar fingerprints of other large molecules and subsets of those molecules. Hence, among those compounds that have fingerprints that fit well to the spectrum, I believe the assignment only if there is a plausible reason why that compound might be present in our chamber. The following classes of compounds would be expected to be seen given the materials in the vacuum chamber and processes used to assemble it:

- Air: Nitrogen, Oxygen, Water, Argon, Carbon Dioxide, Nitrogen Dioxide,
- Solvents and Detergents: Hexane (and relatives - Pentane, Butane, Propane, Ethane), Ethanol, Isopropanol, Acetone, Ammonia, Nonene.
- Fluoropolymers: Fluorine, Hexafluoropropylene Oxide, Difluoroethene
- Nitrile Rubber: Acetonitrile
- Other Oily Stuff: Methane, Ethylene, Benzene, Carbon Dioxide, Possible Large or Biological Molecules

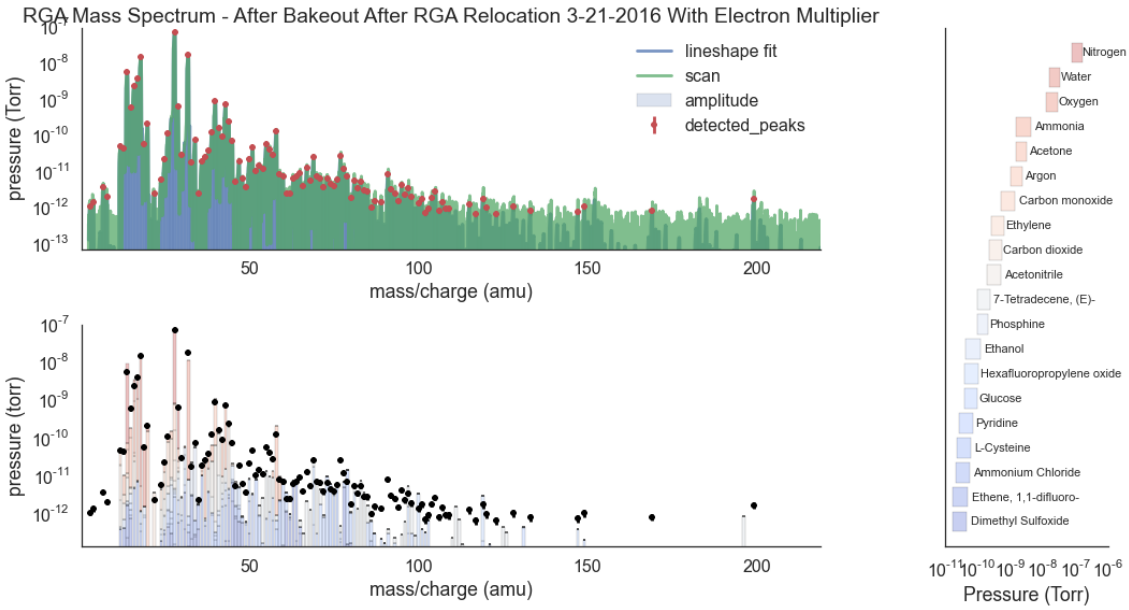

Figure 5.5: A mass spectrum of the contributions to the residual gas in the interaction region vacuum chamber after baking for a few days at $100°C$. The total pressure is about 1×10^{-7} torr and the dominant components to this gas are air and water.

5.5 Detection

5.5.1 A Better Readout Transition

While implementing the ACME II upgrades described above, we also considered the possibility of replacing our ACME I state readout scheme, which consists of optical pumping on $|H, J = 1, \nu = 0\rangle \rightarrow |C, J = 1, \nu = 0\rangle$ and observing a 690 nm photon from spontaneous emission on the $|C, J = 1, \nu = 0\rangle \rightarrow |X, \nu = 0\rangle$ transition, with a different detection transition. The following criteria make a given excited state $|e\rangle$ good for detection in the ACME experiment with the existing detection scheme:

1. The branching ratio b_{eH} from $|e\rangle \rightarrow |H\rangle$ must be small (<10%) since this type of decay reduces measurement contrast and enters linearly in the sensitivity of the measurement to electron's EDM.

2. The state $|e\rangle$ must decay primarily to a single electronic level such that the laser-induced fluorescence is fairly monochromatic at wavelength λ and this narrow band of light can be isolated fairly efficiently using interference filters. There also must be available photodetectors with reasonably high quantum efficiencies (>10%) at the wavelength λ.

3. The radiative lifetime of state $|e\rangle$ must be short compared to the time that the molecules spend in the detection region, $\tau \ll \frac{1\,\mathrm{cm}}{v_\parallel} \approx 50\,\mu s$.

4. The $|H\rangle \rightarrow |e\rangle$ transition must have a reasonably strong transition dipole moment such that with available laser technology we can achieve Rabi frequencies, when resonantly addressing this transition, that are comparable to the state decay rate $\Omega_\mathrm{r} \sim \gamma_e = 1/\tau_e$, with a laser beam spatial profile that has a y-extent large enough to address the full molecule cloud, and an x-extent large enough that the molecules spend several decay times in the molecule beam.

5. The $\left|H, J=1, M=\pm 1, \tilde{\mathcal{N}}\right\rangle \rightarrow |e, J\,M=0, \tilde{\mathcal{P}}\rangle$ transition is reasonably spectroscopically resolved from other transitions for reasonable electric fields in the range of $\mathcal{E} \sim 10 - 1000\,\mathrm{V/cm}$.

Based on some recent spectroscopy [96], we determined that the $|I,\ |\Omega| = 1\rangle$ state satisfies criteria 1-3 and implementation of this new detection transition would not only eliminate any concerns that we had regarding scattered light from the STIRAP lasers interfering with the laser-induced fluorescence signal, but would enable increased sensitivity of the measurement to the electron EDM in ACME II relative to ACME I. The $|I\rangle$ state has a branching ratio to $|H\rangle$ of about 5%, satisfying condition 1, and a branching ratio to $|X\rangle$ of about 91% [96], satisfying condition 2 – in fact, this is larger than approximately 70% branching ratio from $|C\rangle \rightarrow |X\rangle$ implying that we would get more photons per molecule if using the I state. The $|I\rangle \rightarrow |X\rangle$ transition is at $\lambda = 512\,\mathrm{nm}$ at which PMTs can be obtained with a quantum efficiency of 25%, which is a significant improvement relative to the 10% quantum efficiency of the PMTs that were used in ACME I to detect 690 nm [5]. Additionally, the $|I\rangle$ state has a radiative lifetime of about $\tau_I \approx 115\,\mathrm{ns}$, satisfying condition 3, which is faster than the $|C\rangle$ state with a lifetime of $\tau_C \approx 500\,\mathrm{ns}$ which implies that optical pumping through the I state can progress more quickly than in ACME I. As a result it may be possible to use a narrower laser beam and a faster polarization switching rate and still obtain the same efficiency of optical pumping which can make more efficient use of a fixed amount of laser power.

5. Part numbers for the PMTs used in ACME I and ACME II

5.5.2 Measurements of the $H \rightarrow I$ transition

Since the $|I\rangle$ state seemed like a promising state read-out detection transition we sought to find the $|H, J = 1\rangle \rightarrow |I, J = 1\rangle$ transition frequency down to the MHz precision level so that we could address the transition in the molecular beam. This transition had previously been identified in high-temperature emission spectra [50] and the transition frequency determined to be in the vicinity of $14222.46 \pm .02\,\mathrm{cm}^{-1}$. We searched for this transition in the buffer gas cell with an overlapped 943 nm and 703 nm diode lasers. This first laser serves to optically pump on the $|X, J = 1, M = 0\rangle \rightarrow |A, J = 0, M = 0\rangle$ from which a significant fraction of the population decays into $\left|H, J = 1, M = 0, \pm 1, \tilde{\mathcal{P}} = -\right\rangle$. Then we detect the microwave absorption by laser induced fluorescence with optical pumping with the 703 nm laser on the $\left|H, J = 1, M, \tilde{\mathcal{P}} = -1\right\rangle \rightarrow \left|I, J = 1, M, \tilde{\mathcal{P}} = +1\right\rangle$ transition. We identified this signal at the $\approx .5\%$ absorption level with a signal to noise ratio of about 1 – this data is shown in figure 5.5.2 with a Gaussian fit to the observed line indicating a line center of about $14222.4561 \pm .0002\,\mathrm{cm}^{-1}$ which is consistent with the earlier measurement.

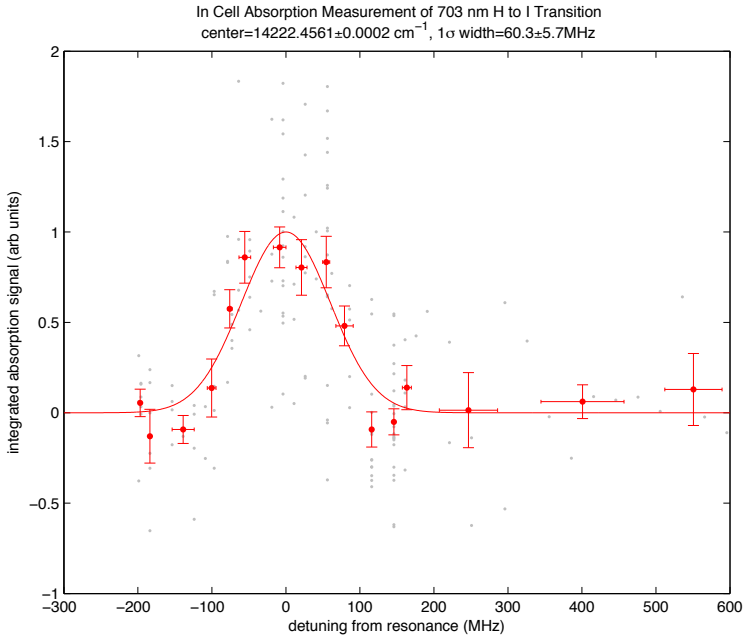

Figure 5.6: Absorption of 703 nm laser light on the $\left|H, J = 1, \tilde{\mathcal{P}} = -1\right\rangle \rightarrow \left|I, J = 1, \tilde{\mathcal{P}} = +1\right\rangle$ transition in the buffer gas cell after populating H by optical pumping on $|X, J = 1, M = 0\rangle \rightarrow |A, J = 0, M = 0\rangle$. The line center is identified to be $1422.4561 \pm .0002\,\mathrm{cm}^{-1}$.

After identifying the transition frequency, we moved on to measurements of the tran-

sition dipole moment on the $H \rightarrow C$ transition. The lifetime and branching ratio measurements suggested a molecule fixed transition dipole moment of $d_{IH}^{\mathrm{mol}} = .69\,\mathrm{Debye}$ [96]. For the purposes of the ACME experiment, we sought to measure the particular transition dipole moment d_{IH} for the transition that we would drive for the state read-out:

$$d_{IH} \equiv \left| \left\langle I, J=1, M=0, \tilde{\mathcal{P}} \left| er_0 \right| H, J=1, M=\pm 1, \tilde{\mathcal{N}} \right\rangle \right| = \frac{1}{\sqrt{8}} d_{IH}^{\mathrm{mol}} \tag{5.17}$$

We performed this measurement in the stem region between the beam source and the interaction region in a region by once again populating the $|H, J=1\rangle$ state with optical pumping with the 943 nm laser, followed by optical pumping with the 703 nm laser. We measured the resulting fluorescence at 512 nm integrated over the molecule pulse and varied both the laser power and detuning so that the detuning was swept through resonance and the power was swept through saturation. These Doppler scans were taken over the course of about an hour, which is long compared to the timescale of molecule number fluctuations from the beam source, so this was a very significant source of noise in this data. Another set of data was taken by sitting on resonance and sweeping the power through saturation quickly enough so that the effect of molecule number fluctuations were reduced and the power values were randomized such that a drift in molecule number results in added noise rather than in a systematic error in the measurement of the saturation intensity. To calibrate the measurement, the laser power was measured before the laser beam entered into the vacuum chamber, and the extent of laser power reduction before interaction with the molecules was left to estimation and the uncertainty in this estimation is a significant source of systematic uncertainty in this measurement. The data that was taken in shown in figure 5.5.2.

These measurements were performed in an electric field with magnitude of roughly $(300V/.75\mathrm{in}) = 158\,\mathrm{V/cm}$ which is sufficient fully mix the opposite parity states in both H and I. We observed a Doppler width of about $2\pi \times 4.5\,\mathrm{MHz}$ which was much bigger than the expected Doppler width of $2\pi \cdot 3.1\,\mathrm{MHz}$ given the collimation geometry used for this experiment. We determined that there was a large variation in the magnitude of the electric field across the molecule beam since the electric field plates used in this experiment had a separation comparable to both width of the plates and the size of the molecule beam which resulted in *Stark broadening* of the transition.

The analysis of the data that is presented in figure 5.5.2 was performed by creating

integrating the Master Equation for a two level system with the empirically obtained spatial intensity profile of the laser, and compare the acquired data with these simulations to generate a Bayesian posterior probability distribution for the transition dipole matrix element d_{IH}, and the Doppler width σ_D assuming that the data is normally distributed about mean values for the true model. After integrating out σ_D as a nuisance parameter, we find that $d_{IH}^{\text{mol}} \approx 1.0 \pm 0.3$ Debye, which is notably higher than, but plausibly consistent with the estimation based on the measured branching ratios.

Given the measurement of the transition dipole moment and after having decided on a beamline geometry as described in section 5.4.1 we sought to determine the required power to drive optical pumping to completion in the state read-out region with polarization switching in ACME II. In order to do this, we performed 3D simulations with molecule trajectories that were randomly chosen from the beam source probability distribution that was previously described that were consistent with geometric collimation constraints. For the molecules admitted to the detection region, we integrated the Master Equation to simulation the polarization-switched optical pumping in the state readout region with a Gaussian laser intensity profile with a 1σ width of 1 mm in the $\hat{x}$ direction, and a 1σ width in the $\hat{y}$ direction that was chosen such that all geometric molecule trajectories fall within $\pm 1\sigma$ of the center of the beam. The results of these simulations, shown in figure 5.5.2, indicate that we can drive optical pumping to completion with the selected beamline geometry and with a fraction of the available few Watts[6] of laser power at 703 nm. Later measurements of optical pumping in the state readout region at 703 nm [128] are consistent with these simulations with respect to the power required to drive optical pumping to completion and the measured Doppler widths.

5.5.3 Additional Improvements to the Collection Optics

As previously mentioned in section 5.4.1, the change in the beamline geometry results in a decrease in the light collection efficiency. The increase in the separation between the electric field plates reduces the solid angle of the detection region subtended by the collection optics. After re-optimization of the angle and packing of the collection optics lenses with a new mounting structure, the efficiency of the collection lenses was estimated to be around 25%,

6. We generate about 4 W of 703 nm light using an M Squared SOLSTIS Ti:Sapph laser seeded by a Lighthouse Photonics Sprout.

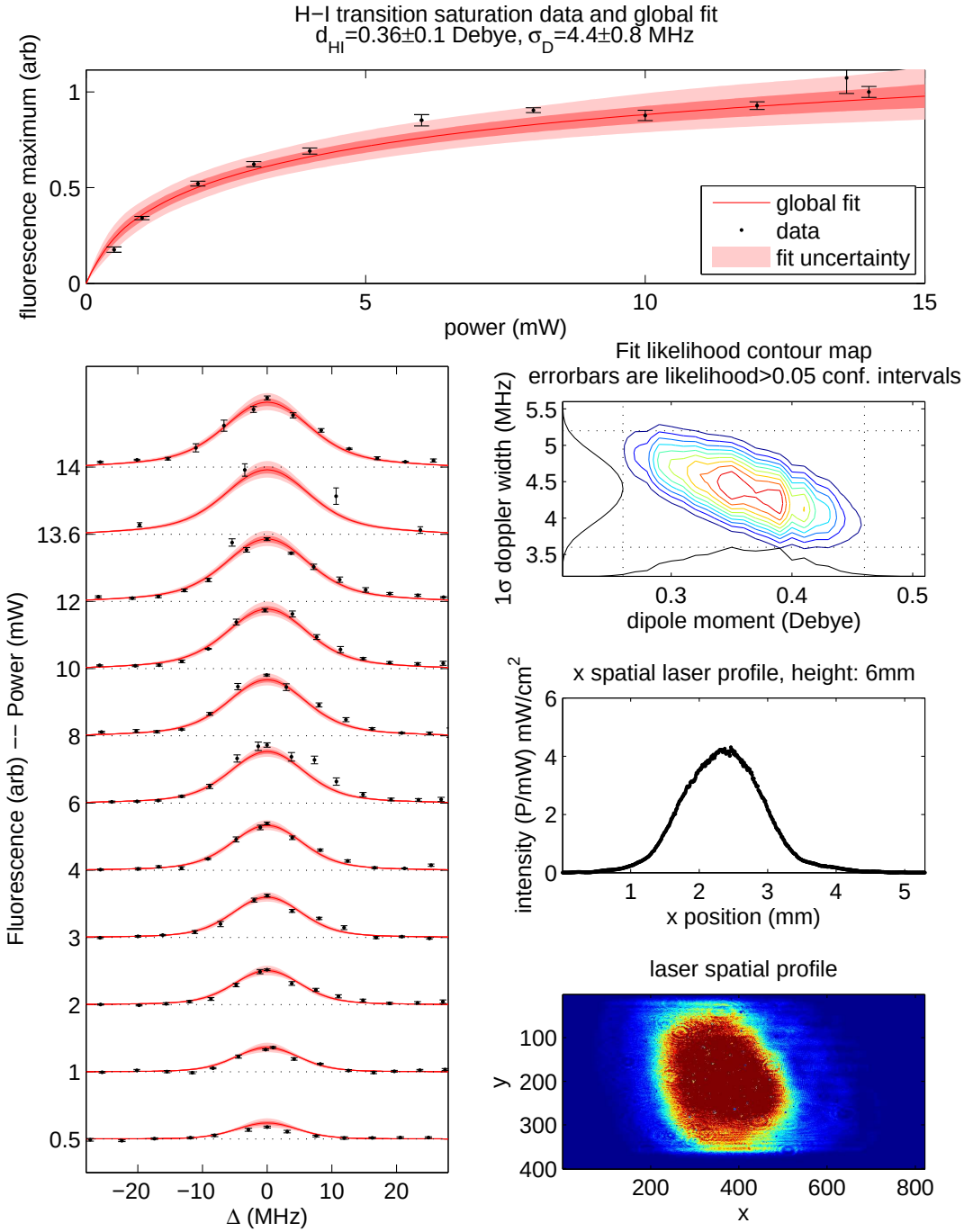

Figure 5.7: Measurements of the transition dipole moment on the $\left|H, J=1, M=\pm 1, \tilde{\mathcal{N}}\right\rangle \rightarrow \left|C, J=1, M=0, \tilde{\mathcal{P}}\right\rangle$ transition in a test apparatus in the stem region. Saturation measurements are shown as data points in black. A global fit to all of the data is shown in red - the fit functions are derived from Master Equation integration taking into account the measured spatial intensity profile of the laser shown on the bottom right. The contour plot in the middle right shows the likelihood function for the two free parameters in this model - the transition dipole moment and the Doppler width.

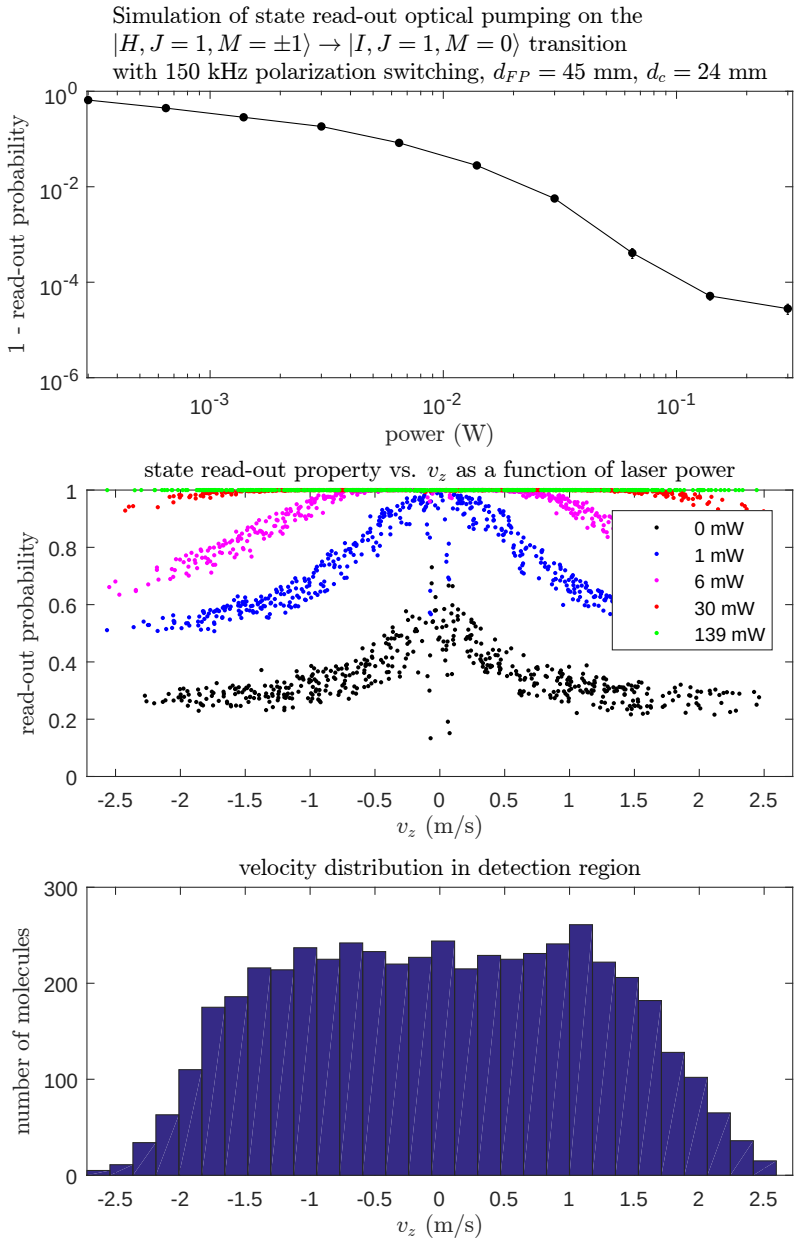

Figure 5.8: Results of a Master Equation simulation of optical pumping in the state readout region with molecule trajectories that are consistent with our model of the beam source and with the geometric constraints along the beamline. Top: Fraction of molecules that are not optically pumped in the state readout-region as a function of increasing laser power. Middle: Fraction of molecules that are optically pumped as a function of molecule velocity v_z along the laser propagation direction. Bottom: Distribution of transverse velocities v_z in the state readout region.

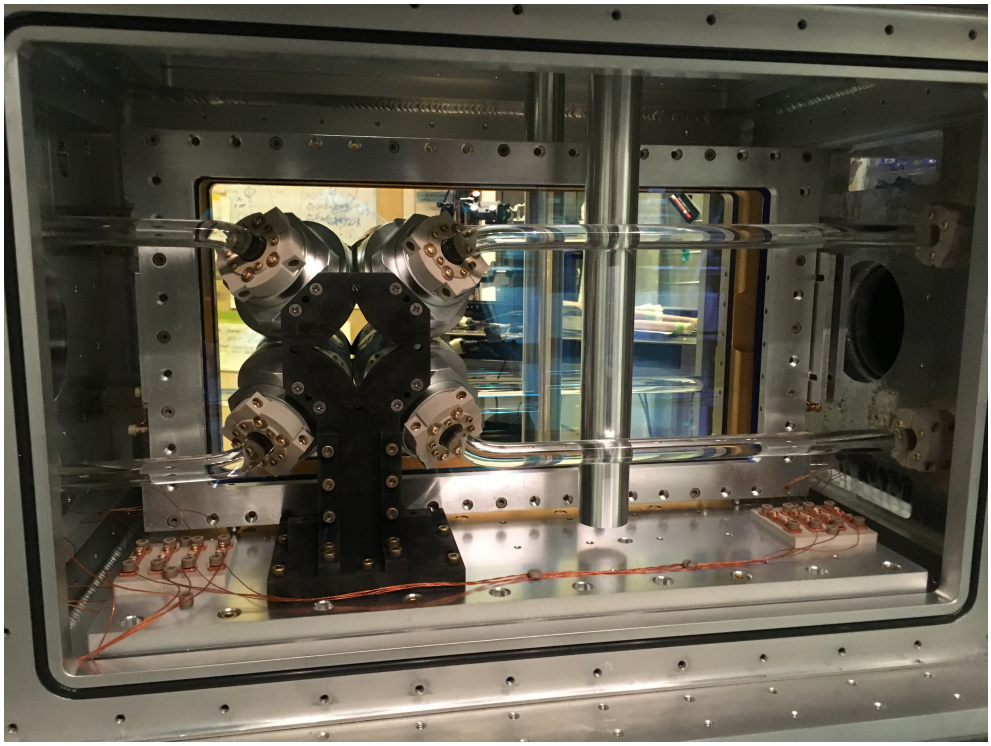

Figure 5.9: A Photograph of the ACME II collection optics system installed in the interaction region vacuum chamber.

which is about 75% as efficient as it was in ACME I [125].

The ACME II light collection system also introduced bent fused silica light pipes that steer the fluorescence photons out of the vacuum chamber, replacing fiber bundles which were previously limited in transmission by the fiber packing fraction of about 65% [158]. This scheme necessitated an increase in the number of light pipe vacuum feedthroughs and the number of photodetectors from the two that were used in ACME I, on which light that had been incident on multiple collection lenses could be combined, to eight in ACME II, one light pipe feedthrough and one photodetector for each collection lens. Additionally in ACME II, the increased size of the molecule cloud leads to an increase in the phase space density of the light that must be collected. However, since we increased the total photodetector area in ACME II this increase in phase space density is not an issue.

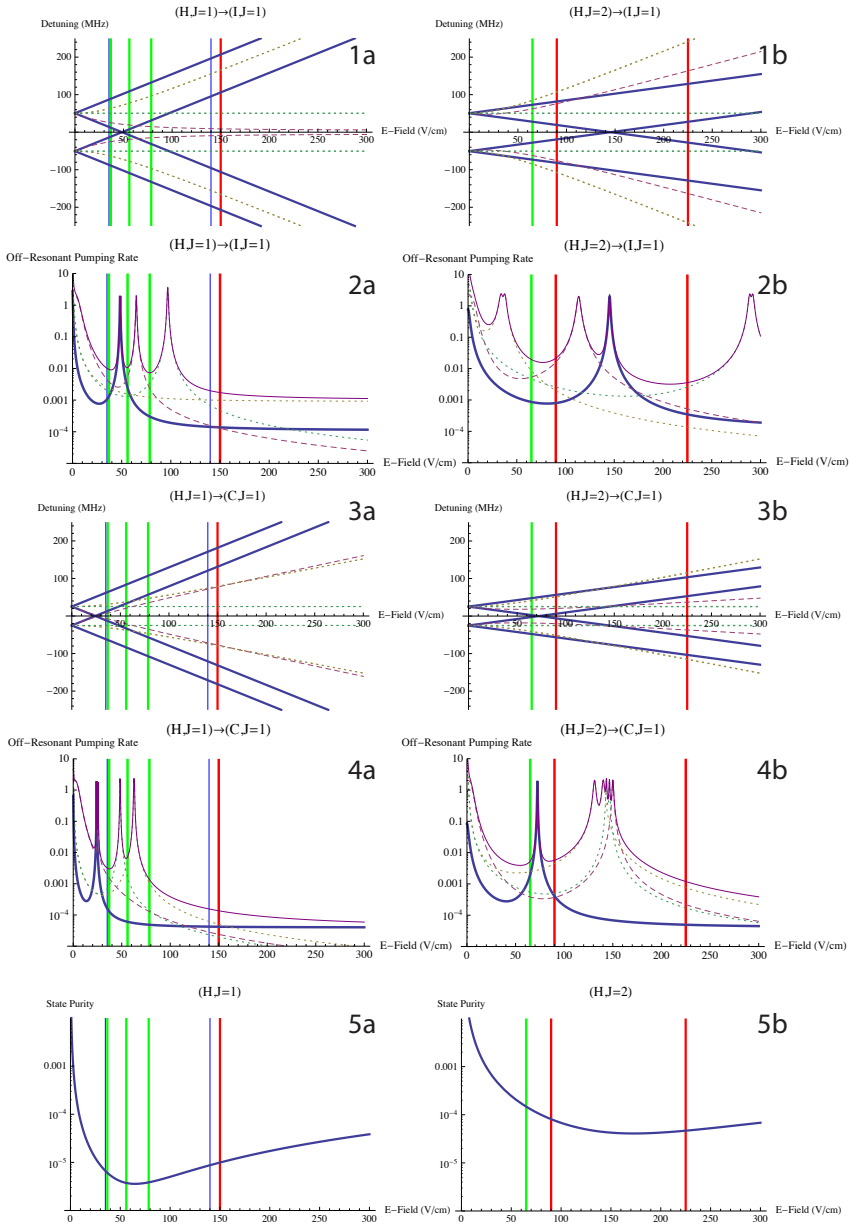

Figure 5.10: Illustration of the selection criteria used to select an electric field magnitude at which to operate the experiment. The different colors and linestyles correspond to different classes of transitions. The vertical green lines correspond to recommended electric field values that can be achieved with the ACME I voltage supply. The vertical red lines correspond to electric field values that are recommended, but require the higher voltage ACME II supply. The thin vertical blue lines correspond to the electric field values that were used in ACME I. The left column pertains to $|H, J = 1\rangle$, and the right column pertains to $|H, J = 2\rangle$. **1.** $|H\rangle \rightarrow |I\rangle$ transition detunings vs. electric field magnitude. **2.** Sum of off resonant optical pumping rates for $|H\rangle \rightarrow |I\rangle$ vs. electric field magnitude. **3.** $|H\rangle \rightarrow |C\rangle$ transition detunings vs. electric field magnitude. **4.** Sum of off resonant optical pumping rates for $|H\rangle \rightarrow |C\rangle$ vs. electric field magnitude. **5.** The deviation in the state from $|H, J = 1, M, \tilde{\mathcal{N}}\rangle = |H, J = 1, M, \Omega = M\tilde{\mathcal{N}}\tilde{\mathcal{E}}\rangle$. In **2.** and **4.** the top solid purple curve corresponds to the sum of the off-resonant optical pumping rates for all of the transition classes.

Detection Modification	Signal Gain
Bent light pipes and other collection optics upgrades	1.8×
Increased quantum efficiency PMTs at 512 nm	2.5×
Increased detection transition branching ratio at 512 nm	1.25×
Transmission of 512 nm through Electric Field Plates	0.75×
All Detection Improvements	$3.5 - 4.5\times$

Table 5.2: Summary of signal gain from changes in molecule detection in ACME II relative to ACME I.

5.6 Electric Fields

5.6.1 Selection of Electric Field Magnitude

In ACME I we set up the experiment so that we could operate at two values of the electric field magnitude, $\mathcal{E} \approx 35, 140\,\mathrm{V/cm}$. The higher electric field magnitude was selected fairly arbitrarily at the start of ACME I. The second electric field magnitude was carefully chosen so that it would be at least a factor of a few different from the higher electric field magnitude, would be achievable with the existing voltage power supplies, and would result in state preparation and state read-out transition frequencies on $\left|H, J=1, M=\pm1, \tilde{\mathcal{N}}\right\rangle \rightarrow \left|C, J=1, M=0, \tilde{\mathcal{P}}\right\rangle$ that would be as far from degeneracy with nearby transitions as possible. If there were other transitions that were nearly degenerate, the state preparation or state readout schemes could interact with these other transitions leading to background fluorescence that can reduce contrast, or lead to interference effects that could result in systematic errors.

In ACME II, due to the increased complexity of the experiment, the selection criteria for a suitable electric field magnitude are more strict, so we decided to formalize the selection process beyond that which drove the analogous decision during ACME I. Here are the factors that are to be taken into account during the selection process:

1. We would like the $\left|H, J=1, M=\pm1, \tilde{\mathcal{N}}\right\rangle \rightarrow \left|I, J=1, M=0, \tilde{\mathcal{P}}\right\rangle$ state read-out transition frequencies to be as far as possible from other nearby transition frequencies.

2. We would like the $\left|H, J=1, M=\pm1, \tilde{\mathcal{N}}\right\rangle \rightarrow \left|C, J=1, M=0, \tilde{\mathcal{P}}=-1\right\rangle$ STIRAP transition frequencies to be as far as possible from other nearby transition frequencies.

3. We would like the prepared spin state in $|H\rangle$ to be as close to a pure rigid rotor $|J, M, \Omega\rangle$ state as possible.

4. We require that the electric field magnitude be acheiveable with the ACME II electric field power supply[7], which can supply electric fields up to around 200 V/cm, and we would prefer that it be achievable also with the ACME I power supply which can supply electric fields up to around 80 V/cm with the ACME II field plates separation of $d_{\mathrm{FP}} \approx 45\,\mathrm{mm}$.

5. We prefer that there be at least two viable electric field magnitudes that differ by at least a factor of 2×.

All of the states that are being considered in this section, H, C, I all have angular momentum projection along the nuclear axis of $|\Omega| = 1$ which have omega doublet structure. Within these states the Stark shifts, in the limit that the scale of the shifts are small compared to the rotational splitting, $D\mathcal{E}/B_R \ll 1$, for a state $|A, J, M, \tilde{\mathcal{N}}\rangle$ are given by

$$E\left(A, J, M, \tilde{\mathcal{N}}\right) = -\tilde{\mathcal{N}}\sqrt{\left(\frac{1}{4}\Delta_A J\left(J+1\right)\right)^2 + \left(\frac{M D_A^{\mathrm{mol}}\left|\mathcal{E}\right|}{J\left(J+1\right)}\right)^2}, \tag{5.18}$$

where I have defined Δ_A is the zero field omega doublet splitting in $J = 1$ of state A, and D_A^{mol} is the molecule fixed electric dipole moment of the state A. The detuning of a transition between state $\left|e, J, M, \tilde{\mathcal{N}}\right\rangle$ and state $\left|g, J', M', \tilde{\mathcal{N}}'\right\rangle$ can be defined as

$$\Delta E\left(e, J, M, \tilde{\mathcal{N}};\, g, J', M', \tilde{\mathcal{N}}\right) = E\left(e, J, M, \tilde{\mathcal{N}}\right) - E\left(g, J', M', \tilde{\mathcal{N}}'\right). \tag{5.19}$$

Using the molecular constants listed in table 5.6.1, these transition frequencies are plotted for $e = C, I$, $g = H$, $J = 1$, $J' = 1, 2$ in figures 5.6.1 1a, 1b, 3a, 3b.

Parameters	Δ_A	D_A	B_A	$\tau_A = 1/\gamma_A$
H	$2\pi \times .362\,\mathrm{MHz}$	$2\pi \times 2.086\,\mathrm{MHz}/V/\mathrm{cm}$	9.78463 GHz	2 ms
I	$2\pi \times 101\,\mathrm{MHz}$	$2\pi \times 2.1\,\mathrm{MHz}/V/\mathrm{cm}$		115 ns
C	$2\pi \times 50.4\,\mathrm{MHz}$	$2\pi \times 1.0\,\mathrm{MHz}/V/\mathrm{cm}$		500 ns

Table 5.3: Molecular parameters that were used in making these plots

In our application, we drive Lambda transitions of the form: $\left|g, J', M' = \pm 1, \tilde{\mathcal{N}}' = \pm 1\right\rangle \rightarrow \left|e, J, M = 0, \tilde{\mathcal{N}} = \pm 1\right\rangle$. All of the other transitions that are possible are unnecessary, and

7. Apex PA89a powered by Acopian supplies and controlled with a BiasDAC.

could possibly lead to unknown systematic errors or reduced sensitivity of the measurement. Hence we would like the unwanted transition detunings to be as far away from the intentionally driven transition as possible. Motivated by the classical optical pumping rate for a two level system, the metric that I have selected to quantify distance between two transition frequencies is a max-normalized Lorentzian function,

$$L\left(\Delta,\gamma\right)=\frac{\left(\gamma/2\right)^{2}}{\Delta^{2}+\left(\gamma/2\right)^{2}}, \tag{5.20}$$

where γ is the natural linewidth of the transition that is intended to be driven and Δ is the difference between the detunings of the transition that is intended to be driven and an unwanted transition. In order to quantify goodness of a given electric field value, I find the sum of the distance factors $L\left(\Delta,\gamma\right)$ for the difference in detunings Δ between every intentionally driven transition frequency, and every other transition frequency that is nearby.

$$\Gamma\left(e,J;\,g,J'\right)=\sum_{\substack{\tilde{\mathcal{N}},\tilde{\mathcal{N}}',\tilde{\mathcal{N}}'',\tilde{\mathcal{N}}'''=\pm1\\ M'',M'''=-J,\ldots,+J}}\left(1-\delta_{\tilde{\mathcal{N}},\tilde{\mathcal{N}}''}\delta_{\tilde{\mathcal{N}}',\tilde{\mathcal{N}}'''}\delta_{M,M''}\delta_{M',M'''}\right)L\left(\Delta E_{eg',e''g'},\gamma_{e}\right) \tag{5.21}$$

$$\Delta E_{eg',e''g'}=\Delta E\left(e,J,M=1,\tilde{\mathcal{N}};g,J',M'=0,\tilde{\mathcal{N}}'\right)-\Delta E\left(e,J,M'',\tilde{\mathcal{N}}'';g,J',M''',\tilde{\mathcal{N}}'''\right) \tag{5.22}$$

Here, I omit any weighting factor for each pair of transitions (which could take into account the extent to which a given transition may stronger or weaker due to the transition matrix elements, or forbidden due to the requirement of imperfect polarization or an even parity transition operator to drive, etc.) indicating that I would like to be equally far from all possible transition level crossings regardless of their likelihood for being driven. I have performed this calculation of $\Gamma\left(e,J,g,J'\right)$ for $e=C,I,\ g=H,\ J=1,\ J'=1,2$, for subsets of unwanted transitions, displayed in figures 5.6.1 2a, 2b, 4a, 4b and for all unwanted transitions in figure 5.6.1.

In addition to distance to nearly degenerate transitions, we also take into the molecular state purity in deciding on an electric field magnitude. When we apply an electric field that is large enough $\Delta_A \ll D_A\mathcal{E} \ll B_A$, the molecule state becomes fully polarized and the system eigenstates are nearly perfect rigid rotor basis states $|J, M, \Omega\rangle$. Nevertheless there is always some mixing between opposite molecular orientation states corresponding to a deviation from the molecule being fully polarized and there is also some Stark rotational mixing. At first order in perturbation theory in both of these effects, the eigenstates of the Stark Hamiltonian can be described as:

$$\left|H, J, M, \tilde{\mathcal{N}}\right\rangle \approx \tag{5.23}$$

$$+ \left|H, J, M, \Omega = +\tilde{M}\tilde{\mathcal{N}}\tilde{\mathcal{E}}\right\rangle \tag{5.24}$$

$$+ \tilde{\mathcal{N}}\frac{1}{8}\left[J\left(J+1\right)\right]^2 \frac{\Delta_H}{|MD_H\mathcal{E}|}\left|H, J, M, \Omega = -\tilde{M}\tilde{\mathcal{N}}\tilde{\mathcal{E}}\right\rangle \tag{5.25}$$

$$- \tilde{\mathcal{E}}\frac{1}{2}\frac{1}{\left(J+1\right)^2}\sqrt{\frac{\left(\left(J+1\right)^2 - M^2\right)\left(\left(J+1\right)^2 - \Omega^2\right)}{\left(2J+1\right)\left(2J+3\right)}}\frac{|D_H\mathcal{E}|}{B_H}\left|H, J+1, M, \Omega = +\tilde{M}\tilde{\mathcal{N}}\tilde{\mathcal{E}}\right\rangle \tag{5.26}$$

$$+ \tilde{\mathcal{E}}\frac{1}{2}\frac{1}{J^2}\sqrt{\frac{\left(J^2 - M^2\right)\left(J^2 - \Omega^2\right)}{\left(2J-1\right)\left(2J+1\right)}}\frac{|D_H\mathcal{E}|}{B_H}\left|H, J-1, M, \Omega = +\tilde{M}\tilde{\mathcal{N}}\tilde{\mathcal{E}}\right\rangle \tag{5.27}$$

$$+ \ldots \tag{5.28}$$

To ensure maximal sensitivity to the electron EDM and to maintain simplicity in the experiment, we would like these eigenstates to correspond as closely as possible to the perfect rigid rotor states. Hence, I define the state impurity as

$$\Xi\left(H, J, M, \Omega\right) = 1 - \left|\left\langle H, J, M, \tilde{\mathcal{N}}|H, J, M, \Omega = \tilde{M}\tilde{\mathcal{N}}\tilde{\mathcal{E}}\right\rangle\right|^2, \tag{5.29}$$

which we can attempt to minimize with respect to our choice for the electric field magnitude. This state purity metric is displayed both for $|H, J = 1, 2\rangle$ in figures 5.6.1 5a, 5b and figure 5.6.1.

To combine all of the factors described above quantitatively, I created an fairly arbitrary

goodness metric $G(J, J')$ which should be minimized in the selection of an electric field,

$$G\left(J, J'\right) = \Gamma\left(I, J, H, J'\right)\Gamma\left(C, J, H, J'\right)\Xi\left(H, J', M = 1, \Omega = 1\right)^2 \tag{5.30}$$

which is displayed in figure 5.6.1 for the cases in which we perform the measurement $\left|H, J, M = \pm 1, \tilde{\mathcal{N}}\right\rangle$ with J =1 or 2. Based on this goodness metric, the recommended electric field magnitudes are listed in table 5.6.1.

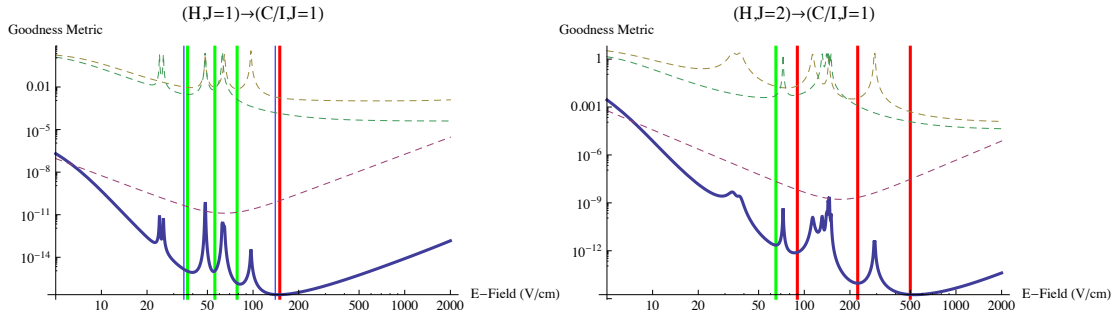

Figure 5.11: Here is a "goodness" metric that was artificially constructed decide which electric field magnitudes would be best to use as a running configuration for both $|H, J = 1\rangle$ (left) and $|H, J = 2\rangle$ (right). Here the red dashed line corresponds to the square of the $|H\rangle$ state Hunds case (c) basis state purity. The yellow dashed curve corresponds to the off-resonant optical pumping rate for $|H\rangle \rightarrow |I\rangle$ and the green dashed curve corresponds to the off-resonant optical pumping rate for the $|H\rangle \rightarrow |C\rangle$ transition. The solid blue line is the product of the three dashed lines above it and is considered to be the "goodness" function (such that the smaller this value is, the better the electric field value is as a candidate electric field magnitude).

Measurement	Recommended $\mathcal{E}-$field Magnitudes (V/cm)
ACME I, $\|H, J = 1\rangle$	**35, 140**
ACME II, $\|H, J = 1\rangle$	**37, 56, 78.5,** 150
ACME II, $\|H, J = 2\rangle$	**65,** 90, 225

Table 5.4: Recommended electric field magnitudes in ACME II. Those displayed in bold are achievable with both the ACME I and ACME II electric field power supplies, and those not in bold are achievable with only the ACME II power supply.

Chapter 6

Mapping Electric and Magnetic Fields

> Acker – Hit the Net, do a search for, oh, two years ought to do it. Any and all, like, "weird news" ... Danni, get me the brightest kids from the Field Theory class and design a computer model of an electromagnetic field ... Map out the anomalies that Acker finds and grunt out the equations.
>
> The Core

6.1 Interferometric Measurements of the Electric Field Plate Spacing

We used an interferometric method to aid in precisely setting the spacing between the two electric field plates which are used to apply a uniform electric field to the molecules in the spin precession region, and to provide a first estimate as to the possible spatial homogeneity and stability of this field given residual variations in the separation as a function of space and time. Similar measurements were performed previously to set the electric field plate spacing in ACME I as described in section [158]. In this section, I will present the methods and data analysis used for these measurements in ACME II, which differ from previous measurements with respect to some details, and I will present the conclusions drawn from these measurements.

The interferometric separation measurement is performed using a "white light" Michel-

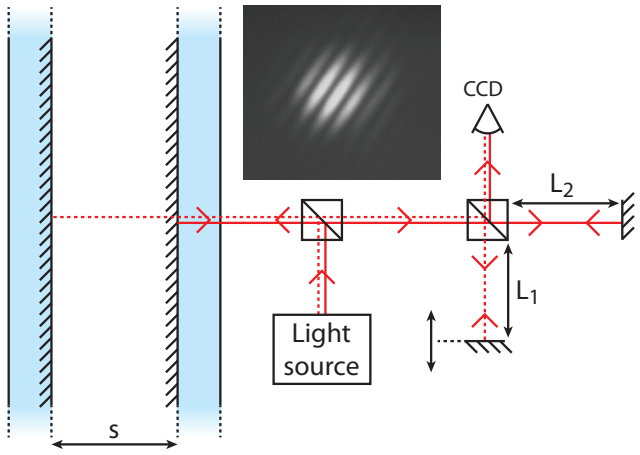

Figure 6.1: Schematic of the apparatus used to perform an interferometric measurement of the electric field plate separation. A spectrally broad light beam is reflected perpendicularly off the field plates and passes into a conventional Michelson interferometer setup with one fixed arm (length L_2) and one movable arm (length L_1). An example of a pair of beam paths of interest is shown as solid and dashed red lines. If the two paths are slightly tilted relative to each other, a spatial interference pattern (inset) is observed on the CCD detector when the path length difference between the two beams is less than the coherence length, e.g. $L_1 + s - L_2 < L_c$.

son interferometer [131]. A schematic of the setup is shown in figure 6.1. A collimated light source with coherence length ℓ_c is directed at normal incidence through the electric field plates in the $\hat{z}$ direction. As a light source, we use a broadband superluminescent diode[1] with a nominal coherence length $\ell \approx 15\,\mu$m. This results in multiple reflected beams, but we will restrict our discussion to the reflections from the ITO conducting surfaces, which are separated by a distance s, as these are of primary interest and were efficiently experimentally isolated from all others. The reflected beams passed into a Michelson interferometer with one arm of fixed length, L_2, and one with length adjustable via a motorized micrometer translation stage[2], L_1, with a CCD camera at the observation port. Interference is observed on the camera when the length of multiple light paths from the source to the camera differ by $\lesssim \ell_c$. The interferometer is intentionally slightly misaligned so that several fringes of interference can be observed as a spatial variation of the light in intensity in the camera image as can be seen in the inset of figure 6.1. The interference condition is met when $L_1 = L_2$ (a reflection from a single surface self-interferes in the interferometer) or when

1. QPhotonics QSDM-680-2.

2. Zaber T- NM17A04SKT02 stepper motor

$L_1 = L_2 \pm s$ (reflections off of the two surface interfere with each other). A measurement of the difference in the movable arm position L_1 between observing two of these interference conditions are sufficient to measure s. Usually, we will measure the "center peak", when $L_1 = L_2$, once and then we will measure the "separation peak", when $L_1 = L_2 + s$, as a function of x and y to extract $s\,(x, y)$. The resulting data is shown in figure 6.1.

The size of the observed interference fringe contrast is quantified by evaluating the 2d power spectrum of the CCD image and integrating over a fixed region of the spectrum which contains the periodicity and orientation of the interference fringes. The interferometer is aligned so that the interference fringes appear at roughly 45° with respect to the camera pixel grid axes since those orientations have a higher background in the power spectrum. A scan of about 80 of these fringe contrast measurements is acquired while moving the interferometer arm to positions to randomly ordered linearly spaced points across the separation peak resonance. This data is fit to a Gaussian fit function, which fits the data quite well, to extract an estimate the separation s between the electric field plates. This measurement is repeated at each point on a rectangular grid in the xy plane, with points separated by about $1.5 - 2\,\text{cm}$.

A final map of the spatial variation in the separation of the ACME II electric field plates is shown in figure 6.1. This data shows that there a bend in the plates along the x direction of magnitude $\approx 9.5\,\mu\text{m/cm}^2$ and there is a significant xy twist – both which were characteristics that were observed in the ACME I electric field plate assembly [158]. This observed variation in the electric field plates is about $10^{-3}\times$ the overall separation. Given that we will likely operate the experiment in ACME II at $\mathcal{E} \approx 80\,\text{V/cm}$ (see section 5.6.1 for a discussion), the variation in the electric field is likely to be around $\delta\mathcal{E} \approx 80\,\text{mV/cm}$ throughout the spin precession region.

This observation was surprising to us given the history of investigations into the source in the ACME I electric field plate bend. After ACME I we found that a bend along the x direction in the electric field plates was correlated with the tension in the field plate clamping mechanism. In fact, a 1 mm bend across the gold-coated copper clamps lead to an order of magnitude increase in the size of the bend. We attempted to eliminate this source of bending by flattening the gold-coated copper clamps and inserting a squishy Viton gasket in between the gold-coated copper clamps and the electric field plates to distribute the clamping force. However, even after the introduction of this gasket the bend remained

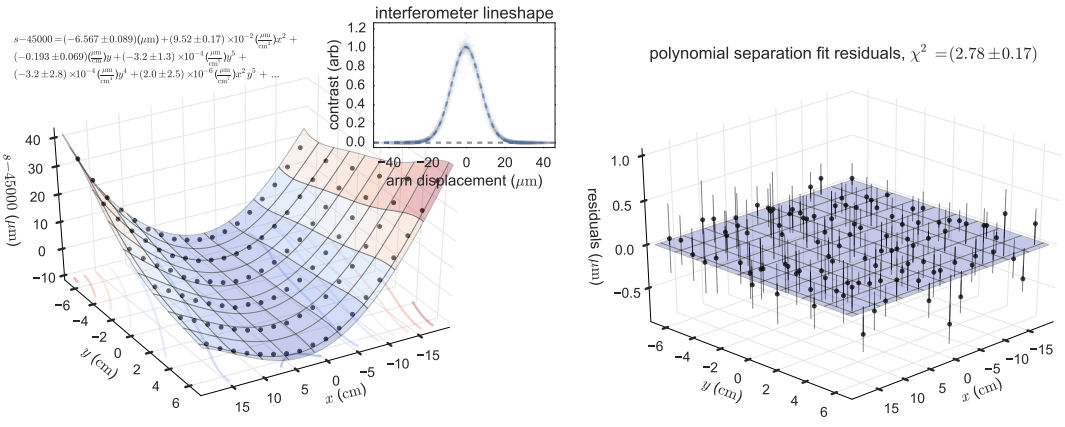

Figure 6.2: Map of the electric field plate separation obtained from white light interferometry. Left: Measurements of the spatial variation in the separation between the electric field plates as a function of x and y dominantly show a bend along the x direction, of magnitude approximately equal to that observed in ACME I [158], in addition to an xy "twist". Inset: An aggregation of all of the interferometer fringe contrast scans scaled by the fit amplitude and shifted by the fit center, for Gaussian fits to the data displays the coherence function of the light source and the typical signal to noise ratio for each scan. Right: The residuals of the data shown on the right with respect to the 2d polynomial fit function show that the fit is good, but the measured $\chi^2 > 1$ indicates that there is some source of noise, apart from the uncertainty in the extraction of the center of each contrast scan, that has not been accounted for. The uncertainties in the extracted fit coefficients have been rescaled in attempt to account for this additional noise.

even in the limit in which the electric field plates were hardly being clamped. This lead us to suspect that there was a bend in the glass itself and that the ACME II plates, which are made from a different material and specified to have a flatness that is much better than the observed bend, would be unlikely to exhibit the same feature. Hence, it was surprising when we observed the same size bend in the electric field plates in ACME II, and the source of the bend still remains unclear, but is more likely than before to be originating from the clamping structure.

Spatial variation of $\vec{\mathcal{E}}$ could lead to the accumulation of geometric phases during the spin precession measurement [134, 163]. There are known mechanisms by which such phases can contribute to electron EDM-like systematic errors, as described in section 3.3, though simple estimates show that these effects are several orders of magnitude below the sensitivity of this measurement. However, additional $\mathcal{E}$-field imperfections such as non-reversing fields, due to e.g. variations in the ITO coating, which could produce patch potentials, are known to contribute to electron EDM-like systematic errors and are only revealed by more direct measurements of the electric field which are discussed in the section 6.2.

We also measured some time variation in the separation between the electric field plates on long time scales as is shown in figure 6.1. During this measurement, we fixed the measurement position to the center of the electric field plates, $x = 0$, $y = 0$, and we alternated between measuring the separation peak position and the center peak position to account for possible long term drifts in the alignment of the interferometer or long term hysteresis in the stepper motor. There was some evidence that the drift in the room temperature was correlated with the drift in the electric field plate separation, but the evidence was certainly not conclusive.

6.2 Mapping the Electric Field with Microwave Depletion Spectroscopy

In ACME I, after having identified, as described in section 4.3, that an AC Stark shift phase can couple to the non-reversing component of the electric field, $\mathcal{E}^{\mathrm{nr}}$, to result in a systematic error in the EDM measurement, we required a method to measure $\mathcal{E}^{\mathrm{nr}}$ so that we could evaluate the size of the corresponding systematic error. We developed three methods to measure the $\mathcal{E}$-field, each of which did so by measuring the Stark shift or changes in the

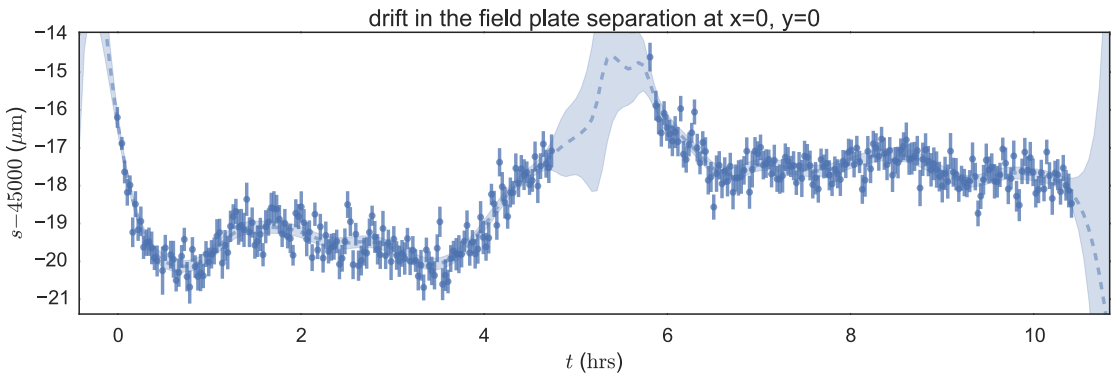

Figure 6.3: Interferometric measurements of drift in the field plate separation over time at the position $x = 0$, $y = 0$ in the center of the electric field plates. The dark blue points with errorbars are measurements of the separation. The light blue shaded region are confidence intervals for a non-parametric local linear regression fit to the data which attempts to extrapolate what the separation might have been at times when there was missing data.

Stark shift in the $|H, J = 1, M = \pm 1, \tilde{\mathcal{N}}\rangle$ levels:

1. Raman spectroscopy by driving the two photon $|B(\hat{x}), \tilde{\mathcal{N}}, \tilde{\mathcal{P}}\rangle \rightarrow |C, J = 0, M = 0, \tilde{\mathcal{P}}\rangle \rightarrow |B(\hat{x}), -\tilde{\mathcal{N}}, \tilde{\mathcal{P}}\rangle$ transition, described in [77], enabling measurements in regions of optical access, $|\mathcal{E}(x_{\text{prep}})|$, $|\mathcal{E}(x_{\text{read}})|$.

2. Off-resonant measurements of the correlated contrast $\mathcal{C}^{\mathcal{NE}} = (\partial\mathcal{C}/\partial\Delta)\, D_{H,J=1}\mathcal{E}^{\text{nr}}(x_{\text{prep}})$ and the correlated laser induced fluorescence signal, $S^{\mathcal{NE}} = (\partial S/\partial\Delta)\, D_{H,J=1}\mathcal{E}^{\text{nr}}(x_{\text{read}})$, described in [158].

3. Microwave depletion spectroscopy, by driving a resonant π-pulse on the $|B(\hat{y}), \tilde{\mathcal{N}}, \tilde{\mathcal{P}}\rangle \rightarrow |H, J = 2, M = 0, \tilde{\mathcal{P}}\rangle$ transition (depicted in figure 6.4) as a measure of $|\mathcal{E}(x)|$ for the region of the beamline between $x = x_{\text{prep}}$ and $x = x_{\text{read}}$, which is described here.

6.2.1 Measurement of $|\mathcal{E}(x)|$ and $\mathcal{E}^{\text{nr}}(x)$

A schematic of the experimental setup used for the microwave depletion measurements is shown in figure 6.4. The measurement procedure began by transferring molecules from $|X, J = 1, M = \pm 1\rangle$ to an incoherent mixture of levels in $|H, J = 1\rangle$ by optical pumping on the $|X, J = 1, M = \pm 1\rangle \rightarrow |A, J = 0, M = 0\rangle$ transition at 943 nm in the state preparation region, just as was done for the ACME I spin precession measurement . The packet of molecules travels through the spin-precession region until it is entirely occupied by the molecule pulse. Then, a π-pulse of microwaves at $2\pi \times 39$ GHz with nominal $\hat{y}$

polarization was applied counter-propagating to the molecule beam along the $-\hat{x}$ direction. When on resonance, this transferred population from $|B(\hat{y}),\tilde{\mathcal{N}},\tilde{\mathcal{P}}\rangle$ to $|H,J=2,M=0,\tilde{\mathcal{P}}\rangle$, as shown in figure 6.4 for choice of $\tilde{\mathcal{N}},\tilde{\mathcal{P}}$. State readout was performed as usual (see section 2.1) by optically pumping with alternating polarizations $\hat{x}$ and $\hat{y}$ on the state read-out transition and detecting the laser-induced fluorescence. The measured asymmetry (as defined in equation 2.4) served as a measure of the microwave transfer efficiency. The x position of the molecules at the time of the microwave pulse was mapped onto their arrival time in the detection region and, with knowledge of the longitudinal molecular beam velocity, $v_{\parallel}$, could be extracted. Thus, by performing this microwave transfer efficiency measurement for microwave frequencies spanning across resonance, the spatial dependence of the resonant frequency, $\omega_{\mathrm{MW}}(x)$, could be extracted from time-dependent asymmetry, $\mathcal{A}(t)$. This transition resonance frequency ω_{MW} is linearly proportional to the Stark shift in $|H,J=1,M=\pm,\tilde{\mathcal{N}}\rangle$ and $|\mathcal{E}(x)|$ could be directly extracted.

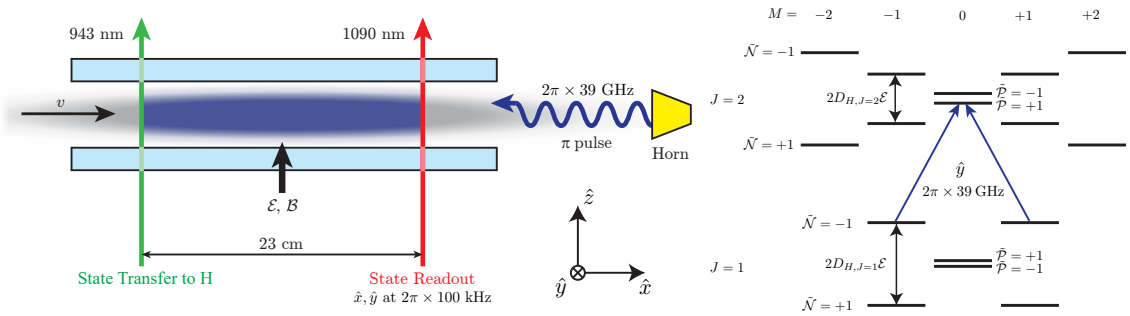

Figure 6.4: Illustration of the microwave depletion spectroscopy used in mapping $|\mathcal{E}(x)|$ and $\mathcal{E}^{\mathrm{nr}}(x)$. Left: Schematic of the experiment. An optical pumping laser at 943 nm transfers population from $|X\rangle$ (gray cloud) to an incoherent mixture of states in $|H,J=1\rangle$ (blue cloud) as described in section 2.1. A horn emits a short π-pulse of microwaves resonant with the $|H,J=1\rangle\rightarrow|H,J=2\rangle$ thereby depleting molecules a particular state in $|H\rangle$, $|B(\hat{y}),\tilde{\mathcal{N}},\tilde{\mathcal{P}}\rangle$, whose population is then read-out via optical pumping with a second laser at 1090 nm, as described in section 2.1. The time of arrival of the molecules in the state read-out region encodes the position at which they absorbed the microwaves enabling spatially resolved spectroscopy. Right: Illustration of the levels in $|H,J=1,2\rangle$ in an applied electric field of magnitude $\Delta_H \ll D_H\mathcal{E} \ll B_H$, and an example of one of the $|B(\hat{y}),\tilde{\mathcal{N}},\tilde{\mathcal{P}}\rangle\rightarrow|H,J=2,M=0,\tilde{\mathcal{P}}\rangle$ transitions that is resonantly driven with a microwave π-pulse at $2\pi\times 39$ GHz (blue arrows).

We observed a resonance linewidth of $\approx 2\pi\times 25$ kHz $\approx 2\pi/T$ which was limited by the microwave π-pulse duration of $T=40\ \mu s$. With our signal-to-noise, we were able to fit the resonance center to a precision of $\sim 2\pi\times 1$ kHz, typically using ~ 50 detuning values and

averaging over ~ 50 molecule pulses per detuning value. Example data obtained via this method are shown in figure 6.5. The resonance exhibits a lineshape that is qualitatively consistent with a two level system driven resonantly by a square pulse with fixed time T. However, the data does not fit very well to this model however, even allowing for deviations from ideal Rabi frequency, $\Omega_r T = \pi$, and allowing for T to vary from that which we applied in the lab. However, it is likely that the microwaves propagating within our apparatus cannot be described by a simple plane wave with fixed polarization and intensity as we implicitly assumed in the simple model that was previously described. For instance, due to boundary conditions at the surface of the electric field plates it is probably that the microwave intensity varies significantly along the $\hat{z}$ direction across the molecule beam, and a co-propagating microwave reflection off of the vacuum chamber walls, which differs in frequency by the Doppler shift relative to the counter-propagating microwaves in the molecule rest frame, is probably simultaneously interacting with the molecules.

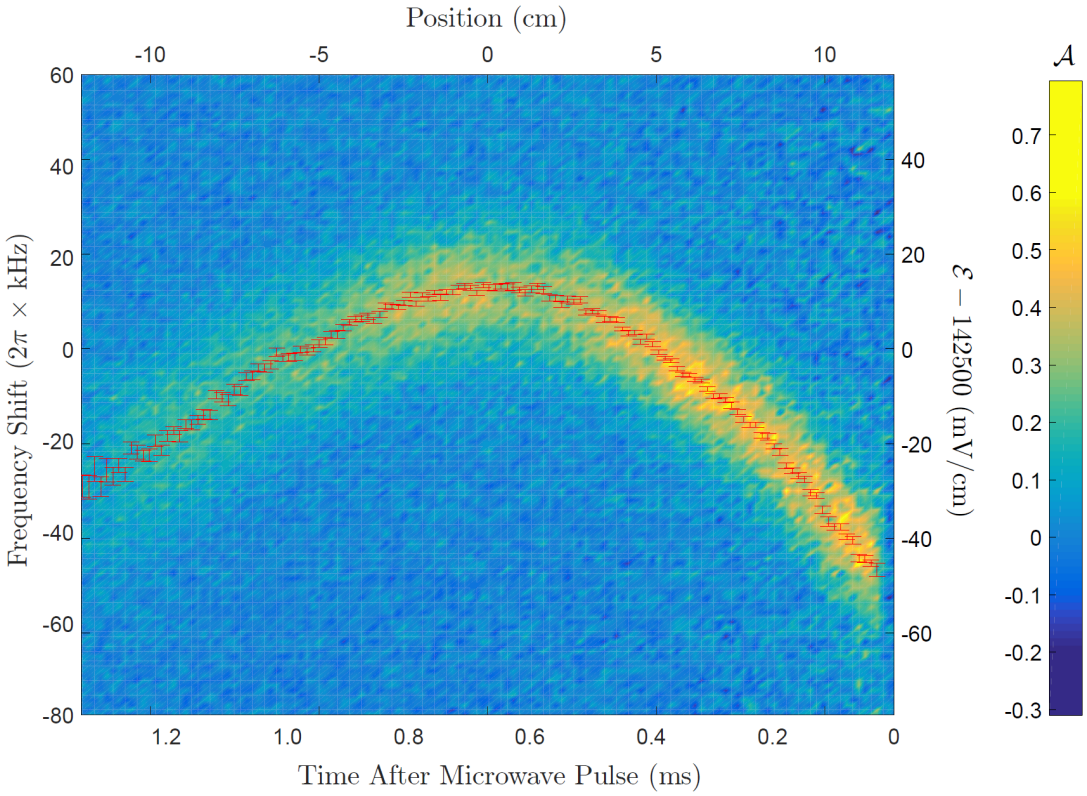

Figure 6.5: Color-map: Plot of the asymmetry $\mathcal{A}$ induced by a microwave pulse as the frequency of the microwaves was scanned across resonance. Red data points: Plot of the extracted center of the resonance signal binned by time after the microwave pulse. The position x at the top of the plot is relative to the center of the spin-precession region.

The data shown in figure 6.5 shows that the resonant frequency of the microwaves varies across the molecule pulse by around $2\pi \times 60$ kHz. The position x of the molecules at the time of the microwave pulse was assumed to be linearly related to the molecule arrival time in the state readout region. The observed spatial variation of $\mathcal{E}$ was roughly consistent with expectations based on the measured variation of the ACME I electric plate spacing described above in section 6.1.

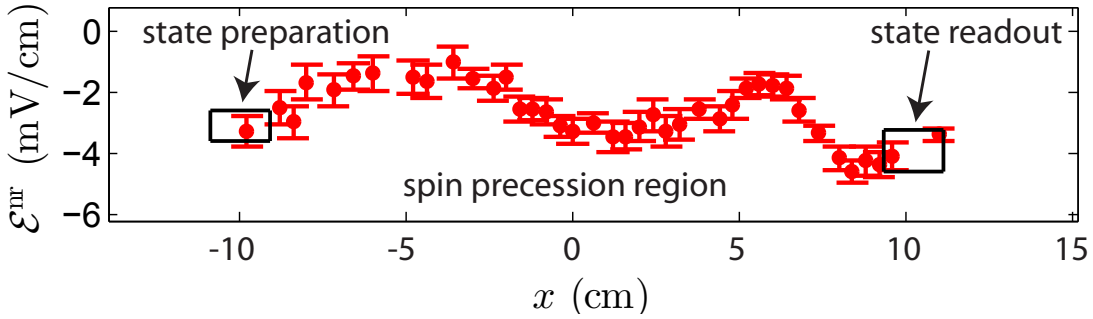

Figure 6.6: A plot of the spatial variation of $\mathcal{E}^{\mathrm{nr}}$. The black points are data obtained via microwave spectroscopy. The blue points are data obtained via Raman spectroscopy. The red data point was obtained by examining the variation of contrast with Δ_{prep}. The approximate position of the state preparation (state readout) laser beam is shown as a red dotted line on the left (right) of the figure. For the microwave spectroscopy data the uncertainty/averaging range of the position is around 21 mm at the left-hand side of the plot and decreases to around 13 mm at the right-hand side — see main text for details.

By switching $\tilde{\mathcal{N}}$ and $\tilde{\mathcal{E}}$ between measurements of the $\mathcal{E}$-field with the method described above, we were able to extract $\mathcal{E}^{\mathrm{nr}}$ from $\omega_{\mathrm{MW}}^{\mathcal{N}\mathcal{E}} = D_{H,J=1}\mathcal{E}^{\mathrm{nr}}$, the $\tilde{\mathcal{N}}\tilde{\mathcal{E}}$-correlated component of resonance frequency. These measurements, shown in figure 6.6, were used to evaluate the size of the $\omega_{\mathcal{E}^{\mathrm{nr}}}^{\mathcal{N}\mathcal{E}}$ systematic error in the ACME I measurement. We observed that $\mathcal{E}^{\mathrm{nr}}(x)$ varies significantly across the spin precession region and the spatial variation with x, as shown in figure 6.6, and this profile was reproducible for the period of several weeks over which these measurements of the electric field were taken. By performing additional measurements of $\mathcal{E}^{\mathrm{nr}}(x)$ while clipping the molecule beam with additional upstream collimators, we also observed significant variation of $\mathcal{E}^{\mathrm{nr}}$ along the z direction as shown in figure 6.2.1.

We are unsure as to the origin of the $\mathcal{E}^{\mathrm{nr}}$ but it is possible that it is generated by patch potentials [142] present on the electric field plates, or by local fixed charges that are not affected by charging and discharging the electric field plates. We observed some unexplained disagreement between the Raman spectroscopy and microwave spectroscopy $\mathcal{E}^{\mathrm{nr}}$ measurements, but note that both report non-reversing fields of a few mV/cm with the

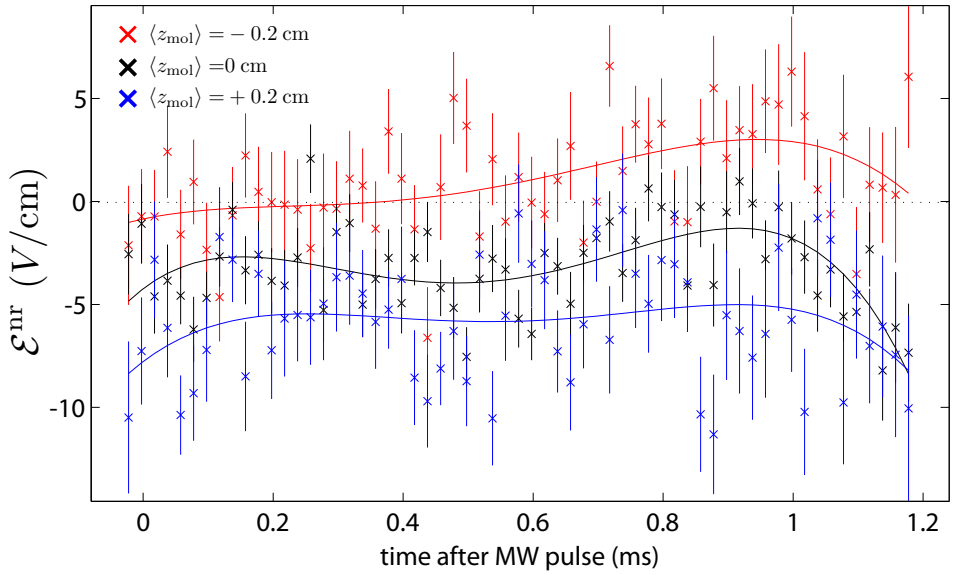

Figure 6.7: Microwave depletion measurement of $\mathcal{E}^{\rm nr}$ variation along $\hat{z}$ using molecular beam clipping. Here $\mathcal{E}^{\rm nr}$ is shown as a function of time after the microwave pulse, which is roughly proportional to the position along x, for three molecule configurations of the adjustable molecule beam collimators. Blue: (Red:) Half of the molecule beam was clipped from the $+\hat{z}$ ($-\hat{z}$) side resulting a mean molecule position along $\hat{z}$ is $\langle z_{\rm mol}\rangle \approx -.2\,$cm ($\langle z_{\rm mol}\rangle \approx -.2\,$cm). Black: The molecule beam is not clipped and the mean molecule position along $\hat{z}$ is $\langle z_{\rm mol}\rangle \approx 0\,$cm.

same sign. It is possible, given the measured z-dependence of $\mathcal{E}^{\mathrm{nr}}$, that this disagreement could be originating from differences in spatial variations along z in the sensitivity of these two methods.

The mapping between arrival time in the detection region and x position during the microwave pulse was approximate, suffering from spatial averaging due to a variety of effects. For example, velocity dispersion led to spatial averaging over length scales $\Delta x \sigma_{v_\parallel}/v_\parallel$, where $\sigma_{v_\parallel}$ is the longitudinal velocity spread of the molecular beam and Δx is the distance between the location of microwave interrogation and state readout laser. This averaging distance was largest, $\approx$ 1.6 cm, at the state preparation region. Spatial averaging also occurred across the $\approx$ 0.7 cm distance traversed during the $T = 40$ μs microwave pulse. Finally, there was averaging of the spatial position of the molecules due to the finite size of the state readout laser beam and the polarization switching; molecules were optically pumped (with varying probability) throughout the $\approx$ 0.5 cm wide laser beam. In addition to spatial averaging, uncertainty in the mean longitudinal velocity contributed an uncertainty in position. Changes of $\approx$ 10 m/s between molecule pulses were quite typical over the course of the $\mathcal{E}$-field measurement, giving an estimated position uncertainty of $\lesssim$ 1 cm.

By adding the above contributions in quadrature we concluded that the range of positions from which the microwave-induced signals could have originated increased from around $\approx$ 1.3 cm at the state readout beam to $\approx$ 2.1 cm at the optical pumping beam. These ranges are shown as the width of the black boxes indicating the estimates of $\mathcal{E}^{\mathrm{nr}}$ in that state preparation and state readout lasers in figure 6.6.

6.2.2 Stroboscopic Measurement of Velocity for Improved Spatial Determination

In order to increase our resolution in determination of the spatial position of the molecules when addressed by the microwave pulse, we also performed microwave depletion measurements while strobing the 943 nm pump laser beam by using an acousto-optic modulator (AOM) as an optical switch. This creates well localized packets of molecules prepared in $|H, J = 1\rangle$, and due to velocity dispersion that occurs between the molecule beam source and the interaction region, narrower distributions of velocities in each packet. We have used this experimental method in the past [93] to calibrate for the Zeeman spin precession time in the interaction region to make an improved measurement of the magnetic moment

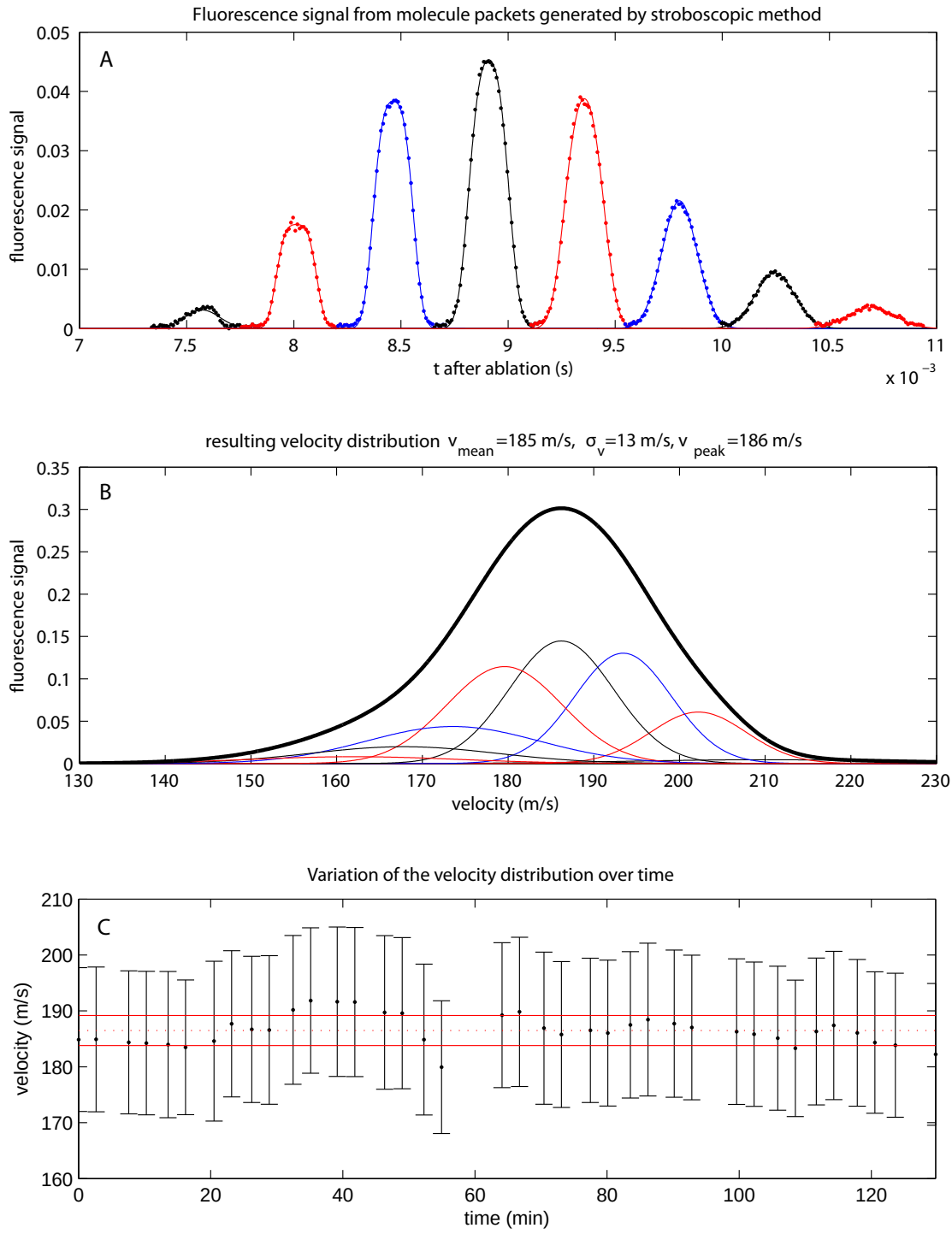

Figure 6.8: Stroboscopic measurements of the longitudinal velocity distribution in the spin precession region. A: Measurement of laser induced fluorescence from a series of strobed pulses arriving detection regions with fits to equation 6.3. B: Inferred velocity distributions for each of the strobed pulses shown in A, with the same coloring, The black line represents the inferred total longitudinal velocity distribution. C: Variation in the total longitudinal velocity distribution, where the mean is denoted by the black dot and $\pm 1\sigma$ region denoted by the errorbars, over a period of 2 hours.

in $|H, J = 1\rangle$.

We analyze this data by assuming that all molecules addressed by a strobe pulse of duration T, are equally likely to have been prepared in $|H, J = 1\rangle$ at each time t_0 while the laser is on, and that those molecules that are prepared have a normally distributed longitudinal velocity with mean $\bar{v}$ and variance σ_v^2,

$$P_0\left(t_0, v\right) = \frac{1}{T}\left(0 < t_0 \leq T\right) \frac{1}{\sqrt{2\pi\sigma_v^2}} \exp\left(-\frac{(v-\bar{v})^2}{2\sigma_v^2}\right) \tag{6.1}$$

This molecule packet undergoes velocity dispersion as it passes through the region of length L between the pump laser beam and the state readout laser beam resulting in a probability distribution $P_1(t_1)$ for the time t_1 of detection,

$$P_1(t_1) = \int P_0(t_1 - v/L, v)dv \tag{6.2}$$

$$\approx \frac{1}{T}\left\{\mathrm{erf}\left(\frac{1}{\sqrt{2}}\frac{L}{\sigma_v}\left[t_1 - \frac{L}{\bar{v}}\right]\right) - \mathrm{erf}\left(\frac{1}{\sqrt{2}}\frac{L}{\sigma_v}\left[t_1 - T - \frac{L}{\bar{v}}\right]\right)\right\} + O\left(\frac{\sigma_v}{\bar{v}}\right). \tag{6.3}$$

The integral in equation 6.2 is approximated using Laplace's method in a perturbative expansion with respect to $\sigma_v/\bar{v}$ which is typically on the order of 2% for these wavepackets. The analytic formula in equation 6.3 is used to fit to the observed time dependence of the fluorescence signal for each strobe pulse to extract $\bar{v}$ and σ_v for each pulse.

An example of the stroboscopic fluorescence data with the fits to the model in equation 6.3 are shown in figure 6.2.2A. The inferred velocity distributions for each strobe pulse are shown in figure 6.2.2B with the same coloring scheme as in 6.2.2A and the inferred total longitudinal velocity distribution is shown with a thick black line. Note that those pulses that arrive later have a lower velocity distribution due to velocity dispersion along the beamline. From this measurement, we can determine that the longitudinal velocity of the buffer gas beam is fairly normally distributed with a mean velocity around $\bar{v} \approx 185$ m/s with a standard deviation of $\sigma_v \approx 13$ m/s. By performing this measurement over longer timescale, we can monitor variations in the longitudinal velocity distribution as illustrated in figure 6.2.2C where we observed variations in the mean velocity roughly between 180 m/s$-$190 m/s over a 2 hour time window.

6.3 Characterizing the Magnetic Field Constrained by Maxwell's Equations

In ACME I, we decided to include limits on possible EDM systematic errors proportional to non-reversing magnetic fields, $\mathcal{B}^{\mathrm{nr}}$, transverse fields, and field gradients, in our systematic uncertainty as discussed in section 3.6.1. We did not observe any systematic errors proportional to these quantities, but since the PbO electron EDM experiment [49] had observed systematic errors when applying transverse magnetic fields and magnetic field gradients and the mechanism was not understood, it is possible that the same mechanism could be present in our experiment so we included the possibility that these effects are present when constructing our systematic uncertainty to be on the safe side. Furthermore, there are known mechanisms by which the residual magnetic field, $\mathcal{B}^{\mathrm{nr}}$, can contribute to the AC Stark shift phase systematic errors and Stark Interference systematic errors are described in sections 4.3 and 4.2.1. Hence it is important that we measure the magnetic field in our apparatus so that we can characterize the size of these systematic errors that contribute to the EDM measurement.

The magnetic field monitoring that we performed during ACME I was not sensitive to the residual field $\mathcal{B}^{\mathrm{nr}}$. Four fluxgate magnetometers were physically attached to the interaction region vacuum chamber, and since these fluxgate magnetometers have fairly large voltage offsets (which correspond to a few mG) that tend to drift significantly in time, we were unable to resolve any $\mathcal{B}^{\mathrm{nr}}$ below that level. After the ACME I experiment had been completed, we opened up the vacuum chamber and inserted a device called the "probulator" [174], depicted in figure 6.3. These measurements showed an unexpectedly large residual magnetic field, $\mathcal{B}^{\mathrm{nr}} \approx 0.7\hat{y}\,\mathrm{mG}$. Later we determined that this field was caused by the magnetization induced in the magnetic shields from Earth's magnetic field $\approx 500\,\mathrm{mG}$ prior to assembling them. Our magnetic shield degaussing scheme provided insufficient current to entirely remove this magnetization since it was engineered to remove the smaller magnetization induced by the the $\approx 20\,\mathrm{mG}$ magnetic fields applied by our coils within the magnetic shields [123].

As described in section 5.4.2, in ACME II, the interaction region has been designed with magnetometer pockets protrude into the interaction region with corresponding access holes through the magnetic field coils and magnetic shields such that we can perform mag-

netometry of the applied magnetic field and the residual magnetic field, as we did with the probulator, along multiple axes within the experiment and without having to break vacuum. In this section, I describe some magnetic field mapping that was performed in the interaction region after the ACME II modifications had been made to the magnetic field coils and the magnetic shields. Here, I also present a method of aggregating magnetic field measurements along different scan axes using a model that satisfies Maxwell's equations to improve our understanding of the magnetic field in spatial regions of the apparatus that were not explicitly mapped. This method may be useful during ACME II to estimate the magnetic field within the spin precession region given measurements of the magnetic field within the magnetometer pockets that surround the spin precession region.

Such models that satisfy Maxwell's equations in free space have been used before to fit magnetic field data in other experiments. The ATLAS experiment performed a nonlinear fit to Fourier-Bessel terms and hyperbolic terms to model their solenoid field [9,73]. The TJ-II Heliac used a linear model of toroidal harmonics in toroidal coordinates to describe a toroidal solenoid field [115]. A search for unexploded ordnance used a nonlinear regression model consisting of the sum of dipole fields was used for the detection of unexploded ordnance [117]. Outside of the magnetosphere, the earths magnetic field has been described using linear regression with a spherical harmonic basis set [112]. In the characterization of the magnetic fields within the ACME experiment, we found it most useful to use a truncated 3d polynomial model constrained to satisfy Maxwell's equations.

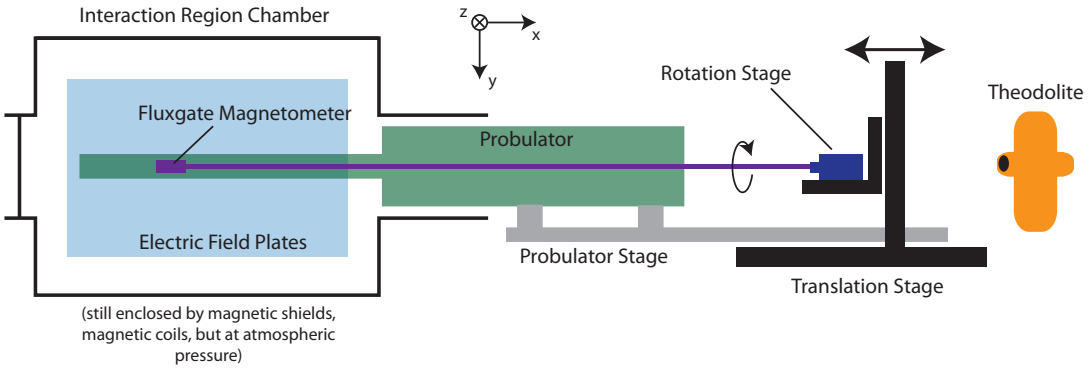

Figure 6.9: Schematic of the set-up used to perform magnetometry along the molecule beamline within the experiment. This consists of the *probulator*, a set of rigidly held tubes that can be precisely aligned along the beamline using a theodolite, and which can support a cylindrical fluxgate magnetometer to perform magnetic field measurements.

6.3.1 Measuring the Magnetic Fields

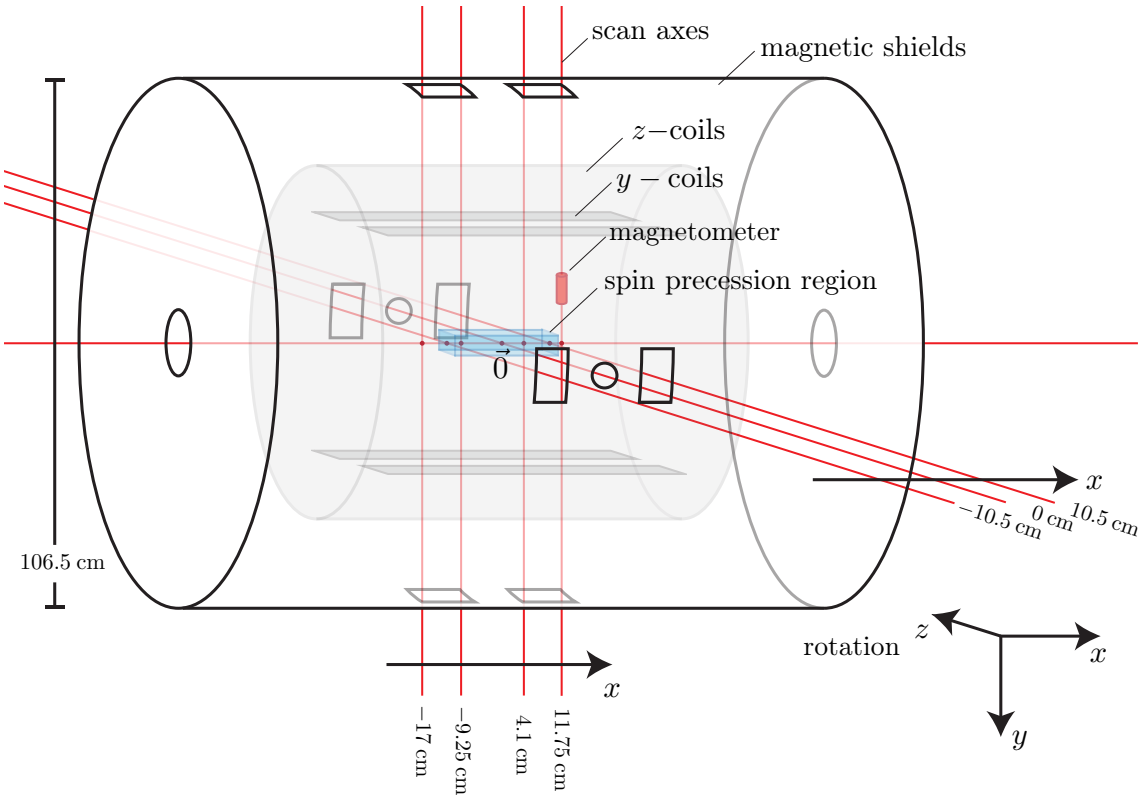

Figure 6.10: Schematic that illustrates the ACME interaction region. The large cylinder denotes the outermost layer of the 5 mu-metal magnetic shields. The smaller concentric cylinder denotes the cosine coils that can be used to apply a magnetic field in the z direction. The rectangles within that cylinder denote a set of coils that can be used to apply a magnetic field in the y direction. The blue region in the center denotes the spin precession region where we would like to carefully map the magnetic fields. The red lines indicate the axes along which we performed scans of the magnetic field. This figure is to scale.

Two 3-axis Bartington Mag-03 fluxgate magnetometers with a sensitivity of about $3\,\mu G/\sqrt{\text{Hz}}$ were used to map applied fields of magnitude ~ 20 mG, and a residual field of magnitude $\sim 30\,\mu G$. These magnetometers are cylindrical with a 2 cm diameter and 5.5 cm length. The magnetometer was fixed inside of a Teflon mount that adapts to the end of an aluminum 6061 drive shaft connected by a nylon flexible coupling. The magnetometer slides linearly within a plastic tube which defines a magnetic field scan axis. The position of the scan axes are fixed with respect to the spin precession region such that their positions and orientations correspond those shown in figure 6.3.1. The magnetometer is translated within the tube using a translation stage, and data points were taken with a spatial sepa-

ration of about 1 cm. Since the magnetometer is larger than the separation between data points, the magnetometer smooths any magnetic field variations shorter than the length of the magnetometer. A rotation stage that is fixed to the translation stage is used to rotate the cylindrical magnetometer within the tube which serves to reverse or interchange the magnetometer probe sensors that are transverse to the scan axis. The axial magnetometer sensor cannot be easily reversed in this set-up.

Within the experiment there are three sets of coils: a set of cosine coils wound on a 70 cm diameter cylindrical polycarbonate mount that apply a magnetic field in the z direction, a rectangular grid of coils to apply a magnetic field in the y direction, and a Helmholtz coil wound around the cosine coil mount to apply a magnetic field in the x direction. The z-coils are used to apply a uniform $\mathcal{B}_z$ within the spin precession region of magnitude ranging from $0 - 50$mG. We have built in the capability to apply uniform fields along the two transverse directions, $\mathcal{B}_x$ and $\mathcal{B}_y$, and the capability to apply all 5 independent first order gradients: $\partial\mathcal{B}_y/\partial x$, $\partial\mathcal{B}_y/\partial y$, $\partial\mathcal{B}_y/\partial z$ (using the $y-$coils), $\partial\mathcal{B}_z/\partial x$, and $\partial\mathcal{B}_z/\partial z$ (using the z-coils). These auxiliary field configurations are used to search for EDM systematic errors that may depend on some of the magnetic field components – as described in section 3.6.1, in ACME I, we put direct limits on possible systematic errors coupled to each of these parameters and included these in the systematic uncertainty.

Outside of the magnetic field coils, there are 5 layers of concentric cylinders of mu-metal with planar end-caps that vary in diameter from 76 cm to 106.5 cm. These magnetic shields have been measured to have a static shielding factor of about 10^5, which suppresses the ambient magnetic field from 500 mG to around $\sim 5\ \mu$G. However, the residual magnetic field in the spin precession region is currently $\sim 30\mu$G and is likely limited by magnetization in the mu-metal. The mu-metal shields have an array of holes for molecule beam access and laser access to the spin precession region. When applying a magnetic field of about $\mathcal{B}_z \approx 20$ mG in the precession region, the inner layer becomes magnetized and results in a change to the residual field of about $\sim 30\mu G$ in the precession region. This magnetization is subsequently removed by degaussing the mu-metal using a set of coils wound around each mu-metal layer which is driven by an oscillating current at 200 Hz with an exponentially decreasing waveform.

The magnetic field in the precession region has been mapped for each of the configurations that we can use to apply uniform fields in each of the 3 Cartesian directions (except for

$\mathcal{B}_x$), and to apply each of the 5 independent first order gradients. The background residual field in the absence of any applied field was also characterized. Each field has been mapped along each of the 8 scan axes shown in figure 6.3.1 which gain access to the spin precession region via holes in the mu-metal shields. The plastic tubes that confined the magnetometer along a given scan axis were aligned to their assigned positions within about $\pm.25$ cm, which also implies an angular tolerance of about ± 5 mrad. For the scans in the x and y directions the rotational alignment of the magnetometers was set by the direction of $\mathcal{B}_z$ generated by the $z-$coils, but for the scans in the z direction, the rotational alignment was set by the direction of the $\mathcal{B}_y$ generated by the y-coils. These geometric alignment uncertainties lead to systematic errors in the magnetic field mapping scheme that are discussed later.

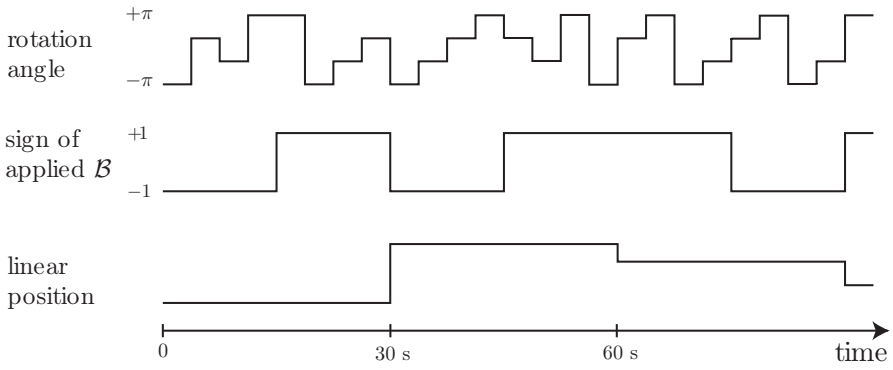

Figure 6.11: Measurement scheme for mapping the magnetic field. The rotation angle of the magnetometer is varied between 4 states, the sign of the applied magnetic field is switched, and the linear position of the magnetometer along the scan axis is varied. All of these parameters are randomized.

The measurement scheme is shown in figure 6.3.1. One magnetometer scan was performed at a time with a given magnetic field configuration. The fluxgate magnetometers that were used in this mapping have electronic offsets that are comparable to the fields that are measured that drift slowly in time. This offset can be subtracted off by physically rotating the magnetometer by π radians, or by reversing the sign of the magnetic field. The effect of the offset drift can be transferred to signal noise by rotating the magnetometer or changing the sign of the magnetic field on a timescale that is fast compared to that of the drift and by randomizing the experiment parameters to transfer the drift into measurement noise.

The magnetometer measurements were averaged over about 2 s and standard normal uncertainties were assigned to each measurement. The rotation angle of the magnetometer

was changed between 4 states varying by $\pi/2$ so as to subtract off the electronic offsets and to interchange the orthogonal magnetometer axes to search for an effect of non-orthogonality of the measurement sensors. After a full set of 4 rotation angle states, the sign of the magnetic field would be reversed by changing the sign of the current running through the coil. In between magnetic field sign states, the mu-metal shields were run through a degaussing cycle in the absence of applied fields to remove the magnetization from the previously applied field. After a full set of 2 magnetic field sign states, the position of the magnetometer was changed. Measurements were taken over a range of 15 cm for scans in the y direction, 30 cm in the z direction and 40 cm in the x direction, and measurements were taken in steps of about 1 cm. Each of the 3 parameters that were varied were randomized.

6.3.2 A Convenient Magnetic Field Model Obeying Maxwell's Equations

Provided that there are no magnetic field sources in the in the spin precession region, then the magnetic field should satisfy Maxwell's equations in free space, $\nabla \cdot \mathcal{B} = 0$, $\nabla \times \mathcal{B} = 0$. In this case, we may express the magnetic field as the gradient of a scalar magnetic potential $\mathcal{B} = \nabla\Phi$, so that the field automatically satisfies the curl condition, $\nabla \times \nabla\Phi = 0$. Since our coils were designed to apply Cartesian field components and first order Cartesian gradients, then it is convenient to model the magnetic field as a polynomial in Cartesian coordinates in which case the fit coefficients are the calibration coefficients. If we truncate the Taylor series at order O, then we may write the magnetic potential fit function as

$$\Phi_{\text{fit}}(\vec{x}) \equiv \sum_{1 \leq \ell+m+n \leq O} a_{\ell mn} x^{\ell} y^{m} z^{n} \tag{6.4}$$

where $a_{\ell mn}$ are the fit coefficients and where the Cartesian magnetic field component along $p \in \{x, y, z\}$ can be obtained from $\mathcal{B}^{p}_{\text{fit}} = \partial\Phi_{\text{fit}}/\partial p$. The magnetic field must be constrained by the divergence condition $\nabla \cdot \mathcal{B}_{\text{fit}} = \nabla^2\Phi_{\text{fit}} = 0$ and hence Φ_{fit} must be a solution to the Laplace equation. This condition leads to a series of linear constraints $S_{\ell mn}(\vec{a})$ on the fit

coefficients,

$$\begin{aligned} S_{\ell mn}\left(\vec{a}\right) = &\left(\ell+2\right)\left(\ell+1\right)a_{\ell+2,m,n} \\ &+\left(m+2\right)\left(m+1\right)a_{\ell,m+2,n} \\ &+\left(n+2\right)\left(n+1\right)a_{\ell,m,n+2} = 0. \end{aligned} \tag{6.5}$$

Note that this fit function constrained by the divergence condition has $N = O\left(O+2\right)$ free parameters even though the total number of coefficients in equation 6.4 increases like $\sim O^3$.

From the magnetometry described above, we have a series of $N_{\mathcal{B}}$ of magnetic field measurements of the form $\left\{\vec{x}_i, \vec{\mathcal{B}}_i, \delta\vec{\mathcal{B}}_i\right\}$ where the index i runs over all of the data points, assuming that each position $\vec{x}_i$ is known exactly, and each magnetic field measurement $\mathcal{B}_i^p$ is a normally distributed random variable with variance $(\delta\mathcal{B}_i^p)^2$. The maximum likelihood estimate for the fit coefficients is obtained by minimizing the negative log likelihood function, which in this case is χ^2. The divergence constraints can be accounted for by adding Lagrange multiplier terms with coefficients $\lambda_{\ell mn}$ for each independent constraint to the χ^2 function, and then minimizing χ^2 with respect to both the fit coefficients $\vec{a}$ and the Lagrange multipliers $\vec{\lambda}$. We can write χ^2 as

$$\chi^2 = \frac{1}{N_{\mathrm{dof}}}\sum_{i=1}^{N_{\mathcal{B}}}\sum_{p=1}^{3}\left(\frac{\mathcal{B}_i^p - \mathcal{B}_{\mathrm{fit}}^p(\vec{x}_i)}{\delta\mathcal{B}_i^p}\right)^2 - \sum_{\ell nm}\lambda_{\ell mn}S_{\ell mn}\left(\vec{a}\right) \tag{6.6}$$

where $N_{\mathrm{dof}} = N_{\mathcal{B}} - N$ is the number of degrees of freedom. Since the gradient of χ^2 with respect to the free parameters $\vec{a}, \vec{\lambda}$ is linear with respect to these parameters, this problem falls in the class of linear regression problems which can be solved efficiently by matrix inversion, and the posterior distribution for $\vec{a}$ is jointly normal and is defined entirely by maximum likelihood estimate of $\vec{a}$ and the covariance matrix. Note that the linear regression problem with linear equality constraints is fairly ubiquitous and a general treatment may be found here [104].

Since the fluxgate magnetometers have unknown electronic offsets, in the case of measuring the residual magnetic field, $\mathcal{B}^{\mathrm{nr}}$, since the residual field cannot be reversed, then the magnetometer axes that cannot be reversed are only known up to a constant. These constants were included as additional fit parameters for the analysis of this field.

6.3.3 Results and Systematic Errors

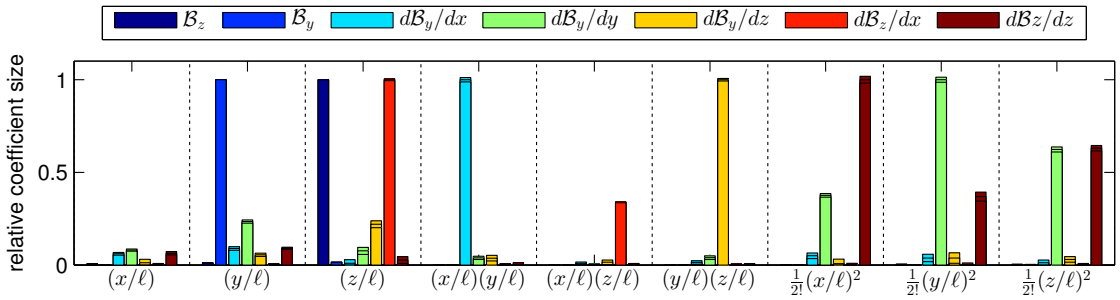

Figure 6.12: Comparison of the fit coefficients for the 7 field configurations that were mapped. The "relative coefficient size", plotted on the y-axis, is the absolute value of the coefficient that multiplies the term on the x-axis in the polynomial expansion for Φ and is normalized such that the largest coefficient for a given field configuration is 1. Here, $\ell = 3.5\,\text{cm}$ is chosen to be a length scale that is characteristic of the size of the spin precession region.

Using the linear regression model described in the previous section, the magnetic field measurements were fit to $O = 8$ polynomial for field configurations intended to generate uniform fields $\mathcal{B}_y$, $\mathcal{B}_z$, and uniform gradients, $\partial\mathcal{B}_y/\partial x$, $\partial\mathcal{B}_y/\partial y$, $\partial\mathcal{B}_y/\partial z$, $\partial\mathcal{B}_z/\partial x$, and $\partial\mathcal{B}_z/\partial z$, and used to measure the residual field $\mathcal{B}^{\text{nr}}$. The relative size of the coefficients extracted for each fit are shown in figure 6.3.3 for 9 lowest order terms in the expansion. An example fit is shown for an applied $\partial\mathcal{B}_y/\partial y$ field in figure 6.3.3. This map illustrates that the global fit is generally pretty good and the data and the fit satisfy the divergence condition $\nabla \cdot \mathcal{B} = 0$.

The residual background magnetic field, $\mathcal{B}^{\text{nr}}$, was also mapped in our system and it was found that the field is fairly constant with a value of about 33μG in the center of the spin precession region with roughly equal components in each of the Cartesian directions as seen in figure 6.3.3. From measurements of the static shielding factor of the magnetic shields, we believe that the residual field is about 3 times larger than the effect of earth's magnetic field. The magnitude of the residual field and the gradient in the field is fairly comparable to that observed in other shielding systems that use mu-metal [92, 160, 162] which tend to be on the order of 10μG and exhibit gradients on the order of $10\mu\text{G}/\ell$ where ℓ is the approximate size of the magnetic shields. To achieve a lower $\mathcal{B}^{\text{nr}}$ we would likely have to actively apply a magnetic field to offset this residual one.

In the absence of systematic errors, using a fit that is constrained to satisfy Maxwell's equations gives higher sensitivity than applying an unconstrained fit of the same order.

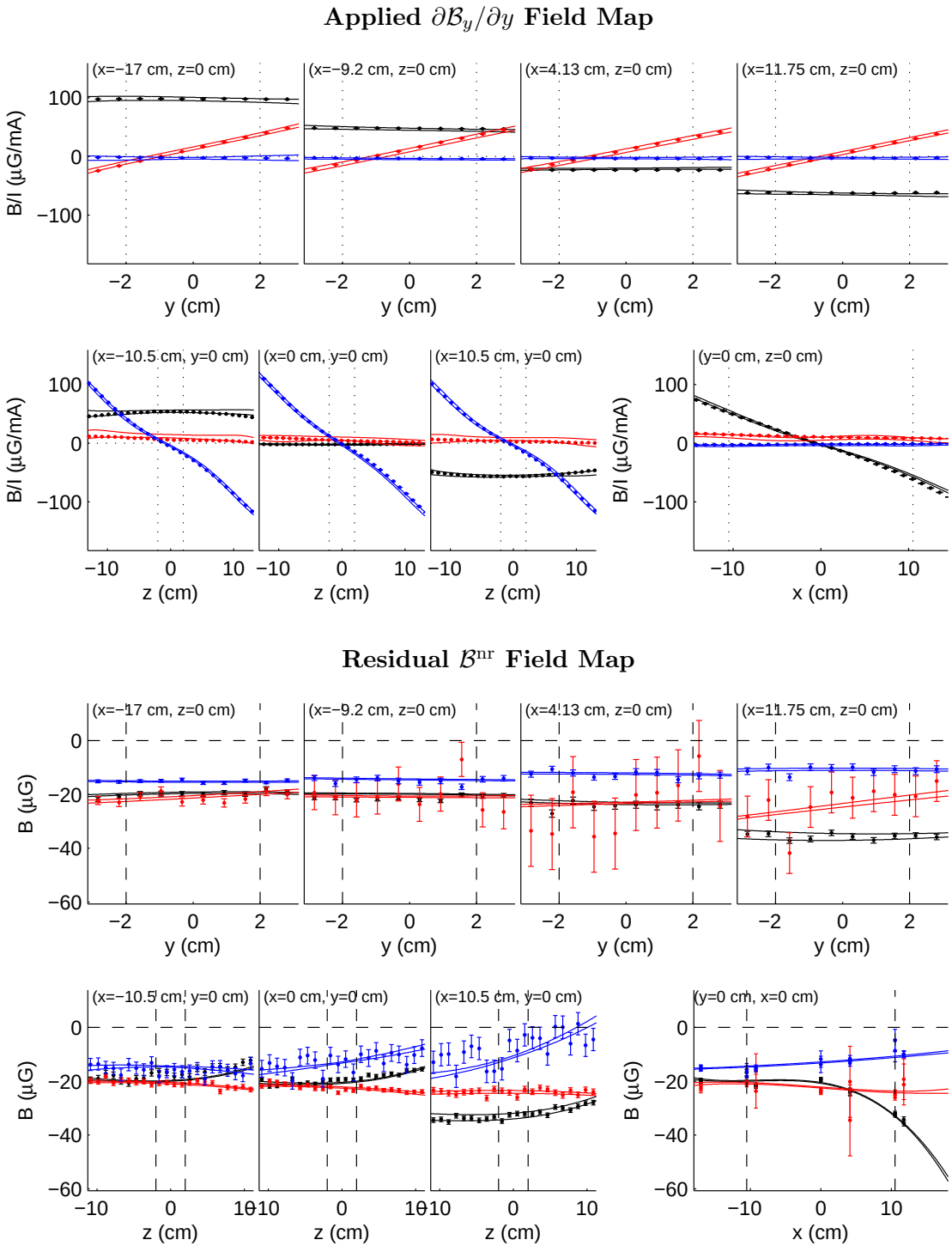

Figure 6.13: Magnetic field map obtained when using the y-coils to apply a $\partial\mathcal{B}_y/\partial y$ gradient. Here, $\mathcal{B}_x$ is black, $\mathcal{B}_y$ is red, and $\mathcal{B}_z$ is blue. The points are magnetic field measurements, and the lines are 1σ confidence intervals for the resulting fit with $O = 8$. The vertical dotted lines denote the extent of the spin precession region.

Applied Field	Fields (μG/mA)		Gradients (μG/mA $\cdot$ cm)				
	$\mathcal{B}_y$	$\mathcal{B}_z$	$\partial\mathcal{B}_y/\partial x$	$\partial\mathcal{B}_y/\partial y$	$\partial\mathcal{B}_y/\partial z$	$\partial\mathcal{B}_z/\partial x$	$\partial\mathcal{B}_z/\partial z$
Best Fit Value	268.44	1201.89	17.04	5.82	20.26	1.17	7.56
Systematic Uncertainty (%)							
Scan Position	.013	.032	.61	.94	.46	.60	.82
Scan Center	.037	.034	.54	1.0	.57	2.2	.76
Rotational Align.	.013	.007	.09	.14	.06	.09	.21
Geometric Error	.042	.048	.82	1.4	.74	2.3	1.2
Fit Error	.058	.076	1.1	1.5	.91	.92	2.3

Table 6.1: Table of best fit values for the primary field coefficients extracted using the Maxwell fit for each of the coil configurations that were mapped. Below is a comparison of systematic uncertainties in the extracted coefficients with the fit output uncertainty. The fit errors agree with the geometric errors within about a factor of 2. The dominant contribution to the geometric error comes from uncertainties in the relative spatial alignment of the 8 scan axes.

However, in this work, the uncertainty is dominated by systematic errors due to deviations between the data and Maxwell's equations with typical reduced χ^2 values on the order of 10^3. The fit residuals are not randomly distributed about zero, but rather hover consistently away or oscillate about zero for a given scan axis and a given magnetic field component. If we are confident that the model does fit the data well in the absence of systematic errors, we can attempt to account for some of these systematic errors by rescaling the fit covariance matrix by the measured value of χ^2.

This method for accounting for systematic errors is not so elegant and in general it is better to try to understand the systematic errors and then account for them. We believe that the dominant systematic errors that contribute to the large χ^2 originate from the following geometric factors:

1. uncertainty in the relative position of the scan axes
2. uncertainty in the position of the center of the spin precession region along each scan axis
3. uncertainty in the relative rotation alignment of the magnetometer axes for each scan axis.

The relative scan axis positions are estimated to be known to within $\pm.25$ cm from uncertainties in the alignment procedure. The uncertainty in the relative rotational alignment of the magnetometers is approximately ± 10 mrad and is determined by the uniformity of the

$\mathcal{B}_y$ and $\mathcal{B}_z$ fields that we can apply. By varying all of the geometric parameters, we determined the sensitivity $\partial a_n/\partial P$ of the fit coefficients a_n to each of the geometric parameters P and estimated the resulting systematic uncertainties $\delta a_n\,(P)$by:

$$\delta a_n^2\,(P) = \left[\left(\frac{\partial a_n}{\partial P}\right)^2 + \left(\delta\frac{\partial a_n}{\partial P}\right)^2\right]\delta P^2. \tag{6.7}$$

where $\delta\partial a_n/\partial P$ is the uncertainty in $\partial a_n/\partial P$, and δP is the uncertainty in P. By observing the variation in the fit χ^2 when varying each parameter P, it was observed that the shifts in the parameters required to minimize χ^2 were comparable to the previously stated uncertainties in the geometric parameters.

The results for the best fit values for the dominant fit coefficients for each of the mapped coil configurations, which may be used as calibration constants, are collected in table 6.3.3. Here, the individual geometric systematic uncertainties are compared, and then the total geometric systematic uncertainty is compared with the χ^2 rescaled fit uncertainty. This table shows that the fit uncertainty agrees with the estimated geometric systematic uncertainty within a factor of $\sim 2\times$. This suggests that rescaling the fit covariance can fairly reasonably account for this class of systematic errors.

Another possible source of systematic error could come from averaging over the volume of the magnetometer. The magnetometer has a 2 cm diameter and a 5.5 cm length, so variations of the magnetic field over shorter length scales than this will be smoothed by the magnetometer thereby changing the measured magnetic field profile in a way that may not satisfy Maxwell's equations. However, the typical length scale for spatial variation of the magnetic field is expected to be on the order of the separation between the magnetometer and the sources of the magnetic field (the mu metal shields and the magnetic field coils), which are a distance of about ~ 40 cm away from the spin precession region.

A significant source of systematic error that does not contribute to the large fit χ^2 is the overall calibration factor for the magnetometer signal. The magnetometers were calibrated within .5% by the factor, and using a set of Helmholtz coils we were able to confirm that they were calibrated to better than 2%. This becomes the dominant source of systematic error in the fit to the $\mathcal{B}_z$ field, but is comparable to the geometric uncertainties for most of the other field configurations.

Chapter 7

Summary and Outlook

> Slow is not the same as deficient. It's just slow. A glacier is slow too, but it gets there, and nothing stops it.
>
> Kim Stanley Robinson, Aurora

In this thesis, I have documented some of my contributions to the ACME experiment during the a time period spanning roughly from May 2012 to May 2016 while I was in residence at Harvard University where the experiment is located. During this time we performed measurements of the electron's EDM using the methods described in chapter 2 with the ACME I apparatus. During the course of these measurements we searched for unforeseen systematic errors and carefully characterized those systematic errors that were observed as described in chapter 3. This resulted in a measurement of the electron's EDM that was consistent with zero with more than an order of magnitude improvement in precision relative to the previous best measurement [6]. In order to understand the systematic errors that we observed in ACME I, so that we may suppress them and anticipate possible new systematic errors in the ACME II apparatus, we developed analytic systematic error models which are documented in chapter 4.

We then constructed a new apparatus, which is described in chapter 5, referred to as ACME II, which introduced a series of improvements that increased the number of detected molecules by more than a factor of 100×. In chapter 6 I documented a series of auxiliary measurements that were performed both during ACME I and ACME II to to characterize the electric field plate separation, the electric fields, the magnetic fields, and the molecule beam velocity distribution.

At the time of this writing, the ACME II apparatus is currently running at full statistical sensitivity in the phase measurement and we are in the process of implementing the experimental switch sequence required to perform the electron EDM measurement. So long as there are no new significant sources of noise or large unanticipated systematic errors, ACME II should be capable of making a measurement of the electron's EDM with an order of magnitude improvement in sensitivity relative to ACME I with a 1σ statistical uncertainty on the order of $\delta d_e \sim 2 \times 10^{-30} e \cdot \text{cm}$. If a non-zero electron EDM is observed during the course of this new measurement it would constitute a direct observation of physics beyond the Standard Model and may shed light on how bariogenesis occurred in the early universe. If the measurement is consistent with zero, a large new swath of SUSY parameter space will be ruled out for the most popular variants of SUSY, as discussed in chapter 1.

Additional improvements to the sensitivity of the electron EDM measurement should be possible for an ACME III apparatus that could follow the ACME II data runs that may facilitate 1σ statistical uncertainties as low as $\delta d_e \sim 1 \times 10^{-31} e \cdot \text{cm}$. These improvements have not been discussed in the previous text and will only be briefly mentioned here. The electron EDM sensitivity scales like $\delta d_e \propto 1/\mathcal{E}_{\text{eff}} \tau \sqrt{\dot{N} T}$, where $\mathcal{E}_{\text{eff}}$ and τ will remain the same if we are to use the same metastable H state in ThO for future measurements, since $\mathcal{E}_{\text{eff}}$ depends on the molecule state wavefunction and τ is currently limited by the lifetime of the state. Hence future improvements in an electron EDM measurement with ThO will come from either increased rate of molecule detection, $\dot{N}$, or increased averaging time, T. Possible future improvements to these quantities include:

- **Thermochemical Beam Source:** In ACME I and ACME II, molecules were generated in pulses at 50 Hz by nano-second ablation of a ceramic pellet of ThO_2 in a cryogenic buffer gas cell with an output aperture. An alternative beam source has been developed by the Doyle group, spearheaded by Elizabeth, in which local laser heating of a pressed pellet consisting of a mixture of ThO_2 and Th in a buffer gas cell results in a chemical reaction $ThO_2 + Th \rightarrow 2ThO$ that proceeds favorably above 2000 K. This beam source has been demonstrated to produce a factor $\sim 10\times$ increase in detected molecule rate relative to the ablation source.

- **Increased Integration Time:** In ACME I the data that contributed to the electron EDM measurement and the statistical uncertainty consisted of about 2 weeks of

continuous data taking. However, the data that went into the systematic error and uncertainty was taken over the course of about 6 months and many of our systematic error contributions were limited by statistics. In ACME II we plan to operate the experiment for a similar duration as in ACME I. However, in ACME III, we could average for a much longer duration for the statistical run – maybe for 6-12 months rather than 2 weeks – and if we focused only on characterizing known systematic errors, we may be able to cut down significantly on the fraction of time required for characterizing systematic errors.

With these two improvements a factor of 10× improvement in sensitivity to the electron EDM may be achievable in ACME III relative to ACME II. Although the improvements listed above are likely to be implemented in a future ACME measurement, the inclusion of other improvements that are being pursued are not so certain. These other possible improvements include:

- **Increased Detected Solid Angle:** In ACME II, we modified the molecular beam collimation geometry and reduced the distance between the beam source and the detection region so that a larger solid angle of the molecule beam could be detected. Even further improvements in the detected solid angle could be achieved by moving the buffer gas beam source much closer to the spin precession region (and possibly even extending the cryogenic region into the magnetically shielded region). Alternatively some improvement may be possible by focusing the molecule beam into the detection region using an electrostatic lens.

- **Increased Detection Efficiency**: We have explored the possibility of detecting photons using Silicon Photomultipler (SIPM) devices which can provide higher quantum efficiencies than the photomultipler tubes used in ACME I and ACME II. Additionally, the detection scheme could be modified such that optical cycling is used to evoke multiple photons per molecule or a high intensity pulsed laser could used to ionize the molecules which could be detected with a multi-channel plate (MCP). In these schemes, the molecules in the detection region may be detected with near unity efficiency. Such schemes would likely first require optical pumping of the projections of the molecule spin state $|\psi\rangle$ in $|H\rangle$ onto two detection states $|B(\hat{X}), \tilde{\mathcal{N}}, \tilde{\mathcal{P}} = \pm 1\rangle$ into opposite parity rotational states $|X, J = 0, 2\rangle$ and $|X, J = 1\rangle$. Then cycling or

ionization can be performed with the resulting populations in $|X\rangle$.

We hope that with these continued efforts we may someday detect the electron's electric dipole moment. This elusive property continues to hold the promise of teaching us something about that which we don't yet understand about laws of nature and the measurements may shed light onto how the early universe developed. Even if we don't observe the electron's EDM in the near future, each incremental step constrains theories of new physics and brings us closer to our goal.

Appendix A

Experimental Control Software

> It is exciting to discover electrons and figure out the equations that govern their movement; it is boring to use those principles to design electric can openers. From here on out, it's all can openers.
>
> Neal Stephenson, Cryptonomicon

A.1 Programming in LabVIEW

The ACME experiment, for better or for worse, is married to LabVIEW for experiment control operations. We have accumulated such a substantial library of LabVIEW code and instrument drivers since the early days of the experiment that starting out again with a new programming language would be impractical. However, it is not clear that we would want to switch away from LabVIEW since it is one of the few programming environments that facilitates fairly simple communication with external instruments and enables the creation of decent and functional user interfaces for interacting with these devices without too much work.

However, LabVIEW tends to evoke strong opinions, which is probably related to the fact that it deviates significantly from the form of the traditional programming environments such as that of C++ or Python. LabVIEW is a visual (rather than text based) programming language that is intended to mimic the electronic circuits. A LabVIEW function (known as a virtual instrument or VI) has inputs and outputs, and there are variables denoted by

wires that link together LabVIEW VIs to perform operations on variables.

When beginning to program in LabVIEW, there are several commonly made mistakes due to unfamiliarity with the LabVIEW programming environment. At their worst, LabVIEW code looks like a mess of wires that became tangled and don't have any hope of becomming untangled. At its best, LabVIEW reads as a nested flow chart that both performs operations and explains itself. Usually VIs fall somewhere between these two extremes. Here I provide some tips (that I have stumbled across the hard way) that help in developping programs that fall on the better side of the spectrum of LabVIEW code.

A.1.1 Tips for Programming in Labview (learned the hard way)

1. Keep the code simple - do not allow a program to exceed the size of your computer screen. If you have to scroll to connect the start and end-points of a wire, you are making the program unreadable and difficult to edit. As soon as your program reaches the size of the screen, bundle parts of the code that perform distinct operations into sub-VIs.

2. Always comment your code. The best way to comment is to edit the icon of a custom subVI and add 2-4 words which explain what that subVI does. Text comments on the block diagram should not be overlooked, but the subVI icon aids in crucial in enabling the code to double as flow chart.

3. Use error propagation for flow control (determining which parts of the code occur before others in time) - avoid sequences if at all possible. If you do not wire errors, and if an error does occur, your code will stop running altogether. Rather you would generally like your code to continue running, resolve the error on its own, display the error on a user interface, and log the error for future reference. If you use sequences for flow control, the code will often run a little slower and the block diagram tends to be a little bit bigger and less readable. Always include inputs and outputs for errors on subVIs *even if the VI does not use or generate errors* since these inputs and outputs are used to regulate flow control.

4. Use clusters to pass data between subVIs. Take all of the relevant variables in the program, bundle those variables as a cluster, define that cluster as a strict type definition, and pass that cluster into and out of subVIs. By using the "bundle by name"

and "unbundle by name" functions, every subVI will have access to all of the relevant variables in the program and those variables can be called and set by using their names. In addition, every subVI can have the nice standard form with a single cluster input and output and a single error input and output (otherwise, attempting to input many variables into a subVI looks like a spiderweb that is difficult to read).

5. Avoid using local variables - use property nodes instead to access data associated with a given front panel object. The property nodes include error terminals that allow you to include accessing variables in setting the flow control, and the property nodes enable access to many properties of a front panel object - not just the "value" which is obtained from the local variables.

6. You can manipulate front panel objects from a subVI within the program. It is not the most elegant feature in LabVIEW, but doing this is often critical to bundling parts of code into subVIs. This is achieved by inputing a front panel object reference into a subVI, and getting or setting data associated with this object by using unbound property nodes that are fed the front panel reference.

7. Avoid using local and global variables for communicating between loops within a single VI or for communicating between different VIs on the same computer - instead use notifiers or queues for data transfer. Queues are used if you have multiple sources that are sending data to a single receiver, and Notifiers are used if you have multiple receivers that need to receive every message.

8. It is usually useful to have two while loops in a given top-level program. One loop contains an event structure that responds and interacts with the user through the user interface. The second loop performs some operation such as saving data or talking to an instrument, etc... The two loops usually communicate with a queue or a notifier.

A.2 The Logging System

A.2.1 Logging

The most important data acquired from the experiment is certainly that which is taken when running the experiment; this includes photomultiplier traces and data from various

sensors monitoring the state of the experiment. However, we also insist on logging the data from the monitoring sensors at all times, although often at a slower rate. This data is useful for quickly detecting and diagnosing problems with experiment hardware which is a critical aspect of maintaining a high duty cycle for operating an experiment. This auxiliary data can be easily overlooked in importance, but the incremental work for implementing continuous data logging is small given that sensor monitoring must already be set-up for the experiment, and the potential gains from such a system can be significant.

This philosophy has been actively adhered to by the ACME collaboration since the beginning of the experiment. The original ACME logging system was constructed by Andrew Speck (a post-doc in the Gabrielse group), and was maintained by Paul Hess (a graduate student in the Gabrielse group). After both of these group members had moved on from the collaboration, most of the knowledge of this system was lost due to scarce documentation, so I sought out to revamp the logging system to ensure that the logging system would meet our ACME Generation II needs and to ensure that the system was user friendly and well documented. This section serves as documentation for the updated ACME logging system.

This logging system is set up with modularity in mind. Various programs on any given computer can communicate with experiment sensors and acquire data. These programs funnel data to the *Logging Mediator* which serves as a gatekeeper to the logging database and ensures that any given channel is not overwhelming the database with too much data. If the logging mediator is not running, or if communication between a client computer and the database fails, the individual programs that communicate with the sensors will not fail, but rather the data will just not be logged.

The logging data is assigned to a *Logging Channel* that corresponds to a time-series of data that consists of timestamps (with millisecond resolution), and real float data from a given experiment sensor. For each sensor, you must write a driver to communicate with and acquire data (more details on this are given in section XX below). To set-up data logging for this particular sensor adhere to the following instructions:

- **Register this logging channel with the database**. If you attempt to log to an unregistered channel with the database, the data will be ignored and lost. There is an easy-to-use LabVIEW form that you can use to register a *Logging Channel* that can be accessed via the *Logging Mediator* VI on the *Logging Status* tab by clicking on the *Add Logging Channel* button as seen in the upper left of figure A.2.1. A new

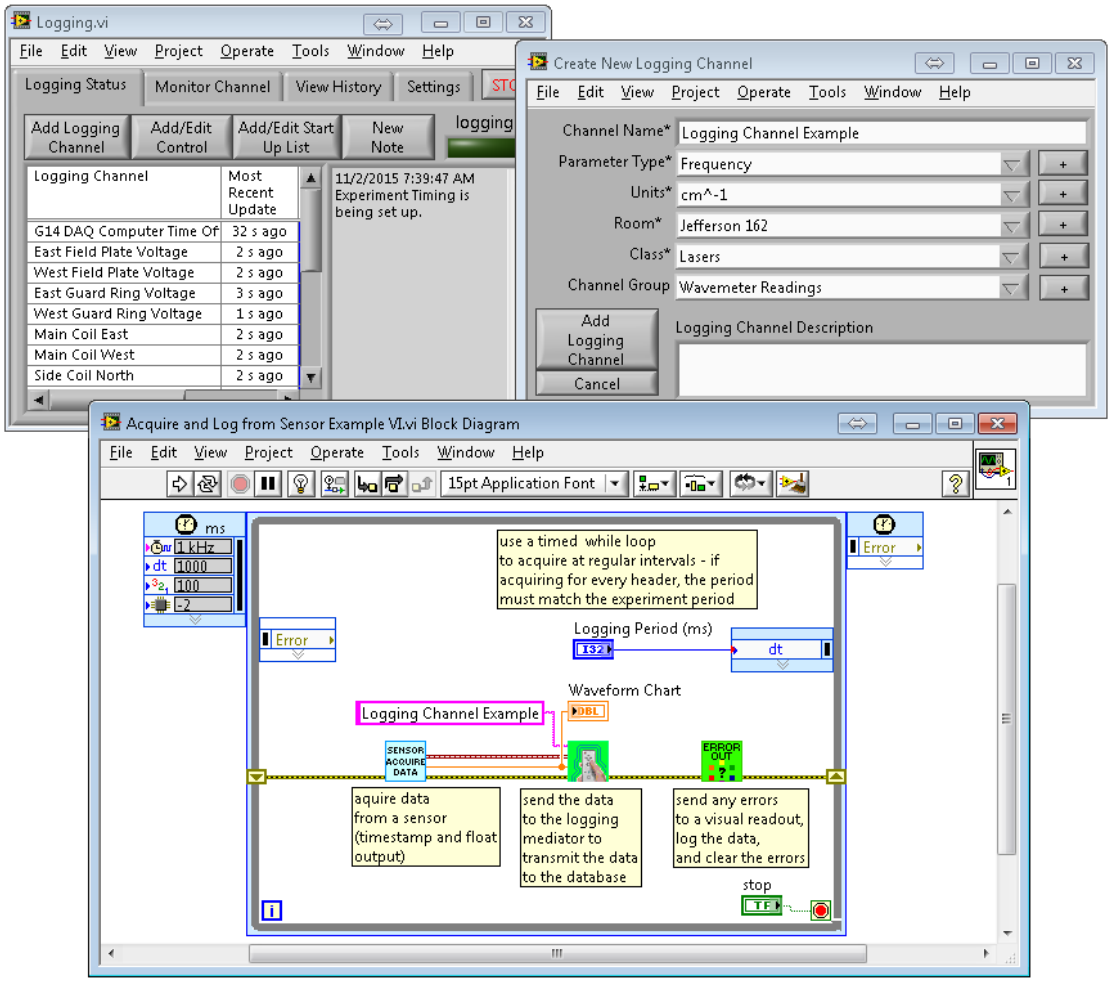

Figure A.1: Adding a Logging Channel. Click the *Add Logging Control* button on the upper left to open the *Create New Logging Channel* window on the right. After registering your logging channel with the database, write a VI to acquire and log data. Please follow the VI style guide shown on the bottom.

window will open that will request information about this new logging channel which is shown on the upper right of figure A.2.1. You should enter all of this information and remember the specified channel name which is refer to your new *Logging Channel*. If you have a new sensor with multiple outputs, then a separate channel should be assigned to output, and the set of channels can be assigned to a new *Logging Channel Group*. *Logging Channel Groups* make it easier to access data from multiple channels at once.

- **Create a VI that acquires the data and logs the data.** A style example for a logging VI is shown in the bottom of figure A.2.1. You should have a sub-VI that communicates with and acquires data from a sensor (style examples for this VI are included in the later section XX) and provides a timestamp that corresponds to when the data was taken. This data should be fed to the *Enqueue Logging Data VI* (available on the Logging menu palette with the image of a remote control on the icon) with the appropriate channel name wired to the string input. This will send the data to the Logging Mediator which will then decide whether or not to log the data, and if so will insert it into the *LogChannelData* table on the *LoggingLogData* database on the *Gandalf SQL Server*.

- **Plot or Download Logging Data.** Once the data acquisition and logging has been set up for a given logging channel, you will want to access the data that is logged. In the *Logging Mediator* VI on the *Monitor Channel* tab, there are drop down menus to select a logging channel or a logging channel group, and there are corresponding buttons to plot data corresponding to the selected channel or group. Upon pressing one of these two buttons, a *Logging Monitor* window will open with a plot of data from the last hour as shown in figure A.2.1. Controls on the upper left side of the window allow you to modify the time range that is being plotted. The upper right side of the plot allows you to save the data that is being shown in the plot to a designated text file. If you would like to access a large amount of data, or would like to automate the process of grabbing logging data periodically, you can set-up database access on any computer using the ACME VPN and access data with scripts that I provide for Matlab or Python as described in section XX.

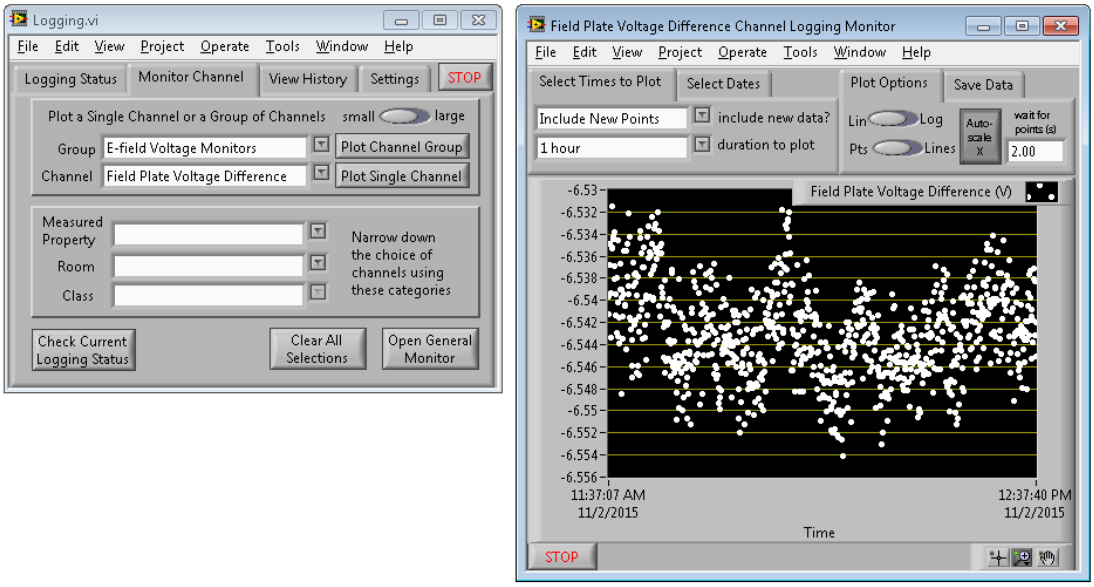

Figure A.2: Plotting Logging Data. Select a *Logging Channel Group* or a *Logging Channel* using the drop down menus and then click the *Plot Channel Group* or *Plot Single Channel* buttons on the left to open a *Logging Monitor* like the one shown on the right. The logging monitor allows you to select the time period that you would like to plot and gives you the option to save data to a text file.

A.2.2 Control State Data and Notifications

In addition to logging real float data from monitoring sensors, I have implemented a *Control State Logging* system that serves to log the state of instruments that control the experiment when there is a state change. In analogy to the data logging system described in the previous section, *Control Channels* take the place of *Logging Channels*, and a discrete set of control states replace the continuous real float data that is logged. Although the method for logging by the *Logging Mediator* is entirely analogous, there is one major practical difference between these two systems. The *Logging Mediator* continuously monitors the database (with a period of 250 ms) for new control state changes and when it detects a state change, it provides notifications in a textbox on the right side of the *Logging Mediator* window on the front *Logging Status* tab (as seen on the lower left of figure A.2.2) and also sends these notifications out in a LabVIEW notifier to any VI that may be listening. Programs can be set up to listen for certain control state changes and can perform operations contingent on receiving such notifications. By this method, the control state logging system can be used as a remote control to send commands between computers on the logging system in

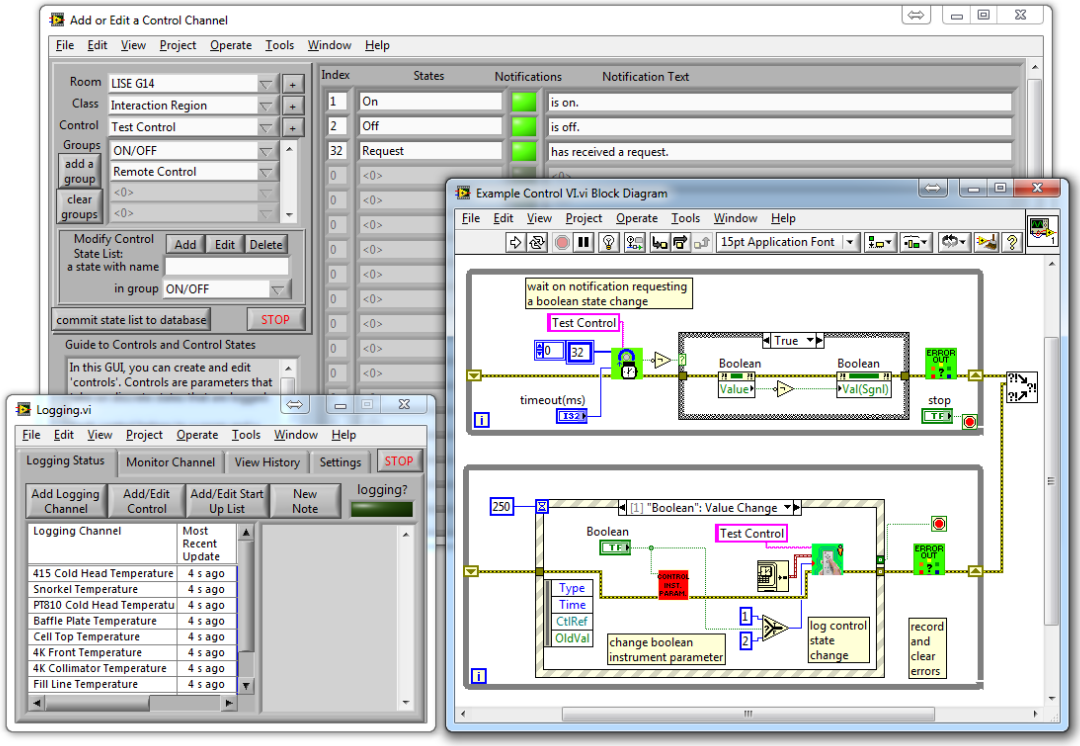

Figure A.3: Adding a Control Channel. Click the *Add/Edit Control* button on the bottom left to open the *Add or Edit a Control Channel* window shown on the top. Here, you can add a Control by clicking on the "+" button next to the Control drop down menu. Then you must assign Control State Groups, as seen in the "Groups" section, and then you must add individual states as seen on the right side of the window. After states have been selected, click "commit state list to database" to save the changes that you have made. After creating a control, follow the VI style guide shown on the bottom right to create a VI that logs control state changes and listens for other control state changes and performs operations contingent on those perceived state changes.

addition to keeping a record of the states of instruments in the experiment.

Follow the instructions below to take advantage of the *Control State Logging* system:

- **Set up a Control Channel.** You must register a *Control Channel*, its possible control states, and the notification text that should accompany each state with the database before inserting data into this channel. On the *Logging Mediator* VI on the first tab *Logging Status,* there is a button with text *Add/Edit Control.* Clicking this button opens a LabVIEW form that allows you to create control channels, control states, and control state groups, and to assign allowed states to a given control channel. On the upper left side of this window, you must specify a *Room* and *Class* that your new *Control Channel* belongs to. To edit an existing control, select a control from the "Control" drop down menu. To add a new control, click the "+" button next to the control drop down menu and enter the new control name in the window that pops up.

- **Assign Allowed States to a Control Channel.** Within the *Add or Edit a Control Channel* window, you must assign states that are associated with your control. Each control subscribes to and array of *Control State Groups* from which assigned states can be chosen. These *Control State Groups* can be created and/or assigned to a given control in the "groups" section of the window right below the "control" drop down menu. You may also add, modify, or delete states within a given *Control State Group.* Note that when you create a new state, you must specify a *State Name* and *Notification Text.* When this state is called, the text that will appear in the notification textbox will be of the form {date}{time}{control name}{notification text}. I like to ensure that the combination ({control name}{notification text}) forms a readable sentence where {control name} is the subject. Now that your desired states exist within *Control State Group*s that are assigned to your control, you may assign specific states to the control on the right side of the window using the "states" drop down menu array. There is a boolean option named "notifications" next to the "states" drop down menu array - I usually set this to true, but currently this option does not have any purpose. I imagine in a future version of the logging system this option would be used to allow states to opt out of displaying notifications, but in the current state, all states display notifications. After assigning a state list, make sure to click "commit state list to

database". You can access this states list at any time by returning to this window and selecting your control from the "control" drop down menu. In order to log or listen for a given state, you will need to refer to the state by the unique "Index" integer to the left of the "states" drop down menu array. This states list window is useful when used as a look-up table for state indices.

- **Create a Control VI that monitors and logs state changes.** A VI style guide for creating a control VI is shown in figure A.2.2 on the bottom right. Here there are two loops - one is a user interface loop that contains an event structure and, in this case, waits for a user to click a certain boolean button that changes that state of an instrument in a subVI. When the button's state changes, the new control state is logged using the *Enqueue Control State Data VI* (which can be found on the Logging Sub-Pallette and has a picture of a remote control and a little person on the icon). The *Enqueue Control State Data VI* sends the data in a queue to the *Logging Mediator* which decides whether or not to log the data, and if so inserts the data into the *LogControlStateData* table in the *LoggingLogData* database on the *Gandalf SQL Server*. The second loop listens for an array of possible notifications from the database, and if it receives one of these notifications it will cause the boolean switch to change state.

- **View or Download Control State data.** In the *Logging Mediator VI* on the third tab *View History* there is button that says *View Notification History* and next to this button is a drop down menu with a list of *Controls*. If you select a control and then push this button, a new window will open that will display notifications from state changes that correspond to the chosen control over a certain time period. The time period that is displayed can be selected on the upper left of this window, and there is an option to save this data to a text file on the upper right side of this window. If a control channel is not selected, then this window will display notifications from all controls over the designated time window. This data can also be accessed by querying the database directly, which is described in section XX.

A.2.3 Global Variables

The *Gandalf SQL Server* is also being used to share global variables among the computers on the ACME network. This is simply a list of string variable names with corresponding string data that is contained within the table *GlobalVariables* on the database *LoggingConfigSQL*. Any computer can read or write values to each one of these variables at any time by using the *Get Global Variable* and *Set Global Variable* VIs that are found in the logging subpallette. You can also request or read multiple variables at once by using the *Get Global Variables* and *Set Global Variables* VIs on the logging subpallette (using these array based VIs are more efficient than using the scalar VIs in a loop because all of the queries on the database are transferred in one packet). Unlike the Logging and Control State Logging systems, the Logging Mediator does not mediate the database communications for Global Variables (this is a relatively safe database operation since it does not increase the size of the database, but only reads or updates a single existing entry).

Global variables serve as a fairly quick (as fast as 10ms) way to communicate between two computers via the *Gandalf SQL Server*. For example, a Global Variable is used to sync the operation of the FPGA DAQ acquisition with the setting of the experiment state in the Master Run VI. The Master Run VI inserts a state name into a global variable. When the FPGA DAQ receives traces, it reads the global variable, uses the information to save the data to the appropriate file, and empties it in acknowledgment of receipt of the data.

Global variables can be also used to control the parameters of a remote operation. Although the Control State Logging system enables software triggers to be sent for remote control between computers, sometimes data needs to be shared between multiple computers to elaborate on instructions for a given operation which can fulfilled by taking advantage of global variables. For example, a doppler scan with a given locked laser can be triggered with a control state notification. However, the number of points and the range of the frequency scan is set by global variables.

A.2.4 Header Queue

The Header Queue is a database table named *Header* on the database *LoggingConfigSQL*. I refer to it as a "queue" in analogy to a LabVIEW queue; the data from many experiment sensors are inserted into the queue from several computers, and all of the data is removed

from the queue periodically by the Master Run VI that uses that data to construct the experiment header files. The transfer of data for insertion into the header is functionally separated from the logging system for two reasons:

- We like to log data at a slower rate (about every 5 seconds) compared to the rate at which we change the state of the experiment and log header files (about every .5 seconds). If these two operations were not functionally separated, we would have to log about 10x as much data as we would otherwise.
- The logging database table grows in time and hence queries on that table become slower over time. Since the header table is periodically emptied by the Master Run VI, the Header table is small and maintained at roughly a fixed size averaged over time such that the query speed against that table is fast and does not change significantly over time.

I have been setting up the various experiment sensors to attempt to log data at the same acquisition rate as the experiment (every .5 seconds) such that one entry per logging channel will be contained in each header. When the experiment is not running, the sensors are acquiring at the same rate but the logging mediator throws away data to enforce a logging rate of once every 5 seconds. When the Master Run VI is turned on, a Control Notification triggers the Logging Mediator on each computer to start inserting all logging data into the Header Queue at the full acquisition rate. When the Master Run VI is shut off, data is no longer inserted into the Header Queue.

A.2.5 Device Drivers

In the ACME experiment, we attempt to set up as many devices as possible to be controlled via Ethernet over the ACME network so that these devices may be accessible from any computer. However, most of the devices in the ACME lab are not directly controllable via Ethernet, but rather controllable via RS-232, RS-485, GPIB, Fiber Ring, USB, NI DAQ, etc... In general we use Comtrol DeviceMasters to control RS-232, RS485, and Fiber Ring devices via Ethernet. The serial communications settings (baud rate, parity,stop bits, terminating character, etc...) can be set from the Portvision software on *Gandalf* for each port. We use NI GPIB-ENET devices to communicate with GPIB devices over Ethernet. Note that a computer must have the GPIB-ENET drivers installed and must have each

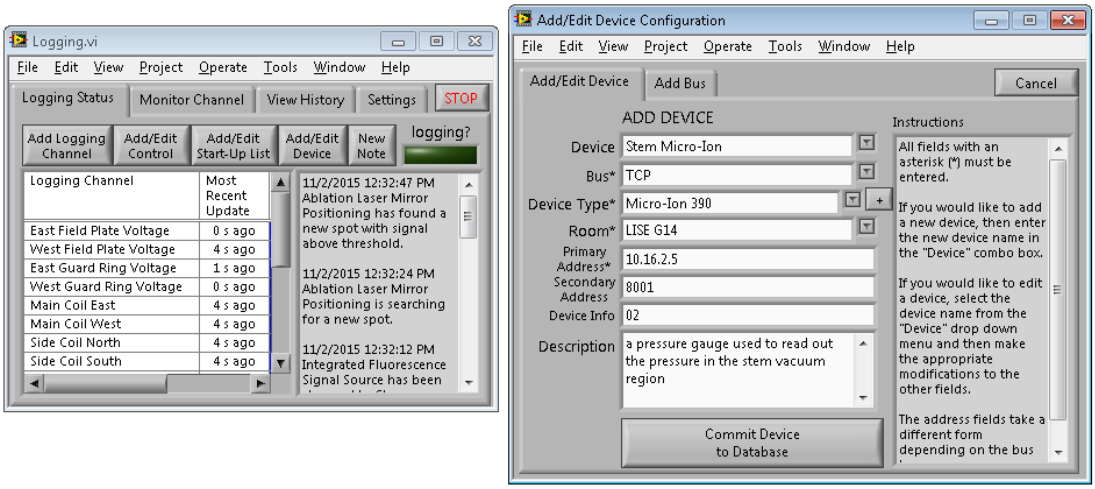

Figure A.4: Adding a Device. Click the *Add/Edit Device* button on the left to open the window on the right. This form allows your to register the communication protocol and address of a given device in the lab with the database.

GPIB-ENET devices registered with NI MAX with the appropriate name before you can communicate over one of these devices. We have not yet found a way to make a USB or NI DAQ device available for communication over the ACME network, so for the time being, these devices are tethered to a given computer and can only communicate with that computer.

Before you can communicate with a given Device on the ACME network, you must register your device with the database. By clicking on the *Add/Edit Device* button on the first tab *Logging Status* on the *Logging Mediator* VI, you can access a simple form that allows you to register your device with the database as shown in figure A.2.5. You must assign a unique *Device Name* to your device which will be used as the handle to communicate with your device. You must also specify the *Device Type* (a new device type may be added using this form, however if you have certain start-up and close VIs that must be run before you can communicate with a device, then you must create your device type on Gandalf and you must register the start-up and close VIs) the *Bus* the *Room* and you must enter an address for your device. The form of the address fields will depend on the device type and the bus, but in general we only have a few ways to specify the address. The easiest way to figure out how to specify the address is to look at examples of devices already on the network with the same protocol as yours and mimic the address form. For Ethernet and Comtrol devices the primary address is the IP address of the device. For GPIB devices, the primary

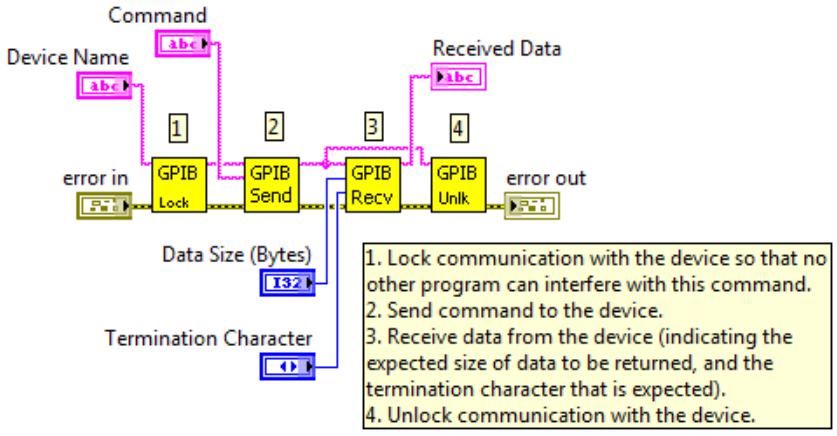

Figure A.5: Creating a Device Driver. After having registered your device's address with the database, follow this VI style guide to create a device driver for communicating with a device. These VIs can be found on the GPIB subpalette.

address is the GPIB address integer. For Ethernet devices, there is no secondary address. For Comtrol Devices, the secondary address correponds to the port number on the Comtrol device. For GPIB addresses, there is usually not a secondary address except for the rare case where a secondary GPIB address integer is required to specify the location of a device.

We have a set of robust LabVIEW VIs which have been tried and tested and work for communication with devices with a variety of communication protocols - *it is strongly recommended that you use these VIs to write device drivers*! These VIs are yellow and are found within the "GPIB" subpalette, though the VIs do not apply only to GPIB devices. If you do not believe that these VIs cannot accommodate the communication protocol that you are using, then these VIs should be modified to do so. An example of an instrument communication driver using these VIs is shown in figure A.2.5. Note that the the instrument is designated only by the *Device Name* that has been registered with the database. The first time you attempt to communicate with a device with a given *Device Name*, these VIs query the database to determine the communication protocol and address of this device. Then these programs cache the address information open a communication session with the device. Once a communication session is open with a device, you generally cannot communicate with this device from another computer until you manually close the communication session using the "Close VISA Session" VI.

A common problem that arises when writing device drivers comes about due to improper

reading from a device. If you attempt to read from an instrument and you specify an incorrect terminating character, in some cases the device driver can hang (while continuously probing this device, using a lot of the CPU!) for a few seconds and can cause all operations on the computer to lag even if all of the data from the device was read within the first few milliseconds to the operation. You should test your instrument drivers to ensure that this is not happening and that you are reading from the device as quickly as possible. If the device does have a long wait time before providing responses, you may want to put in a delay between your write and read operations so that the computer is not using up resources by continuously probing the device in the meantime.

A.2.6 Start-Up Protocols

When using LabVIEW to control an experiment, it is nearly inevitable that you will end up with a myriad of programs each with its own window, each of which is necessary for the operation of the experiment. Opening all of the necessary programs can be tedious and adds to the start-up time of the experiment. To facilitate the start-up process, I have set-up a system so that we can have an array of different start-up configurations that are specific to certain computers in the lab. On the desktop of each experiment control computer I have put a shortcut to the "Run VI Loader". Double-Clicking on this icon will open LabVIEW (if it is not already open), and will display a small window with a drop-down menu. From this menu you can select the start-up configuration that you would like to initiate. After making a selection the corresponding VIs will be opened and will start running if the start-up list indicates that they should open on start-up.

You can add a new start-up list, or modify a start-up list for any computer in the lab by clicking on the *Add/Edit Start-Up List* on the first tab *Logging Status* of the *Logging Mediator* VI. Pressing this button opens a new window as shown in figure A.2.6. After selecting a computer, you can select an existing start-up list from the "Start Up Config" drop down menu, or you can add a new start-up list by clicking on the "+" button next to the drop down menu. After having selected a start-up list, you can edit the list of VIs that should be opened in the "Start-Up Configuration Details" box. There an array of "VI Names" which are drop down menus with a list of all VIs that have been registered with the database. The VIs are opened in order from the top of the list to the bottom of the list. If you would like to add a VI to a start up list that is not yet in the drop-down menus,

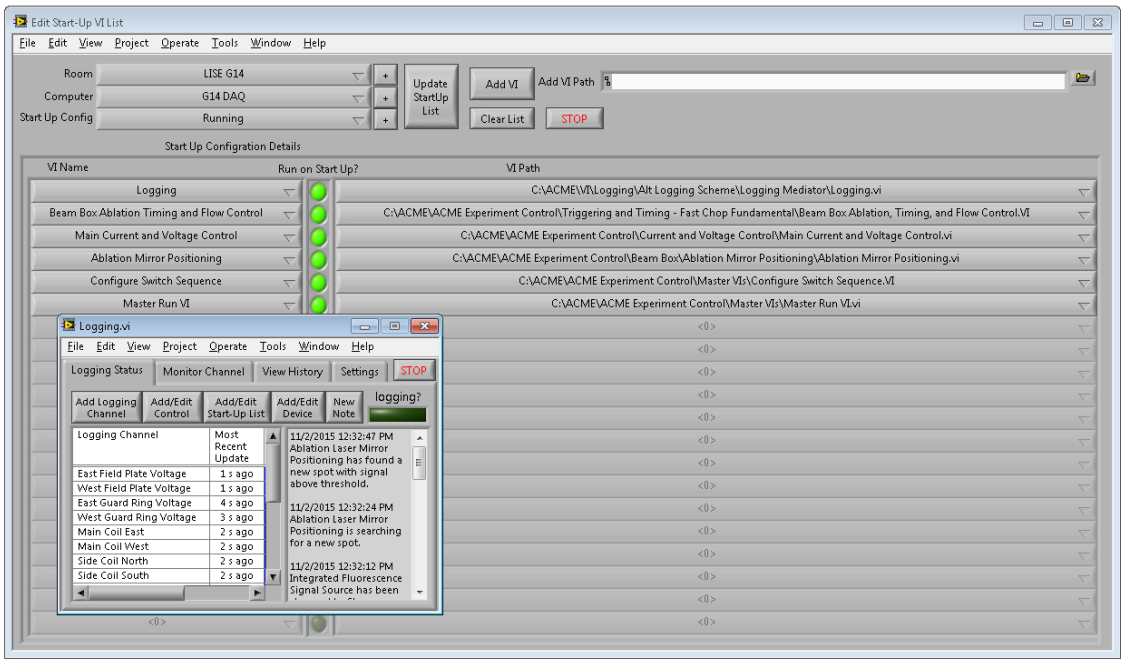

Figure A.6: Start Up Lists. Click the *Add/Edit Start-Up List* button on the bottom left to open the window shown in the background. Here, you can create a list of VIs that will automatically open and start running after clicking the "Run VI Loader" shortcut on the desktop.

then you can add a VI to this list by inserting the path to this VI in "Add VI Path" on the upper right of the window, and then you must lick the button "Add VI". If the VI has a complicated name, the VI may complain and give an error; if this happens, please make a copy of the VI with a less complicated name and then add that VI path. After adding the VI, it should show up in the drop down list of "VI Names". After you are satisfied with the start-up list modifications, click the large button that says "Update StartUp List" to commit the changes to the database. If you don't do this, your start-up list modifications will be lost.

A.2.7 Doppler Scan Logging

Most of the data that we log fits nicely into the framework described in the Logging system described in section XX. However, we have been logging a specialized format of data each time we take a doppler scan that does not fit so nicely within that framework. Hence, I created a specialized table *DopplerScanData* on the *LoggingLogData* database to accomodate doppler scan logging. If we find that we would like to be logging many types of "scan"

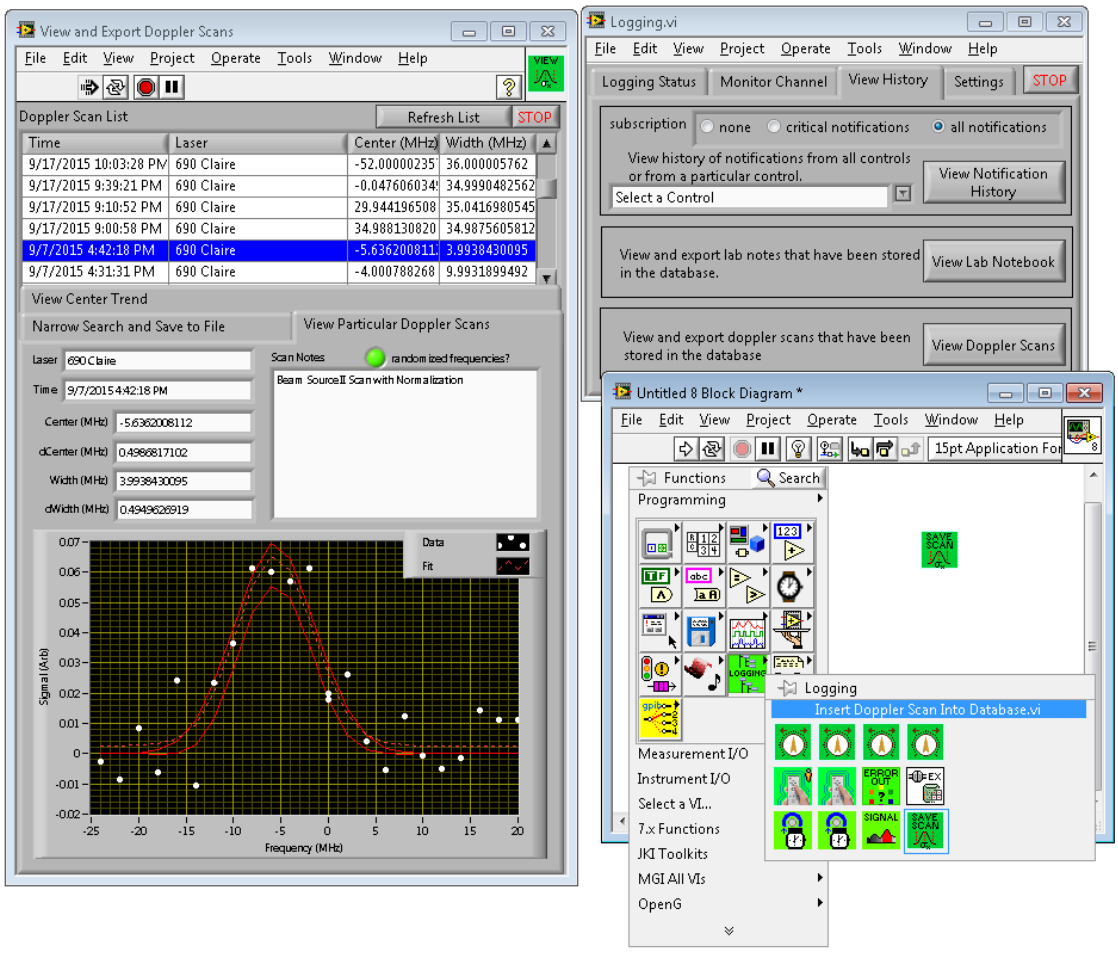

Figure A.7: Doppler Scan Logging. By using the *Insert Doppler Scan Into Database* VI, shown in the Logging subpalette on the bottom right, you can log doppler scan data. By clicking the *View Doppler Scans* button on the top right, the window on the left will open which will allow you to search, view, and save-to-txt doppler scans that have been inserted into the database.

data, we can generalize the *DopplerScanData* table to accomodate these other scan types, but at present we have no need to do so. Any program that takes doppler scans can log the resulting frequency vs signal data on the database by using the *Insert Doppler Scan into Database* VI that can be found in the logging subpalette that is shown on the bottom right of figure A.2.7. The doppler scan data that has been save can then be viewed or downloaded by going to the *View History* tab of the *Logging Mediator* and pressing on the *View Doppler Scans* button. This will open a new window which will allow you to search through the existing doppler scans by laser or date, and you can also view trends in the center frequencies or widths of the doppler scans for a given laser in time.

A.2.8 Quick Lab Notes

I found that I was often taking notes while in lab in my personal email account, and searching my email later when I wanted to refer back to those notes. After thinking about this system, I decided to formalize it and make it easier to implement with the *Lab Note* functionality of the ACME Logging system. On the *Logging Mediator* VI on the first tab *Logging Status*, there is a button that says *New Note*. Clicking on this button opens a *Note Editor* window where you can specify the lab member who is writing the note, the title of the note, and the text of the note as shown in figure A.2.8. I implemented an auto-save feature such that if the window is open for a few minutes and there is text in the note, it will automatically save the note to the database, and the program automatically saves when closing the note. There are buttons at the top of the window which allow you to quickly email the note to yourself and/or to other group members. You can also view and edit previous entries by using the *Lab Notebook* which can be accessed by navigating to the third tab *View History* in the *Logging Mediator VI* and clicking on the *View Lab Notebook* button. This will open a window which at the top will display a list of previous entries. You can filter the entries in the list by lab member or by category. By double-clicking on an entry, it will open the text of the lab note in the text box below. By default, you cannot edit the text of the lab notebook, but if you press the *Allow Editing of Body* button, you can edit the note within the *Lab Notebook.* Alternatively, you can click the *Open Note in Editor* button to load the selected note in an editor window for editing.

A.2.9 Error Handling

It is easy to overlook the importance of error handling in LabVIEW. However, as described in the LabVIEW tips section, ignoring error propagation can physically stop your program, whereas proper error handling will overcome the error and inform the user so that the problem can be fixed. I have implemented an error handling protocol for the ACME experiment which makes proper error handling simple. In the logging subpalette, there is a VI named *Clear Errors and Log*. This VI should be placed inside all while loops in your program at the end of the set of operations for your loop as seen in the VI style examples in figures A.2.1 and A.2.2. This VI sends the errors to the *Logging Mediator* where the errors will be displayed in the same textbox as the Control State notifications. If the "Log Errors" button

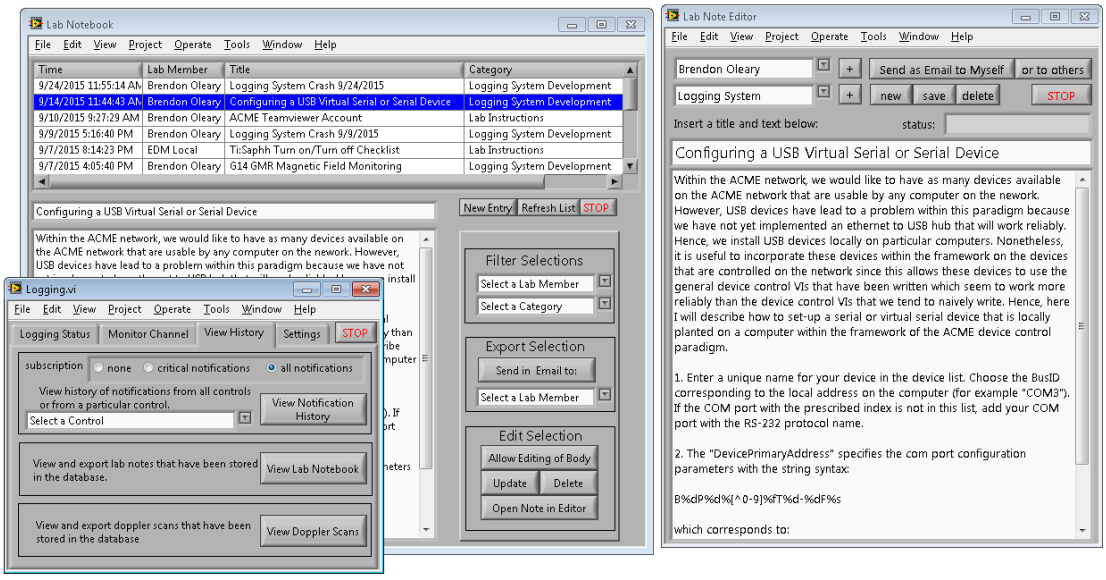

Figure A.8: Quick Lab Notes. By clicking the *New Note* button on the *Logging Mediator*, a window like that on the right will open which will allow you to jot down some notes in the lab and then save the note and quickly email it to yourself or to others. By clicking the *View Lab Notebook* button on the bottom left the window in the background on the left will appear that will allow you to search, view, and edit the existing entries.

on the settings tab is pressed, then these errors will also be logged in the *LogProgramErrors* table on the *LoggingLogData* database.

A.2.10 Details on the Database Structure and Maintenance

We are constantly adapting the *Gandalf SQL Server* databases to suit our needs. Nevertheless, the more infrastructure that we build around the existing database model, the more permanant it becomes. Hence, in this section, I will document the more permanant parts of the database model for future use. There are two primary databases that are currently in use:

- *LoggingConfigSQL* - contains mostly "configuration data" - this database is fairly small in size and does not change significantly in size over time. You can read and write fairly quickly to this database.
  - *Devices* - a list of devices that are accessible via the ACME network with their communication protocols and addresses
  - *LogChannels* - a list of all of the logging channels along their properties such as

the parameter type and units that are being locked

- *LogControls* - a list of the logging controls and their properties
- *StartUpConfigs* - a list of all of the registered LabVIEW start-up configurations on all of the lab computers
- *SwitchConfigurations* - a list of all saved switch configurations generated by the *Configure Switch Sequence VI.*
- *Triggers* - a list of all of the hardware trigger configurations that are being used for the experiment hardware timing.
- *Lasers* - a list of all of the lasers in the lab along with their locations, locking method, and wavemeter channel
- *GlobalVariables* - a list of global variables that can be read or modified by any computer in the lab
- *DefaultValues* - a list of values for experiment parameters that should be used if these parameters are not explicitly set.

- *LoggingLogData* - This database consists mostly of stored data, can be quite large in size, and grows over time. Queries on this database can be fairly slow so this database is mostly used for write-only operations.

  - *LogChannelData* - a compilation of all of the logged data from the experiment.
  - *LogControlStateData* - a compilation of all of the logged control state changes in the experiment.
  - *LogLabNotes* - a list of all of the saved lab notes.
  - *LogProgramErrors* - a list of all logged program errors from various labview programs.
  - *DopplerScanData* - a list of all logged doppler scans.
  - *AblationMirrorPositioning* - a map of where we have ablated on the ablation target
  - *Header* - a queue of logging data that is used to transfer header data to the master run VI

Since the *LoggingLogData* database is continuously increasing in size over time eventually, old data will eventually need to be archived so that the database size remains managable. After starting the *LoggingLogData* in August 2015, by October 2015 I found that simple queries (SELECT MAX(TimeStamp) FROM LogChannelData) would require at least 10 seconds to complete, and larger queries would timeout. I found that this was happening because there was no primary index on the *LogChannelData* so each time a query was performed

A.2.11 Accessing the Database from Your Office Computer

The ACME logging system saves data in databases hosted on a Microsoft SQL Server. Gandalf (10.16.1.2 on ACME Network, located in Jefferson 162) is the server on the ACME Network and hosts the SQL Server as well. The logging VIs on the computers in the lab communicate with this SQL server over the ACME network via LabSQL. However, we would like to access the logging data from computers that aren't necessarily on the ACME network, and using programming languages that are not necessarily LabVIEW. Hence i am providing instructions for setting up a connection between a computer and Gandalf, and instructions on how to extract data from the database using Python and Matlab.

Gandalf is connected to the ACME Network and to the Gabrielse Network, and can access the internet only through the Gabrielse firewall. We are using a VPN to connect between computers on the internet and the SQL Server on.

Instructions:

- Install the VPN LogMeIn Hamachi (select unmanaged mode). Once installed, open the program, and click on the button that looks like the 'on' button for a computer. This will connect the VPN to the internet and assign an IP address to the computer on the VPN. You will be prompted to log into LogMeIn - you can use the experiment credentials:
  - edm.experiment@gmail.com
  - (usual password)
- Once logged in, you should be able to click 'Join existing VPN' with credentials:

  - VPN Name: ACME-Database
  - VPN Password: (usual password)

- You should now be on the VPN, and the LogMeIn Hamachi window should show that Gandalf.acme.harvard.edu is also on the VPN (if not, open the VPN on Gandalf). By right clicking on Gandalf, you can choose to ping Gandalf to test the connection.
- You need to install the SQL Server Client 32 bit version or 64 bit version which will allow you to make connections to an SQL server.
- Now, depending on the programming language that you are using, you will may need to download some package to send commands and grab data from a database. I have have able to do this in python and in matlab and will provide instructions for both:

Access via Python 2.7

- Download and install the package pyodbc (this is easily done by using the command 'pip install pyodbc' in the command prompt)
- Follow the documentation for pyodbc to issue SQL commands to the database and retrieve data. I have written some sample code and provide it here.

Access via MATLAB (>2013)

- Click on the MATLAB 'apps' tab and click on the database explorer. If this is not present then you will need to download the database toolbox. If it is present, then it might prompt you to connect to an existing database, but since you don't have any configured yet, click 'cancel'. Click the down arrow on the 'new' button at the top of the matlab database explorer window, and then select 'new odbc data source'. This will open a new window with a list of existing configured databases. Click 'add' and another window will pop up asking you to select a driver for the connection. Click 'SQL Server Native Client 10.0' and click finish. Give this database connection the same name as the database 'LoggingLogData', and enter 'gandalf' as the server. Specify that you would like to connect with SQL server authentication with username 'sa' and the usual password. Select the default database to be 'LoggingLogData'. Now you should see 'Logging Log Data' in the list of ODBC data sources. Add another

source repeating each step but for the 'LoggingConfigSQL' database. Now that these databases are configured in Matlab, you can 'browse' the data in the database. Since most of the data is in a very large single table (LogChannelData), then this browser is essentially useless, and you should find your desired data by using SQL in scripts.

- Now that the database connections are set-up you can follow the database toolbox documentation to issue SQL commands to the database and retrieve data. I have written some sample code and provide it here.

SQL Queries

- If you want to do something complicated with grabbing data, you will need to learn some SQL commands. There are some simple tutorials online such as this one.
- If you just want to grab some data from a given channel between a certain set of times, I have provided some python code here and some MATLAB code here.

WARNING

In the real world people work really hard to set up permissions to their SQL databases and carefully regulate which clients have write and read access to different parts of the database and try to keep the clients from doing stupid things. We have not done anything of the sort and only have a single login to the database and so you have the full capability to access and destroy all of the data. Here are some tips for interacting with the database:

- DO NOT DELETE DATA!!!
- Only insert data if you know what you are doing. Even if you know what you are doing, do not overload Gandalf with insert requests - BE REASONABLE!
- DO NOT DOWNLOAD TOO MUCH LOGGING DATA!!!!! there is a lot of data in gandalf and if you request all of the logging data, the server will probably get overloaded for a while and might crash.

Good luck with your database access. If you want to add some functionality to the database, please consult the database administrator (this is Brendon currently).

A.3 Experiment Control Software

A.3.1 Ablation Mirror Positioning

The *Ablation Mirror Positioning* VI allows you to control mirror motors that control the pointing of the YAG ablation laser onto the ablation target in the buffer gas cell so that the laser is addressing a new *spot* on the target. There is a set of 8 buttons that allow you to move the mirror motors in 2d across the target on the upper left side of the program.

Finding a New Spot

AI for Automated Spot Finding

Integration with the Database

The *Ablation Mirror Positioning* VI is one special case of a program that interacts with the database independent of the *Logging Mediator* VI. This VI first grabs the most recent x and y positions of the mirror motors from a database global, and then it loads into memory all of the data from the most recent *MapID* regarding previous ablation spot locations (x and y), a timestamp for when the laser moved to that location, and a duration of time during which the YAG was on file firing at that spot.

After switching between ablation targets, or after realigning the YAG ablation optics, the current ablation map is no longer applicable and so a new map should be initialized. This can be done by going to the 'configuration' tab and clicking the 'New Target' (which will prompt you to specify which target you are now shooting at), or clicking the 'Realigned Optics' button. The data from the previous ablation maps remains saved in the database after these operations for future access.

Troubleshooting

In case you are troubleshooting problems with the VI, here some suggestions:

- **The Mirror Motors need to be reinitialized.** The mirror motors sometimes need to be re-initialized before they will work again. You can do this by clicking on the 'initialize' button on the 'settings' tab. This will move the mirror motors to the "zero" of the coordinate system, and then will return to the setpoint.

- **The assigned COM ports are incorrect.** The mirror motors are controlled by USB and are registered with the computer as virtual COM ports and sometimes the computer will reassign a new number to the virtual COM ports. Go to the Device Manager and determine the current COM port for the devices and then make sure this matches up with the COM port assignments on the 'settings' tab of the ablation mirror positioning VI.

A.3.2 Beam Box Ablation and Timing

Beambox Controls and Limits

Experiment Hardware Timing

A.3.3 Main Current and Voltage Control

A.3.4 Configure Switch Sequence

The *Configure Switch Sequence* VI allows you to customize the experiment that you are performing on any given day. You input the parameters that you would like to vary, whether or not their should be a complete set of states with respect to this parameter, the values that they should take on, and the way and the rate at which they should be varied and then the program will generate a sequence that will be forwarded to the *Master Run* VI to perform the experiment. A switch configuration consists of a list of *Switch* objects. These objects contain information about how the switch should be performed and contains a list of switch states to to step through. Switch states themselves can be Switch objects as well, which leads to nested switch structures. I refer to the deepest nesting level as the "block", and the next nesting level as the "superblock", and the next after that is an "uberblock". This switch structure can be represented as a tree where the leaves are the individual switch states.

The code works with a custom Python class:

```
Switch(name,states,timescale,degeneracy,force_unique,configuration)
```

The input parameters are described as follows:

name – a name string corresponding to a given switch. the list of allowed names are included in *LoggingConfigSQL* under the view called *Switches*. These names must not

have spaces or special characters such as "—", and must be correct, otherwise the master run VI might throw an error.

states – a list of states. For binary switches this is usually just $[-1, +1]$, but for continuous parameters, this can be an arbitrarily long list of real numbers. In the case of nested block, superblock structures, the states list can also include switch objects.

timescale – this is an integer$n \geq 0$ which indicates the timescale on which this switch should live relative to the other switches. On any given switch nesting level, $n = 0$ is the fastest switch timescale (unless no switch is assigned to $n = 0$ in which case the fastest switch is the one with the smallest assigned timescale). Only the ordering of the timescales matters, not the difference in their values (if we only have two switches, with timescales 0 and 2, the behavior will be the same as if we have two switches with timescales 0 and 1).

degeneracy – this is an integer $n \geq 1$. This will indicate how much degeneracy there should be in a given switch. If we configure an AB binary switch with degeneracy 2, then a sequence ABAB will be generated before moving on to the next timescale.

force_unique – this is a boolean (True or False). For a set of switches on a given nesting level, we may want a unique set of all possible state combinations for those switches. force_unique indicates whether or not to include this switch in that set of switches on which we will enfore the unique state condition on each nesting level. If two or more switches are forced to be unique on the same timescale within the same nesting level, then other instructions indicating the switch method are overconstraining the problem. The code handles this by ignoring the specified switch configuration and introducing randomness.

configuration – is a specially formatted list with two inputs. The first input is one of the following strings: 'sequence','random permutation', 'serial sequence' or 'random sequence'.

- If the first input is 'sequence': the second input should be a 1D list of indices corresponding to states that should be called. These states will be called in the sequence provided.

  - If the first input is 'random permuation': the second input should also be a 1D list of indices. The states that are called will be a random permutation of these indices.
  - If the first input is 'serial sequence' or 'random sequence': the second input should be list of lists. When the sequence is called, it will step through each sequence (for 'serial sequence') or it will randomly permute the sequences in the list and and step through them (for 'random sequence').

- There are also some shortcuts so that you don't always have to include a configuration list of indices.
  - configuration='sequence' is equivalent to configuration= ['sequence', xrange(0,len(states))]
  - configuration='random permutation' is equivalent to configuration= ['random permutation', xrange(0,len(states))]
  - configuration='ascend/descend' is equivalent to configuration= ['serial sequence', [xrange(0,len(states)), xrange(len(states)-1,-1,-1)]]
  - configuration='in to out' generates a configuration which starts in the middle of the states list an alternates between states on the left and the right of center, working its way to the outside of the list.
  - configuration='in to out and back' generates a configuration equivelent to the 'in to out' configuration, but then repeats the sequence in the reverse order the next time it is called.

- if you have a binary switch, there are some additional options included for convenience,
  - configuration='AB' is equivalent to 'sequence', configuration= ['sequence', [0,1]]
  - configuration='rand(A,B)' is equivalent to 'random permutation', configuration= ['random permutation', [0,1]]
  - configuration='ABBA' is equivalent to configuration= ['sequence', [0,1,1,0]]
  - configuration='rand(AB,BA)' is equivalent to configuration= ['random sequence', [[0,1],[1,0]]]
  - configuration='rand(ABBA,BAAB)' is equivalent to configuration= ['random sequence', [[0,1,1,0],[1,0,0,1]]]

How to Create a Switch Sequence

This program is fairly sophisticated and as such, it takes a litttle while to learn how to program it. It will probably suffice to load various sequence instructions from the database into the "Configure Switch Sequence VI" and stare at the instructions and the resulting switch sequence to understand intuitively the mapping between the two. Nevertheless, I will provide instructions here for creating a switch sequence using the LabVIEW user interface.

When you open the program, an existing switch sequence will be probably be present. To start from scratch on a new experimental switch sequence, you can click the *Delete Sequence* button. All switch configurations that are generated are saved to the database so you don't have to worry about deleting someone elses configuration. Click the *Add Switch* button to add a new switch parameter to the experiment. Note that a switch parameter doesn't have to have multiple states and can be static throughout the experiment. Clicking on this button opens a new window which allows you to configure all of the switch properties described in the previous section, except for the states list. There are drop-down menus to select the switch name and the configuration types - as described earlier, for some configuration types you must include a configuration list, but for others you need not.

After adding a switch, you must add states for that switch to switch amongst. You can add these by hightlighting the switch that you would like to add states to by clicking on it's text and then clicking on the button *Add Child State Array*. This button will open a new window where you can add a list of strings that correspond to states. There are shortcuts on the right side of this window to populate the states array with binary switch states or linearly varying real switch values. Note here that the states that you enter here must be recognized by the subVIs in the Master Run VI that set that instrument states given the experimental switch state inputs. You can repeat this process for several switches, which would then constitute block switch sequence. To nest the switches to generate a superblock switch sequence, you can click the *Nest All Switches* button. If you want a given parent switch to switch between multiple child switches, you can highlight the parent switch and then click the *Add Child Switch* button, which will open the switch configuration window again, and will create a second switch so that the parent switch can switch between two switch configurations.

Click the *Generate Sequence From Configuration* button to create a sequence. After

doing so, the status indicator should show that the program is working and then after a few seconds, it should generate a new figure on the right side of the VI which schematically shows the new sequence that has been generated. The sequence instructions have also been saved to the database and can be recalled at any time.

Save a Sequence or Access an Existing Sequence

When generating a sequence from a new configuration, the program automatically saves the configuration instructions to the database as an *unnamed* switch configuration. You can also deliberately save a configuration to the database with a name and a descriptions (so that it is easy to recall and load later) by going to the Save/Load from Database, entering a sequence name and description and then clicking the *Save Current Configuration* button on the right side of the tab control. On the left side of the tab control you should now be able to find your sequence in the *Named Sequence* drop down menu. Later you can select this option and click *Load Named Config* to load the switch configuration that you have made. If you are searching for a sequence that you did not explicitly save, you can check the *Autosaved Sequences from the Last Week* drop down menu. Here, it refers to configurations only by the date and time they were autosaved.

A.3.5 Master Run VI

The Master Run VI is the program that controls the experiment when it is running. Within this program there are three while loops:

1. User interface loop - for interacting with the user via an event structure.
2. Experiment loop - to perform the experiment, and the stop the operation of the experiment when instructed to.
3. Header Saving Loop - to asynchronously aggregate and save the header data (which contains information regarding the experiment parameter set-points and measurements during a given spin precession measurement) to disk.

I will first describe the operation of the experiment loop and i will mention when there is experiment behavior that can be modified by the user via the user interface loop.

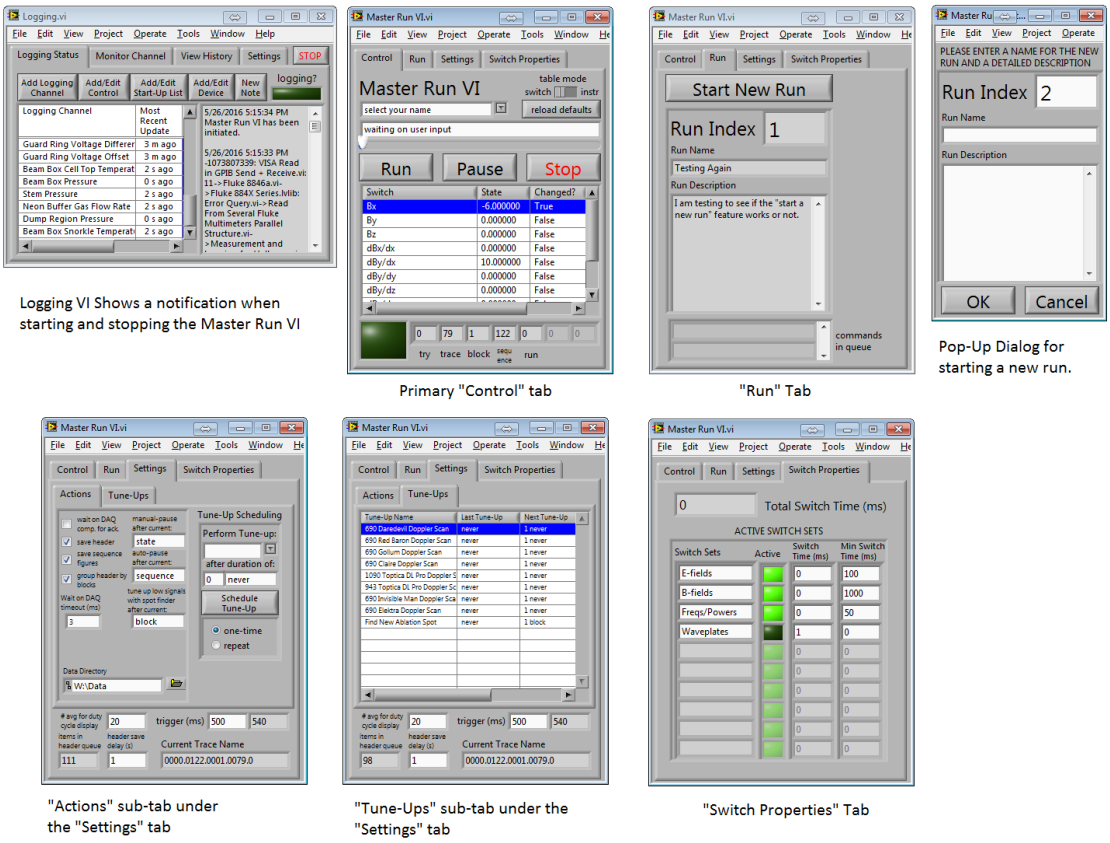

Figure A.9: View of the various tabs in the front panel GUI interface to the Master Run VI program.

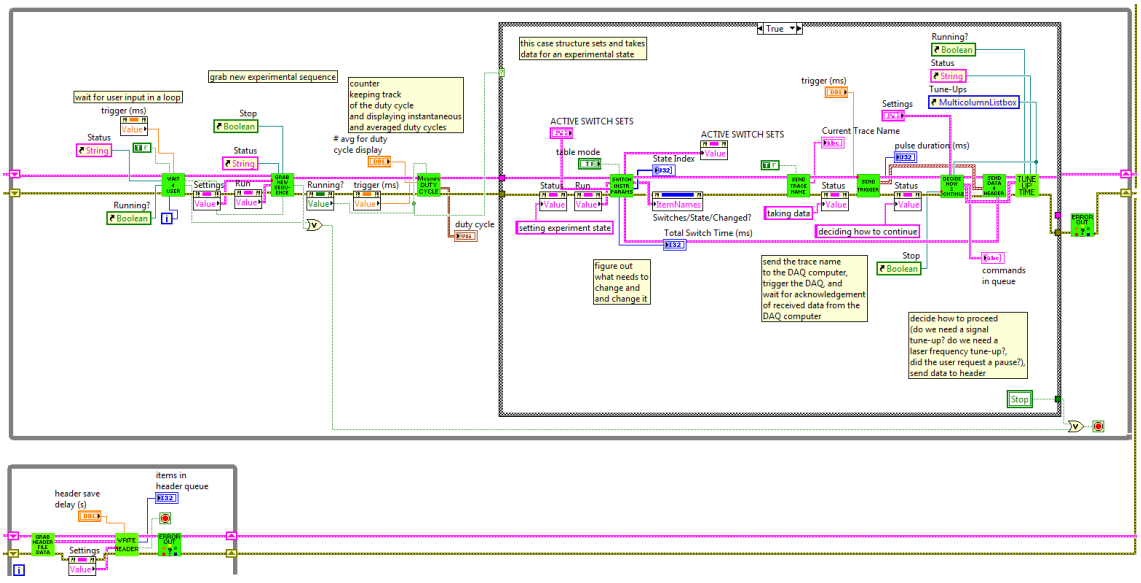

Figure A.10: Main experiment control loop (top), and Header saving loop (bottom) within the Master Run VI program.

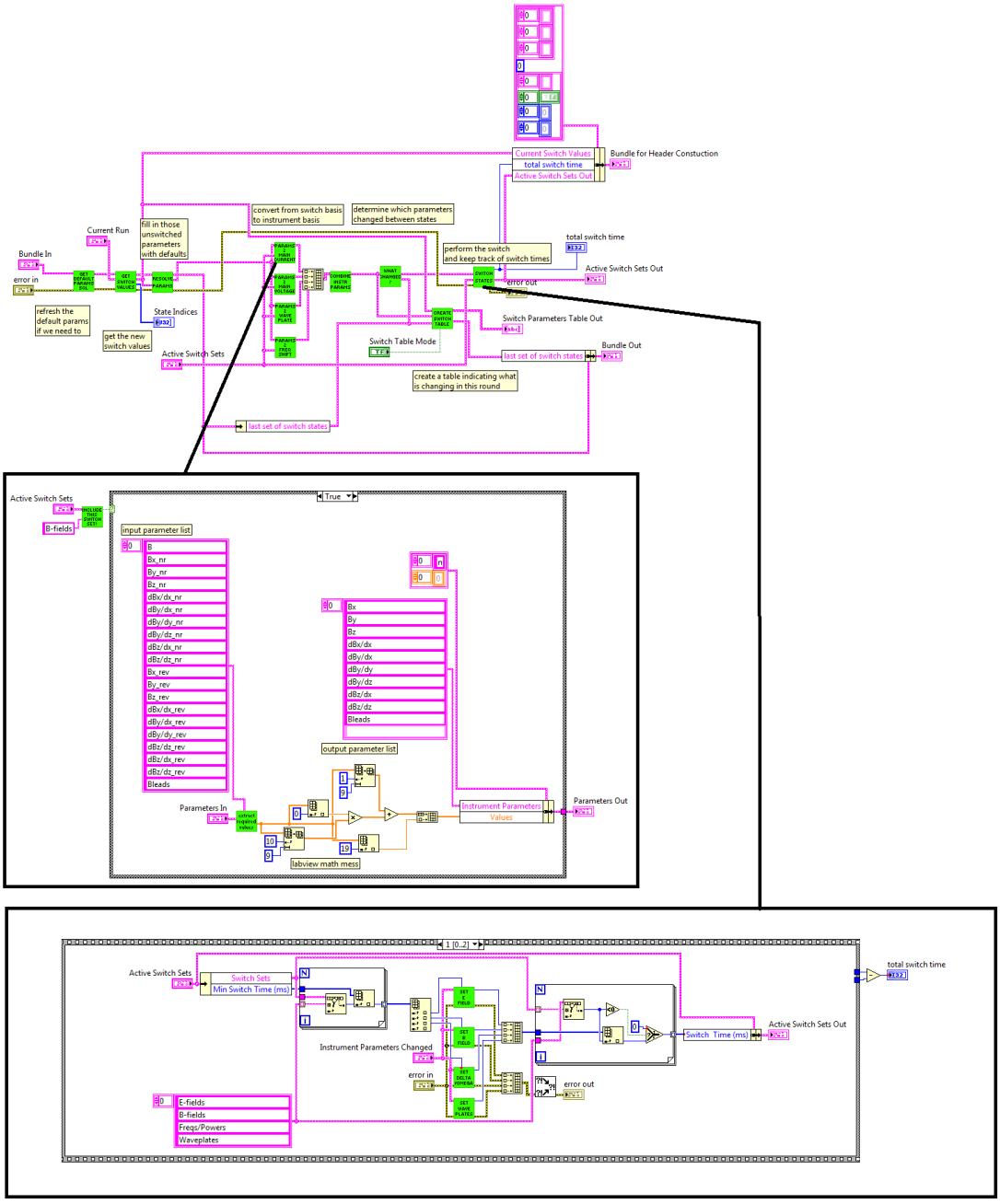

Figure A.11: Detail showing the code of the *Switch Instrument Parameters* Sub-VI and Sub-VIs within this function.

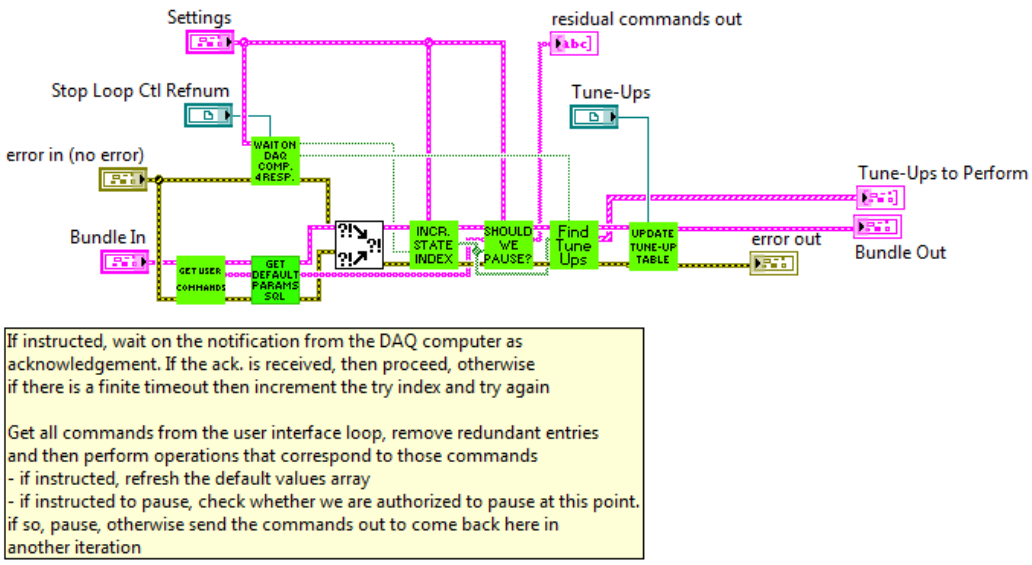

Figure A.12: Detail showing the code within the *Decide How to Continue* Sub VI within the Master Run VI.

Description of Experiment Loop

1. *Wait for User* - When the program starts running, the program operates this function that waits for a command from the user to start the operation of the experiment. Whenever the experiment is not running, the experiment loop should be hanging in this function. This periodically checks the user interface notifier for notifications.

2. *Grab New Sequence* - When the program has finished running, or if the previous experiment sequence has finished, this function grabs a new experiment sequence from the 'generate_switch_sequence' queue. This queue is stocked by the *Configure Switch Sequence VI* which must be running in the background with the appropriate experiment switch configuration in order for this feature to work.

3. *Measure Duty Cycle* - This function updates its measurement of the experiment duty cycle. This averages over a fixed number of iterations of this loop that is specified by an interger "# avg for duty cycle display" in the Settings tab. The duty cycle is displayed by a sliding bar on the Control tab.

4. *Switch Instrument Parameters* - This function sets the experiment state for the current spin precession measurement. This function determines which instrument parameters need to be varied, and varies them. Within this VI there are a series of functions:

(a) *Get Default Parameters SQL* - Grabs all of the default parameters for the experiment parameters that can be varied from the database if the default parameters did do not currently exist in the experiment loop bundle. This grabs from the *DefaultValues* table in the *LoggingConfigSQL* database.

(b) *Get Switch Values* - Grabs the values for each experiment switch for the current experiment state from the experiment switch sequence.

(c) *Resolve Parameters* - Takes all of the default parameters and replaces all of the default values with the current switch values for the parameters that are currently being switched. Now we have all of the parameters that we need to set the current state of the experiment.

(d) *Parameters 2 X* - This is a group of Sub-VIs that are run in parallel to convert from the experiment switch parameters to instrument parameters. Currently we have a Sub-VI for the magnetic field current controls, electric field voltage controls, the waveplate rotations state controls, and the AOM frequency shift controls.

(e) *Combine Instrument Parameters* - This function merges the array of instrument parameters that must be set into a single array.

(f) *What Changed?* - This function determined which instrument setpoint values changed between the last experiment state and the current experiment state. All of those instrument parameters that have not changed will not be set in thie round of setting instruments.

(g) *Create Switch Table* - This function creates the table that is displayed on the Control Tab of the front panel of the Master Run VI that indicates which parameters or instruments are being switched, their current values, and whether their value changed during the last switch.

(h) *Switch States* - This is the function that actually sets all of the instrument parameters for the current experiment state. Here, I will describe the operations performed within this function. This function takes in the instrument parameters that have changed and hence must be set and their values. This function also takes in data that is set on the Switch Properties tab of the Master Run VI. This data specified which sets of parameters should be allowed to switch, and

if so, what delay time to provide when switching one of these parameters. For example, after we set the electric fields,we typically wait for about 50 ms for the electric field to settle before allowing the experiment data taking to continue. Similarly, we wait at least a second for the magnetic field to settle after setting the magnetic field state. This function additionally monitors the switch time required for each set of instruments, and monitors the total switch time. The switching of the states is the dominant determiner of the total duty cycle and the switching times are displayed on the Switch Properties tab and are saved to the header files.

5. *Send Trace Name* - This function creates the "name" for the given experiment state. An example of a trace name is something like "0001.0122.0002.0039.0". The way to read this from left to right is in terms of indices regarding possible experiment timescales from slowest to fastest: {run index}.{sequence index}. ... .{block index}.{state index}.{try index}. The "try index" is a feature that is not currently used, but could be implemented in the future. If we modified the program such that is could retake experimental states if there was a detected problem with a given measurement, then we could advance the "try index". The length of the name depends on the amount of nesting in the experiment switch sequence (whether the highest level is at the block, superblock, uberblock, etc. level). This function "sends" this trace name to the Data Acquisition computer via the *GlobalVariables* table in the database before data acquisition begins. This ensures that we know which PMT traces, which are saved by a separate computer, are sychronized with the corresponding header files, saved on this computer.

6. *Send Trigger* - this function sends a digital pulse of duration of the averaging time for a single trace (currently specified to be .5 s). This digital pulse is mixed with the scope acquisition trigger that produces pulses as 50 Hz sychronous with the laser ablation with a time-offset set by the Timing VI. This will trigger the FPGA scope the appropriate number of times for the current experiment state. FPGA has acquired the correct number of traces, it clears the trace name from the *GlobalVariables* table to signal that the acquisition is complete.

7. *Decide How to Continue* - This function continually checks to the database for the

prevously described signal that the data acquisition for the current state is computer, provided that "wait on DAQ comp. for ack." is checked on the Settings tab. This should always be checked for normal experiment operation, and should only be unchecked for testing purposes. This function then checks the user interface notifier to see if the user requested any changes to the operation of the experiment (whether it should be paused, or whether it should tune up some parameter, or whether the instrument default parameters need to be refreshed from the database).

8. *Send Data For Header* - This function takes the experiment switch parameters, the instrument setpoint parameters, the measured switch times, and the starting time and ending time to the current state, and sends that information to the Header saving loop via a queue. The header saving loop continually acquires logging data via the database and matches up data that was acquired in the appropriate time range with experiment states. The header saving loop is operated with a delay with respect to the main experiment loop to ensure that the header saving loop doesn't miss any relevant data that might be a little slow to be transferred via the database to the Master Run VI. This header delay time is set on the Settings tab, and the defauly is currently a second.

9. *Tune Up Time* - This function performs experiment parameter tune-ups if those tune-ups are scheduled to happen at this point in the experiment. Note that this function purely calls other programs to perform operations and waits for them to respond indicating that the operation was complete. If the operation does not complete, the tune-up will timeout with a specified timeout time. The parameters that are scheduled to be tuned up, the periodicity with which that are being tuned up, and their time-out values can be viewed in the Tune-Ups tab that is under the Settings tab. There is a form for modifying the tune up schedule on the Actions tab under the Settings tab. Currently the available "Tune-Ups" are doppler scans for various lasers, and finding a new ablation spot. In the future, we would like to implement pointing measurement and correction for the lasers as a "Tune-Up". The list of tune-ups and how they operate is controled by the *TuneUpControls* table on the *LoggingConfigSQL* database, or can be viewed in the view *TuneUpControlsInfo*. These Tune-Ups have a name which is mapped onto a certain LogControl, and LogControlStates that are

issued as notifications to initiate a tune-up, and indicate that a tune-up has completed or failed.

Appendix B

Laser Spectrum Shaping with Random Phase Modulation

This work describes a method of creating arbitrary shapes of the power spectral density of a laser using random radio frequency phase modulation. First, it is shown that the space of all power spectral densities that can be achieved by phase modulation is a small subset of the space of all possible power spectral densities. Then, the phase waveform is expanded as the arctangent of a fourier series with random, gaussian distributed coefficients. It is shown that in the limit that the phase modulation simulates digital modulation of the amplitude, the power spectrum of the wave closely resembles that of the input fourier series, but there remains a high frequency tail in the power spectrum that falls off like ω^{-1} or faster and is suppressed compared to the main feature by at least an order of magnitude.

B.1 Introduction

Phase modulation has been used extensively to sinusoidally dither the central laser frequency with phase waveform $\phi(t) = \beta \sin(\omega t)$ using electro-optic modulators (EOMs). In the limit of small modulation depth, $\beta \ll 1$, then in the fourier domain, the spectrum consists mostly of 3 discrete bands: the carrier and two sidebands, which are spaced by frequency ω_0 from the carrier, which have a fixed phase relationship. If this laser light is introduced into a system with resonances, then the sidebands lead to intensity beating at ω_0 or some harmonic of ω_0. This principle has been used with great success in many atomic, molecular and optical systems, with some of the most widespread applications being FM spectroscopy

and Pound-Drever-Hall laser locking. The previously mentioned applications require the fixed phase relationship between the laser modes, but in other applications, EOMs have been used to simply broaden the laser spectrum. For example in the laser cooling of SrF, several hyperfine levels were addressed using several of EOM sidebands for $\beta \sim 1$.

Phase modulation has generally been limited to sinusoidal modulation because conventional EOMs require resonant circuits to achieve modulation depths up to $\beta \sim 1$, but can only do so in a small frequency range on the order of $1 - 10\,\mathrm{MHz}$. Fiber EOMs on the other hand can bypass the typical restrictions. They use waveguides rather than resonant circuits to increase the useful bandwidth to tens of GHz, and the nonlinear crystal can be made to have a diameter on the order of μm rather than mm since it is situated inside of an optical fiber that allows for large modulation depths, $\beta > 1$. This work discusses broadband phase modulation with fiber electro-optic modulators to broaden and shape the laser spectrum in the RF regime.

B.2 Phase Modulation is Not Almighty

Consider the electric field component, $\mathcal{E}(t)$, of a laser beam of a single frequency, ω_c, with polarization $\hat{\epsilon}$. We send this beam through an EOM across which we are applying a voltage waveform $V(t)$ that results in phase modulation $\phi(t) = \pi V(t)/V_\pi$ of the beam (where V_π is a constant that is a property of the crytal material in the EOM).

$$\vec{\mathcal{E}}(t) = \mathrm{Re}\left\{\hat{\epsilon}\mathcal{E}_0 e^{-i\omega_c t + i\phi(t)}\right\} \tag{B.1}$$

Given that ω_c is a THz laser frequency and the bandwidth of an EOM is typically in the RF and can be as high as the microwave regime, then $\dot{\phi}(t) \ll \omega_c$. Hence, the components of the fourier spectrum with positive and negative frequencies do not interfere, and are mirror images of each other. It will be sufficient to characterize the light field spectrum in the RF viscinity of $\omega = -\omega_c$, from which we can infer the light field spectrum in the RF viscinity of $\omega = +\omega_c$.

B.2.1 Unitary Complex Amplitude

I will consider a complex time varying amplitude (in the rotating frame, rotating at angular frequency $\omega = -\omega_c$) of the form:

$$\mathcal{A}(t) = e^{i\phi(t)} \tag{B.2}$$

which I can express as a continuous fourier series,

$$\mathcal{A}(t) = \int_{-\infty}^{\infty} d\omega\, e^{-i\omega t} \mathcal{A}(\omega) \tag{B.3}$$

Here, the power spectral density is simply $S(\omega) = \left\langle |\mathcal{A}(\omega)|^2 \right\rangle$, where the brackets indicate to average over all possible waveforms weighted by the probability of those waveforms, if $\mathcal{A}(t)$ is a random process.

Since there is only phase modulation, and no amplitude modulation, then the complex amplitude has the unitary property, $|\mathcal{A}(t)|^2 = 1$. This puts a serious constraint on the fourier transform function,

$$\int_{-\infty}^{\infty} d\omega\, \mathcal{A}(\omega + \Omega)\, \mathcal{A}^*(\omega) = \delta(\Omega) \tag{B.4}$$

This says that the fourier transform must be translationally orthogonal to itself in frequency space. Similarly, if we have a discrete frequency spectrum with frequencies spaced by ω_0, then we can write the fourier transform as:

$$\mathcal{A}(\omega) = \sum_{n=-\infty}^{\infty} \mathcal{A}_n \delta(\omega - n\omega_0) \tag{B.5}$$

in which case, the unitarity constraint yields:

$$\sum_{m=-\infty}^{\infty} \mathcal{A}_{n+m} \mathcal{A}_m^* = \delta_{n,0} \tag{B.6}$$

B.2.2 Satisfying Unitarity is Not a Trivial Task

Any phase modulated waveform must have a spectrum that obeys equation B.4 (or equivalently equation B.6 in the discrete case). Lets consider one simple example to show how this constraint can be fulfilled. In the case of sinusoidal phase modulation, $\phi(t) = \beta \sin \omega t$,

we can use the Bessel function expansion to obtain a fourier series,

$$\mathcal{A}(t) = e^{i\beta \sin \omega t} = \sum_{n=-\infty}^{\infty} J_n(\beta) e^{in\omega t} \tag{B.7}$$

In terms of the notation used in equation B.5, the fourier series can be written as $\mathcal{A}_n = J_n(\beta)$. The discrete unitarity constraint requires that:

$$\sum_{m=-\infty}^{\infty} J_{n+m}(\beta) J_m(\beta) = \delta_{n,0} \tag{B.8}$$

which arises naturally from Bessel addition theorem,

$$\sum_{m=-\infty}^{\infty} J_{n+m}(x) J_m(y) = J_n(x-y) \tag{B.9}$$

and the property that $J_n(0) = \delta_{n,0}$. Hence, the resulting spectrum from sinusoidal phase modulation satifies B.4.

B.2.3 Phase Modulation Needs Breathing Room

Now, suppose that I wanted to determine a waveform $\phi(t)$ such that $\mathcal{A}(\omega)$ would be non-zero only in a finite frequency range. Let us first consider the discrete case in which the spectrum has a finite number N of added frequency bands, in addition to the carrier ($N+1$ total frequency bands). In this case, the unitarity constraint is:

$$\sum_{m=0}^{N-n} \mathcal{A}_{n+m} \mathcal{A}_m^* = \delta_{n,0} \tag{B.10}$$

This constitutes a system of $N+1$ equations with $N+1$ complex free parameters. For $n = N \neq 0$, the sum has only 1 term, $\mathcal{A}_N \mathcal{A}_0^* = 0$, which forces us to elliminate one of the bands on the boundaries of the spectrum to satisfy it. We now find that our range has been reduced from $N+1$ to N bands. We can perform this procedure interatively to find that the only spectrum with a finite number of frequency bands that satisfies unitarity is the case in which there is only 1 frequency band, $\mathcal{A}_n = \delta_{n,0}$, which results from the absence of phase modulation altogether, $\phi(t) = 0$, or from linear phase modulation, $\phi(t) = \omega_a t$ for some ω_a.

We can similarly show that the same applies in the continuous frequency picture, but the proof is not as obvious. If we constrain our spectrum to the range $\omega_a < \omega < \omega_b$, then we have the unitarity constraint, for $\Omega > 0$,

$$\int_{\omega_a - \Omega}^{\omega_b} d\omega \, \mathcal{A}(\omega + \Omega) \, \mathcal{A}^*(\omega) = 0 \tag{B.11}$$

We can zoom in on the boundary $\omega = \omega_b$, such that $\Omega = \omega_a - \omega_b + \epsilon$. Assuming that $\mathcal{A}(\omega)$ varies smoothly close to the boundary such that $\mathcal{A}(\omega)$ varies negligibly over the small but finite range ϵ, then we can taylor expand about small ϵ resulting in $\epsilon \, \mathcal{A}(\omega_a) \, \mathcal{A}^*(\omega_b) = 0$. Just as before, this equation requires us to perpetually narrow our range until it becomes an infinitesimal sliver.

B.2.4 Spectral Symmetry

Let us assume that $\phi(t)$ is a stationary random waveform (the probability distribution that governs the waveform $P(\phi(t)) = P(\phi)$, is independent of time, and hence the moments, $\langle \phi^n(t) \rangle = \langle \phi^n \rangle$ are also independent of time). In this particular case, we can solely obtain power spectra that are symmetric about $\omega = 0$, $S(\omega) = S(-\omega)$. I can write this relation as

$$\left\langle \left| \int e^{-i\omega t + i\phi(t)} dt \right|^2 \right\rangle = \left\langle \left| \int e^{-i\omega t + i\phi(t)} dt \right|^2 \right\rangle \tag{B.12}$$

then taylor expand about $\phi(t) = 0$ to all orders, reverse the order of integration for one of the integrals, $dt \to -dt$, and then we find that it is satisfied if

$$\left\langle \phi^n(t) \, \phi^m\left(t'\right) \right\rangle = \left\langle \phi^n(-t) \, \phi^m\left(-t'\right) \right\rangle \tag{B.13}$$

for all m, n, t, t'. This is clearly satisfied since the probability distribution governing $\phi(t)$ is indepent of time.

However, that is not to say that it is difficult to obtain spectra with different symmetry properties. For example, if we phase modulate with the random waveform with an added linear component in time, $\phi_a(t) = \phi(t) + \omega_a t$, then we will similarly find that the power spectrum is symmetric about $\omega = \omega_a$, $S(\omega + \omega_a) = S(-\omega + \omega_a)$. For a phase modulation to which we have added a nonlinear component in time, $\phi_b(t) = \phi(t) + (\omega_b t)^n$, such that n is a positive, odd integer such that $n \geq 3$, the power spectrum will be strictly nonsymmetric

about any frequency, $S(\omega+\omega') \neq S(-\omega+\omega'), \forall \omega'$. Additionally, there is the possibility of giving the probability distribution $P(\phi(t))$ time dependence for which it is not very difficult to create asymmetric power spectra. For the remainder of this paper, I will only consider stationary random phase modulation like that of $\phi(t)$.

In this section, we have been able to deduce three things about power spectra resulting from phase modulated signals:

1. The space of all possible power spectra obtained through phase modulation does not span the space of all possible power spectra, but is rather only a small subset of it.

2. Phase modulation leads to a power spectrum that cannot be confined to a finite frequency range.

3. For processes that produce stationary random phase modulation, the resulting power spectrum is symmetric about $\omega = 0$, $S(\omega) = S(-\omega)$.

B.3 Shaping the Power Spectrum

Although we cannot create any shape of power spectrum that we may desire using phase modulation, there are ways by which we can closely approximate many shapes, if we can tolerate a power spectrum pedestal that is suppressed by one or two orders of magnitude compared to the main feature.

I propose the following approach. Write down a function of time $x(t)$.

$$x(t) = x_{rms} \int_0^\infty d\omega\, \varphi(\omega)\, \sin(\omega t) \tag{B.14}$$

such that the fourier amplitudes $\varphi(\omega)$ are random variables with zero mean, $\langle \varphi(\omega) \rangle = 0$ that are gaussian distributed. The probability distribution for selecting $\varphi(\omega)$ is $P(\varphi(\omega))$,

$$P(\varphi(\omega)) = \frac{1}{\sigma(\omega)\sqrt{2\pi}} \exp\left\{ -\frac{\varphi^2(\omega)}{2\sigma^2(\omega)} \right\} \tag{B.15}$$

such that $\sigma^2(\omega)$ is the ideal spectrum that we would like to map onto our laser power spectrum. This function is normalized such that,

$$2 = \int_0^\infty \sigma^2(\omega)\, d\omega \tag{B.16}$$

With this normalization, x_{rms} is indeed the root mean square value of the waveform $x(t)$ (where the root mean square value is defined by $x_{rms} = \sqrt{\frac{1}{T}\int_0^T dt\ \langle x^2(t)\rangle}$). Then, we can apply phase modulation with the signal,

$$\phi(t) = \arctan(x(t)) \tag{B.17}$$

Examples of the phase modulation signal for various values of x_{rms} are shown in figure B.3 for a top hat power spectrum, $\sigma^2(\omega) = \frac{1}{\omega_0}(0 < \omega < \omega_0)$ (in this notation, the inequality takes on a value of 1 when true and a value of 0 when false). In the limit that $x_{rms} \ll 1$, the phase waveform is equal to the fourier transform waveform, $\phi(t) \approx x(t)$, and in the limit that $x_{rms} \gg 1$, the phase waveform looks like a digital waveform, taking on two discrete values, $\phi(t) \approx \frac{\pi}{2}\mathrm{sgn}(x(t))$.

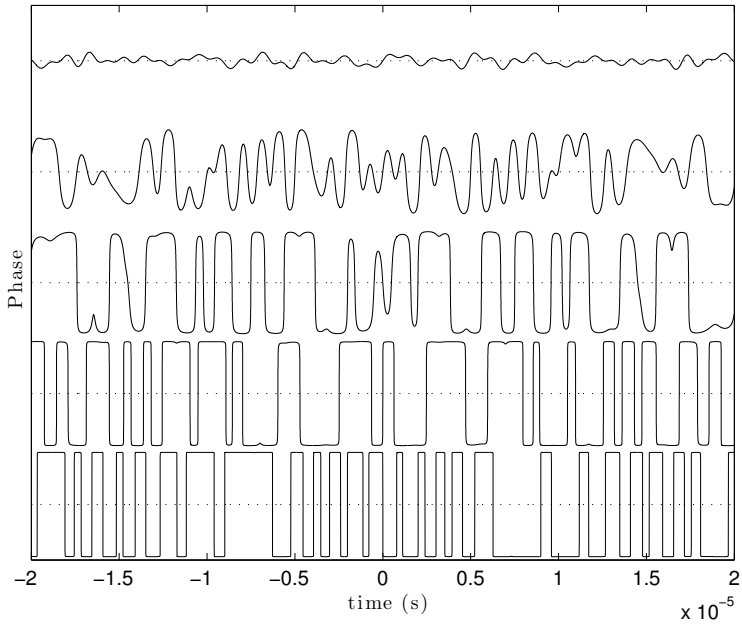

Figure B.1: Examples of the phase waveform $\phi(t)$ for various values of x_{rms}. Here, the Carrier frequency $\omega_0 = 2\pi \cdot 1\,\mathrm{MHz}$. From top to bottom, $x_{rms} = 10^{-1}$, 10^0, 10^1, 10^2, 10^3. The peak to peak amplitude of the bottom plot is π radians, setting the scale for the plot.

For this phase modulation signal, we obtain a simple relation between the complex amplitude and the signal $x(t)$,

$$\mathcal{A}(t) = \frac{1 + ix(t)}{\sqrt{1 + x^2(t)}} \tag{B.18}$$

In the limit that $x_{rms} \ll 1$,

$$\mathcal{A}(t) \approx 1 + ix(t) \tag{B.19}$$

we obtain the desired spectral shape since the amplitude is proportional to $x(t)$, however the large majority of the power is still in the carrier band, a delta function spike at the origin,

$$S(\omega) \approx \delta(\omega) + \frac{1}{4} x_{rms}^2 \sigma^2(|\omega|) \tag{B.20}$$

where the power spectral density of the complex amplitude is normalized such that $\int_{-\infty}^{\infty} d\omega\, S(\omega) = 1$.

In the limit that $x_{rms} \gg 1$, then

$$\mathcal{A}(t) \approx i \operatorname{sgn}(x(t)) \tag{B.21}$$

In this case all the power is in the new spectral feature, however, the sgn function has added 'sharp corners' to the waveform in the time domain, which manifests itself as the introduction of a high frequency tail in the power spectral density. The signal now resembles that of a digital signal.

In this limit, I can represent the amplitude as a series of digital pulses,

$$\mathcal{A}(t) = i\left[2\sum_{k=-\infty}^{\infty}(t_{2k} < t < t_{2k+1}) - 1\right] \tag{B.22}$$

such that $t_k > t_{k-1}$ for all k and t_k are the zeros of the random waveform, defined by $x(t_k) = 0$.

The fourier transform of the complex amplitude is

$$\mathcal{A}(\omega) = i\left[2\sum_{k=-\infty}^{\infty} e^{i\omega T_k}\, \delta t_k \operatorname{sinc}\left(\frac{\omega \delta t_k}{2}\right) - \delta(\omega)\right] \tag{B.23}$$

which is a sum of many interfering sinc functions, with widths that depend on the spacing

between the zeros,

$$T_k = \frac{1}{2}\left(t_{2k+1} + t_{2k}\right) \tag{B.24}$$

$$\delta t_k = t_{2k+1} - t_{2k} \tag{B.25}$$

If the ideal power spectral density, $\sigma^2(\omega)$ is confined to a finite frequency range, $0 < \omega < \omega_a$, then the minimum possible spacing between the zeros would correspond to $\delta t_k = \frac{2\pi}{\omega_a}$, and the power spectral density for $|\omega| > \omega_a$ would be likely dominated by $\text{sinc}\left(\pi\frac{\omega}{\omega_a}\right) \sim \omega^{-1}$. Hence, in the worst case scenario, the power spectral density of the complex amplitude would fall off with ω^{-1} just beyond the desired spectral feature, but the power spectrum could in principle fall off more quickly.

This method of phase modulation proposed above gives nearly the correct power spectral density for all x_{rms}, but the ratio of power in the carrier to that in the added spectral feature changes with x_{rms}, and as $x_{rms} \gg 1$, then we obtain a high frequency pedestal that falls off faster than ω^{-1}. As an example of this method, I choose the top-hat spectrum, for which $\sigma^2(\omega) = \frac{1}{\omega_0}(\omega < \omega_0)$. The resulting power spectral densities obtained from phase modulation are shown in in figure B.3 for various values of x_{rms}. Here the spectrum is shown on both linear and logarithmic scales. On the linear scale, we can clearly see that in the limit that $x_{rms} \gg 1$, $\sigma^2(\omega) \approx S(\omega)$. The logarithmic scale shows the unwanted power law pedestal that lies just one order of magnitude below the desired feature. It also shows that for all values of x_{rms}, the desired spectral feature is present, but with a varying ratio of power in the carrier to power in the spectral feature.

This method of spectral shaping is not limited to to the top hat spectrum, but can rather be applied to create a large variety of spectral shapes. Figure B.3 shows some triangular and pyramidal power spectral densities as an example.

B.3.1 Getting the Amplitude Right

If you are correctly keeping tabs, in the limit of $x_{rms} \gg 1$, the phase is almost discretely jumping between values of $\pm\pi/2$. This requires choosing the correct amplitude of the phase

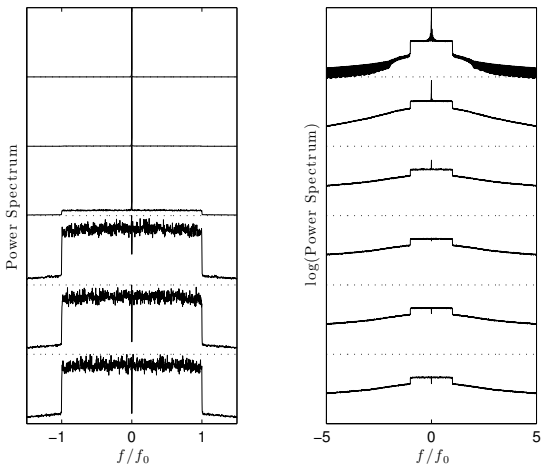

Figure B.2: Resulting spectrum for $\sigma^2(f) = (|f| < f_0)$ for varying x_{rms}. From top to bottom, $x_{rms} = 10^{-1}$, 10^0, 10^1, 10^2 10^3, 10^4. On the left the power spectra are presented with a linear scale (note that each of the plots have been normalized to have the same height). On the right, the same power spectra are presented on a logarithmic scale (but here there is no normalization; the scales for each plot are the same).

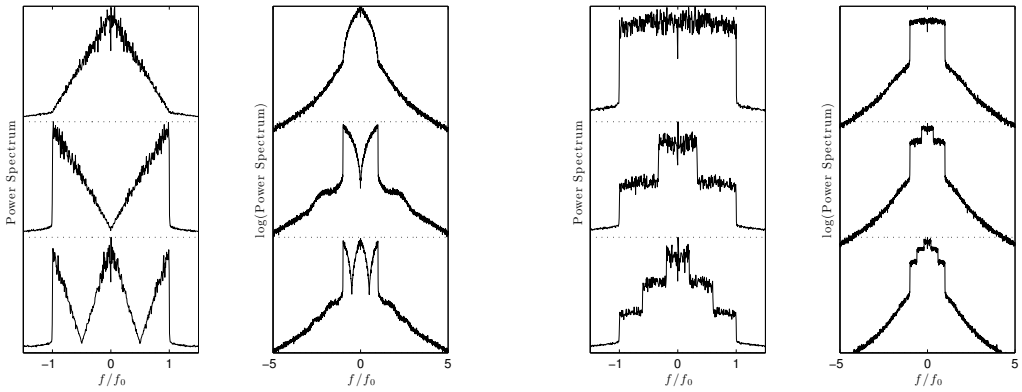

Figure B.3: Left: Triangular Spectra: from top to bottom, resulting power spectral densities for $\sigma^2(f) = \frac{4}{f_0}\left(1 - \frac{f}{f_0}\right)$, $\sigma^2(f) = 4f$, $\sigma^2(f) = \frac{4}{f_0}\left|\frac{2f}{f_0} - 1\right|$, which are non-zero only for $f \in (0, f_0)$ for each. Right: Pyramidal Spectra: from top to bottom, $\sigma^2(f) = \frac{2}{f_0}(0 < f < f_0)$, $\sigma^2(f) = 2\left(\frac{3}{4f_0}\right)\left\{(0 < f < f_0) + \left(0 < f < \frac{1}{3}f_0\right)\right\}$, $\sigma^2(f) = 2\left(\frac{5}{9f_0}\right)\left\{(0 < f < f_0) + \left(0 < f < \frac{3}{5}f_0\right) + \left(0 < f < \frac{1}{5}f_0\right)\right\}$.

waveform. Suppose that I modulate between $\pm\frac{\pi}{2}(1+\epsilon)$ for $\epsilon \ll 1$, then

$$\mathcal{A}(t) = \exp\left(i(1+\epsilon)\arctan(x(t))\right) \tag{B.26}$$

$$\approx \frac{1+ix(t)}{\sqrt{1+x^2(t)}}\left(1+\epsilon\arctan(x(t))+O\left(\epsilon^2\right)\right) \tag{B.27}$$

$$\tag{B.28}$$

In the limit that $x_{rms} \ll \epsilon$, the imperfect amplitude helps us,

$$\mathcal{A}(t) \approx 1+(i+\epsilon)x(t) \tag{B.29}$$

but in the limit that $x_{rms} \gg 1$, this small imperfection ϵ can become troublesome,

$$\mathcal{A}(t) \approx i\epsilon\frac{\pi}{2} + i\mathrm{sgn}(x(t)) + O\left(\epsilon^2\right) \tag{B.30}$$

in that it leads to a delta function spike at the origin of the power spectrum whose size is proportional to ϵ^2.

B.3.2 Shaping a Finite Width Laser

For systems in which the width of the desired spectral feature is comparable to (but necessarily larger than) the initial starting spectral width of the laser, then we can no longer neglect the finite width of the laser. In this case, the power spectrum resulting after phase modulation, $\tilde{S}(\omega)$, will be the convolution of the laser power spectrum, $S_0(\omega)$, with the power spectrum of the phase modulated amplitude, $S(\omega)$,

$$\tilde{S}(\Omega) = \int d\omega\, S(\omega)\, S_0(\Omega-\omega) \tag{B.31}$$

From this relation, we can extract $S(\omega)$, the spectrum that we wish to obtain by means of phase modulation by the convolution theorem,

$$S(\Omega) = \int dt\, e^{i\Omega t}\frac{\int d\omega\, e^{-i\omega t}\,\tilde{S}(\omega)}{\int d\omega'\, e^{-i\omega' t}\, S_0(\omega')} \tag{B.32}$$

In the special case that the laser power spectrum $S_0(\omega)$ is Gaussian, and the desired power spectrum, $\tilde{S}(\omega)$ is a top hat spectum, then we obtain

$$S_0(\omega) = \frac{1}{\sigma\sqrt{2\pi}} \exp\left(-\frac{\omega^2}{2\sigma^2}\right) \tag{B.33}$$

$$\tilde{S}(\omega) = \frac{1}{2f_0} \left(|f| < f_0\right) \tag{B.34}$$

$$S(\omega) = \frac{1}{4\omega_0} \left\{ \operatorname{erf}\left(\frac{\omega+\omega_0}{\sqrt{2}\sigma}\right) - \operatorname{erf}\left(\frac{\omega-\omega_0}{\sqrt{2}\sigma}\right) \right\} \tag{B.35}$$

The required $S(\omega)$ is ultimately a top hat spectrum with Gaussian tails.

B.3.3 Smoothing of Dispersive Features with Laser Broadening

Suppose that there is a dispersive feature that I observe in an experiment using a single frequency laser that consists of the carrier band that has a form like that of the derivative of a Lorentzian,

$$\phi(\omega) = A \frac{\omega}{\left(\omega^2 + (\gamma/2)^2\right)^2} \tag{B.36}$$

for some Lorentzian width γ and amplitude A. To obtain this feature, I would need to tune the frequency of the ω, and measure ϕ at each point.

If we then use phase modulation to create a broadened power spectral density laser, $S(\omega)$ and we redo the same experiment, then we will observe the feature $\tilde{\phi}(\omega)$ that can be obtained by a convolution of $\phi(\omega)$ with the power spectral density, $S(\omega)$,

$$\tilde{\phi}(\Delta) = \int d\omega\, S(\omega)\ \phi(\Delta - \omega) \tag{B.37}$$

$\tilde{\phi}(\omega)$ will have a similar, but distorted dispersive shape, but it will be widened and reduced in amplitude. Since $\phi(\omega)$ changes very wildly close to resonance, $\omega = 0$, then we may wish to reduce $\phi'(\omega = 0)$ by using phase modulation to spectrally broaden and shape the lasers power spectral density. The reduction in the $\phi'(\omega)$ can be calculated by:

$$\frac{\tilde{\phi}'(0)}{\phi'(0)} = \frac{\int d\omega\, S(\omega)\, \phi'(-\omega)}{\phi'(0)} \tag{B.38}$$

For example, take the flat top spectrum, $S(\omega) = \frac{1}{2\omega_0}(\omega < |\omega_0|)$. In this case there is a Lorentzian reduction of the $\phi'(0)$ with the width of the spectrum, ω_0:

$$\frac{\tilde{\phi}'(0)}{\phi'(0)} = \frac{(\gamma/2)^2}{\omega_0^2 + (\gamma/2)^2} \tag{B.39}$$

So, provided that $\omega_0 > \gamma$, we can obtain significant suppression of the slope. So, now a question naturally arises: what is optimum shape of the power spectral density to minimize $\phi'(0)$? One approach is to use the flat top spectrum but let $\omega_0 \to \infty$, but this is impractical as the power spectral density also goes to zero for all frequencies. Another approach is to strategically place delta function frequency bands such that $\phi'(\omega) = 0$. Taking this approach, we find that an optimum power spectral density is

$$S(\omega) = \frac{1}{2}\left(\delta\left(\omega - \gamma/\sqrt{6}\right) + \delta\left(\omega + \gamma/\sqrt{6}\right)\right) \tag{B.40}$$

Unfortunately, as we deduced in a previous section, we cannot create a frequency spectrum with a finite number of discrete frequencies using phase modulation. One possible alternative is the 'dual top-hat' spectrum, $\sigma^2(\omega) = \frac{1}{(\omega_0 - \omega_1)}(\omega_1 < |\omega| < \omega_0)$. If we use the proposed method above to obtain this spectrum by using phase modulation, thenwe obtain the power spectral densities which are displayed in figure B.3.3 for various values of ω_0/ω_1. In the limit that $\omega_0/\omega_1 \to 1$, the spectrum consists of very narrow frequency bands, but as a necessity, a fourier series of other narrow frequency bands arise at higher frequencies spaced by $2\omega_0$. On the other hand, for $\omega_0/\omega_1 \gg 1$, the width of the top hat widths are comparable or larger than the spacing between them, and the pedestal approaches a well behaved power law, just as that seen for the single top hat spectrum that is displayed in figure B.3.

Even with this finite width spectrum, we can still obtain $\tilde{\phi}'(0) = 0$. If I define $\omega_0 = \tilde{\omega} + \epsilon\frac{\gamma}{2}$ and $\omega_1 = \tilde{\omega} - \epsilon\frac{\gamma}{2}$, then we find that

$$\tilde{\omega} = \frac{\gamma}{\sqrt{6}}\sqrt{2\sqrt{1 + \epsilon^2 + \epsilon^4} + \epsilon^2 - 1} \tag{B.41}$$

satisfies $\tilde{\phi}'(0) = 0$. In this case, the two extreme solutions that were previously discussed

can be recovered from $\epsilon \to 0$ and $\epsilon \to \infty$. Since the power spectrum has many high frequency narrow bands in the limit that $\epsilon \to 0$ and the power spectral density is very wide in the limit that $\epsilon \to \infty$, then I would like to sit somewhere in the middle. If we arbitrarily choose that we would like $\tilde{\omega} = \epsilon\gamma$ (which is equivalent to $\omega_0/\omega_1 = 3$ in figure B.3.3), then we find $\phi'(0) = 0$ for $\epsilon = \sqrt{3/5}$.

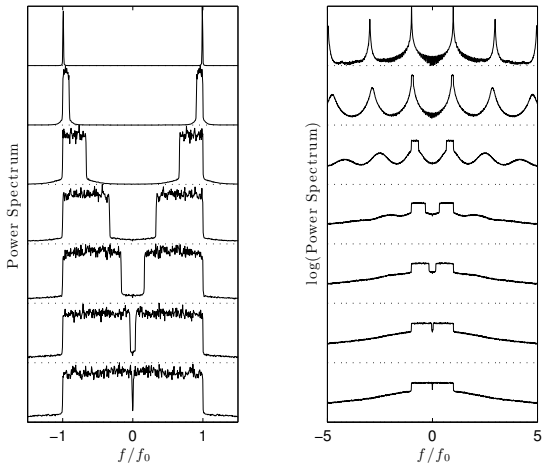

Figure B.4: Resulting spectrum for $\sigma^2(f) = \frac{1}{(f_1 - f_0)}$ $(f_1 < |f| < f_0)$. From top to bottom, f_1 is defined by $\frac{f_0}{f_1} = 1.01$, 1.1, 1.5, 3, 6, 25, 100.

B.4 Realization

As a proof of principle, I have implimented the above procedure by using waveforms that have been randomly generated by a Matlab script, and generated by an arbitrary waveform generator (model Euvis AWG 272). The signal was amplified by a broadband amplifier (Minicircuits ZHL-1-2W) and sent to an optical fiber electro-optic modulator (model EOspace PM-0K5-10-PFA-PFA-1090-UL).

An interferometer was constructed to measure the power spectrum of the laser after having been broadened by the fiber EOM. This interferometer beats together the phase modulated beam with the original beam that is potentially offset by a constant frequency, ω_{AO}, (for doing a 'lock-in measurement', to move the applied spectrum away from the electronic noise that is large near zero frequency). A schematic of the interferometer is

shown in figure B.4. The intensity beating between these two beams is given by:

$$I(t) \propto \left| a\, e^{i(\omega+\omega_{AO})t} + b\, e^{i\omega t+\phi(t)} \right|^2 \tag{B.42}$$

$$\propto a^2 + b^2 + 2ab\cos\left(\omega_{AO}t - \phi(t)\right) \tag{B.43}$$

where a and b are constants. A 150 MHz bandwidth photodiode (Thorlabs model PDA10CF) was used to measure the intensity beating, and a spectrum analyzer was used to compute the power spectral density of the intensity beating (model Agilent e4402b). The procedure was applied for a top hat spectrum and $\omega_{AO} = 0$. The resulting spectrum is shown in figure B.4. The amplitude of the RF was varied while monitoring the amplitude of the power spectrum; the power spectrum amplitude should be maximized when the phase peak to peak amplitude is π. Such an maximum was observed.

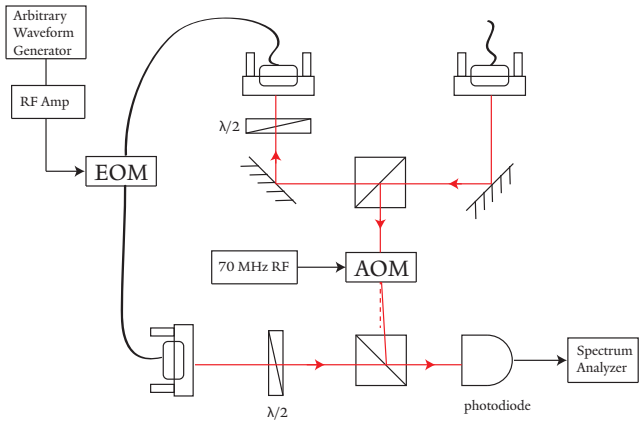

Figure B.5: Schematic of interferometer used to measure the phase modulation spectrum inprinted on the laser by the fiber EOM

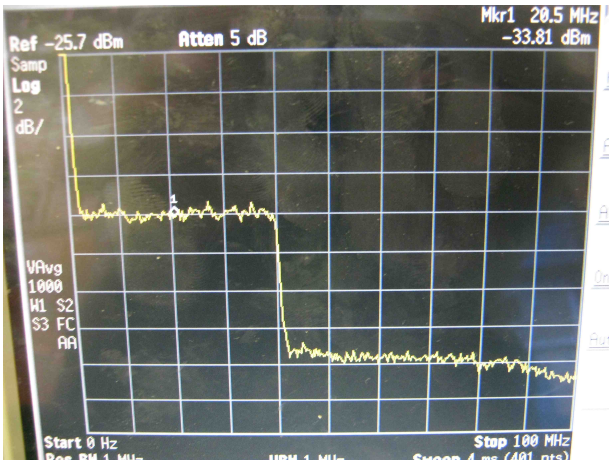

Figure B.6: Spectrum Analyzer trace for interferometer in the case that the AOM frequency is set to zero (and hence the center of the spectrum is at 0) and for a top hat spectrum, $\sigma^2(f) = \frac{2}{f_0}\,(0 < f < f_0)$ such that $f_0 = 40\,\mathrm{MHz}$.

Bibliography

[1] G. Aad et al. Summary of the atlas experiment's sensitivity to supersymmetry after lhc run 1 — interpreted in the phenomenological mssm. *Journal of High Energy Physics*, 2015(10):1–76, 2015.

[2] G. Aad et al. Search for the electroweak production of supersymmetric particles in $\sqrt{s} = 8$ TeV pp collisions with the atlas detector. *Phys. Rev. D*, 93:052002, Mar 2016.

[3] M. Aartsen et al. Improved limits on dark matter annihilation in the sun with the 79-string icecube detector and implications for supersymmetry. *Journal of Cosmology and Astroparticle Physics*, 2016(04):022, 2016.

[4] K. Abdullah, C. Carlberg, E. D. Commins, H. Gould, and S. B. Ross. New experimental limit on the electron electric dipole moment. *Phys. Rev. Lett.*, 65:2347, 1990.

[5] M. Abe, G. Gopakumar, M. Hada, B. P. Das, H. Tatewaki, and D. Mukherjee. Application of relativistic coupled-cluster theory to the effective electric field in ybf. *Phys. Rev. A*, 90:022501, 8 2014.

[6] ACME Collaboration. Order of magnitude smaller limit on the electric dipole moment of the electron. *Science (New York, N.Y.)*, 343(6168):269–72, Jan. 2014.

[7] R. Agnese et al. New results from the search for low-mass weakly interacting massive particles with the cdms low ionization threshold experiment. *Phys. Rev. Lett.*, 116:071301, Feb 2016.

[8] D. S. Akerib et al. First results from the lux dark matter experiment at the sanford underground research facility. *Phys. Rev. Lett.*, 112:091303, Mar 2014.

[9] M. Aleksa, F. Bergsma, L. Chevalier, P.-a. Giudici, J. C. Hart, a. Kehrli, M. Losasso, P. S. Miyagawa, X. Pons, H. Sandaker, and S. W. Snow. Results of the ATLAS solenoid magnetic field map. *Journal of Physics: Conference Series*, 110(9):092018, May 2008.

[10] F. Ambrosino et al. First observation of quantum interference in the process $\phi \to k_s k_l \to \pi^+\pi^-\pi^+\pi^-$: A test of quantum mechanics and *cpt* symmetry. *Physics Letters B*, 642(4):315 – 321, 2006.

[11] V. Andreev. Second generation polarimetry. `https://bussle.rc.fas.harvard.edu/lablog_graduate_2015-Vitaly_Andreev/2016/08/presentation.html` (2016/08/17).

[12] J. R. Barber. *Elasticity, Solid Mechanics and its Applications.* Springer, 3rd ed. edition, 2010.

[13] P. Bargassa. Supersymmetry searches at cms-summary of selected supersymmetry searches of cms at s= 8 tev. In *EPJ Web of Conferences*, volume 71, page 00010. EDP Sciences, 2014.

[14] R. Barlow. Systematic errors: Facts and fictions. *arXiv preprint hep-ex/0207026*, 2002.

[15] S. M. Barr and A. Zee. Electric dipole moment of the electron and of the neutron. *Phys. Rev. Lett.*, 65:21–24, Jul 1990.

[16] G. W. Bennett et al. Measurement of the negative muon anomalous magnetic moment to 0.7 ppm. *Phys. Rev. Lett.*, 92:161802, 4 2004.

[17] K. Bergmann, H. Theuer, and B. W. Shore. Coherent population transfer among quantum states of atoms and molecules. *Rev. Mod. Phys.*, 70:1003–1025, Jul 1998.

[18] J. Beringer et al. Review of particle physics. *Phys. Rev. D*, 86:010001, Jul 2012. Particle Data Group.

[19] H. G. Berry, G. Gabrielse, and A. E. Livingston. Measurement of the Stokes parameters of light. *Applied Optics*, 16(12):3200–5, Dec. 1977.

[20] G. Bertone, D. Hooper, and J. Silk. Particle dark matter: Evidence, candidates and constraints. *Physics Reports*, 405(5):279–390, 2005.

[21] S. Bickman, P. Hamilton, Y. Jiang, and D. DeMille. Preparation and detection of states with simultaneous spin alignment and selectable molecular orientation in PbO. *Physical Review A*, 80:023418, Aug. 2009.

[22] S. D. Biller and S. M. Oser. Another look at confidence intervals: Proposal for a more relevant and transparent approach. *Nuclear Instruments and Methods in Physics Research Section A: Accelerators, Spectrometers, Detectors and Associated Equipment*, 774:103 – 119, 2015.

[23] M. Bishof, R. H. Parker, K. G. Bailey, J. P. Greene, R. J. Holt, M. R. Kalita, W. Korsch, N. D. Lemke, Z.-T. Lu, P. Mueller, T. P. O'Connor, J. T. Singh, and M. R. Dietrich. Improved limit on the ^{225}Ra electric dipole moment. *Phys. Rev. C*, 94:025501, Aug 2016.

[24] M. Booth. The electric dipole moment of the w and electron in the standard model. *arXiv preprint hep-ph/9301293*, 1993.

[25] I. I. Boradjiev and N. V. Vitanov. Stimulated raman adiabatic passage with unequal couplings: Beyond two-photon resonance. *Phys. Rev. A*, 81:053415, May 2010.

[26] M. Bouchiat and C. Bouchiat. Parity Violation Induced by Weak Neutral Currents in Atomic Physics. *Journal de Physique*, 34(12):899–927, 1974.

[27] J. M. Brown and A. Carrington. *Rotational Spectroscopy of Diatomic Molecules.* Cambridge University Press, 2003.

[28] D. Budker, D. Kimball, and D. DeMille. *Atomic physics: An exploration through problems and solutions*. Oxford University Press, USA, 2008.

[29] B. W. Carroll and D. A. Ostlie. *An introduction to modern astrophysics and cosmology*, volume 1. 2006.

[30] S. Chatrchyan, V. Khachatryan, A. M. Sirunyan, A. Tumasyan, W. Adam, E. Aguilo, T. Bergauer, M. Dragicevic, J. Erö, C. Fabjan, et al. Observation of a new boson at a mass of 125 gev with the cms experiment at the lhc. *Physics Letters B*, 716(1):30–61, 2012.

[31] X. Chen, F. Huang-Hellinger, B. Heckel, and E. Fortson. Measurement of a linear stark interference effect on the rubidium D1 absorption line. *Physical Review A*, 50(6):4729–4732, 1994.

[32] J. H. Christenson, J. W. Cronin, V. L. Fitch, and R. Turlay. Evidence for the 2π decay of the k_2^0 meson. *Phys. Rev. Lett.*, 13:138–140, 1964.

[33] E. Commins, S. Ross, D. DeMille, and B. Regan. Improved experimental limit on the electric dipole moment of the electron. *Physical Review A*, 50(4), 1994.

[34] E. D. Commins and D. DeMille. The Electric Dipole Moment of the Electron. In B. L. Roberts and W. J. Marciano, editors, *Lepton Dipole Moments*, chapter 14, pages 519–581. World Scientific, 2010.

[35] E. D. Commins and D. P. DeMille. *The Electric Dipole Moment of the Electron*, chapter 14, pages 519–581. World Scientific, 2009.

[36] E. D. Commins, J. D. Jackson, and D. P. DeMille. The electric dipole moment of the electron: An intuitive explanation for the evasion of Schiffs theorem. *American Journal of Physics*, 75(6):532, 2007.

[37] Corning. Corning 7980 Fused Silica Datasheet. Technical report, 2003.

[38] J. W. Dally and W. F. Riley. *Experimental Stress Analysis*. McGraw-Hill, third edit edition, 1991.

[39] J. Danzl, E. Haller, M. Gustavsson, M. Mark, R. Hart, N. Bouloufa, O. Dulieu, H. Ritsch, and H.-C. Ngerl. Quantum gas of deeply bound ground state molecules. *Science*, 321(5892):1062–1066, 8 2008.

[40] H. Dehmelt, R. Mittleman, R. S. Van Dyck, and P. Schwinberg. Past electron-positron $g-2$ experiments yielded sharpest bound on CPT violation for point particles. *Phys. Rev. Lett.*, 83:4694–4696, 12 1999.

[41] D. DeMille, F. Bay, S. Bickman, D. Kawall, L. Hunter, D. Krause, S. Maxwell, and K. Ulmer. Search for the electric dipole moment of the electron using metastable PbO. In *Art and Symmetry in Experimental Physics*, volume 596, pages 72–83. AIP, 2001.

[42] D. DeMille, F. Bay, S. Bickman, D. Kawall, D. Krause, S. Maxwell, and L. Hunter. Investigation of PbO as a system for measuring the electric dipole moment of the electron. *Physical Review A*, 61(5):52507, Apr. 2000.

[43] D. DeMille, S. B. Cahn, D. Murphree, D. a. Rahmlow, and M. G. Kozlov. Using Molecules to Measure Nuclear Spin-Dependent Parity Violation. *Phys. Rev. Lett.*, 100(2):023003, Jan. 2008.

[44] M. Dine and A. Kusenko. Origin of the matter-antimatter asymmetry. *Reviews of Modern Physics*, 76(January):1–30, 2004.

[45] J. DiSciacca, M. Marshall, K. Marable, G. Gabrielse, S. Ettenauer, E. Tardiff, R. Kalra, D. W. Fitzakerley, M. C. George, E. A. Hessels, C. H. Storry, M. Weel, D. Grzonka, W. Oelert, and T. Sefzick. One-particle measurement of the antiproton magnetic moment. *Phys. Rev. Lett.*, 110:130801, 3 2013.

[46] R. W. P. Drever, J. L. Hall, F. V. Kowalski, J. Hough, G. M. Ford, A. J. Munley, and H. Ward. Laser phase and frequency stabilization using an optical resonator. *Applied Physics B*, 31(2):97–105, 1983.

[47] V. A. Dzuba, V. V. Flambaum, and C. Harabati. Relations between matrix elements of different weak interactions and interpretation of the parity-nonconserving and electron electric-dipole-moment measurements in atoms and molecules. *Phys. Rev. A*, 84:052108, Nov 2011.

[48] V. A. Dzuba, V. V. Flambaum, and C. Harabati. Erratum: Relations between matrix elements of different weak interactions and interpretation of the parity-nonconserving and electron electric-dipole-moment measurements in atoms and molecules [phys. rev. a **84**, 052108 (2011)]. *Phys. Rev. A*, 85:029901, Feb 2012.

[49] S. Eckel, P. Hamilton, E. Kirilov, H. W. Smith, and D. DeMille. Search for the electron electric dipole moment using Ω-doublet levels in PbO. *Physical Review A*, 87(5):052130, May 2013.

[50] G. Edvinsson, A. Bornstedt, and P. Nylén. Rotational Analysis for a Perturbed $^1\Pi$ state in ThO. *Ark. Phys.*, 38:193, 1968.

[51] G. Edvinsson and A. Lagerqvist. A low-lying Ω=2 state in the ThO molecule. *J. Mol. Spectrosc.*, 113:93, 1985.

[52] G. Edvinsson, L.-E. Selin, and N. Aslund. On the band spectrum of ThO. *Ark. Phys.*, 30(22):283–319, 1965.

[53] S. Eisenbach and H. Lotem. Thermally induced window birefringence in high-power copper vapor laser. *SPIE 8th Meeting on Optical Engineering in Israel*, 1972, 1992.

[54] J. Engel, M. J. Ramsey-Musolf, and U. van Kolck. Electric dipole moments of nucleons, nuclei, and atoms: The Standard Model and beyond. *Progress in Particle and Nuclear Physics*, 71:21–74, July 2013.

[55] W. Erikson and S. Singh. Polarization properties of maxwell-gaussian laser beams. *Physical Review E*, 49(6):5778, 1994.

[56] G. A. et al. Observation of a new particle in the search for the standard model higgs boson with the atlas detector at the lhc. *Physics Letters B*, 716(1):1–29, 2012.

[57] D. Farkas. *An Optical Reference and Frequency Comb for Improved Spectroscopy of Helium*. PhD thesis, Harvard University, 2006. (advisor: G. Gabrielse).

[58] G. J. Feldman and R. D. Cousins. Unified approach to the classical statistical analysis of small signals. *Physical Review D*, 57(7):3873–3889, Apr. 1998.

[59] J. L. Feng. Naturalness and the status of supersymmetry. *arXiv preprint arXiv:1302.6587*, 2013.

[60] R. P. Feynman, R. B. Leighton, and M. Sands. *The Feynman Lectures on Physics, Desktop Edition Volume I*, volume 1. Basic books, 2013.

[61] T. Fleig and M. K. Nayak. Electron electric dipole moment and hyperfine interaction constants for tho. *J. Mol. Spectrosc.*, 300:16–21, 2014.

[62] L. Fratta, P. Debernardi, G. P. Bava, C. Degen, J. Kaiser, I. Fischer, and W. Elsäßer. Spatially inhomogeneously polarized transverse modes in vertical-cavity surface-emitting lasers. *Phys. Rev. A*, 64:031803, Aug 2001.

[63] O. Gagnon and G. D. Moore. Limits on lorentz violation from the highest energy cosmic rays. *Phys. Rev. D*, 70:065002, 9 2004.

[64] U. Gaubatz, P. Rudecki, S. Schiemann, and K. Bergmann. Population transfer between molecular vibrational levels by stimulated raman scattering with partially overlapping laser fields. a new concept and experimental results. *The Journal of Chemical Physics*, 92(9), 1990.

[65] M. B. Gavela, P. Hernández, J. Orloff, and O. Pène. Standard model *cp*-violation and baryon asymmetry. *Modern Physics Letters A*, 09(09):795–809, 1994.

[66] G. Giudice and A. Romanino. Electric dipole moments in split supersymmetry. *Physics Letters B*, 634(23):307 – 314, 2006.

[67] B. Graner, Y. Chen, E. G. Lindahl, and B. R. Heckel. Reduced limit on the permanent electric dipole moment of ^{199}Hg. *Phys. Rev. Lett.*, 116:161601, Apr 2016.

[68] W. Griffith, M. Swallows, T. Loftus, M. Romalis, B. Heckel, and E. Fortson. Improved Limit on the Permanent Electric Dipole Moment of ^{199}Hg. *Physical Review Letters*, 102(10):101601, Mar. 2009.

[69] Y. V. Gurevich. *Preliminary Measurements for an Electron EDM Experiment in ThO*. PhD thesis, Harvard Univ., 2012. (advisor: G. Gabrielse).

[70] P. Hamilton. *Preliminary results in the search for the electron electric dipole moment in PbO*. PhD thesis, Yale University, 2010.

[71] P. Hamilton. *Preliminary results in the search for the electron electric dipole moment in PbO**. PhD thesis, Yale University, 2010.

[72] D. Hanneke, S. Fogwell, and G. Gabrielse. New Measurement of the Electron Magnetic Moment and the Fine Structure Constant. *Physical Review Letters*, 100(12):120801, Mar. 2008.

[73] J. C. Hart, P. S. Miyagawa, and S. W. Snow. Software representation of the ATLAS solenoid magnetic field. *Journal of Physics: Conference Series*, 119(3):032022, July 2008.

[74] M. Hennrich, T. Legero, A. Kuhn, and G. Rempe. Vacuum-stimulated raman scattering based on adiabatic passage in a high-finesse optical cavity. *Phys. Rev. Lett.*, 85:4872–4875, Dec 2000.

[75] G. Herzberg. *The Spectra and Structures of Simple Free Radicals*. Cornell University Perss, Ithaca, 1971.

[76] G. Herzberg. *Molecular Spectra and Molecular Structure: Spectra of Diatomic Molecules , 2nd ed.* Krieger, 1989.

[77] P. Hess. *Improving the Limit on the Electron EDM: Data Acquisition and Systematics Studies*. PhD thesis, Harvard Univ., 2014. (advisor: G. Gabrielse).

[78] E. A. Hinds. Testing time reversal symmetry using molecules. *Phys. Scr.*, T70:34–41, 1997.

[79] J. Hodgdon, B. Heckel, and E. Fortson. Calculation of a linear-Stark effect in D-line absorption in rubidium. *Physical Review A*, 43(7):3343–3347, 1991.

[80] M. A. Hohensee, P. L. Stanwix, M. E. Tobar, S. R. Parker, D. F. Phillips, and R. L. Walsworth. Improved constraints on isotropic shift and anisotropies of the speed of light using rotating cryogenic sapphire oscillators. *Phys. Rev. D*, 82:076001, 10 2010.

[81] M. A. Hohensee, P. L. Stanwix, M. E. Tobar, S. R. Parker, D. F. Phillips, and R. L. Walsworth. Improved constraints on isotropic shift and anisotropies of the speed of light using rotating cryogenic sapphire oscillators. *Phys. Rev. D*, 82:076001, 10 2010.

[82] J. J. Hudson, D. M. Kara, I. J. Smallman, B. E. Sauer, M. R. Tarbutt, and E. a. Hinds. Improved measurement of the shape of the electron. *Nature*, 473(7348):493–496, May 2011.

[83] P. Huet. Electroweak baryogenesis and the standard model. *arXiv preprint hep-ph/9406301*, 1994.

[84] P. Huet and A. E. Nelson. Electroweak baryogenesis in supersymmetric models. *Phys. Rev. D*, 53:4578–4597, Apr 1996.

[85] M. T. Hummon, M. Yeo, B. K. Stuhl, A. L. Collopy, Y. Xia, and J. Ye. 2D Magneto-Optical Trapping of Diatomic Molecules. *Physical Review Letters*, 110(14):143001, Apr. 2013.

[86] N. Hutzler. *A New Limit on the Electron Electric Dipole Moment: Beam Production, Data Interpretation, and Systematics*. PhD thesis, Harvard University, 2014. (advisor: J. Doyle).

[87] N. R. Hutzler, H.-I. Lu, and J. M. Doyle. The buffer gas beam: an intense, cold, and slow source for atoms and molecules. *Chemical Reviews*, 112(9):4803–27, Sept. 2012.

[88] N. R. Hutzler, M. F. Parsons, Y. V. Gurevich, P. W. Hess, E. Petrik, B. Spaun, A. C. Vutha, D. DeMille, G. Gabrielse, and J. M. Doyle. A cryogenic beam of refractory, chemically reactive molecules with expansion cooling. *Physical Chemistry Chemical Physics : PCCP*, 13(42):18976–85, Nov. 2011.

[89] G. Jungman, M. Kamionkowski, and K. Griest. Supersymmetric dark matter. *Physics Reports*, 267(5):195–373, 1996.

[90] D. Kawall, F. Bay, S. Bickman, Y. Jiang, and D. DeMille. Progress towards measuring the electric dipole moment of the electron in metastable PbO. In *AIP Conference Proceedings*, volume 698, pages 192–195. AIP, 2004.

[91] J. F. Kenny and E. S. Keeping. *Mathematics of Statistics*. Van Nostrand, New York, 2nd edition, 1951.

[92] I. B. Khriplovich and S. K. Lamoreaux. *CP Violation Without Strangeness*. Springer, 1997.

[93] E. Kirilov, W. C. Campbell, J. M. Doyle, G. Gabrielse, Y. V. Gurevich, P. W. Hess, N. R. Hutzler, B. R. OLeary, E. Petrik, B. Spaun, a. C. Vutha, and D. DeMille. Shot-noise-limited spin measurements in a pulsed molecular beam. *Physical Review A*, 88(1):013844, July 2013.

[94] M. Kobayashi and T. Maskawa. *cp*-violation in the renormalizable theory of weak interaction. *Prog. Theor. Phys.*, 49:652, 1973.

[95] W. Koechner. Thermal Lensing in a Nd:YAG Laser Rod. *Applied optics*, 9(11):2548–2553, Nov. 1970.

[96] D. L. Kokkin, T. C. Steimle, and D. DeMille. Branching ratios and radiative lifetimes of the u, l, and i states of thorium oxide. *Phys. Rev. A*, 90:062503, Dec 2014.

[97] V. A. Kostelecký and R. J. Van Kooten. *cpt* violation and b-meson oscillations. *Phys. Rev. D*, 82:101702, 11 2010.

[98] M. G. Kozlov and L. N. Labzowsky. Parity violation effects in diatomics. *Journal of Physics B: Atomic, Molecular and Optical Physics*, 28(10):1933–1961, May 1995.

[99] W. Kuchle, M. Dolg, H. Stoll, H. Preuss, W. Kikhle, and H. Stall. Energy-adjusted pseudopotentials for the actinides. Parameter sets and test calculations for thorium and thorium monoxide. *J. Chem. Phys.*, 100(10):7535–7542, 1994.

[100] S. Lamoreaux and E. Fortson. Calculation of a linear Stark effect on the 254-nm line of Hg. *Physical Review A*, 46(11):7053–7059, 1992.

[101] S. K. Lamoreaux, J. P. Jacobs, B. R. Heckel, F. J. Raab, and N. Fortson. New constraints on time-reversal asymmetry from a search for a permanent electric dipole moment of ^{199}hg. *Phys. Rev. Lett.*, 59:2275, 1987.

[102] L. D. Landau and E. M. Lifshitz. *Quantum Mechanics: Non-relativistic Theory*. Butterworth-Heinemann, 1981.

[103] Z. Lasner. Summary of rotational cooling gains. https://bussle.rc.fas.harvard.edu/lablog_EDMgraduate_2014-Zach_Lasner/2016/09/summary-of-rotational-cooling-gains.html (2016/09/13).

[104] C. Lawson and R. Hanson. *Solving Least Squares Problems*. Society for Industrial and Applied Mathematics, 1995.

[105] A. E. Leanhardt, J. L. Bohn, H. Loh, P. Maletinsky, E. R. Meyer, L. C. Sinclair, R. P. Stutz, and E. A. Cornell. High-resolution spectroscopy on trapped molecular ions in rotating electric fields : A new approach for measuring the electron electric dipole moment. *Journal of Molecular Spectroscopy*, 270(1):1–25, 2011.

[106] T. D. Lee and C. N. Yang. Parity nonconservation and a two-component theory of the neutrino. *Phys. Rev.*, 105:1671–1675, 3 1957.

[107] T. H. Loftus, M. D. Swallows, W. C. Griffith, M. V. Romalis, B. R. Heckel, and E. N. Fortson. Measurement of Linear Stark Interference in 199Hg. *Physical Review Letters*, 106(25):253002, June 2011.

[108] H. Loh, K. C. Cossel, M. C. Grau, K.-K. Ni, E. R. Meyer, J. L. Bohn, J. Ye, and E. A. Cornell. Precision spectroscopy of polarized molecules in an ion trap. *Science*, 342(6163):1220–1222, 2013.

[109] C. M. Marian, U. L. F. Wahlgren, O. D. D. Gropen, and P. Pyykko. Bonding and electronic structure in diatomic ThO: quasirelativistic effective core potential calculations. *J. Mol. Struct.*, 169:339, 1987.

[110] S. P. Martin. A supersymmetry primer. *Adv. Ser. Direct. High Energy Phys*, 21(515):1–153, 2010.

[111] S. E. Maxwell, N. Brahms, R. DeCarvalho, D. R. Glenn, J. S. Helton, S. V. Nguyen, D. Patterson, J. Petricka, D. DeMille, and J. M. Doyle. High-Flux Beam Source for Cold, Slow Atoms or Molecules. *Physical Review Letters*, 95(17):173201, Oct. 2005.

[112] G. Mead. Deformation of the Geomagnetic Field by the Solar Wind. *Journal of Geophysical Research*, 69, 1964.

[113] E. Meyer, J. Bohn, and M. Deskevich. Candidate molecular ions for an electron electric dipole moment experiment. *Physical Review A*, 73(6):062108, June 2006.

[114] Y. Michimura, N. Matsumoto, N. Ohmae, W. Kokuyama, Y. Aso, M. Ando, and K. Tsubono. New limit on lorentz violation using a double-pass optical ring cavity. *Phys. Rev. Lett.*, 110:200401, 5 2013.

[115] B. P. V. Milligen and A. L. Fraguas. Expansion of vacuum magnetic fields in toroidal harmonics. 81:74–90, 1994.

[116] N. S. Mosyagin, M. G. Kozlov, and A. V. Titov. Electric dipole moment of the electron in the YbF molecule. *Journal of Physics B: Atomic, Molecular and Optical Physics*, 31(19):L763–L767, Oct. 1998.

[117] M. Munschy, D. Boulanger, P. Ulrich, and M. Bouiflane. Magnetic mapping for the detection and characterization of UXO: Use of multi-sensor fluxgate 3-axis magnetometers and methods of interpretation. *Journal of Applied Geophysics*, 61(3-4):168–183, Mar. 2007.

[118] S. A. Murthy, D. Krause, Z. L. Li, and L. R. Hunter. New limits on the electron electric dipole moment from cesium. *Phys. Rev. Lett.*, 63:965–968, 8 1989.

[119] K.-K. Ni, S. Ospelkaus, M. H. G. de Miranda, A. Pe'er, B. Neyenhuis, J. J. Zirbel, S. Kotochigova, P. S. Julienne, D. S. Jin, and J. Ye. A high phase-space-density gas of polar molecules. *Science*, 322(5899):231–235, 2008.

[120] R. Nicholls. Approximate formulas for franck–condon factors. *The Journal of Chemical Physics*, 74(12):6980–6981, 1981.

[121] d. NIST Mass Spec Data Center, S.E. Stein. Mass spectra. In P. Linstrom and W. Mallard, editors, *NIST Chemistry WebBook, NIST Standard Reference Database Number 69*. National Institute of Standards and Technology, `http://webbook.nist.gov`, 2016.

[122] B. Oleary. Average ellipticity in readout combined with polarization switching gives ac stark shift phase. `http://tinyurl.com/ac-stark-shift-phase-mechanism` (2015/07/20).

[123] B. OLeary. Characterization of degaussing set-up with exponential waveform. `https://bussle.rc.fas.harvard.edu/lablog_EDMgraduate_2011-Brendon_OLeary/2012/06/characterization_of_degaussing.html` (2012/06/30).

[124] B. Oleary. χ^2 discrepancy (and resolution?). `https://bussle.rc.fas.harvard.edu/lablog_EDMexperiment/2013/09/statistics_chi2_discrepancy_an.html` (2013/09/04).

[125] C. Panda. Gen ii collection optics. `https://bussle.rc.fas.harvard.edu/lablog_EDMexperiment/2015/02/gen-ii-collection-optics.html` (2015/02/12).

[126] C. Panda. Gen ii stem monte carlo simulations and collection optics. `https://bussle.rc.fas.harvard.edu/lablog_graduate_2013-Chris_Panda/2015/04/gen-ii-stem-monte-carlo-simulations-and-collection-optics.html` (2015/04/28).

[127] C. Panda. Preliminary fluorescence traces in the interaction region at sensitivity. `https://bussle.rc.fas.harvard.edu/lablog_EDMexperiment/2016/09/preliminary-fluorescence-traces-in-the-interaction-region-at-sensitivity.html` (2016/09/07).

[128] C. Panda. Signals in the interaction region doppler width checks. `https://bussle.rc.fas.harvard.edu/lablog_EDMexperiment/2015/10/signals-in-the-interaction-region-doppler-width-checks.html` (2015/10/12).

[129] C. D. Panda, B. R. O'Leary, A. D. West, J. Baron, P. W. Hess, C. Hoffman, E. Kirilov, C. B. Overstreet, E. P. West, D. DeMille, J. M. Doyle, and G. Gabrielse. Stimulated raman adiabatic passage preparation of a coherent superposition of tho $H^3\Delta_1$ states for an improved electron electric-dipole-moment measurement. *Phys. Rev. A*, 93:052110, May 2016.

[130] A. S. Parkins, P. Marte, P. Zoller, and H. J. Kimble. Synthesis of arbitrary quantum states via adiabatic transfer of zeeman coherence. *Phys. Rev. Lett.*, 71:3095–3098, Nov 1993.

[131] R. A. Patten. Michelson Interferometer as a Remote Gauge. *Applied Optics*, 10(12):2717–2721, 1971.

[132] D. Patterson and J. M. Doyle. Bright, guided molecular beam with hydrodynamic enhancement. *The Journal of Chemical Physics*, 126(15):154307, Apr. 2007.

[133] J. Paulovic, T. Nakajima, K. Hirao, R. Lindh, and P. A. Malmqvist. Relativistic and correlated calculations on the ground and excited states of ThO. *J. Chem. Phys.*, 119(2):798–805, 2003.

[134] A. Petrov. ac stark effect in tho h 3 δ 1 for the electron electric-dipole-moment search. *Physical Review A*, 91(6):062509, 2015.

[135] A. Petrov, L. Skripnikov, A. Titov, N. Hutzler, P. Hess, B. OLeary, B. Spaun, D. DeMille, G. Gabrielse, and J. Doyle. Zeeman interaction in ThO H ˆ{3}\Delta_{1} for the electron EDM search. *arXiv:1404.4024v1*, pages 1–8, 2014.

[136] M. A. Player and P. G. H. Sandars. An experiment to search for an electric dipole moment in the $^3P_2$ metastable state of xenon. *J. Phys. B*, 3:1620–1635, 1970.

[137] M. Pospelov and A. Ritz. Electric dipole moments as probes of new physics. *Ann. Phys.*, 318(1):119–169, July 2005.

[138] M. E. Pospelov and I. B. Khriplovich. Electric Dipole Moment of the W boson and the Electron in the Kobayashi-Maskawa Model. *Yad. Fiz.*, 53:1030–1033, 1991.

[139] E. M. Purcell and N. F. Ramsey. On the Possibility of Electric Dipole Moments for Elementary Particles and Nuclei. *Phys. Rev.*, 78(6):807, June 1950.

[140] B. Regan. *A Search for Violation of Time-Reversal Symmetry in Atomic Thallium.* PhD thesis, Berkeley, 2001.

[141] B. Regan, E. Commins, C. Schmidt, and D. DeMille. New Limit on the Electron Electric Dipole Moment. *Physical Review Letters*, 88(7):18–21, Feb. 2002.

[142] N. A. Robertson, J. R. Blackwood, S. Buchman, R. L. Byer, J. Camp, D. Gill, J. Hanson, S. Williams, and P. Zhou. Kelvin probe measurements: investigations of the patch effect with applications to ST-7 and LISA. *Classical and Quantum Gravity*, 23(7):2665–2680, Apr. 2006.

[143] R. Sachs. *The Physics of Time Reversal.* University of Chicago Press, 1987.

[144] A. D. Sakharov. Violation of CP Invariance, C Asymmetry, and Baryon Asymmetry of the Universe. *JETP Lett.*, 5:27–30, 1967.

[145] E. E. Salpeter. Some atomic effects of an electronic electric dipole moment. *Phys. Rev.*, 112:1642–1648, 1958.

[146] P. G. H. Sandars. The Electric Dipole Moment of an Atom. *Physics Letters*, 14(3):194, Feb. 1965.

[147] P. G. H. Sandars and E. Lipworth. Electric Dipole Moment of the Cesium Atom. A New Upper Limit to the Electric Dipole Moment of the Free Electron. *Physical Review Letters*, 13(24):718, 1964.

[148] B. Sauer, J. Hudson, D. Kara, I. Smallman, M. Tarbutt, and E. Hinds. Prospects for the measurement of the electron electric dipole moment using YbF. *Physics Procedia*, 17:175–180, Jan. 2011.

[149] L. I. Schiff. Measurability of Nuclear Electric Dipole Moments. *Physical Review*, 132(5):2194, 1963.

[150] Schott. Schott Borofloat Glass Product Information. Technical Report 502, Schott, 2013.

[151] J. Schwinger. The theory of quantized fields. i. *Phys. Rev.*, 82:914–927, Jun 1951.

[152] P. K. Sinervo. Definition and treatment of systematic uncertainties in high energy physics and astrophysics. In *Statistical Problems in Particle Physics, Astrophysics, and Cosmology*, volume 1, page 122. Citeseer, 2003.

[153] L. V. Skripnikov, A. N. Petrov, and A. V. Titov. Communication: Theoretical study of ThO for the electron electric dipole moment search. *The Journal of chemical physics*, 139(22):221103, Dec. 2013.

[154] L. V. Skripnikov and A. V. Titov. Theoretical study of thorium monoxide for the electron electric dipole moment search: electronic properties of $h(3)\delta(1)$ in tho. *J. Chem. Phys.*, 142:024301, 2015.

[155] N. Solmeyer, K. Zhu, and D. S. Weiss. Note: mounting ultra-high vacuum windows with low stress-induced birefringence. *The Review of scientific instruments*, 82(6):066105, June 2011.

[156] J. L. Sorensen, D. Mller, T. Iversen, J. B. Thomsen, F. Jensen, P. Staanum, D. Voigt, and M. Drewsen. Efficient coherent internal state transfer in trapped ions using stimulated raman adiabatic passage. *New Journal of Physics*, 8(11):261, 2006.

[157] M. Sozzi. *Discrete Symmetries and CP Violation: From Experiment to Theory*. OUP Oxford, 2008.

[158] B. N. Spaun. *A Ten-Fold Improvement to the Limit of the Electron Electric Dipole Moment*. PhD thesis, Harvard University, 2014. (advisor: G. Gabrielse).

[159] T. S. Stein, J. P. Carrico, E. Lipworth, and M. C. Weisskopf. Electric dipole moment of the cesium atom. a new upper limit to the electric dipole moment of the free electron. *Phys. Rev. Lett.*, 19:741, 1967.

[160] T. J. Sumner, J. M. Pendlebury, and K. F. Smith. Conventional Magnetic Shielding. *J. Phys. D*, 20:1095–1101, 1987.

[161] M. D. Swallows, T. H. Loftus, W. C. Griffith, B. R. Heckel, E. N. Fortson, and M. V. Romalis. Techniques used to search for a permanent electric dipole moment of the ^{199}hg atom and the implications for *CP* violation. *Phys. Rev. A*, 87:012102, Jan 2013.

[162] J. Voigt, S. Knappe-Grüneberg, A. Schnabel, R. Körber, and M. Burghoff. Measures to reduce the residual field and field gradient inside a magnetically shielded room by a factor of more than 10. *Metrology and Measurement Systems*, 20(2):239–248, 2013.

[163] A. Vutha and D. DeMille. Geometric phases without geometry. *arXiv*, July 2009.

[164] A. C. Vutha. *A search for the electric dipole moment of the electron using thorium monoxide*. PhD thesis, Yale University, 2011.

[165] A. C. Vutha, W. C. Campbell, Y. V. Gurevich, N. R. Hutzler, M. Parsons, D. Patterson, E. Petrik, B. Spaun, J. M. Doyle, G. Gabrielse, and D. DeMille. Search for the electric dipole moment of the electron with thorium monoxide. *Journal of Physics B*, 43(7):74007, Apr. 2010.

[166] A. C. Vutha, B. Spaun, Y. V. Gurevich, N. R. Hutzler, E. Kirilov, J. M. Doyle, G. Gabrielse, and D. Demille. Magnetic and electric dipole moments of the H ˆ{3}\Delta_{1} state in ThO. pages 1–4.

[167] A. C. Vutha, B. Spaun, Y. V. Gurevich, N. R. Hutzler, E. Kirilov, J. M. Doyle, G. Gabrielse, and D. DeMille. Magnetic and electric dipole moments of the $H^3\Delta_1$ state in ThO. *Physical Review A*, 84(3):034502, Sept. 2011.

[168] M. C. Weisskopf, J. P. Carrico, H. Gould, E. Lipworth, and T. S. Stein. Electric dipole moment of the cesium atom. a new upper limit to the electric dipole moment of the electron. *Phys. Rev. Lett.*, 21:1645, 1968.

[169] T. Wentink and R. J. Spindler. The isoelectronic series ScF through ThO, I notes on the band spectra of TiO, HfO and ThO. *Journal of Quantitative Spectroscopy and Radiative Transfer*, 12(11):1569–1590, Nov. 1972.

[170] A. West. Alignment of lenses for pointing feedback. `https://bussle.rc.fas.harvard.edu/lablog_EDMpostdoc_2013-Adam_West/2016/02/alignment-of-lenses-for-pointing-feedback.html` (2016/02/08).

[171] A. West, Z. Lasner, D. DeMille, E. West, C. Panda, J. Doyle, G. Gabrielse, A. Kryskow, and C. Mitchell. An underappreciated radiation hazard from high voltage electrodes in vacuum. *arXiv preprint arXiv:1607.01389*, 2016.

[172] E. West. Beam attenuation. `http://www.doylegroup.harvard.edu/files/internal/Beam_Attenuation_Doyle_Group_11.14.12.pdf` (2012/08/21).

[173] E. West. Steeringthemolecularbeam withtwocollimators. `https://bussle.rc.fas.harvard.edu/wp-content/uploads/EDMexperiment/2011/07/21/Elizabeth-ACME_Collaboration_Presentation_7.21.2011.pdf` (2011/07/21).

[174] E. West. Testing magnetometer guide structure. `https://bussle.rc.fas.harvard.edu/lablog_EDMgraduate_2009-Elizabeth_Petrik/2013/08/testing_magnetometer_guide_str_1.html` (2013/08/14).

[175] C. S. Wood, S. C. Bennett, D. Cho, B. P. Masterson, J. L. Roberts, C. E. Tanner, and C. E. Wieman. Measurement of Parity Nonconservation and an Anapole Moment in Cesium. *Science*, 275:1759–1763, 1997.

[176] C. S. Wu, E. Ambler, R. W. Hayward, D. D. Hoppes, and R. P. Hudson. Experimental test of parity conservation in beta decay. *Phys. Rev.*, 105:1413–1415, Feb 1957.

[177] L. P. Yatsenko, B. W. Shore, and K. Bergmann. Detrimental consequences of small rapid laser fluctuations on stimulated raman adiabatic passage. *Phys. Rev. A*, 89:013831, Jan 2014.

[178] A. Zee. *Quantum field theory in a nutshell*. Princeton university press, 2010.